# Drug-discovery tools for cystic fibrosis: optical probes to quantify gating and trafficking of ΔF508-CFTR

*Emily Langron*

A thesis submitted to

**University College London**

for the degree of

**Doctor of Philosophy**

Department of Neuroscience, Physiology and Pharmacology
University College London

19th July 2016

*I, Emily Langron, confirm that the work presented in this thesis is my own. Where information has been derived from other sources, I confirm that this has been indicated in the thesis.*

# Abstract

Cystic fibrosis (CF) is a debilitating disease caused by mutations in the cystic fibrosis transmembrane conductance regulator (*CFTR*) gene, which codes for the CFTR anion channel. ΔF508, the most common CF-associated mutation, causes both a gating and a trafficking defect in the CFTR protein.

This thesis describes the optimisation and use of two fluorescence assays, capable of measuring the two defects caused by the ΔF508 mutation.

Yellow fluorescent protein (YFP)-CFTR, in which halide sensitive YFP is tagged to the N-terminal of the CFTR coding sequence, is a functional assay, used to test for ΔF508-CFTR potentiator activity. CFTR-pHTomato, in which the pH sensor is tagged to the fourth extracellular loop of CFTR, is used to measure membrane density and internal CFTR expression.

Human embryonic kidney cells (HEK293 cells), expressing YFP-ΔF508-CFTR were used to screen a pilot library of compounds with some structural similarity to known potentiator VX-770. Ligand-based virtual screening was then used to construct two further libraries, based on VX-770 and the lead hit compound from the pilot screen. A number of novel ΔF508-CFTR potentiators were identified in each of the screens.

Recently published studies suggest that chronic treatment with VX-770 decreases ΔF508-CFTR density at the plasma membrane, potentially limiting its clinical effectiveness. ΔF508-CFTR-pHTomato was used to show that a number of hit compounds from our screens did not decrease membrane density of ΔF508-CFTR.

The YFP-CFTR assay was also used for studies investigating the mechanism of potentiation by VX-770. We provide evidence that WT-CFTR does not require phosphorylation for potentiation by VX-770, which has not been reported previously. Additionally, studies using gating mutations do not support the current hypothesis that VX-770 stabilises the post-hydrolytic open state in the CFTR gating cycle.

# Acknowledgments

I am very grateful to my supervisor, Dr. Paola Vergani, for her unwavering encouragement, guidance and teaching throughout the course of my PhD. Also, thanks to all members of the Vergani and Moss labs, both past and present, for many useful conversations and for making my time at UCL so enjoyable. I would like to thank Dr. David Benton particularly, for patient teaching of the patch clamp technique, and tissue culture support.

Finally, thanks to my family, friends and Todd, whose support made this possible.

# Contents

# List of Figures

# List of Tables



# Imaging movies

# Chapter 1

# Introduction

## 1.1 Cystic fibrosis disease overview

### 1.1.1 Cystic Fibrosis

Cystic fibrosis (CF) is the most common life-threatening hereditary disease in the Caucasian population, affecting approximately 10,500 patients in the UK (UK CF Registry annual report 2014). The disease is caused by mutations in the cystic fibrosis transmembrane conductance regulator (*CFTR*) gene, which codes for the CFTR chloride ($Cl^-$) channel. To date, over 2,000 mutations have been identified in the *CFTR* gene (www.cftr2.org).

Due to widespread expression of CFTR in the body, CF manifests as a multi-organ disease, although the severity of specific symptoms varies between patients. Clinically, the most prevalent symptom of CF is lung disease - characterised by persistent coughing, wheezing and repeated chest infections. Colonisation of lung epithelium by bacteria such as *Pseudomonas aeruginosa*, which forms antibiotic-resistant biofilms (Singh et al., 2000), induces a chronic infection and inflammation cycle, leading to progressive organ degeneration. 85% of CF patients have pancreatic insufficiency, causing malnutrition and poor weight gain, and an abnormality of the *vas deferens* development leaves most male patients infertile (Lubamba et al., 2012). Life expectancy of CF patients has improved dramatically since the disease was first described in the 1930s, from infancy to a projected survival age of 50 for children born with CF since 2000 (Dodge et al., 2007). However, the increased age of the patient population has exposed multiple CF co-morbidities, such as CF-related diabetes, osteoporosis and arthritis.

With no cure available, the majority of CF patients are treated only for symptoms. Despite vast improvements in care, the life of a CF patient is still blighted by a daily treatment regimen of physiotherapy, antibiotics, bronchodilators, and enzyme tablets.

### 1.1.2 CF pathophysiology

The CFTR anion channel is expressed on the apical membrane of epithelial cells, where it plays a role in regulating transepithelial fluid flow in many organs. In CF, $Cl^-$ transport through CFTR is reduced or eliminated. Although this is known to be the basis of the disease, the order of events leading to the development of symptoms is not entirely

understood. Many theories exist as to how mutations in CFTR contribute to progression of CF pathology.

### 1.1.2.1 Dehydrated airway surface liquid hypothesis

Airway surface liquid (ASL) is a film of fluid lining the airway lumen, covering the epithelial surface. It is composed of the airway mucus layer, separated from the epithelium by the watery periciliary liquid layer. In healthy lungs, the periciliary liquid layer allows beating of cilia, resulting in mucus movement towards the pharynx and eventual clearance, defending from infection by removing particles which become trapped in the mucus layer. In CF, mucociliary clearance is impaired, making airways more vulnerable to infection and inflammation, ultimately leading to respiratory failure (Boucher, 2007).

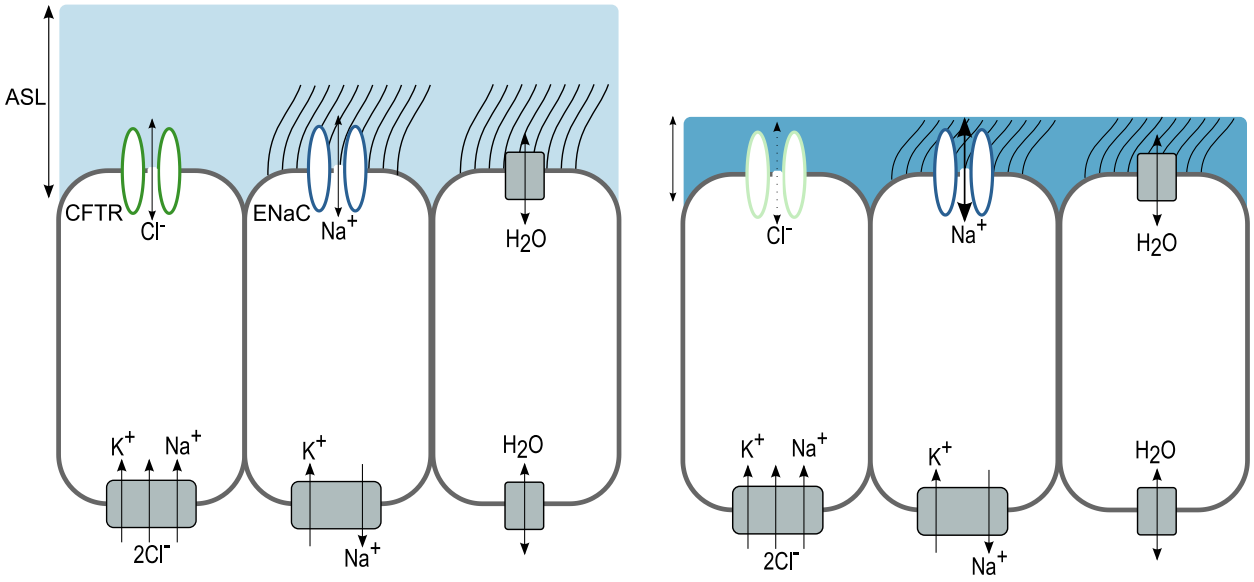


**Figure 1.1 ASL regulation in healthy and CF airways.** Left: In healthy airways, transepithelial $Cl^-$ transport via CFTR (apical) and NKCC1 (basolateral), and $Na^+$ transport via ENaC (apical) and the $Na^+/K^+$ ATPase (basolateral) regulates the water content of the ASL. A sufficiently large volume of watery ASL allows mucociliary clearance of the airways. Right: In CF, $Cl^-$ transport via CFTR is reduced or eliminated, $Na^+$ transport via ENaC is increased, and the volume of watery ASL is reduced. Dense mucus prevents cilia from beating.

One widely accepted theory claims that reduced mucociliary clearance in CF is due to dehydration of the ASL. Decreased apical $Cl^-$ efflux via CFTR and increased sodium ($Na^+$) absorption via epithelial $Na^+$ channels (ENaC) reduces the water content of the ASL (Figure 1.1). Dehydrated, heavy mucus lining the airways of CF patients is difficult to shift by coughing, and prone to infection.

Nasal potential difference (NPD) measurements are used to assess the apical $Cl^-$ and $Na^+$ permeability of nasal cells, providing useful information for CF diagnosis. As well as reduced $Cl^-$ permeability, CF patient NPD recordings show transepithelial potentials very strongly altered by the ENaC channel blocker amiloride (Middleton and House, 2010), suggesting increased ENaC activity. It is not clear whether this is due to direct regulation of ENaC by CFTR (Stutts et al., 1995), or an indirect effect, for example mediated by reduced $Cl^-$ permeability (Bachhuber et al., 2005).

#### 1.1.2.2 Bicarbonate and pH hypothesis

CFTR is also permeable to bicarbonate ions ($HCO_3^-$), with a permeability ratio of 0.14 compared to $Cl^-$ (calculated from bi-ionic reversal potential shifts; Linsdell et al., 1997). CFTR function, therefore, has the capacity to influence local pH on epithelial surfaces. The pH of the ASL in CF airways is ~0.5 pH units lower than that of healthy epithelia (Coakley et al., 2003). This has the potential to affect pH-dependent processes on the apical membrane. For example, secreted protein short palate, lung, and nasal epithelial clone 1 (SPLUNC1), a regulator of ENaC, is unable to interact with ENaC in the acidic pH of CF ASL (Garland et al., 2013). Dysregulation of ENaC allows hyperabsorption of $Na^+$, and likely contributes to dehydration of the ASL. Low pH-ASL also has reduced bactericidal properties, which contributes to the chronic airway infections associated with CF (Pezzulo et al., 2012)

#### 1.1.2.3 Immune response hypothesis

Upon exposure to bacteria, a large inflammatory response is launched in the CF lung. However, this response is ineffective in eradicating infections. It remains unclear whether chronic inflammation is a secondary symptom of the disease, caused by increased pathogen exposure, or a primary defect in CF (Ratner and Mueller, 2012).

CFTR mutations have been associated with constitutive inflammatory status and neutrophil accumulation in the naive CF airway (Tirouvanziam et al., 2000). This suggests that even before pathogen exposure, CF airways are in an inflammatory state. An intrinsic inability to eradicate bacteria, as seen in the newborn pig, has been suggested as the defect which initiates the inflammatory pathology seen in CF (Stoltz et al., 2010).

It has also been hypothesised that expression of CFTR on immune cells is the cause of irregularities in the immune response (Mueller et al., 2011). The fact that CF patients do not suffer with widespread infections casts doubt upon this theory.

The progression of CF disease is likely to be influenced by some, or all, of the events discussed here, but the respective weight of these factors is disputed. Whilst multiple

theories of CF disease aetiology exist, most would agree that correction of $Cl^-$ transport via CFTR would be, at least somewhat, successful in treating the disease. Indeed, the clinical success of Ivacaftor (Vertex Pharmaceuticals; Ramsey et al., 2011), the first approved drug to target CFTR directly, supports this concept.

#### 1.1.2.4 CF-causing mutation classes

CFTR mutations are grouped into classes I to VI, according to the nature of the effect on the CFTR protein (Figure 1.2). Class II includes deletion of phenylalanine at position 508 (ΔF508), which is the most common CF-causing mutation, found on at least one allele in ~90% of patients (UK CF Registry annual report 2014).

The native mutation carried by ΔF508-CF patients is not a straightforward loss of the triplet encoding F508. Rather, it is the loss of the last one or two nucleotides of the triplet encoding isoleucine 507 (ATC), and of the first one or two nucleotides of the triplet encoding phenylalanine 508 (TTT). The loss of these three nucleotides, therefore, also results in a synonymous codon change at I507 (ATC to ATT). The synonymous mutation itself contributes to the ΔF508-CFTR phenotype by changing the rate of cotranslational folding and CFTR:chaperone interactions, which affects endoplasmic reticulum (ER)-associated degradation (ERAD) (Lazrak et al., 2013; Shah et al., 2015).

Due to the prevalence of this mutation in the patient population, this project focussed on CF caused by ΔF508, and the associated drug discovery effort. All ΔF508-CFTR work was carried out using plasmids encoding the native human ΔF508-CFTR, including the synonymous I507-ATT mutation.

## 1.2 WT-CFTR gating

CFTR is a member of the ATP-binding cassette (ABC) transporter superfamily, unique in that it functions as an ion channel rather than as an active transporter. Two membrane spanning domains (MSDs), formed of 12 transmembrane helices (TMs), form an anion selective pore in the plasma membrane (Figure 1.3). TMs are linked by intracellular loops (ICLs) and extracellular loops (ECLs). Gating is controlled by intracellular domains: two nucleotide binding domains (NBDs) and the regulatory (R)-domain. Protein kinase A (PKA)-dependent phosphorylation of multiple sites on the R-domain is generally thought to be necessary as a pre-requisite for CFTR gating. Once phosphorylated, gating of the pore is controlled by adenosine triphosphate (ATP)-dependent NBD dimerisation and separation.

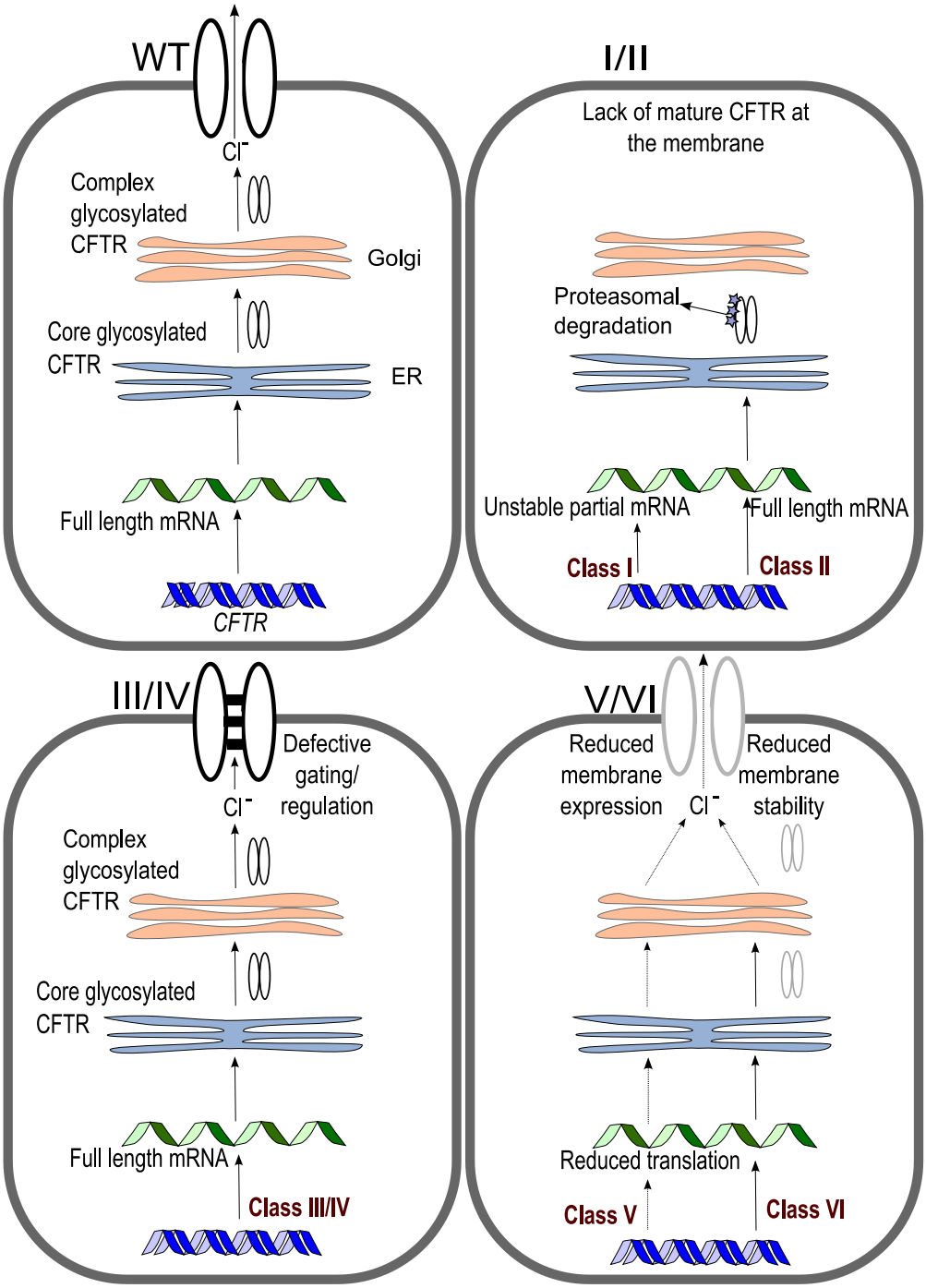


**Figure 1.2 CFTR mutation classes.** Modified from Boyle & De Boeck 2013. Top left: WT-CFTR is processed at the ER and trafficked to the Golgi, where it undergoes complex glycosylation. Mature CFTR is expressed at the membrane with a long half-life (~16 h; Sharma et al., 2004). Top right: Class I mutations introduce premature stop codons, which produce unstable partial mRNA strands, incapable of undergoing translation. Class II mutations cause a folding defect, recognised by quality control mechanisms and targeted for proteasomal degradation. Bottom left: Classes III and IV cause functional defects, either by a gating defect (class III), or reduced single-channel conductance (class IV). Bottom right: Class V mutations are mostly splicing defects, which reduce the amount of correct CFTR mRNA, so protein expression is reduced. Class VI mutations reduce stability at the membrane.

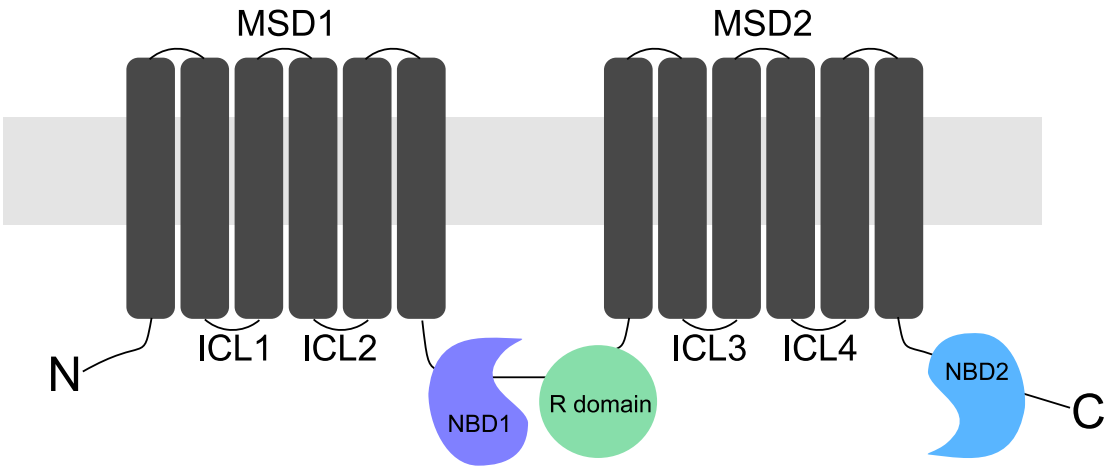


**Figure 1.3 CFTR topology.** CFTR is formed of two MSDs, each formed of six TMs. The two MSDs are linked by NBD1, and the R-domain, unique to CFTR. The C-terminal of MSD2 is followed by NBD2. CFTR activation is regulated by PKA-dependent phosphorylation of the R-domain.

The NBDs form a head-to-tail dimer, creating two ATP-binding sites at the interface: non-catalytic site 1 and catalytic site 2 (Figure 1.4). ATP binds and remains bound at site 1 throughout many gating cycles (Tsai et al., 2010). Upon ATP binding at site 2, NBD dimerisation is favoured, and a conformational change is transmitted to the TMs, such that the CFTR pore opens ($O_1$ state; Vergani et al., 2005). The channel remains open until ATP-hydrolysis occurs at site 2, whereby CFTR enters a short-lived post-hydrolytic open state ($O_2$ state), and eventually closes (Jih et al., 2012b; Jih and Hwang, 2013). Due to the stability of the $O_1$ state, very few wild type (WT)-CFTR gating events terminate via the non-hydrolytic pathway (Csanády et al., 2010).

The mechanism by which phosphorylation of the R-domain regulates CFTR gating is not entirely clear. The R-domain is a ~200 amino acid, intrinsically disordered structure, unique to CFTR. Crystal structures of other members of the ABC transporter superfamily do not contain the R-domain and flexibility of the domain means crystallisation has so far been impossible. Low resolution 3D structural studies suggest the R-domain lies in close proximity to the ICLs, in unphosphorylated CFTR (Zhang et al., 2011). Little else is known about the location of the R-domain in inactive and gating CFTR, which makes deduction of the regulatory mechanism challenging.

Fifteen phosphorylation sites have been identified on the R-domain, with no specific site critical for activation, but rather phosphorylation of multiple sites has a cumulative effect (Chang et al., 1993). It appears that the unphosphorylated R-domain has an inhibitory effect on the channel, as CFTR with the R-domain missing (CFTR-ΔR) is capable of normal gating in the absence of phosphorylation (Chan et al., 2000). Studies of the isolated R-domain have

demonstrated dynamic interdomain interactions in CFTR. For example, the unphosphorylated R-domain interacts strongly with NBD1, whereas the phosphorylated R-domain interacts with the C-terminal (Kanelis et al., 2010; Bozoky et al., 2013).

One hypothesis for regulation is that the R-domain is located in an inhibitory position, physically preventing NBD dimerisation. Upon phosphorylation, a conformational shift causes the R-domain to move away from NBD1 and bind either another domain, such as the C-terminal, or an accessory protein, to allow NBD dimerisation and gating (Kanelis et al., 2010; Bozoky et al., 2013).

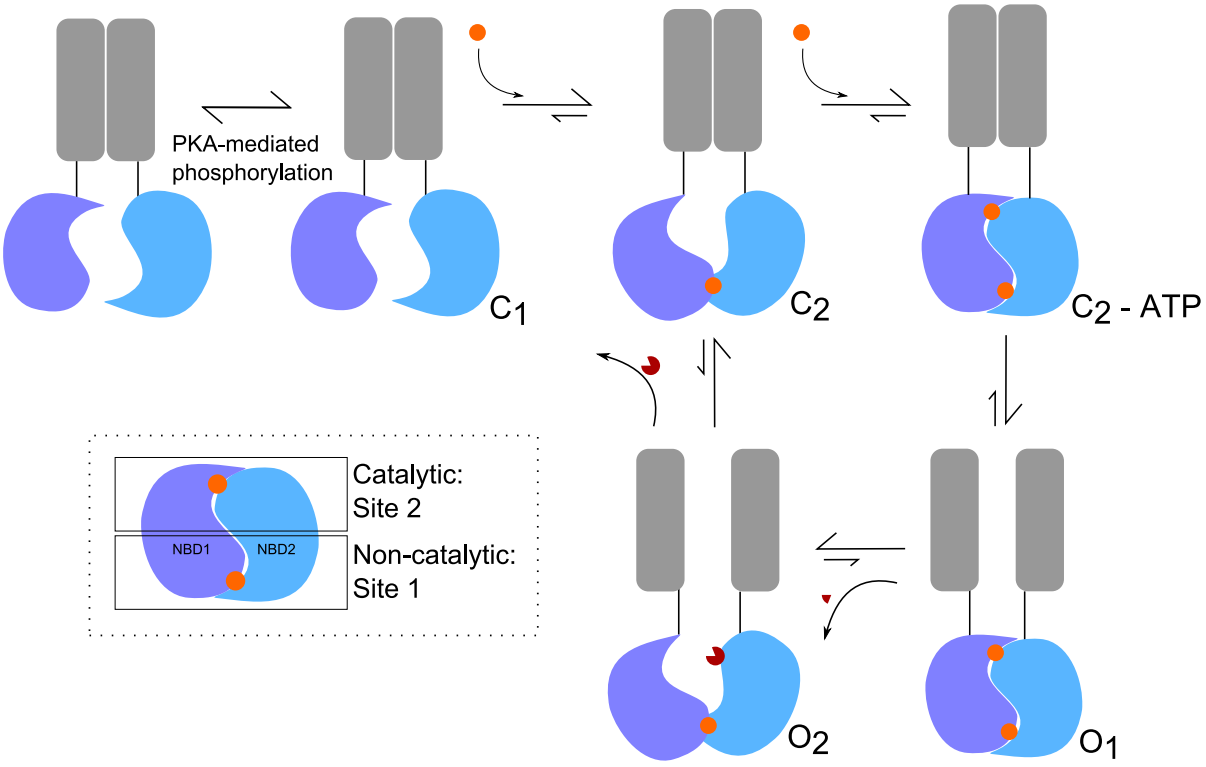


**Figure 1.4 WT-CFTR gating mechanism**. Following phosphorylation of the R-domain by PKA, ATP binds the two ATP-binding sites located at the interface of the NBD dimer ($C_2$-ATP). ATP remains bound at non-catalytic site 1 (see inset) for many gating cycles. Upon ATP binding at site 2, and NBD dimerisation, the channel opens ($C_2$-ATP ↔ $O_1$). Channel closure is triggered by ATP hydrolysis at site 2 ($O_1$ ↔ $C_2$, via the short-lived $O_2$). Orange = ATP.

## 1.3 ΔF508-CFTR: Causes of the gating defect

The ΔF508 mutation affects the folding of CFTR during biosynthesis, causing production of an aberrant protein, which is recognised by quality control mechanisms and targeted for proteasomal degradation. There are ways in which this can be overcome in the laboratory to enable the study of ΔF508-CFTR ion channel function at the plasma membrane.

Single channel patching of rescued ΔF508-CFTR showed a ~15-fold reduction in open probability ($P_o$), caused mainly by a decrease in the opening rate (Dalemans et al., 1991; Miki et al., 2010). The cause of the gating defect is unknown. It is unlikely to be caused by a disruption of ATP binding, because although F508 is located in NBD1, homology models suggest that it is not positioned at the NBD dimer interface (Serohijos et al., 2008). Strong phosphorylation of ΔF508-CFTR demonstrates that normal gating can be achieved. In these conditions, the dose-response curve to ATP is not shifted, suggesting that indeed affinity for ATP binding is unchanged (Wang et al., 2000). Moreover, isolated NBDs do not display reduced ATP binding affinity when ΔF508 is introduced (Rabeh et al., 2012).

Homology models suggest the functional defect is more likely caused by altered interdomain interactions. One such interaction is at the NBD1:ICL4 interface, an interaction which is modified in ΔF508-CFTR (Serohijos et al., 2008). It is possible that the trigger for opening, which comes from NBD dimerisation, is not effectively transmitted to the TMs that form the pore, due to disruption at this interface. Cross-linking residues on either side of the interface abolishes gating (Serohijos et al., 2008). This suggests that dynamic interaction between the two domains is necessary to allow CFTR gating.

The slow opening rate associated with ΔF508-CFTR is indicative of a higher energetic barrier to opening, i.e. a higher-energy transition state with respect to the closed state. It has recently been shown that the transition state of CFTR contains dimerised NBDs, but the pore remains closed (Sorum et al., 2015). This suggests that a great deal of molecular strain exists between the NBDs and the pore, likely at the interface at which F508 is located, underlying the high-energy transition state of CFTR gating. It is likely that loss of F508 creates extra strain at this interface, destabilising the transition state with respect to the closed state, to slow opening (Sorum et al., 2015). Indeed comparing gating characteristics of F508C, before and after reacting with an aromatic sulfhydryl reactive reagent (Cui et al., 2006), suggests that partially repairing this interaction goes some way to correcting the gating defect.

Phosphorylation of the R-domain also appears to contribute to the ΔF508-CFTR gating defect. As mentioned, high concentrations of PKA can overcome the defect resulting in gating with a $P_o$ similar to that of WT-CFTR (Wang et al., 2000). In these conditions, macroscopic ΔF508-CFTR patches are much slower to reach steady state activation following exposure to PKA. Others have recently shown that there is a reduction in phosphorylation at specific sites when comparing activated ΔF508-CFTR and WT-CFTR (Pasyk et al., 2015). These studies suggest that ΔF508-CFTR is not as good a substrate for PKA as WT-CFTR, but if maximal phosphorylation is obtained, gating is not abnormal.

As discussed below, loss of F508 induces a global conformational change in CFTR. Such a change is expected to impact many interactions, some of which are likely to be involved in gating. It seems probable that the gating defect is caused by both a change in phosphorylation propensity, and altered interdomain interactions required for opening of the pore.

### 1.3.1 ΔF508-CFTR potentiator compounds

A number of CFTR potentiators have been identified, with Ivacaftor (in which the active component is VX-770) approved in 2012 for the treatment of CF caused by G551D and a number of other gating mutations (Van Goor et al., 2009, 2013; Yu et al., 2012). This class of mutations (class III, Figure 1.2) is the most promising group for treatment by CFTR potentiators, because, for these mutant CFTR molecules, trafficking and maturation is normal (Gregory et al., 1991; Bompadre et al., 2007). As the only approved CFTR potentiator, VX-770 was used throughout this project as a benchmark compound and positive control.

Successful clinical trials using VX-770 to treat G551D-CF patients - 15% improvement in lung function (measured by forced expiratory volume in one s; $FEV_1$), sweat $Cl^-$ levels reduced to below that which indicates CF, and increased weight gain (Ramsey et al., 2011; Davies et al., 2013) – led to the approval of VX-770 for the treatment of G551D-CF patients.

Following promising *in vitro* data (Van Goor et al., 2009), VX-770 was tested as a treatment for ΔF508-CF, but failed to have a clinical effect (Flume et al., 2012), presumably because an insufficient number of ΔF508-CFTR molecules are located at the membrane (class II, Figure 1.2). Therefore, combination treatment using VX-770 alongside processing corrector compound Lumacaftor (Vertex Pharmaceuticals; active component VX-809), which promotes trafficking of ΔF508-CFTR to the membrane, was tested in clinical trials (Wainwright et al., 2015). In 2015, Orkambi (Vertex Pharmaceuticals; VX-770/VX-809 combination treatment) was approved for the treatment of ΔF508-CF homozygous patients, despite much smaller clinical gains than those obtained by VX-770 treatment of G551D-CF patients.

The mechanism by which VX-770 exerts potentiator effects is only partially understood. Generally, compounds stabilise the open state or increase the opening rate in order to potentiate CFTR gating. For example, slowing ATP hydrolysis (as seen with VRT-532; Wellhauser et al., 2009), or stabilising the NBD dimer (e.g. with non-hydrolysable ATP analogues), potentiates CFTR gating.

Single channel patch traces of WT-CFTR and G551D-CFTR show an increase in $P_o$ in the presence of VX-770, achieved mainly by an increase in mean open time (Van Goor et al., 2009; Yu et al., 2012). Whilst open time of WT-CFTR is dependent on ATP-hydrolysis, G551D-CFTR does not undergo ATP-hydrolysis, and gates only via infrequent ATP-independent events (possibly via $C_2 \leftrightarrow O_2$; Li et al., 1996; Bompadre et al., 2007). Stabilisation of the $O_2$ state has been proposed as a mechanism by which both ATP-dependent and ATP-independent open events could be prolonged (Figure 1.4; Jih and Hwang, 2013).

## 1.4 WT-CFTR folding and trafficking

Although potentiation of ΔF508-CFTR gating is a key step in reversing the molecular defect caused by the mutation, this method has so far been ineffective in the clinic (Flume et al., 2012). Assuming this is caused by a lack of ΔF508-CFTR at the plasma membrane, effective trafficking correctors (such as VX-809) might enable potentiators to exert a clinical effect. The ΔF508-CFTR folding defect is complex and first requires a description of WT-CFTR folding and trafficking.

Full length WT-CFTR exists in three distinct forms: unglycosylated, core-glycosylated, and complex-glycosylated CFTR. The three glycosylation states can be clearly identified by size when visualised on an immunoblot, and are often referred to as bands A, B and C, respectively. Core-glycosylation occurs at the ER, and thus represents immature, ER-associated CFTR. Complex-glycosylation occurs at the Golgi, and therefore is present only on mature, membrane-associated CFTR (Cheng et al., 1990). Due to cotranslational glycosylation, band A is not detected in cellular extracts.

CFTR folding takes place both cotranslationally within the ER membrane (Lu et al., 1998), and posttranslationally (Du et al., 2005). Individual domain folding, interdomain interactions and domain swapping must occur in a precise manner, in order to influence each other appropriately. A mutation in one domain can therefore influence the folding and structure of other domains, or even the entire protein (Du and Lukacs, 2009). Figure 1.5A shows the interdomain interactions that occur during WT-CFTR folding. During translation, NBD1 interacts with MSD1 and MSD2, to form a compact, four domain unit (MSD1, NBD1, R-domain and MSD2) capable of export from the ER. NBD2 is incorporated posttranslationally to form a folded, functioning channel inserted in the plasma membrane. WT-CFTR remains at the membrane with a half-life of ~16 h (Sharma et al., 2004), where it is maintained via endosomal recycling, or targeted to lysosomes for degradation (Ameen et al., 2007).

## 1.5 ΔF508-CFTR – the folding defect

The loss of phenylalanine at position 508 prevents maturation to complex-glycosylated, membrane-associated CFTR (Cheng et al., 1990). A global misfolding of the protein causes retention of ΔF508-CFTR at the ER, from where it is degraded by ERAD mechanisms. Any ΔF508-CFTR which escapes ERAD to acquire plasma membrane localisation has a short half-life (< 4 h; Lukacs et al., 1993) due to increased degradation and reduced recycling (Okiyoneda et al., 2010).

The ΔF508 mutation destabilises the NBD1 domain, where it is located, and disrupts interdomain interactions with MSD1 (via ICL1) and MSD2 (via ICL4) during cotranslational folding. This, in turn, prevents posttranslational incorporation of NBD2. NBD1 destabilisation and interface disruption are the two primary folding defects associated with ΔF508-CFTR (Figure 1.5B).

CFTR homology models, based on crystal structures of ABC exporters, indicate that F508 is located on the surface of NBD1, at the proposed interface between NBD1 and ICL4 (Serohijos et al., 2008). Initially, this lead to the assumption that the mutation did not perturb NBD1 structure, but rather the defect was caused by defective interdomain assembly. Repair of the NBD1:ICL4 interaction using revertant mutation R1070W, which introduces an alternative aromatic residue to the interface, increases the appearance of mature ΔF508-CFTR. Additionally, introducing the R1070W mutation in the WT-CFTR background decreases maturation, presumably by disrupting the NBD1:ICL4 interaction (Thibodeau et al., 2010). This suggests that the NBD1:ICL4 interaction is necessary for proper folding, and disturbance of the interface causes a folding defect similar to that of ΔF508-CFTR.

ΔF508-CFTR/R1070W also improves the $P_o$ compared to ΔF508-CFTR (Rabeh et al., 2012). This again highlights the importance of the NBD1:ICL4 interface in determining the energetic barrier to CFTR gating (Sorum et al., 2015).

Publication of the ΔF508-NBD1 crystal structure, which was similar to WT-NBD1, supported the interface theory, as the only noticeable difference was seen at the proposed ICL4 interface (Lewis et al., 2005). However, it has since been shown that ΔF508 also impacts on both the thermodynamic and kinetic stability of isolated NBD1 (Hoelen et al., 2010; Rabeh et al., 2012). It is possible that the similarity of the ΔF508-NBD1 and WT-NBD1 crystal structures was caused by greatly reduced protein dynamics at the low temperature required for crystallisation.

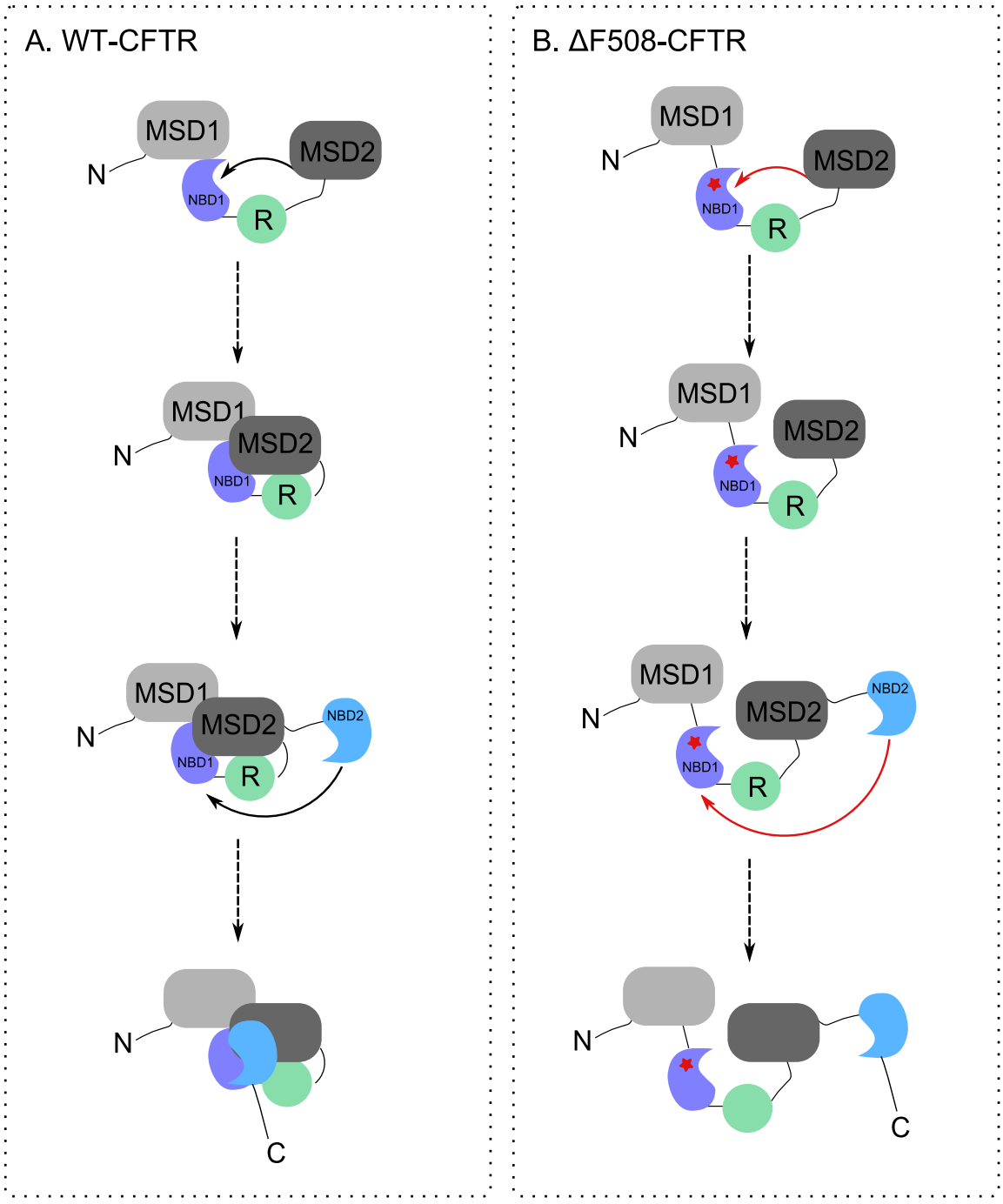


**Figure 1.5 Simplified CFTR folding model.** Modified from Cui et al. 2007 and Okiyoneda et al. 2013. A) WT-CFTR: NBD1 interacts with MSD1 and MSD2 during cotranslational folding. This four domain unit can be glycosylated and exported from the ER. NBD2 is incorporated posttranslationally. B) ΔF508-CFTR: Due to the ΔF508 mutation (red star), NBD1 cannot interact appropriately with either MSD1 (via ICL1) or MSD2 (via ICL4). Improper folding prevents export from the ER and NBD2 folding and incorporation.

Further to interdomain interactions, many chaperones interact with CFTR during folding and trafficking. Interactions with accessory proteins, such as calnexin (Farinha and Amaral, 2005) and heat shock protein (Hsp)70/Hsp90 (Yang et al., 1993; Loo et al., 1998), decide the fate of CFTR molecules, depending upon the protein conformation.

Multiple chaperone interactions are altered by ΔF508, due to misfolding of CFTR. For example, normally buried arginine framed tripeptides (which act as ER retention signals) are exposed in ΔF508-CFTR, promoting retention in the ER and subsequent proteasomal degradation (Chang et al., 1999; Roxo-Rosa et al., 2006). CFTR also contains at least one di-acidic ER exit motif. Exposure of the exit motif recruits COP-II vesicle machinery, allowing export to the Golgi (Wang et al., 2004). Exposure of multiple ER retention signals, and concealment of an export motif, contributes to ER retention of ΔF508-CFTR.

ΔF508-CFTR retained at the ER displays altered interactions with chaperones, such as Hsp90 (Coppinger et al., 2012) and CHIP (Meacham et al., 2001), which increase ubiquitination and subsequent degradation. Similar mechanisms target peripheral ΔF508-CFTR, favouring lysosomal degradation and reducing membrane half-life (Okiyoneda et al., 2010).

### 1.5.1 Correction of ΔF508-CFTR

Correction of ΔF508-CFTR folding defect can be achieved by low temperature incubation, revertant mutations, or small molecule correctors.

#### 1.5.1.1 Low temperature incubation

Although not clinically relevant, low temperature incubation is often used in the laboratory as a tool for studying ΔF508-CFTR ion channel function. Incubation at 30°C for 24 h increases mature CFTR (compared to total CFTR) to ~25% that of WT-CFTR, allowing the study of the mutant channel at the membrane (Denning et al., 1992). Temperature rescued ΔF508-CFTR acquires complex glycosylation, but membrane half-life is still reduced compared to WT-CFTR (Heda et al., 2001; Sharma et al., 2001). Therefore, whilst capable of promoting maturation, low temperature incubation does not appear to induce native folding of ΔF508-CFTR, which is still targeted by peripheral quality control.

The existence of cell-type specific effects of temperature correction led to the hypothesis that other biological components, such as chaperones, are involved in the mechanism of temperature correction (Wang et al., 2008).

#### 1.5.1.2 Revertant mutations

Revertant mutations capable of promoting folding and trafficking of ΔF508-CFTR have been identified throughout the CFTR protein. By introducing a mutation in *cis,* revertants repair a specific aspect of the folding defect. Mutations include those that stabilise NBD1, and those that repair the NBD1:ICL4 interface. ΔF508-NBD1 thermodynamic and kinetic instability can

be partially repaired by mutations such as G550E, R553Q and R555K (Roxo-Rosa et al., 2006; Rabeh et al., 2012). As mentioned, R1070W is a revertant mutation located in ICL4 which promotes trafficking of ΔF508-CFTR (Thibodeau et al., 2010; Okiyoneda et al., 2013).

Again, although not clinically relevant, revertant mutations allow study of the ΔF508-CFTR ion channel function by promoting plasma membrane localisation. Identifying revertant mutations also allows us to better understand the trafficking defect caused by ΔF508. For example, the trafficking improvement caused by R1070W confirmed that the NBD1:ICL4 interface, originally identified in homology models (Serohijos et al., 2008), plays a role in ΔF508-CFTR misfolding. This interface is now also a well-established target for corrector compounds.

Using revertant mutations alongside corrector compounds can help elucidate the mechanism of correctors. The extent to which a compound can synergise with specific revertants indicates the likely mechanism. Compounds which have a small effect alongside R1070W, but a large effect alongside NBD1 stabilising mutations, most likely share a mechanism of action with R1070W. Okiyoneda *et al.* (2013) recently employed this tactic to demonstrate that most corrector compounds identified to date target the NBD1:ICL4 interface.

#### 1.5.1.3 ΔF508-CFTR corrector compounds

ΔF508-CFTR trafficking can be improved by pharmacological chaperones, which bind to CFTR to stabilise domain or interdomain interactions and to promote folding; or by proteostasis regulators, which target other molecules to promote folding or reduce proteasomal degradation. This project will focus on corrector mechanisms that directly target the folding of CFTR by binding to the mutant protein. In the search for ΔF508-CFTR treatments, compounds that directly target the CFTR are less likely to display off-target effects. Additionally, these compounds can help better understand the folding of ΔF508-CFTR, and be used as tools to further study this defect and the structure of CFTR.

VX-809, the corrector compound used alongside VX-770 in the recently approved combination treatment Orkambi, was used as a positive control throughout this project. Using the revertant mutation synergy assay described above, the mechanism of correction by VX-809 was identified as a stabilisation of the NBD1:ICL4 interface. Alongside NBD1 stabilising mutations, VX-809 restores membrane density to ~100% of WT-CFTR, whereas the correction alongside R1070W is modest (Farinha et al., 2013b; Okiyoneda et al., 2013). VX-809 binds directly to the ΔF508-CFTR protein (Eckford et al., 2014), to improve membrane density ~2-fold (He et al., 2013; Okiyoneda et al., 2013). *In silico* docking studies

suggest a number of putative binding sites at interdomain interfaces (Farinha et al., 2013b; He et al., 2013; Okiyoneda et al., 2013), which have yet to be further investigated.

## 1.6 ΔF508-CFTR destabilisation by chronic potentiator treatment

Orkambi (VX-770/VX-809 combination treatment) was recently approved for the treatment of ΔF508-CF homozygous patients. A Phase III study revealed a mean absolute improvement in lung function ($FEV_1$) of 2.6% – 4% (Wainwright et al., 2015). Compared to *in vitro* results using acute VX-770 treatment alongside VX-809-mediated correction (conductance up to 30% of WT-CFTR; Van Goor et al., 2011), this was a relatively small improvement.

A possible explanation for the disappointing clinical results came with the publication of two papers in July 2014. Two groups independently reported a decrease in ΔF508-CFTR membrane stability following chronic treatment with VX-770, which was unrelated to channel function (Cholon et al., 2014; Veit et al., 2014). During drug development, it is likely this effect was missed because potentiators were only tested acutely for ability to improve CFTR function. Due to the absence of validated CF animal models available at the time, and a lack of VX-770 activity on murine CFTR (Van Goor et al., 2009), animal tests, which could have identified issues with chronic dosing, were carried out for toxicology and distribution purposes only.

Chronic treatment of ΔF508-CFTR bronchial cells with 100 nM VX-770 destabilised CFTR at the membrane, decreasing mature ΔF508-CFTR by up to 40%, regardless of the method of rescue. This decrease appears to be caused by reduced biogenesis or increased cotranslational degradation, increased degradation of mature CFTR, reduced recycling and a small decrease in folding efficiency from immature to mature ΔF508-CFTR. A decrease in membrane-localised CFTR was reflected in functional studies using primary cell monolayers (Cholon et al., 2014; Veit et al., 2014).

Promoting ΔF508-NBD1/2 dimer stability by reducing ATPase activity (using mutation E1371S), protected ΔF508-CFTR from the negative effects of VX-770. Docking studies suggested a number of putative VX-770 binding sites accessible in the partially unfolded ΔF508-NBD1/2 dimer, which are not accessible in WT-CFTR, and presumably would not be accessible in ΔF508/E1371S-CFTR (Veit et al., 2014). Therefore, VX-770 could be binding to the partially unfolded state, accessible due to the folding defect, to stabilise a structure with greater propensity for recognition by quality control mechanisms. This could explain the variety of changes to the fate of the protein, from increased cotranslational degradation, to reduced recycling.

It has been disputed whether this would really occur *in vivo.* Five day VX-770 treatment with 450 mg resulted in a plasma concentration of 14 µM. Due to high levels of binding in plasma, the concentration of *free* VX-770 following patient treatment could be as low as 8 nM (Matthes et al., 2015). When tested in 100% human serum, the $IC_{50}$ for the negative effects caused by VX-770 was 23 nM (Veit et al., 2014). Allowing for accumulation of VX-770 in cell membranes during chronic treatment, which does appear to take place (Cholon et al., 2014), the potency of VX-770, to induce negative effects on CFTR stability, does seem clinically relevant.

Veit *et al.* (2014) went on to show a reduction of ΔF508-CFTR plasma membrane density with every tested potentiator, except one: P5 (Yang et al., 2003). A library of P5 analogues has since been screened and shown a number of compounds which also lack destabilisation effects (Phuan et al., 2015). This suggests a different binding site for P5, with molecular dynamics and evidence from docking studies supporting different binding sites which do not overlap with putative VX-770 binding sites (Veit et al., 2014). The fact that almost all tested potentiators have a negative effect on stability of ΔF508-CFTR highlights the importance of screening for this characteristic when identifying novel ΔF508-CFTR potentiators. Missing the effect of chronic treatment will lead to disappointments in clinical trials.

## 1.7 Current screening methods for measuring CFTR function

Over the last 15 years, high-throughput screening has transformed the study of CFTR potentiators. Identification of VX-770 was made possible by industry screening efforts, and many other compounds have been identified in academia.

### 1.7.1 Cytosolic halide sensitive yellow fluorescent protein (YFP) expression

Most of the CFTR screening work in academia has come from the Verkman lab, following their development of a halide sensitive yellow fluorescent protein (YFP (H148Q/I152L); Galietta et al. 2001a, 2001b). The YFP assay is discussed in detail in Chapter 3. Briefly, stable cell lines co-express halide sensitive YFP in the cytosol, and CFTR. YFP has a higher affinity for iodide ($I^-$) than $Cl^-$, allowing the function of CFTR to be measured by the influx of $I^-$. In the presence of an extracellular $I^-$ buffer, if CFTR is expressed at the membrane and gating, $I^-$ enters the cell and quenches YFP fluorescence. In the case that CFTR is either not membrane-localised, or not gating, $I^-$ has no route into the cell and YFP fluorescence remains high.

The screen for potentiators involves 24 h low temperature incubation of ΔF508-CFTR to increase membrane expression (Denning et al., 1992), and addition of a test compound in

the presence of forskolin. Forskolin activates adenylate cyclase, causing an accumulation of cyclic adenosine monophosphate (cAMP), which activates PKA, which in turn phosphorylates CFTR. For ΔF508-CFTR, only slow quenching occurs, due to the gating defect. In the presence of a test compound, increased quenching rate indicates CFTR potentiation.

### 1.7.2 Membrane potential

During drug discovery efforts, which eventually led to identification of VX-770, Vertex employed a fluorescence resonance energy transfer (FRET) assay. A pair of membrane-soluble dyes, one of which partitions into the outer membrane leaflet and acts as a fixed FRET donor, are used to measure changes in membrane potential of cells expressing ΔF508-CFTR, following addition of test compounds with forskolin (Van Goor et al., 2006). The FRET acceptor dye is negatively charged, and also partitioned into the membrane outer leaflet at resting membrane potential. Upon membrane depolarisation, the acceptor flips to the inner leaflet of the membrane, reducing the FRET signal (González et al., 1999).

### 1.7.3 Functional screens as an indirect measure of membrane density

The YFP and membrane potential functional screens have also been utilised to indirectly measure CFTR membrane-localisation in screens for ΔF508-CFTR corrector compounds. Screening for correctors requires 24 h incubation with the test compound, followed by addition of forskolin and a potentiator to induce CFTR activation. Increased quenching rate or membrane potential change compared to buffer-incubated ΔF508-CFTR is used as an indicator of successful correction of CFTR trafficking. These assays have identified a number of active compounds, which are now used in the clinic and as tools to study CFTR.

Neither the FRET screen, nor the cytosolic YFP assay, has the ability to quantify CFTR membrane expression independently of function, which is critical when screening corrector compounds on the severe gating mutant ΔF508-CFTR. Using function as an indirect measure of membrane density, compounds with unusual or complex mechanisms may be missed. For example, correctors which stabilise a conformation capable of trafficking, but which cannot be gated by the activating compounds used in the assay, or indeed compounds that inhibit the channel function, will not be detected.

## 1.8 Current methods for measuring CFTR membrane density

CFTR maturation is most often studied using visualisation on an immunoblot, using standard Western blot techniques. Band B is used to quantify immature, ER-associated CFTR, with band C reflecting membrane-localised, mature CFTR. CFTR membrane-localisation is often

quantified using the ratio of mature/total CFTR. Whilst this is an important measure of CFTR trafficking, it is not the only parameter of interest. For example, an increase in total CFTR which does not affect the ratio of mature/total would still be a viable ΔF508-CFTR treatment option. This technique is laborious, time consuming and difficult to quantify. Recently, a number of high-throughput assays capable of measuring CFTR localisation have been developed.

### 1.8.1 Haemagglutinin-epitope

Carlile *et al.* (2007) developed a CFTR membrane density assay which involved the use of a haemagglutinin epitope (HA)-tagged CFTR. An extracellular HA tag at position 901, which is known to be a permissive site for insertion in CFTR, allows fluorescent antibody labelling of CFTR expressed at the membrane (Carlile et al., 2007; Robert et al., 2008). Whilst this assay was the first published assay capable of screening with respect to membrane-localised CFTR, it does require antibody incubation, and it is not capable of measuring internal CFTR.

### 1.8.2 Horseradish Peroxidise

In a recent screen for CFTR correctors showing synergistic activity with VX-809, a Horseradish Peroxidise (HRP)-tag was introduced at position 901 (Phuan et al., 2014). This allows quantification of CFTR membrane density by addition of an HRP substrate, which luminesces when oxidised by HRP. Again, this assay is only capable of measuring membrane-localised CFTR.

### 1.8.3 Fluorogen activating protein

Fluorogen activating proteins (FAPs) are single chain antibody fragments which bind to greatly enhance the fluorescence of fluorogens (Holleran et al., 2012; Larsen et al., 2015). Using an extra TM added to the N-terminal of CFTR, Larsen *et al*. (2015) tagged CFTR with an extracellular FAP. Extracellular, impermeant, malachite green (MG) binds the FAP and fluoresces brightly to quantify membrane-localised CFTR. Total cellular distribution can be measured using a cell permeable MG-ester, which is then cleaved and trapped inside the cell. However, the two measurements cannot be made on the same sample.

### 1.8.4 mCherry/FLAG

The most recently reported high throughput CFTR trafficking assay was a double-tagged mCherry/FLAG CFTR. This screen involves total CFTR detection via fluorescence intensity reflecting an N-terminal mCherry tag, and membrane CFTR detection via a FLAG epitope

inserted at position 901 (Botelho et al., 2015). This assay is therefore capable of measuring both total CFTR (via mCherry) and membrane CFTR (via FLAG). However, quantification of membrane CFTR still relies on antibody staining, with the associated incubations and washes. Additionally, this assay, as with the other fluorescence and luminescence assays to measure CFTR membrane density, critically depends on a low variability in the levels of expression of the probe.

## 1.9 Other clinical implications of the study of CFTR

The study of CFTR pharmacology could have an impact outside CF. The prevalence of CFTR mutation carriers has been attributed to a partial protection, in the heterozygote state, against secretory diarrhoeas. Such diseases are caused by bacteria similar to *Vibrio cholerae*, which produce toxins that activate CFTR in the intestine, causing water loss through diarrhoea. Cholera is responsible for approximately 50,000 deaths per year in the developing world (Lozano et al., 2012). Animal models of diarrhoea have demonstrated that CFTR inhibitors can block fluid secretion (Ma et al., 2002). CFTR inhibitors, therefore, have clinical implications in the treatment of secretory diarrhoea.

Chronic obstructive pulmonary disorder (COPD) is an air pollution and smoke-induced lung disease, with some pathological traits similar to CF, including mucus stasis and accumulation. Exposing cultured epithelial cells to smoke in the laboratory causes a decrease in CFTR-dependent anion transport, due to reduced CFTR mRNA and protein expression (Cantin et al., 2006). CFTR potentiators with activity on WT-CFTR have been tested *in vitro*, with some success, for the treatment of COPD (Sloane et al., 2012).

## 1.10 Aims of this research

The study of CFTR pharmacology is paramount in the quest to treat the debilitating disease of CF. Furthermore, understanding the trafficking and function of this ion channel has far reaching implications, such as in the treatment of COPD, which affects millions of people worldwide. The aim of this research was to develop tools to better enable the study of CFTR pharmacology, initially in the setting of ΔF508-CFTR.

Targeting ΔF508-CF will likely require combination therapy with a trafficking corrector and a gating potentiator. Furthermore, the potentiator must not have a negative effect on biosynthesis and stability, unlike most potentiators identified to date. Identification of such compounds will require high-content screening tools, capable of quantifying function and membrane density of ΔF508-CFTR.

The specific aims of this project were to:

- *Optimise YFP-CFTR assay for screening ΔF508-CFTR potentiators*
- *Design an optical assay for measuring localisation of CFTR*
- *Screen compound libraries to identify ΔF508-CFTR potentiator compounds*
- *Use fluorescence assays to probe VX-770 mechanism of action*

# Chapter 2

# Methods

## 2.1 Molecular biology (Construction of YFP-CFTR and CFTR-pHTomato fusion proteins)

### 2.1.1 Overview of YFP-CFTR fusion protein construction

Green fluorescent protein (GFP)-CFTR, in which enhanced GFP (eGFP) is tagged to the N-terminal of CFTR via a 23 amino acid linker, was provided by Bruce Stanton (Geisel School of Medicine, NH, USA) in pcDNA3.1 plasmid. YFP (H148Q/I152L) in pcDNA3, and WT-CFTR in pcDNA3.1, were provided by Luis Galietta (Istituto Giannina Gaslini, Genova).

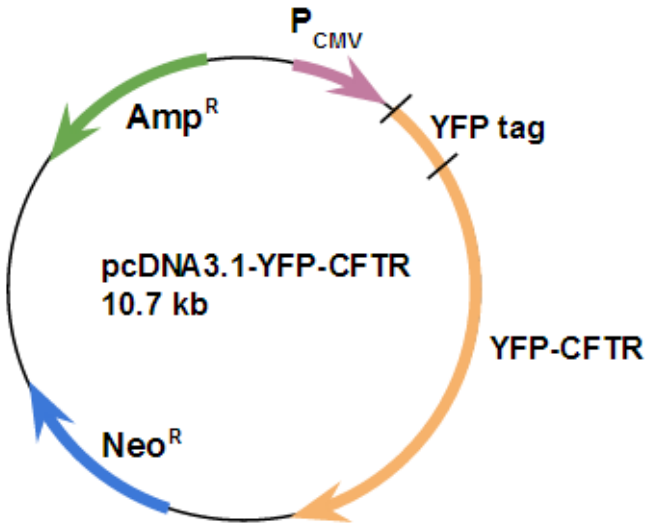


**Figure 2.1 Plasmid map of pcDNA3.1-YFP-CFTR.** YFP-CFTR is under the control of a cytomegalovirus immediate-early promoter ($P_{CMV}$). The plasmid contains coding sequences for ampicillin resistance ($Amp^R$) for bacterial selection and neomycin resistance ($Neo^R$) for mammalian cell selection. The YFP tag is shown at the N-terminal.

In order to produce YFP-CFTR, eight mutations were introduced in GFP-CFTR. This was done using site-directed mutagenesis (SDM). Each SDM reaction was used to transform chemically competent *E. Coli* cells, amplified by culturing the bacteria, from which the DNA was purified using midi prep protocols. The success of each SDM reaction was checked by sequencing the mutated segment, while the whole coding region was sequenced after the final mutagenesis. The steps involved in this process are detailed below.

### 2.1.2 Site-directed mutagenesis

SDM uses polymerase chain reaction (PCR) and mutagenic primers to introduce mutations into a plasmid at a designated point. The protocol we used is essentially identical to the Quikchange protocol marketed by Stratagene, but individual components were obtained from various suppliers. Sequence alignment of YFP (H148Q/I152L) with GFP-CFTR

identified eight amino acid differences: F46L, L64F, S65G, V68L, S72A, H148Q, I152L and T203Y. Forward and reverse complementary primers containing each desired mutation were made to order (Eurofins MWG Operon, Germany). Each primer contained the mutation, flanked by approximately ten complementary bases to allow annealing to the correct location on the plasmid.

The SDM reaction contained 100 ng template DNA, into which the mutation was to be introduced, 20 µl Phusion high fidelity buffer (New England Biolabs (UK) Ltd., Hitchin, UK), 0.5 µM forward and reverse primers, 80 µM (each) deoxynucleotide triphosphates (dNTPs, New England Biolabs), and 2 units Phusion polymerase enzyme (New England Biolabs), mixed in a 0.2 ml thin-walled PCR tube (Starlab (UK) Ltd., Milton Keynes, UK). The mixture was made up to 95 µl in distilled water ($dH_2O$), and 5 µl of DMSO was added to minimise formation of secondary structures. The following SDM cycle was run in a Thermal Cycler PCR machine (Applied Biosystems, UK):

**Table 2.1 SDM PCR cycle.**

| Temp | Time | Cycle step | |
|---|---|---|---|
| 98°C | 30 s | Initialisation | |
| 98°C<br>53°C<br>72°C | 10 s<br>30 s<br>5 min | Denaturation<br>Annealing<br>Elongation | 18 cycles |
| 72°C | 10 min | Final elongation | |
| 38°C | Finish | Storage hold | |

Following thermal cycling, 2 h incubation at 37°C with 40 units *Dpn* I (New England Biolabs) destroyed the template, methylated DNA, leaving only nicked plasmids containing the mutation. For *Dpn* I treatment, samples were moved to 1.5 ml microcentrifuge tubes (Sarstedt Ltd., Leicester, UK).

Following *Dpn* I treatment the DNA was precipitated by addition of 250 µl 100% ethanol and 10 µl 3 M sodium acetate (NaOAc), and incubated at -20°C for 20 min. The DNA was pelleted by a 20 min, 16,100 *g* spin at 4°C in a microcentrifuge (5415R Eppendorf centrifuge, Eppendorf UK Ltd, UK). The pellet was washed with 400 µl 70% ethanol, spun as above and resuspended in 10 µl 10 mM tris pH 8.

The SDM reaction was used to transform chemically competent *E. Coli* for amplification of the plasmid.

### 2.1.3 Transformation of chemically competent *E. Coli*

3 µl of SDM reaction was chilled on ice in a 13 ml culture tube (Sarstedt). 50 µl of chemically competent *E. Coli* (Life Technologies, Paisley, UK) was added to the plasmid, and incubated

on ice for 30 min. The mixture was heat shocked at 42°C for 45 s, returned to ice for 2 min, and mixed with 950 µl Super Optimal broth with catabolite repression (SOC, Life Technologies). The *E. Coli* suspension was incubated at 37°C in a swirling incubator, for 1 h.

Agar plates containing antibiotics were used to select for successfully transformed *E. Coli* cells. Molten Luria Bertani broth (LB broth, Sigma-Aldrich Company Ltd., Dorset, UK) supplemented with 1.5% (w/w) agar, containing 100 µg/ml ampicillin or 50 µg/ml kanamycin, was poured into 100 mm dishes (BD Biosciences, Oxford, UK) and allowed to set.

Following the 1 h 37°C incubation, 50 µl of *E. Coli* in SOC medium was pipetted onto an agar plate and spread using an ethanol-sterilised glass spreader. Plates were incubated at 37°C overnight. Following successful transformation, only bacteria containing the antibiotic resistance encoded by the transforming plasmid were able to grow and form colonies on antibiotic-containing agar plates.

### 2.1.4 Midi prep to purify the plasmid

For every midi prep sample, a single *E. Coli* colony was used to inoculate 50 ml LB broth in a conical flask, using a flame sterilised inoculating loop. The *E. Coli* culture was grown overnight (~17 h for ampicillin resistant bacteria) in a 37°C swirling incubator (250 rpm). The culture was spun at 1,811 *g* for 20 min in a centrifuge (5810R Eppendorf centrifuge) to pellet the bacteria. The supernatant was discarded and the midi prep carried out using a Qiagen midi prep kit, according to manufacturer's instructions (Qiagen Ltd., Manchester, UK). This protocol exploits an alkaline lysis procedure, followed by purification on an anion exchange column.

The plasmid in the 5 ml of eluate was precipitated by addition of 3.5 ml isopropanol, and pelleted by a 24,500 *g*, 30 min spin at 4°C, in a Beckman J2-M1 centrifuge (Beckman Coulter (UK) Ltd., High Wycombe, UK). The supernatant was discarded and the pellet washed with 2 ml 70% ethanol, spun as above for 10 min, the ethanol discarded and the air-dried pellet resuspended in 100 µl 10 mM tris pH8. The expected yield from the Qiagen midi prep kit is approximately 1 µg/µl. This was checked using gel electrophoresis.

### 2.1.5 Gel electrophoresis

Each midi prep sample was visualised using gel electrophoresis, to determine the approximate length of the DNA fragment in base pairs, and the plasmid concentration. A 0.8% solution was prepared by dissolving 0.32 g agarose (Starlab) in 40 ml 1X TAE buffer (Life Technologies), followed by 1 min heating in a standard microwave oven (1 min, 800 W). 1 µl of 10 mg/ml ethidium bromide solution (Sigma-Aldrich) was added to the agar solution,

which was poured into a plastic mould to set. 260 ml 1X TAE buffer was used to submerge the gel.

2 µl of 6X cyan-yellow Track-It dye (Life Technologies) was added to 10 µl of plasmid sample, which was loaded into the wells at the top of the gel. A potential difference of 100 V attracted the negatively charged DNA to the positive end of the chamber, in order to separate by size. The faster the sample travelled, the smaller the DNA in base pairs. Each gel was run for 40 min.

DNA on a gel is visualised under UV light, as ethidium bromide increases in fluorescence when intercalated with nucleic acid. A 1kb ladder was run alongside each set of samples (Life Technologies). This ladder is composed of many fragments of known size. Therefore, the size of each fragment can be estimated by comparing how far the band has travelled in relation to the known fragments on the ladder.

As well as estimating sample size in base pairs, gel electrophoresis was used to estimate plasmid concentration. To estimate midi prep concentration, a 10-fold sample dilution was run alongside the concentrated midi prep sample, to enable more accurate comparison with the 1 kb ladder. Within the ladder is a 1.6 kb sample of known concentration (5 ng/µl). Comparison of the midi prep 10-fold dilution with this fragment on the ladder allowed estimation of the concentration of DNA in the sample.

### 2.1.6 Sequencing

The success of each SDM reaction was checked using sequencing. This method required the design of location-specific primers (Eurofins), approximately 20 bases long, which annealed at least 100 bases upstream of the region to be sequenced.

Big dye 1.1 (Life Technologies) provided a mix including polymerase, dNTPS for strand elongation, and fluorescently labelled dideoxynucleotides (ddNTPs), which terminated strand elongation when incorporated. Each ddNTP base type in the mixture (A, T, G and C) was linked to a different fluorescent molecule. Due to the mixture of dNTPs and ddNTPs, strands were terminated at different lengths, giving a mixture of strands from one base long to approximately 700 bases. Using a 3100-Avant Genetic Analyzer (Applied Biosystems), the mixture of strands was drawn up a fine glass capillary into a gel matrix, which separated the fragments by size. Reading fluorescence after separation of fragments by capillary electrophoresis, produced a chromatogram trace, read to give the sequence.

2 µl of Big Dye 1.1, 0.3 µM primer, and ~100 ng of sample were mixed in a 0.2 ml PCR tube and made up to 10 µl using $dH_2O$. The following protocol was run on a PCR machine:

| Temp | Time | Cycle step | |
|---|---|---|---|
| 94°C | 30 s | Initialisation | |
| 94°C<br>50°C<br>60°C | 10 s<br>30 s<br>5 min | Denaturation<br>Annealing<br>Elongation | 25 cycles |
| 4°C | Finish | Storage hold | |

**Table 2.2 Sequencing PCR cycle.**

The mixture was precipitated by adding 10 µl $dH_2O$, 50 µl 100% ethanol and 2 µl 3M NaOAc, chilled on ice for 10 min and spun at 16,100 *g* for 15 min at 4°C. The supernatant was removed, the pellet washed with 100 µl 70% ethanol, and the spin repeated as above. Following removal of the supernatant the pellet was left to air dry for 2 h before sending for capillary electrophoresis and reading of the sequence (UCL Sequencing, Gower Street, London, UK).

### 2.1.7 Overview of CFTR-pHTomato fusion construction

pHTomato in pRham plasmid was provided by Dr Li (Peking University) and Prof. Richard Tsien (NYU School of Medicine, NY). Restriction enzyme sites were introduced into CFTR in pcDNA3.1 to allow insertion of pHTomato into the fourth extracellular loop (ECL4).

For reasons discussed in Chapter 4, CFTR-pHTomato was later subcloned into a pIRES2-eGFP plasmid (Figure 2.2), which contains an internal ribosome entry site (IRES). This plasmid directs transcription of one strand of mRNA, containing coding sequences for both CFTR-pHTomato and eGFP, but translation of two separate proteins (CFTR-pHTomato and eGFP). CFTR in pIRES2-eGFP was provided by Prof. David Gadsby (Rockefeller University, New York, USA).

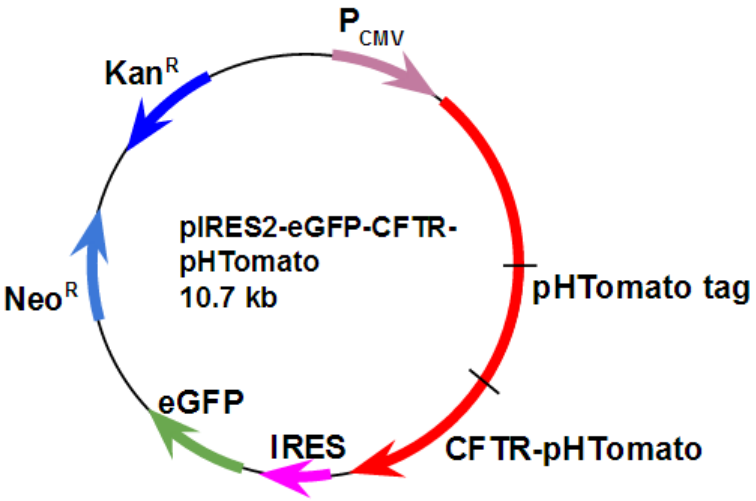


**Figure 2.2 Plasmid map of pIRES2-eGFP-CFTR-pHTomato.** CFTR-pHTomato is expressed in pIRES2, under control of $P_{CMV}$. The plasmid contains kanamycin resistance ($Kan^R$) for bacterial selection and neomycin resistance ($Neo^R$) for mammalian cell selection. Between the CFTR-pHTomato coding region and eGFP coding region is an IRES.

### 2.1.8 Introduction of restriction enzyme sites and pHTomato in ECL4

In order to insert pHTomato at ECL4 of CFTR in pcDNA3.1, *Age* I and *Bmt* I restriction enzyme sites were introduced on either side of the insertion site using an overlap extension strategy. The same sites were introduced as non-annealing tags on primers, then used for PCR amplification of the pHTomato coding sequence, resulting in a PCR product in which *Age* I and *Bmt* I sites flanked pHTomato. This work was carried out by an undergraduate student during a summer project (Stefan Constantinou, supported by a UCL Dean's summer studentship). Restriction enzyme digest with *Age* I and *Bmt* I, of both CFTR in pcDNA3.1 and pHTomato in the PCR product, followed by ligation, resulted in the insertion of pHTomato in ECL4 of CFTR. The latter steps were carried out by undergraduate student Mahesh Pillai, supported by a CF Trust summer studentship.

### 2.1.9 Subcloning CFTR-pHTomato into pIRES2-eGFP plasmid

To transfer CFTR-pHTomato from pcDNA3.1 to pIRES2, a 4.4 kb region of CFTR including pHTomato was subcloned within the WT-CFTR coding sequence on the pIRES2 plasmid, using *Sal* I and *BspE* I restrictions sites, present in WT-CFTR. Digests of both vector (WT-CFTR-pIRES2) and insert (CFTR-pHTomato) were carried out at 37°C for 3 h, then run on a preparative 0.8% agarose gel to separate the fragments. The fragments were purified using Wizard® SV Gel and PCR Clean-up System, according to manufacturer's instructions (Promega UK Ltd., Southampton, UK).

For ligation, a 1:1 molar ratio of vector:insert was mixed in ATP-containing ligation buffer and T4 ligase enzyme (New England Biolabs) was added, before incubation at 16°C overnight. The reaction was then used to transform *E. Coli* as described above, and plated on agar plates containing 50 µg/ml kanamycin. Colonies were inoculated in 50 ml LB broth with 50 µg/ml kanamycin, grown overnight and plasmid preparations were purified by midi prep.

### 2.1.10 Introducing CFTR mutations

This project involved the study of many CFTR mutations, each of which was introduced separately into the YFP-CFTR and CFTR-pHTomato plasmids as required, using SDM.

## 2.2 HEK293 cell culture and transfections

### 2.2.1 HEK293 cell culture

HEK293 cells were maintained in Dulbecco's Modified Eagle Medium (DMEM) supplemented with 2 mM L-glutamine, 100 U/ml penicillin and streptomycin, and 10% foetal bovine serum (FBS, all Life Technologies). Cells were cultured in tissue culture treated T25

flasks (Nunc, Fisher Scientific Ltd., Leicestershire, UK) in a 37°C incubator supplied with 5% $CO_2$. Confluent flasks were passaged every 2-3 days. Medium was discarded and cells were rinsed with 5 ml Hank's Buffered Salt Solution (HBSS, Life Technologies). 1 ml 0.05% trypsin (Life Technologies) was added to the flask and left to detach the cells for 3 min. 9 ml medium was added to deactivate the trypsin, and the solution was transferred to a 15 ml plastic tube (Falcon, Fisher Scientific). The 10 ml cell suspension was spun at 180 *g* for 2 min. The supernatant was removed and the pellet resuspended in 10 ml medium. For passage of the cells, 2 ml of this cell suspension was added to 8 ml medium in a T25 flask, for a 1:4 dilution.

### 2.2.2 Plating HEK293 cells for imaging

For fluorescence imaging cells were seeded in poly-D-lysine (PDL)-coated black walled 96-well plates (Costar, Fisher Scientific). Flasks of confluent cells were detached as above, pelleted, diluted 1:3 (cell suspension:medium), and plated at 100 µl per well the day before transfection.

### 2.2.3 Lipofectamine transient transfection

Lipofectamine transfection was used for all imaging experiments. Cells plated in 96-well plates as described above were transiently transfected with the required plasmid using Lipofectamine 2000 (Life Technologies), according to manufacturer's instructions. Following transfection, cell plates were returned to the 37°C incubator for 24 h.

### 2.2.4 Plating HEK293 cells for patching

Following detachment using trypsin, as described above, cells were pelleted, resuspended in 10 ml media and diluted 1:9 (cell suspension:medium). Cells were plated in 35 mm plastic petri dishes (Nunc, Fisher Scientific) at 2 ml per dish. Cells were transfected using the calcium phosphate technique approximately 6 h after plating.

### 2.2.5 Calcium phosphate transient transfection

Lipofectamine transfection reduced seal stability when cells were used in excised patch experiments. A calcium phosphate transfection protocol, thought to damage membrane structure less, was therefore used to transfect HEK293 cells intended for use in excised patch experiments (Groot-Kormelink et al., 2002).

8.9 µl 2 M $CaCl_2$ solution was added to 1.4 µg CFTR plasmid, together with 40 ng GFP plasmid, and made up to 73 µl with $dH_20$. This mixture was added slowly to 73 µl HBS

solution (274 mM NaCl, 1.5 mM $Na_2HPO_4$, 54.55 mM HEPES, pH 7), then added dropwise to the cells. Cell dishes were incubated for 16-24 h before patching.

## 2.3 Fluorescence imaging plate reader (FLIPR)

### 2.3.1 FLIPR overview

The fluorescence imaging plate reader (FLIPR Tetra, Molecular Devices, Wokingham, UK) is an automated 96-well plate reader with fluidics component. The overhead pipettor enabled compound addition from drug plates to the cell plate, whilst fluorescence readings were taken simultaneously from each well over a period of time. Light from LEDs passed through an excitation filter to illuminate the bottom of the plate, and emitted light passed through an emission filter for detection by a CCD camera.

Two 96-well drug plates enabled two different solutions to be added to each well in the cell plate. Following a protocol created using the equipment software, the FLIPR took readings at multiple time points, and added the required volumes from the drug plates at programmed time points.

### 2.3.2 Acquiring YFP readings in FLIPR

24 h after transfection, medium was removed from all wells using a multichannel pipette. Each well was washed twice with 100 µl standard buffer (140 mM NaCl, 4.7 mM KCl, 1.2 mM $MgCl_2$, 5 mM HEPES, 2.5 mM $CaCl_2$, 11 mM Glucose, pH 7.4).

Each cell plate required the use of two drugs plates (Falcon, Fisher Scientific), labelled drug plate 1 and drug plate 2, for the 1$^{st}$ and 2$^{nd}$ fluid additions in the protocol. The treatments in the drug plates exactly replicated the designated treatment of the cell plate, so the cells in B1 would receive fluid additions from B1 in drug plate 1 and from B1 in drug plate 2.

FLIPR Protocol:

Cell plate contained 100 µl standard buffer

- Acquire image every second for 10 s
- Add 50 µl from drug plate 1
- Acquire image every second for 10 s
- Acquire image every 15 s for 45 s
- Acquire image every second for 10 s
- Add 50 µl from drug plate 2
- Acquire image every second for 190 s

Drug plate 1 contained $I^-$ buffer (as standard buffer above, with 140 mM NaCl replaced with 300 mM NaI), designed to create an extracellular [$I^-$] of 100 mM. $I^-$ was diluted 1:2 in the original buffer when added to the cell plate (300 mM NaI for a final concentration of 100 mM). Drug plate 2 contained the specific well treatment (for example, forskolin), made in 100 mM $I^-$ buffer so as to preserve the extracellular $I^-$ concentration. Plates were kept at 37°C throughout recordings. The excitation/emission filters used for FLIPR readings of YFP were 470/495 nm and 515/575 nm respectively. The exposure time was 0.8 s.

### 2.3.3 Analysis of FLIPR data

The output from FLIPR recordings is the average fluorescence in each well, at every time point, which is exported to a Microsoft Excel worksheet. Fluorescence was normalised to the fluorescence at 85 s, a time point after the second addition, when any fluid addition artefact was complete (for more information on the artefact see Chapter 3).

To quantify CFTR activation, the gradient of the fluorescence reading was calculated at every time point, to find the maximal quenching rate per second.

## 2.4 High-content fluorescence imaging (ImageXpress)

### 2.4.1 ImageXpress overview

ImageXpress (ImageXpress Micro XLS, Molecular Devices) is a widefield inverted fluorescent microscope with CMOS camera, and robotics which add compounds to cell plates whilst imaging a region of the well. Illumination, fluid additions and image acquisition occur at a single well at a time, not simultaneously at all wells as in the FLIPR system. Laser autofocus uses the manually entered position of the plate to rapidly focus on fluorescent cells. A xenon lamp light source illuminates the well through an excitation filter. Emitted light passes through an emission filter for detection by the camera. Each filter cube contains excitation and emission filters, and a dichroic mirror.

The cell plate was loaded above the optics in a temperature controlled chamber. Above the imaged well is a small retractable window, which opens at the time of fluid addition to allow access to the pipette tip. The drug plates were located to the side of the optics, in a separate chamber with environmental control. Alongside the drug plates were located two pipette tip racks. Instructed by a fluid addition protocol created using the dedicated software (MetaXpress, Molecular Devices), the fluidics component collects a clean tip, draws 50 µl of solution from the drug plate, moves to the cell plate, where the retractable window opens, and dispenses 50 µl of solution.

ImageXpress was used for both YFP-CFTR and CFTR-pHTomato imaging.

### 2.4.2 YFP-CFTR image acquisition and analysis

Cell plates were prepared as for FLIPR and loaded into the ImageXpress chamber. YFP-CFTR quenching experiments required two drug plates, labelled drug plate 1 and drug plate 2 for the 1st and 2nd additions. As for FLIPR, drug plates were organised with respect to the cell plates.

Two protocols were in use in YFP-CFTR imaging. These protocols are referred as $I^-$ first addition and $I^-$ second addition, and are described in Chapter 3 and Chapter 6, respectively.

$I^-$ first addition protocol:

Cell plate contained 100 µl standard buffer

- Acquire image every 2 s for 20 s
- Add 50 µl from drug plate 1
- Acquire image every 2 s for 40 s
- Add 50 µl from drug plate 2
- Acquire image every 2 s for 90 s

Drug plate 1 contained 300 mM $I^-$ buffer (final extracellular concentration 100 mM). Drug plate 2 contained the well treatment made in 100 mM $I^-$ to preserve the extracellular $I^-$ concentration.

$I^-$ second addition protocol:

Cell plate contained 100 µl standard buffer

- Acquire image every 2 s for 20 s
- Add 50 µl from drug plate 1
- Acquire image every 2 s for 90 s
- Add 50 µl from drug plate 2
- Acquire image every 2 s for 40 s

Drug plate 1 did not contain $I^-$, only the well treatment. The second addition contained 400 mM $I^-$ buffer (final concentration 100 mM) with the treatment concentration maintained.

YFP-CFTR was imaged using a 20X objective, and excitation/emission filters 472 ± 30 nm and 520 ± 35 nm (Figure 2.3). Although the filters were not optimised for YFP imaging, excitation was sufficient to allow visualisation of YFP-CFTR. For all plates, the laser intensity

and exposure were changed to achieve the highest possible fluorescence whilst avoiding both photo-bleaching and saturation. For most plates, this meant an illumination intensity of 100/225 c.d., and exposure time 0.15 s. However, these settings were tested and optimised at the start of each experiment. The parameter used to guide this selection was the pixel intensities of cells compared to background regions. Ideal cell fluorescence was > 1000 grey units higher than background. To reduce the storage size required for the images, and increase the speed of image analysis, a camera binning of 5x5 pixels was used when recording YFP-CFTR. This reduced image resolution, but did not have a negative impact on accuracy of quenching measurements.

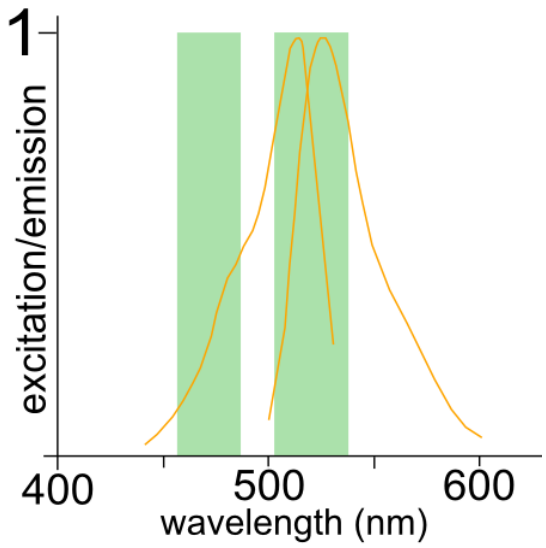


**Figure 2.3 YFP excitation/emission spectrum with ImageXpress filters.** Modified from Galietta, Haggie, & Verkman, 2001. YFP excitation and emission peaks are seen at 513 nm and 525 nm respectively. Green shading highlight the bandwidth of the excitation and emission filters used in the ImageXpress protocol. A dichroic mirror allowed transmission > 502 nm.

Acquired 16-bit images were analysed using ImageJ (http://rsbweb.nih.gov/ij/). Each well was exported as a stack, with each time point represented by an image in the stack. Using the image obtained at the time point immediately before $I^-$ addition, fluorescent cells were selected using an appropriate threshold (Figure 2.4 A and B). The threshold was selected manually for each plate, and maintained throughout the plate. The aim of the threshold was to select as many cells as possible, whilst excluding background regions.

Each region was expanded by seven pixels in every direction (Figure 2.4C) to define areas of the image to be analysed as ‘cells’. As the fluidics component is mounted directly onto the microscope, movement which occurs in picking up a tip, injecting solution and dispensing the tip can, on rare occasions, move the cell plate and therefore the field of view by a small amount. If the regions had not been expanded, this movement would cause an artefact: a sharp decrease in ‘cell’ fluorescence and corresponding increase of ‘background’ reading. By expanding the regions, small movements of the cell plate in any direction did not alter the fluorescence reading. This expansion did result in a slight underestimate of fluorescence

intensity at each time point. However, our readout (determined by the normalised gradient of this reading over time, see Chapter 3), was little affected.

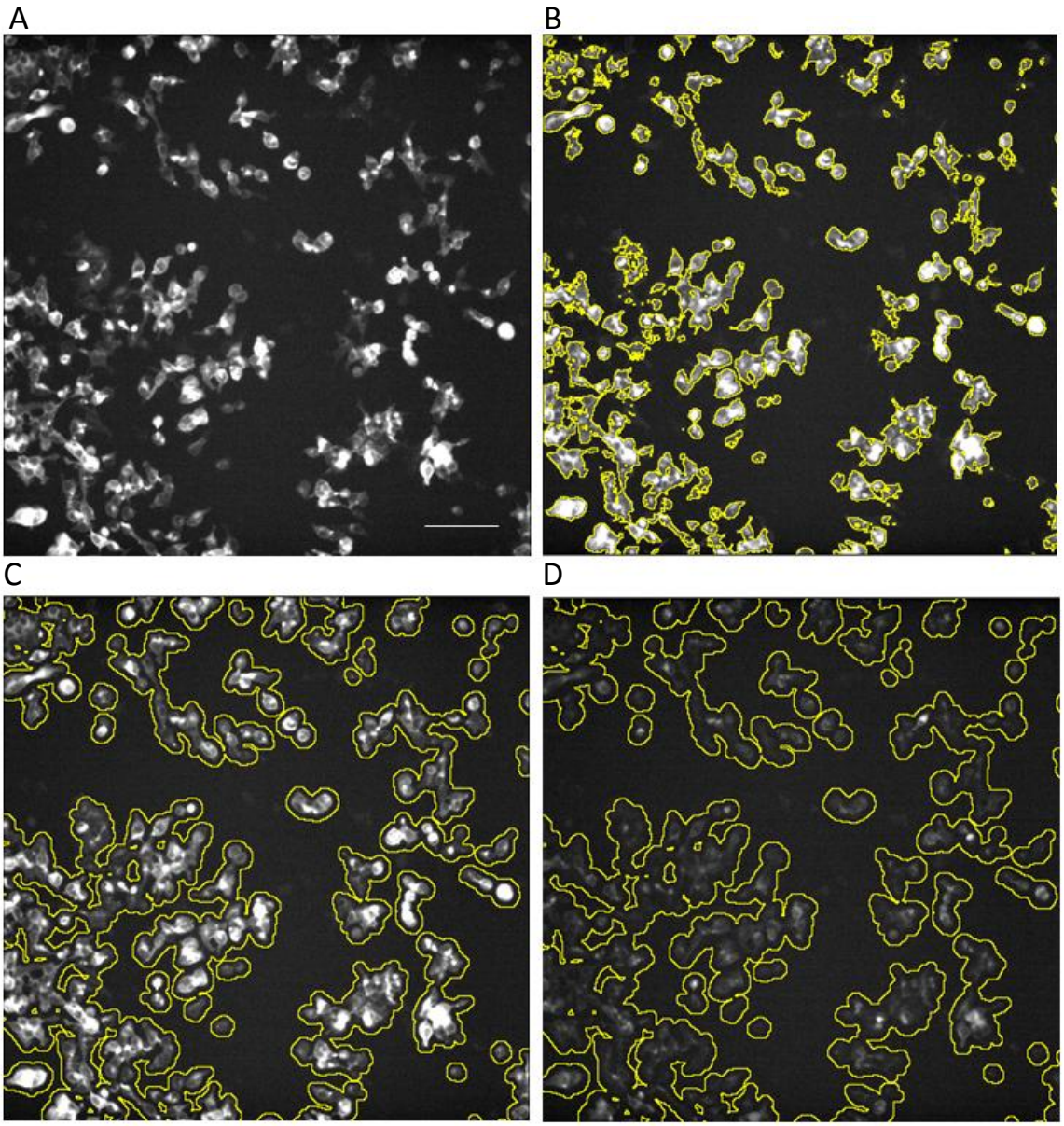


**Figure 2.4 YFP-CFTR image analysis.** A) Greyscale YFP-WT-CFTR image at 58 s during $I^-$ first addition protocol (i.e. immediately before forskolin addition). Scale bar = 100 µm. B) Threshold used to select fluorescent cells (areas above threshold are surrounded by yellow lines). C) Regions with fluorescence above threshold expanded by seven pixels in every direction. Cells expressing YFP-CFTR are within the yellow line, while areas outside this line are analysed as background. D) Image obtained at time point 150 s, after fluorescence quenching in response to 30 µM forskolin.

The mean fluorescence intensity within the selected cell regions was measured at every time point. The selection was then inverted, to obtain a mean fluorescence reading of the

background at every time point. Subtracting the background measurement from the cell measurement at each time point gave a trace of YFP fluorescence against time.

### 2.4.3 CFTR-pHTomato imaging and image analysis

CFTR-pHTomato imaging involved reading baseline pHTomato fluorescence in pH 7.4 standard buffer, decreasing pH using MES buffer (as standard buffer, with HEPES replaced with 10 mM MES, pH 5.5), increasing pH using Tris buffer (as standard buffer, with HEPES replaced with 100 mM tris, pH 9.5), and finally neutralising lumen pH of internal vesicles using 40 mM $NH_4Cl$. eGFP fluorescence reading and Hoechst nuclear stain were also acquired, and used for analysis.

CFTR-pHTomato protocol:

Cell plate contained 100 µl standard buffer

- Acquire image every 2 s for 4 s
- Add 50 µl MES buffer
- Acquire image every 2 s for 4 s
- Add 50 µl Tris buffer
- Acquire image every 2 s for 4 s
- Add 50 µl $NH_4Cl$ buffer
- Acquire image every 2 s for 4 s

| | Excitation | Emission | Dichroic mirror |
|---|---|---|---|
| **Hoechst** | 377 ± 25 nm | 447 ± 30 nm | 327-404 nm (R)<br>415-950 nm (T) |
| **eGFP** | 472 ± 30 nm | 520 ± 35 nm | 350-488 nm (R)<br>502-950 nm (T) |
| **pHTomato** | 531 ± 20 nm | 593 ± 20 nm | 350-555 nm (R)<br>569-950 nm (T) |

**Table 2.3 Hoechst, eGFP and pHTomato ImageXpress filter cubes.** Excitation and emission filters, and dichroic mirror. R = reflected, T = transmitted.

50 µl 1 µg/ml Hoechst (Sigma-Aldrich) was added to each well in cell medium, and incubated for 20 min. Cells in cell plates were washed as for YFP-CFTR imaging and plates loaded into the ImageXpress chamber. Wells were subject to individual chronic treatment, but during imaging all wells received identical fluid additions, with no requirement for well-specific treatments. Therefore, drug plates of specific treatments were not necessary.

Images were taken every 2 s. At the first time point, images were acquired sequentially using all three filter cubes (Table 2.3). At subsequent time points, only pHTomato images were acquired. CFTR-pHTomato imaging was done with a 20X objective.

Figure 2.5 shows that imaging the three fluorescent probes in parallel did not cause cross-talk between spectra.

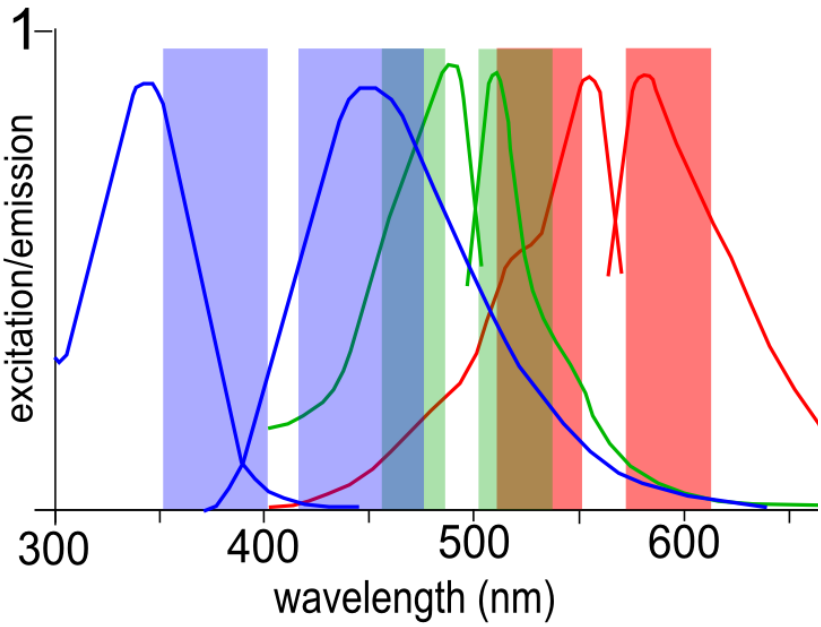


**Figure 2.5 Hoechst, eGFP and pHTomato spectra, shown with ImageXpress filters.** Modified from Li and Tsien (2012). Blue (Hoechst), green (eGFP) and red (pHTomato) lines and shading highlight the respective spectrum and excitation/ emission filters used in the ImageXpress protocol.

As for YFP-CFTR analysis, acquired 16-bit images were analysed using ImageJ. For pHTomato images, each well was exported as a stack, with each time point represented by an image in the stack. Hoechst and eGFP images, as there was only one time point per well, were exported as single 16-bit images.

Cells were selected based on eGFP fluorescence (Figure 2.6A), using a manually selected threshold which identified the maximal number of cells, without selecting background regions. Each region was expanded by seven pixels, to avoid fluid addition artefacts as for YFP-CFTR imaging. The mean eGFP fluorescence of each region was measured.

On the pHTomato image, the eGFP region locations were loaded and the mean pHTomato fluorescence of each region was measured at all time points (Figure 2.6B). This allowed the fluorescence of each region in the pHTomato image to be normalised to the respective region in the eGFP image, to allow for differences in total protein expression.

Each region was then weighted for the cell count (Figure 2.6C), estimated from the fraction of the area which was stained with Hoechst. In one case where Hoechst staining was not possible, the area of the GFP regions was used to estimate cell count. Regions containing saturated pixels were removed from the analysis.

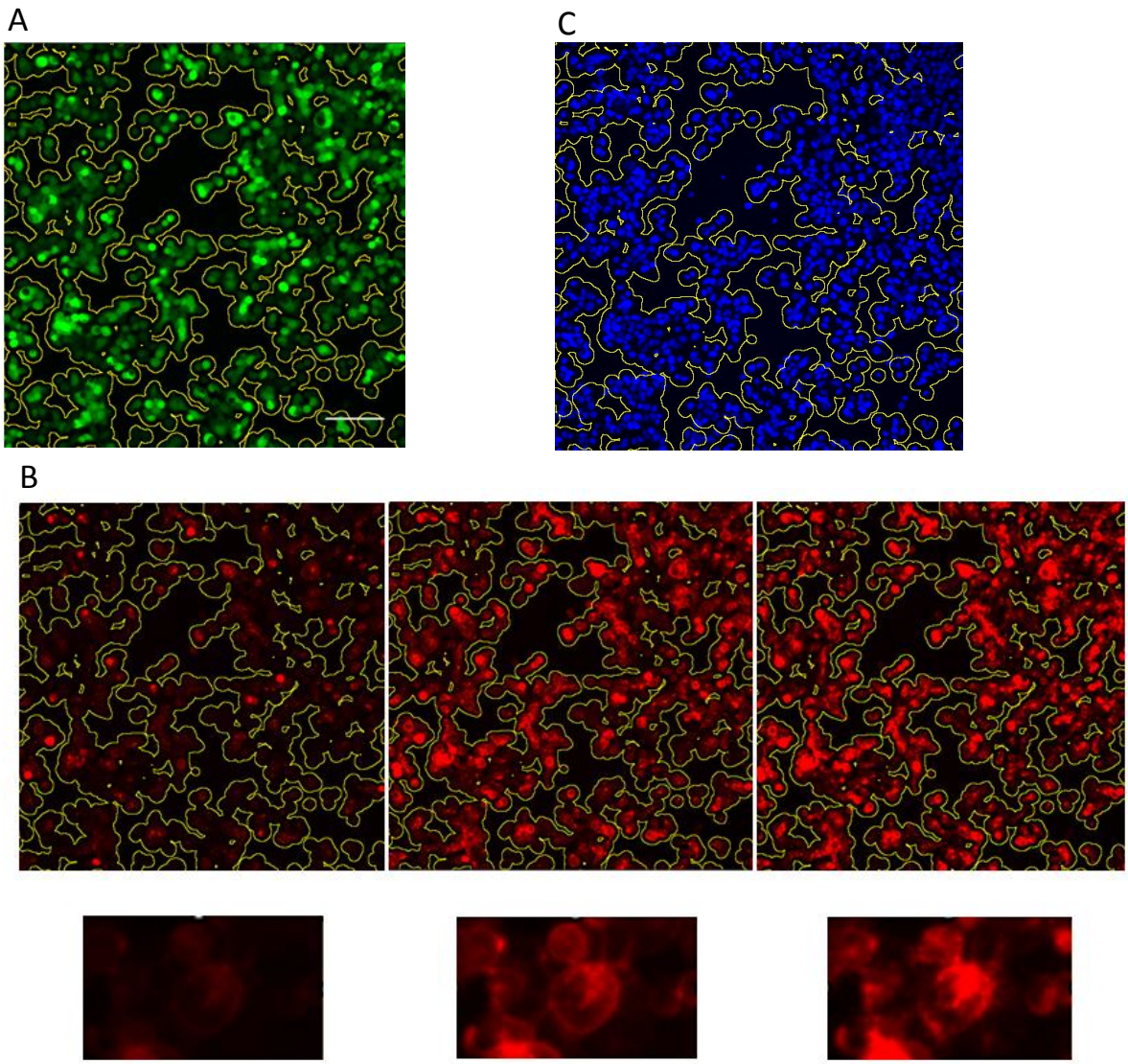


**Figure 2.6 CFTR-pHTomato image analysis.** A) Regions selected using eGFP fluorescence threshold, shown by yellow outline. Regions were expanded by seven pixels in every direction. Scale bar = 100 µm. B) pHTomato in acidic buffer (left), basic buffer (middle) and after addition of 40 mM $NH_4Cl$ (right). Lower panels show small expanded region in corresponding conditions. C) Hoechst nuclear stain used to weight fluorescence based on cell number.

### 2.4.4 Low temperature and chronic exposure incubation

Different experimental pre-incubation conditions were added to these protocols in order to study mutations or drug effects. Temperature correction of ΔF508-CFTR involved transfection of HEK293 cells with ΔF508-CFTR, incubation at 37°C for 24 h, followed by incubation at 30°C for 24 h before imaging. Chronic compound treatment (24 h) was tested by beginning incubation with the compound 24 h after transfection.

## 2.5 High-throughput confocal imaging

Cells were prepared as for ImageXpress YFP-CFTR imaging, including a Hoechst nuclear stain. The plates were loaded into the Opera High Content Screening System (PerkinElmer Life and Analytical Sciences, Bucks, UK). Cells were imaged with a 40X objective at 37°C. The Opera uses a triple bandpass filter (488/561/640 nm) for excitation of YFP, and a triple excitation dichroic mirror. UV light was used to excite Hoechst and a 425 nm dichroic longpass mirror with UV bandpass filter 450 ± 25 nm used to detect Hoechst emission.

Images were analysed using ImageJ. For membrane density analysis, a line was drawn across a cell in both the YFP and Hoechst image, and fluorescence along the line was plotted as a function of distance along the line.

## 2.6 Single channel patch clamp technique

### 2.6.1 Excised patch technique

HEK293 cells in 35 mm dishes, expressing the channel of interest (WT-CFTR or YFP-WT-CFTR), along with GFP as a marker of transfection, were used for voltage-clamp recording, in the excised inside-out patch configuration. Excised patch recordings were made using an EPC9 amplifier and Pulse acquisition software (HEKA Instruments Inc., MA, US). Cells were mounted in 35 mm dishes above an inverted fluorescence microscope (Nikon Eclipse TE200), with mercury light source and GFP filters (excitation/emission 450-500 nm/510-560 nm, dichroic mirror transmitted > 505 nm). The microscope was placed on an air table, and enclosed in a Faraday cage. The pipette was controlled via a micromanipulator (Narishige MHW-3, Digitimer Ltd., Hertfordshire, UK). The bath electrode consisted of a silver chloride bead immersed in the bath. All metal components were grounded.

Cells were perfused with bath solution (134 mM NMDG, 134 mM HCl, 2 mM $MgCl_2$, 5 mM HEPES, 0.5 mM EGTA, pH 7.1). Pipette solution contained 136 mM NMDG, 136 mM HCl, 2 mM $MgCl_2$ and 5 mM HEPES (pH 7.4). Pipettes were pulled from borosilicate glass capillaries of outer diameter 1.5 mm and inner diameter 0.86 mm (Harvard Apparatus Ltd., Cambridge, UK) using a vertical pipette puller (Narishige PP-830, Digitimer Ltd.). Pipettes were coated with Sylgard (Sigma-Aldrich) to reduce pipette capacitance, and fire polished using a microforge (Narishige MF-830, Digitimer). Pipettes, filled with pipette solution and measured in bath solution, typically had a resistance of ~12 MΩ.

To obtain a seal, a micromanipulator was used to move the pipette towards the cell surface. An increase in resistance indicated the pipette was nearing the cell surface. At this point, a small amount of suction was applied to the pipette. Upon establishing a seal, the

micromanipulator was used to quickly and sharply pull the pipette upwards, excising the patch in the inside-out configuration.

To apply treatments, a microperfusion system was made using glass capillaries (Harvard Apparatus) gravity fed from 25 ml syringes connected by flexible silastic tubing (Harvard Apparatus). Treatments made in bath solution were applied to the cytosolic face of the patch by moving the pipette within the perfusion system, into the appropriate stream. Continuous recordings were made at room temperature with the pipette potential held at + 60 mV (- 60 mV membrane potential).

### 2.6.2 Analysis of patch data

Records were exported to ClampFit (Molecular Devices), and filtered digitally at 50 Hz. Programs developed and provided by László Csanády (Semmelweis University, Hungary) were used to analyse traces. A detailed description of multichannel dwell-time distribution analysis is published (Csanády, 2000). Briefly, baseline correction removed drift in the trace to more clearly show changes in conductance caused by channel opening. An events list was produced, by applying half-amplitude threshold crossing on the baseline corrected trace, which records the conductance level (i.e. closed, one open channel, two open channels) and the length of each event. The events list was used to produce dwell time histograms, which showed the number of events observed at each conductance level, binned according to the length of dwell-times. The time axis was logarithmic and contained six bins per *e*-fold (Figure 2.7, yellow histograms).

The distribution of dwell times was fit to a three-state gating model ($C_1 \leftrightarrow O \leftrightarrow C_2$), in which $C_1 \leftrightarrow O$ represents a simplified opening and closing (entry and exit from bursts), and $O \leftrightarrow C_2$ represents ATP-independent fast, flickery closures. Parameters were obtained by Maximum Likelihood fitting of dwell-time histograms at all conductance levels to identify the most likely opening rate ($r_{CO}$), closing rate ($r_{OC}$) and rates of entry ($r_{OF}$) and exit ($r_{FO}$) from brief flickery closures for the channel, and thus the most likely interburst duration ($T_{ib} = 1/r_{CO}$), and open burst duration ($T_b = (1/r_{OC})*(1+r_{OF}/r_{FO})$).

Both $r_{CO}$ and $r_{OC}$ can be reliably estimated when the number of channels in the patch is known. To calculate the probability of there being another, unseen, channel in the patch, the same events list was fit to the model assuming n + 1 channels (with n being the maximum number of simultaneously open channels observed). For example, in the data in Figure 2.7, $r_{CO}$ would be estimated assuming that this distribution was obtained from three channels rather than from two. Given the cumulative length of time the channel spends in the top conductance state, the probability of missing the $(n+1)^{th}$ channel was calculated. In cases

where the probability of not seeing this putative additional channel was < 0.05, the number of channels in the patch was assumed to be known. These records were fit to obtain $P_o$, $r_{CO}$ and $r_{OC}$.

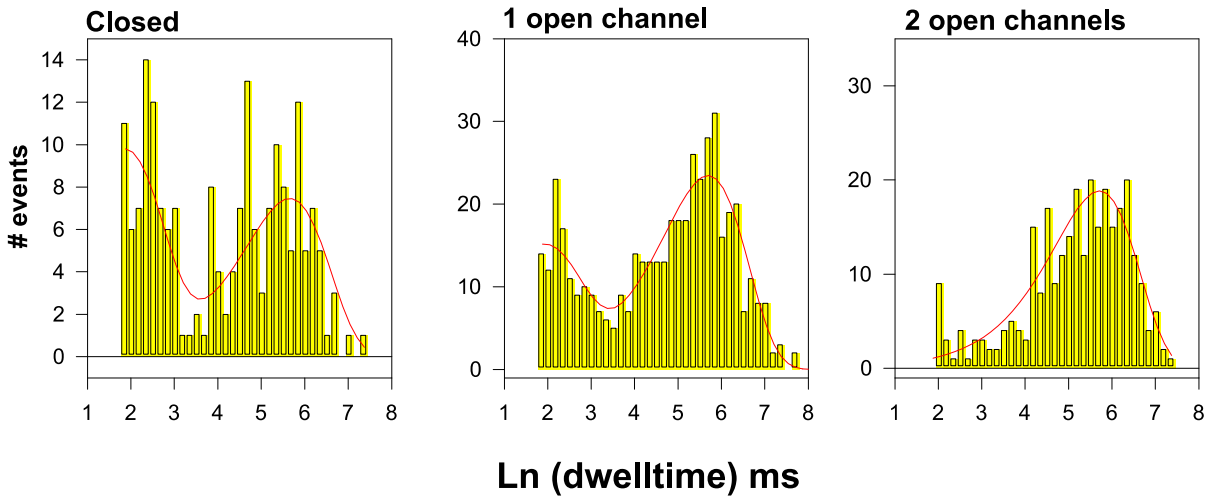


**Figure 2.7 Dwell time distribution of WT-CFTR.** The patch, containing two gating channels, was activated with 300 nM PKA + 2 mM ATP. Yellow histograms show the number of events at each dwell time (in six bins for each ln unit). Red lines represent the expected distribution following fitting to the three state model: $C_1 \leftrightarrow O \leftrightarrow C_2$.

However, in most CFTR recordings the number of channels in the patch could not reliably be estimated (probability of missing the $(n+1)^{th}$ channel > 0.05). In these circumstances, noise analysis was used to estimate $P_o$, using the relationship between mean and variance for binomially distributed samples:

$$\sigma^2(I) = Ii(1 - P_0) \qquad \text{[Equation 2.1]}$$

Where $\sigma^2(I)$ is the variance of the current samples, $I$ is the mean of the current samples (pA), and $i$ is the single channel current (pA). The gradient of a line between the origin and $\sigma^2/i$ against $I$ gives $(1 - P_o)$. In these cases, $T_b$ can still be estimated from dwell time distributions, as it is not steeply dependent on the number of channels. Therefore, when the number of channels in a patch could not be determined, $P_o$ was obtained from noise analysis, $T_b$ from Maximum Likelihood fitting of dwell-time histograms, and $T_{ib}$ from Equation 2.2.

$$\tau_{ib} = \frac{\tau_b(1-P_o)}{P_o} \qquad \text{[Equation 2.2]}$$

## 2.7 Figures and statistics

All average plots including error bars in this thesis represent mean ± SEM. In cases where two groups were compared using statistics, this was carried out using paired or unpaired t-tests, as appropriate. When more than two groups were compared, this was done using a

one way analysis of variance (ANOVA), followed by a post-hoc Tukey's test (for all pairwise comparisons) or a Dunnett's test (for comparisons vs. a control). In cases where plots or statistics differ from what is described here, for example if a data set failed the normality test and was subsequently compared using a non-parametric test, this is stated in the figure legend.

All statistics were carried out using SigmaPlot.

# Chapter 3

# YFP-CFTR: Gating sensitive fluorescent probe

## 3.1 Introduction

Halide sensitive YFP (H148Q/I152L) has been in use in CFTR research for a number of years (see Galietta et al., 2001a, 2001c; Muanprasat et al., 2004; Pedemonte et al., 2005a), following optimisation by the Verkman lab (Galietta et al., 2001b). This chapter introduces the properties of YFP (H148Q/I152L), before describing the utilisation of the fluorescent protein in our project.

### 3.1.1 GFP

YFP (H148Q/I152L) is a modified form of GFP, a naturally occurring 238 amino-acid protein from the *Aequorea victoria* jellyfish. GFP is an 11 strand β-barrel formed around a central helix, within which the chromophore, generated by an autocatalytic reaction involving residues 65 to 67, is located (Heim et al., 1994). Fluorescence occurs when absorption of a photon causes excitation of an electron in the chromophore, which, when relaxing back to the ground state, releases energy as light of longer wavelength.

The original GFP has two excitation peaks, at 395 nm and 475 nm, and an emission peak at 509 nm (Chalfie et al., 1994; Heim et al., 1994). The GFP chromophore can be ionised at the phenol group derived from tyrosine residue 66, with the protonated and deprotonated states responsible for the two peaks on the GFP excitation spectrum (Heim et al., 1994). Mutations to enhance fluorescence following excitation at 475 nm, and increase the rate of post-translational modification (Heim et al., 1995; Cormack et al., 1996), produced eGFP, the form of GFP currently used by most labs.

### 3.1.2 Halide sensitive YFP

Publication of the crystal structure of GFP allowed rational design of mutations, such as those which alter excitation and emission spectra to obtain different coloured fluorescent proteins. Introducing an aromatic ring at position 203 (T203Y), close to the chromophore, caused a red shift in the spectrum, producing the first YFP. Mutations S65G, V68L and S72A enhanced the brightness of YFP in living cells (Ormo et al., 1996).

Like GFP, YFP (T203Y/S65G/V68L/S72A, hereafter referred to as YFP) exists in protonated and deprotonated states (excitation peaks at 416 nm and 514 nm, respectively). Introduction of the H148Q mutation increased the $pK_a$ of protonation to ~7.1 (Jayaraman et al., 2000; Wachter et al., 2000). The two protonation states are the basis of YFP halide sensitivity.

Binding of $Cl^-$ to the protein destabilises the deprotonated state, causing a decrease in absorbance at 514 nm (Figure 3.1A). This causes a shift in the $pK_a$, as the protonated form remains favourable in increasingly alkaline conditions (Figure 3.1B).

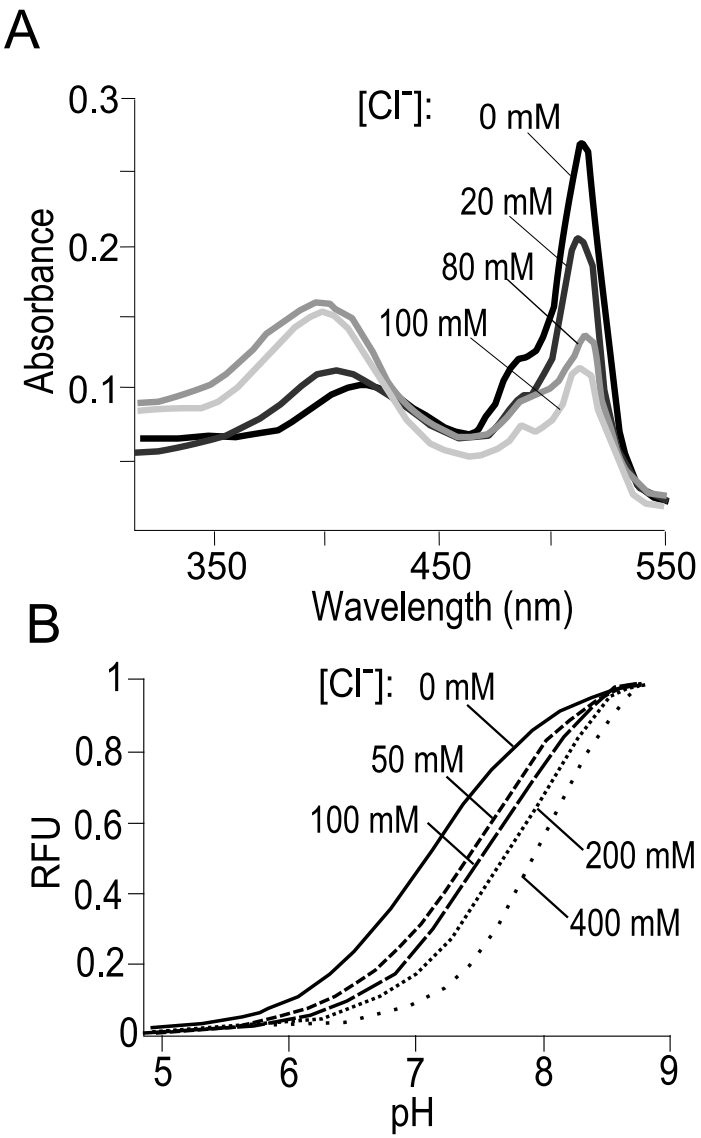


**Figure 3.1 YFP (H148Q) absorbance and $Cl^-$ sensing properties.** Modified from Jayaraman et al. 2000. A) Absorbance spectrum in the presence of increasing $[Cl^-]$, measured at pH 6.4. Absorbance at peak 514 nm falls as $[Cl^-]$ increases. This occurs alongside an increase in absorbance at peak 416 nm, which is not excited during YFP imaging. B) pH titration in the presence of increasing $[Cl^-]$. Fluorescence emission measured following excitation at 514 nm. At physiological pH 7.4 the relative fluorescence units (RFU) decrease in increasing $[Cl^-]$. Note the YFP variant used in this figure (YFP (H148Q)) is different to that which is used in subsequent work (YFP (H148Q/I152L)). Introduction of I152L did not appreciably alter pH dependence (Galietta et al., 2001b).

Structures of crystals obtained in the presence of 100 mM $I^-$ showed the halide bound in close proximity to the chromophore (Wachter et al., 2000). The negative charge on the chromophore shifts the equilibrium of protonation away from the deprotonated state.

### 3.1.3 YFP (H148Q/I152L) in CFTR research

In order to utilise YFP (H148Q) in CFTR research, it was necessary to increase the affinity for $I^-$ compared to $Cl^-$. Intracellular $[Cl^-]$ ($[Cl^-]_i$) is approximately 20 mM (Bregestovski et al., 2009). YFP variants with high $Cl^-$ affinity would be largely quenched at physiological levels of $[Cl^-]_i$, regardless of CFTR activity. However, physiological levels of $I^-$ are extremely low (i.e. $[I^-]_i$ is close to zero). $Cl^-/I^-$ exchange protocols offered a possibility for the study of CFTR function, taking advantage of the relatively high permeability of CFTR to $I^-$ (Anderson et al., 1991; Linsdell et al., 1997).

In order to improve affinity for $I^-$, mutations were made to the halide binding site, with I152L producing the lowest $K_I$ (2 mM) compared to $K_{Cl}$ (85 mM) (Galietta et al., 2001b). This property is exploited to assess CFTR channel function because, when co-expressed with CFTR in the presence of an extracellular $I^-$ buffer, YFP (H148Q/I152L) fluorescence will only be quenched if CFTR is open, allowing $I^-$ to enter the cell (Figure 3.2).

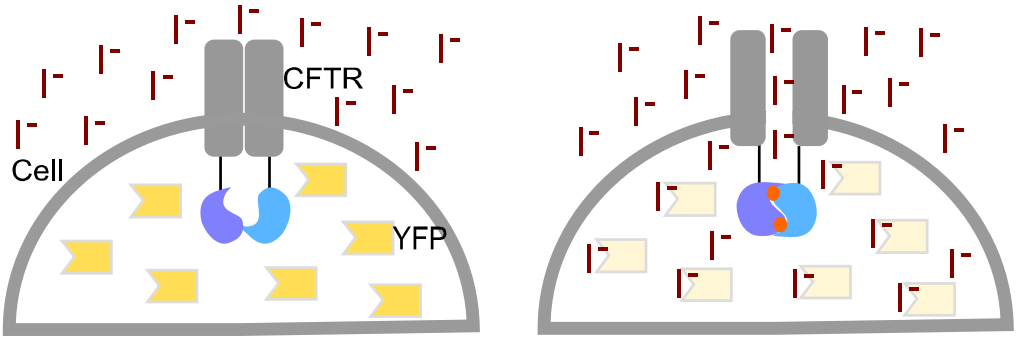


**Figure 3.2 $Cl^-/I^-$ exchange protocol to study CFTR activity.** Left: CFTR is not gating, $I^-$ cannot enter the cell and YFP (H148Q/I152L) fluorescence remains bright. Right: CFTR is gating, and the driving force for $I^-$ entry allows large influx. $I^-$ binds YFP (H148Q/I152L), and fluorescence decreases.

This assay has been used to screen for ΔF508-CFTR potentiators, as described earlier (Introduction). In this chapter, some initial control experiments were done using YFP expressed in the cytosol, co-expressed with CFTR. Cytosolic YFP quenching was measured using a plate reader (FLIPR). Subsequent work describes the optimisation of a YFP-CFTR fusion protein, in which YFP is fused to the N-terminal of CFTR. In most cases, YFP-CFTR was monitored using an automated fluorescence image acquisition system, exploiting a

wide-field microscope (ImageXpress). Throughout this thesis, YFP (H148Q/I152L) is referred to as YFP.

### 3.1.4 YFP-CFTR fusion protein

YFP-CFTR was obtained by mutating GFP-CFTR (Moyer et al., 1998), already in use in other labs (donated by Bruce Stanton, Geisel School of Medicine, NH, USA). GFP-CFTR was originally designed to study the role of cAMP in targeting of CFTR to the membrane. GFP-WT-CFTR colocalises with antibody-stained WT-CFTR (Moyer et al., 1998), as well as with a membrane stain (Ban et al., 2007), which suggests that trafficking is not affected by the tag. Whole cell and single channel patch clamping show unchanged channel conductance, selectivity and blocker sensitivity in GFP-tagged CFTR (Moyer et al., 1998; Vais et al., 2004).

The N-terminal is known to be involved in both gating and trafficking of CFTR, raising concerns that the tag would affect one, or both, of these processes. Expressing CFTR lacking the N-terminal (Δ2-72) produced only core-glycosylated, immature CFTR with no membrane expression (Prince, 1999). Mutations which inhibit interactions between the N-terminal and other CFTR domains, cause reduced $P_o$, characterised by decreased burst duration (Naren et al., 1999). Similar effects are seen for D58N, an N-terminal mutation associated with a mild form of CF (Fu et al., 2001). An N-terminal FLAG epitope also reduces $P_o$, but in this case opening rate is most affected (Chan et al., 2000).

Based on these observations, we gave some thought to inserting the YFP tag elsewhere in the CFTR protein. Owing to the lack of a CFTR full-length crystal structure, rational design of insertional fusions is difficult. Due to the important roles of the NBDs, the R-domain, and the ICLs in gating and trafficking, an intracellular tag would most likely need to be fused via the internal end of a TM. However, the location and length of the TMs are not entirely known. For this reason, a random insertion protocol was used to create a library of insertional fusions. However, comparison of the random insertion YFP-CFTR fusions, with the N-terminal YFP-CFTR fusion, showed that the latter had preferable characteristics. Experiments described in this chapter led us to conclude that the function and trafficking of the YFP-CFTR N-terminal fusion protein were sufficiently similar to those of the WT-CFTR protein. Therefore, work on insertional fusions was discontinued.

## 3.2 The HEK293 cellular environment

When planning experiments involving expression of a genetically encoded probe, the cell line in which the protein of interest will be expressed is an important choice, as cell

background can affect protein function. When selecting the cell line, three main questions were considered: (*i*) are all proteins essential for processing and function of CFTR present? (*ii*) Will endogenous CFTR and other anion pathways affect the assay? (*iii*) Will transfected CFTR be phosphorylated by endogenous PKA under basal, unstimulated conditions?

Human embryonic kidney (HEK293) cells are a commonly used cell line, often selected for their rapid growth rate and ease of transfection. Results in this chapter, and obtained previously by others, suggest that WT-CFTR is successfully trafficked to the membrane of HEK293 cells, whilst ΔF508-CFTR is retained at the ER, as expected (Domingue et al., 2014). Whilst it is unlikely that trafficking of CFTR in HEK293 cells is identical to that occurring in native epithelial cells *in vivo*, it appears that the cellular machinery for function and essential processing of CFTR is available, to a suitable degree.

The work presented in this thesis involved the expression of many different CFTR mutations, testing of which would have been affected by the presence of endogenous WT-CFTR. Domingue *et al.* (2014) found no detectable CFTR mRNA or protein in untransfected HEK293 cells. To confirm the absence of CFTR in HEK293 cells, cells transfected only with YFP (CFTR-null cells, YFP expressed in the cytosol) were treated with 200 nM or 5 µM forskolin. 200 nM forskolin has a small effect on CFTR, whilst 5 µM induces near maximal WT-CFTR activation (see page 62). CFTR-null cells treated with 200 nM or 5 µM forskolin had similar quenching rates (Figure 3.3, $p = 0.5$). This suggested that there was no detectable endogenous CFTR in untransfected HEK293 cells.

Many endogenous ion channels and G-protein coupled receptors (GPCRs) are expressed in HEK293 cells (Dautzenberg et al., 2000; Shaw et al., 2002). CFTR is phosphorylated by PKA, a kinase downstream of cAMP, the levels of which would be affected by both $G\alpha_S$- and $G\alpha_I$-coupled GPCRs. CFTR-positive cell quenching rate in the absence of forskolin was not significantly different to that of CFTR-null cells (Figure 3.3, $p = 0.439$). This suggested that transfected CFTR was not phosphorylated by endogenous PKA in unstimulated HEK293 cells. CFTR-positive cells were activated by 200 nM or 5 µM forskolin to demonstrate rates achieved by CFTR activation (Figure 3.3).

Other groups have detected $GABA_A$ (Shaw et al., 2002), TMEM16A and $ClC_2$ (Domingue et al., 2014) mRNA in HEK293 cells, all of which would provide alternative anion pathways in the assay. The slow quenching rates observed in CFTR-null and untreated CFTR-positive cells were most likely caused by $I^-$ entry via these anion pathways (Figure 3.3), and were considered sufficiently low as to not affect assay readout to a significant degree.

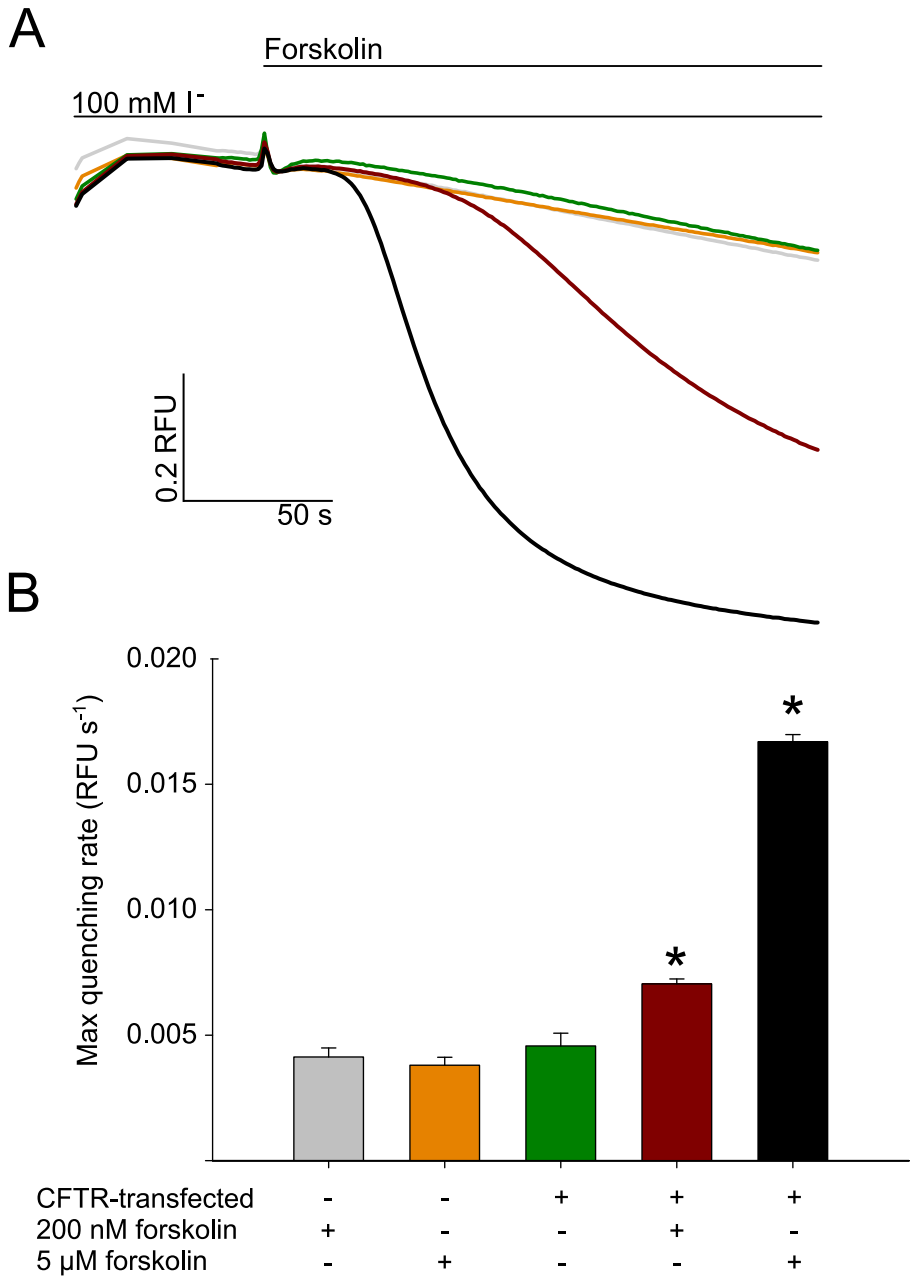


**Figure 3.3 Quenching of cytosolic YFP in CFTR-null and CFTR-positive cells.** A) YFP quenching in response to forskolin in HEK293 cells transfected with cytosolic YFP ± WT-CFTR. Forskolin is added to each well in the presence of 100 mM $I^-$. Trace colours correspond to bar colours in B. B) Quenching quantified by maximal rate per s (RFU $s^{-1}$), as in papers by Galietta *et al.* (2001c). * indicates $p < 0.05$ vs. untreated CFTR-positive cells. n = 12 for CFTR-null cells, n = 6 for untreated CFTR-positive cells, and n = 18 for forskolin-treated CFTR-positive cells.

Galietta *et al.* (2001) reported that endogenous anion flux was low in Chinese hamster ovary (CHO) cells compared to other cell lines. However, in our assay, the anion permeability of CFTR-null CHO cells was higher than CFTR-null HEK293 cells ($9 \pm 0.7\ 10^{-3}$ RFU $s^{-1}$ vs. $4 \pm 0.2\ 10^{-3}$ RFU $s^{-1}$). Additionally, the expression of YFP by CHO cells was lower, seen as ~2-

fold decrease in average fluorescence, compared to HEK293 cells. Therefore, for the remainder of this work, CFTR was expressed in HEK293 cells by transient transfection.

### 3.3 YFP-CFTR fusion assayed using FLIPR

The function of YFP-CFTR as an anion channel was initially assessed using FLIPR. Comparison of 0 µM and 5 µM forskolin treated YFP-WT-CFTR showed that the YFP-CFTR fusion protein functioned as an anion channel when activated by forskolin (Figure 3.4). Figure 3.4A shows large artefacts, which occur upon fluid addition to the wells. Due to the low signal (approximately 10% of that obtained with cytosolic YFP) the artefact affected readout more in YFP-CFTR than in separately expressed YFP and CFTR. Figure 3.4B shows the traces from immediately after the second addition artefact, with the fluorescence axis expanded so quenching can be seen more clearly.

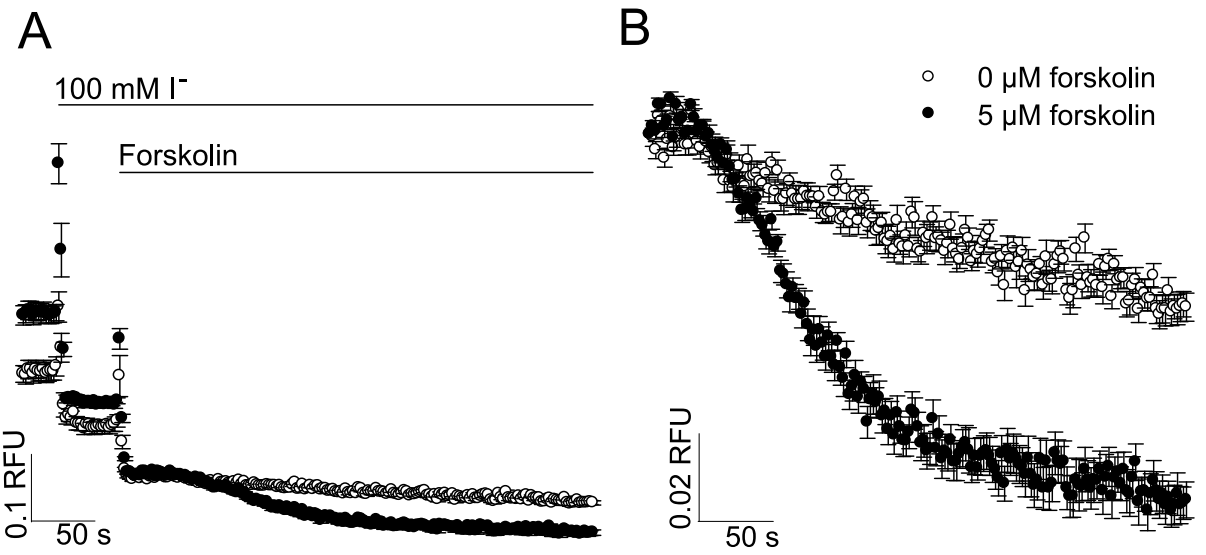


**Figure 3.4 YFP-WT-CFTR function measured in FLIPR.** A) Quenching traces of HEK293 cells expressing YFP-WT-CFTR in response to 0 µM or 5 µM forskolin. B) Traces shown from after second addition artefact (notice change in *y*-axis scale). Signal was normalised to a point immediately after second addition artefact in both A and B. n = 8.

These results demonstrated that the N-terminal tag did not render the CFTR non-functional, or entirely prevent trafficking to the membrane. However, Figure 3.4 shows a noisy signal with large addition artefacts and high fluorescent background which remained following quenching of YFP (91% of fluorescence remained). These factors had the potential to limit the sensitivity of the assay.

## 3.4 YFP-CFTR fusion assayed using ImageXpress

ImageXpress is a high-content, automated wide-field fluorescence microscope with 96-well plate holder and fluidics capabilities. Cells expressing YFP-WT-CFTR were imaged in the absence and presence of 5 µM forskolin. Comparison of Figure 3.5 with Figure 3.4 shows that ImageXpress recordings resulted in a dramatic improvement of the signal-to-noise ratio, smaller addition artefacts, and lower background signal (approximately 40% YFP fluorescence remained after quenching). All following fluorescence imaging experiments were therefore conducted using ImageXpress acquisition and image analysis.

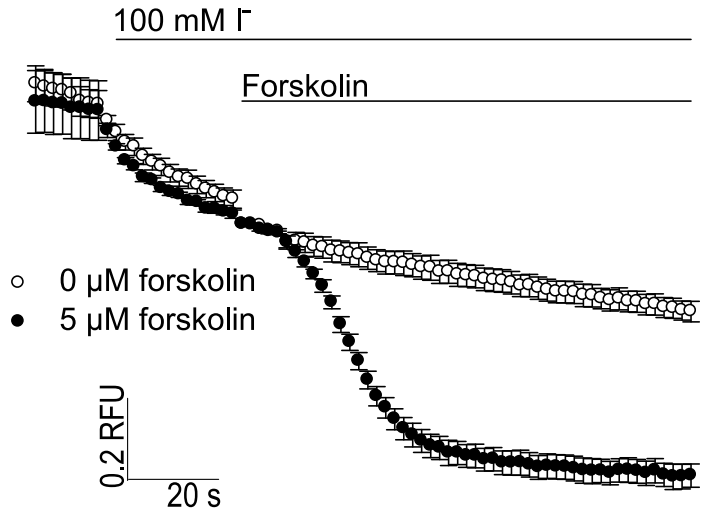


**Figure 3.5 YFP-WT-CFTR function measured in ImageXpress.** ImageXpress quenching traces of YFP-WT-CFTR in response to 0 µM or 5 µM forskolin. Signal was normalised to the point immediately after addition of forskolin. n = 7.

## 3.5 Quantification of quenching as a measure of CFTR ion channel function

In order to further understand the relationship between YFP-CFTR quenching and $[I^-]$ at the chromophore, we measured fluorescence after equilibrating the cells with different $[I^-]_e$.

YFP-WT-CFTR was activated by maximal (20 µM) forskolin, in the presence of different $[I^-]_e$. After a short delay, the fluorescence signal decayed exponentially to reach a steady state level (Figure 3.6). This quenching reflects $I^-$ entry into the cytosol (until $[I^-]_i$ is at equilibrium with $[I^-]_e$), and binding of $I^-$ to YFP. Fluorescence was normalised to the time point immediately before addition of extracellular $I^-$. At this time point, there was no $I^-$ at the YFP chromophore, and fluorescence was maximal. Figure 3.6A shows quenching in the presence of $[I^-]_e \leq 100$ mM. For $[I^-]_e > 100$ mM, the concentration was changed after maximal activation of CFTR in the presence of 100 mM $I^-$ (Figure 3.6B). Experiments of both kinds were used to generate Figure 3.6C: fluorescence as a function of $[I^-]_e$. These data points are well described by a single site binding equation (Equation 3.1).

$$F = 1 - \frac{B_{max}[I^-]_e}{K_{0.5} + [I^-]_e} \quad \text{[Equation 3.1]}$$

Where F is normalised fluorescence, $B_{max}$ is the maximal proportion of fluorescence quenched at saturating $[I^-]_e$ and $K_{0.5}$ is the $[I^-]_e$ giving half maximal binding. Best fit parameter estimates obtained were: $K_{0.5}$ = 39.3 mM ± 3 mM and $B_{max}$ = 0.98 ± 0.02. The $K_{0.5}$ obtained from Equation 3.1 represents the $[I^-]_e$ which, at equilibrium, resulted in an $[I^-]$ at the chromophore equivalent to the YFP binding affinity for $I^-$. A $B_{max}$ of ~1 indicated that when the $I^-$ site was occupied, YFP fluorescence was entirely quenched ($F_{UNBOUND}$ = 1; $F_{BOUND}$ = 0).

In addition, the good fit suggested that varying $[I^-]_e$ did not lead to major changes in steady state membrane potential ($V_M$), and that the YFP expressed in HEK293 cells, fused to CFTR, has very similar characteristics to those of the purified protein (Galietta et al., 2001b). By rewriting the equation for unbound receptors (normalised fluorescence as a function of $[I^-]$ at the chromophore: Equation 3.2), we can express $[I^-]$ at the chromophore as a function of measured fluorescence (Equation 3.3).

$$F = 1 - \frac{[I^-]}{K_I + [I^-]} \quad \text{[Equation 3.2]}$$

$$[I^-] = K_I \frac{(1-F)}{F} \quad \text{[Equation 3.3]}$$

Where F is fluorescence and $K_I$ is the published binding affinity (Galietta et al., 2001b).

Using Equation 3.3, fluorescence values (Figure 3.7A) were converted to $[I^-]$ at the chromophore (Figure 3.7B). Differentiation of the $[I^-]$ curve in Figure 3.7B gave the rate of $I^-$ entry (Figure 3.7C). CFTR activation was quantified using the maximal observed rate of $I^-$ entry ($d[I^-]/dt$ in mM $s^{-1}$). This method of quantification was used to construct a concentration-response curve to forskolin (Figure 3.7D). The rate of $I^-$ entry is related to channel $P_o$, the proportion of YFP-CFTR proteins located at the membrane, and the driving force for $I^-$ entry.

In published literature on halide sensitive cytosolic YFP, the quenching protocol is run in one of two ways. Either, it is run in a similar manner to that which has been described here (i.e. $I^-$ as a first addition, for example see Galietta et al., 2001c), or, by activating CFTR in the absence of $I^-$, followed by addition of extracellular $I^-$ (i.e. $I^-$ as a second addition, for example see Pedemonte et al. 2005). The majority of the work in this thesis was carried out using the $I^-$ first addition protocol, as in Figure 3.5.

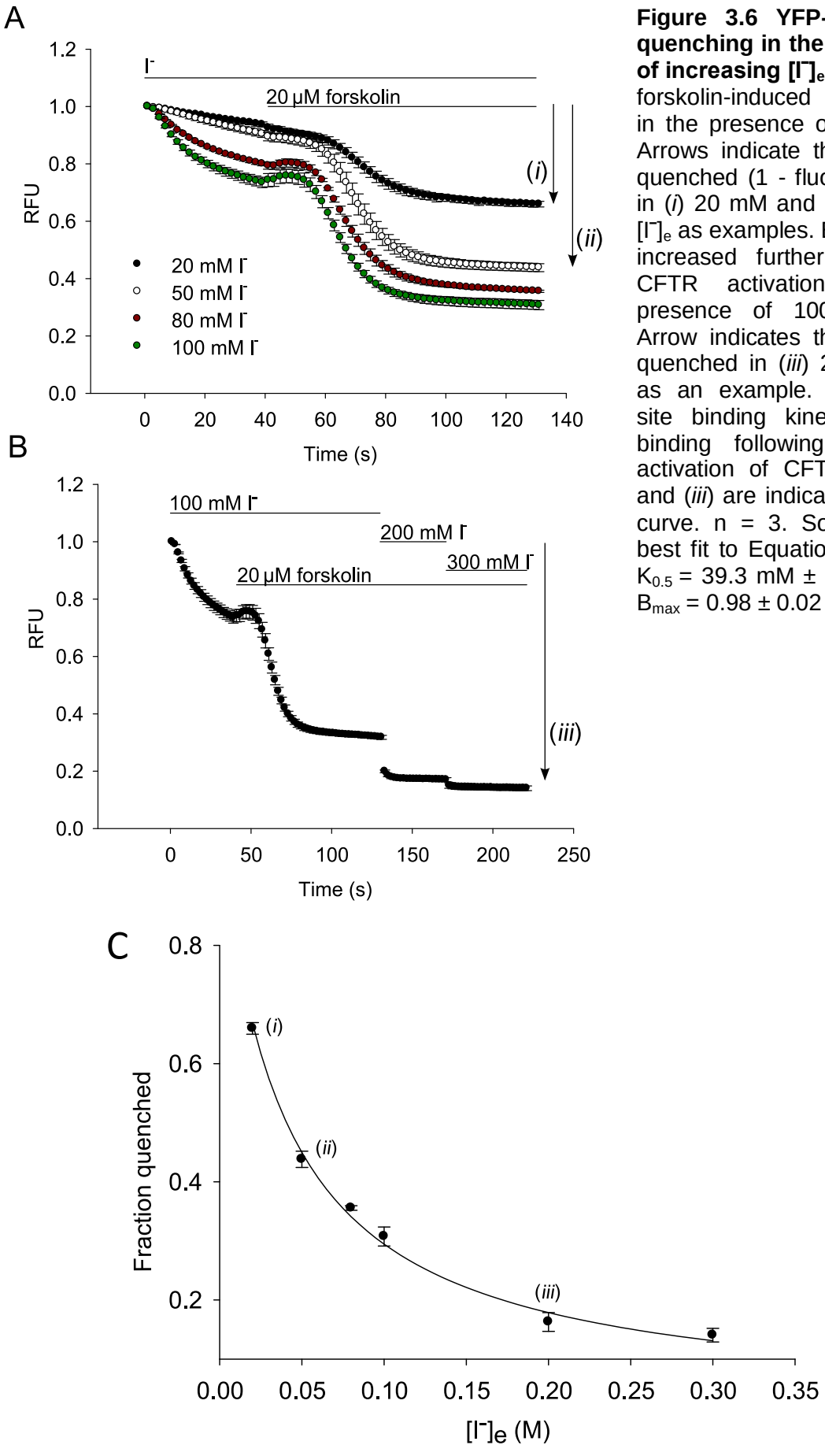


**Figure 3.6 YFP-WT-CFTR quenching in the presence of increasing $[I^-]_e$.** A) 20 µM forskolin-induced quenching in the presence of low $[I^-]_e$. Arrows indicate the fraction quenched (1 - fluorescence) in (*i*) 20 mM and (*ii*) 50 mM $[I^-]_e$ as examples. B) $[I^-]_e$ was increased further following CFTR activation in the presence of 100 mM $I^-$. Arrow indicates the fraction quenched in (*iii*) 200 mM $I^-$ as an example. C) Single site binding kinetics of $I^-$ binding following maximal activation of CFTR. (*i*), (*ii*) and (*iii*) are indicated on the curve. n = 3. Solid line is best fit to Equation 3.1 with $K_{0.5}$ = 39.3 mM ± 3 mM and $B_{max}$ = 0.98 ± 0.02

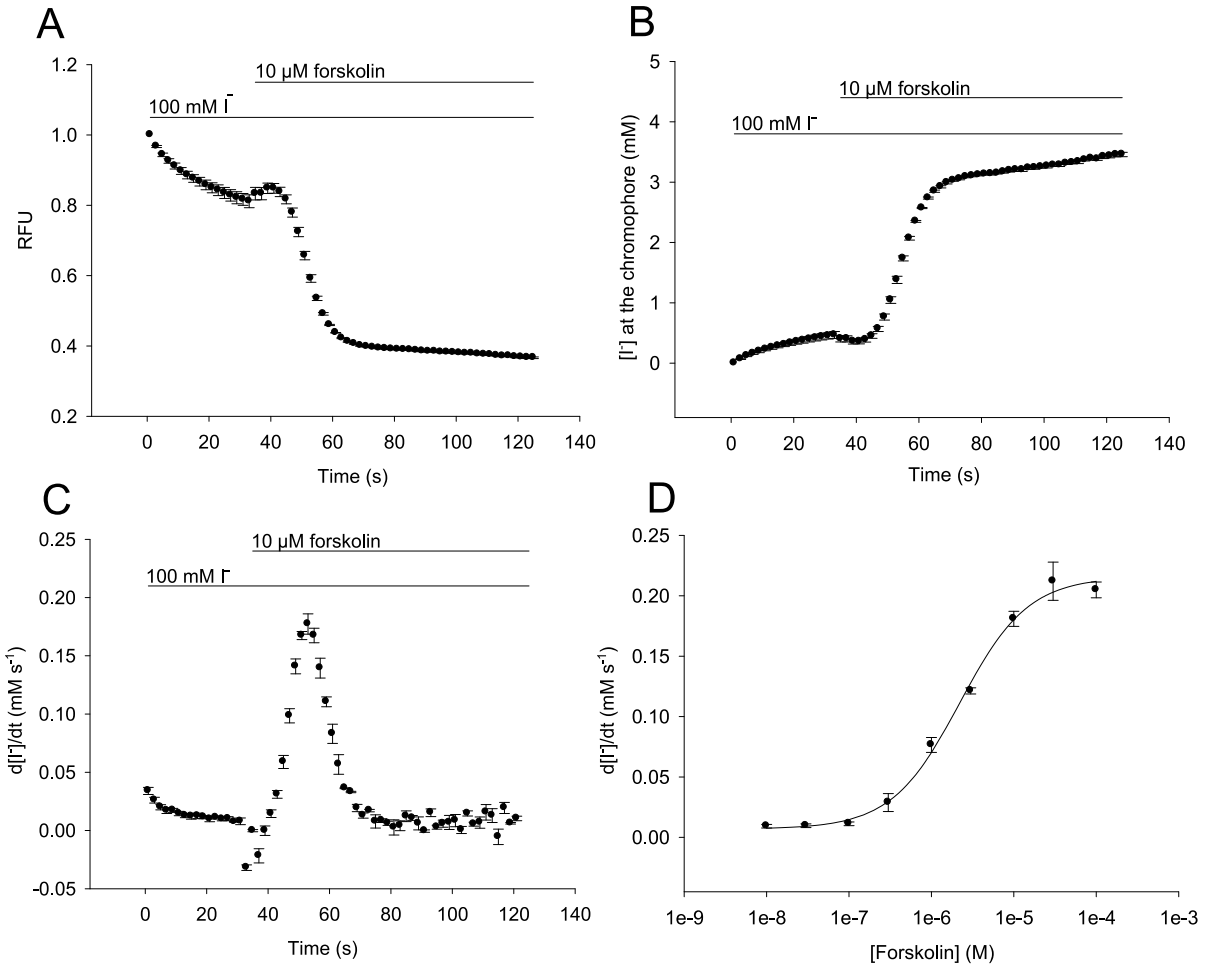


**Figure 3.7 Quantification of CFTR ion channel function using YFP-WT-CFTR quenching.** A) Normalised fluorescence quenching in response to 10 µM forskolin. B) [$I^-$] at the chromophore increases in response to 10 µM forskolin. C) The gradient of the trace in B) show the rate of $I^-$ entry in response to 10 µM forskolin at each time point. D) Forskolin concentration-response curve using fastest observed $I^-$ entry rate (d[$I^-$]/dt mM $s^{-1}$) to quantify CFTR activation. $EC_{50}$ = 2.2 µM ± 0.3 µM. n = 3.

This protocol was chosen to allow observation of the time course of CFTR activation. This protocol also minimised the consequences of fluid addition artefacts (seen in Figure 3.5). These are small, largely unavoidable changes in fluorescence associated with fluid additions. Due to the short delay after forskolin addition, before CFTR opening and therefore quenching begins, the time points of interest do not occur immediately after any fluid addition (for example see Figure 3.7A-C). Therefore, the artefacts have little effect on the final readout.

The alternative protocol, in which CFTR is activated in the absence of $I^-$, and quenching time course is followed immediately after $I^-$ addition, can also be useful. For these experiments, CFTR is activated for 90 s, at which point steady state activation is assumed to have been

achieved. $I^-$ is then introduced, causing immediate quenching. This, the $I^-$ second addition protocol, is described in detail in Chapter 6. This protocol is useful when steady state conditions are the focus of investigation.

## 3.6 YFP-WT-CFTR vs. untagged WT-CFTR ion channel function

Although the literature reported little effect of the N-terminal GFP tag on CFTR channel function, due to the importance of the N-terminal in function and trafficking, and the differences in experimental set-up, YFP-WT-CFTR function as an anion channel was compared with untagged WT-CFTR in HEK293 cells.

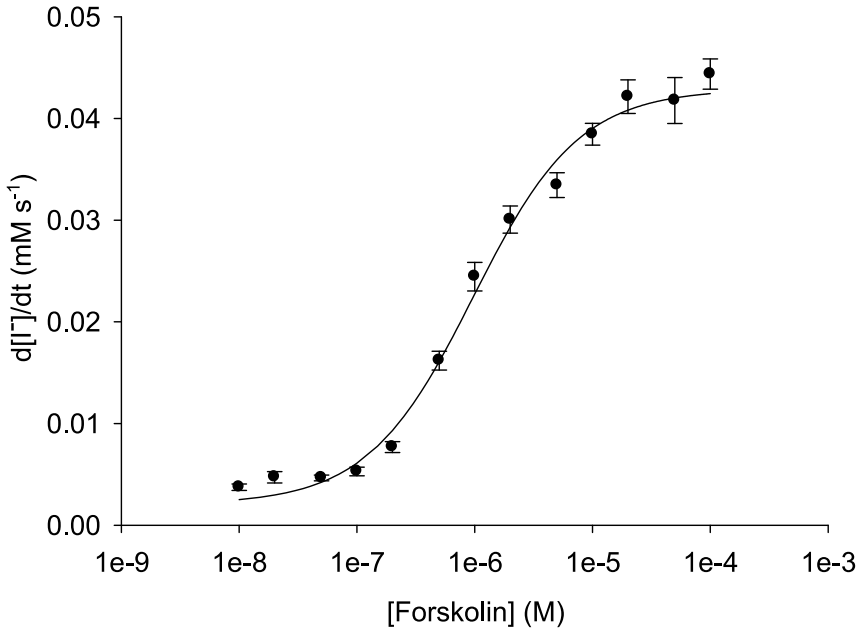


**Figure 3.8 Untagged WT-CFTR forskolin concentration-response curve.** CFTR activation quantified using maximal rate of $I^-$ entry, as Figure 3.7. $EC_{50}$ = 0.97 µM (± 0.1 µM, 6 ≤ n ≤ 18). Data points obtained using FLIPR, and co-expressing CFTR and cytosolic YFP, as in Figure 3.3.

The forskolin $EC_{50}$ obtained for YFP-WT-CFTR (2.2 µM ± 0.3 µM, Figure 3.7D) was similar to that obtained for WT-CFTR ($EC_{50}$ = 0.97 µM ± 0.1 µM, Figure 3.8) and to that of WT-CFTR obtained in a mouse mammary epithelial cell line (500 nM; Haws et al., 1996). The similar forskolin $EC_{50}$ of tagged and untagged CFTR confirmed that the N-terminal tag did not severely affect gating or sensitivity to PKA-mediated phosphorylation.

To further compare the gating kinetics of YFP-WT-CFTR and WT-CFTR, both were expressed in HEK293 cells for single channel analysis using patch-clamping. Excised inside-out patches were activated with 300 nM PKA and 2 mM ATP for approximately 3 min. Once steady state activation was reached, 300 nM PKA was removed leaving only 2 mM ATP. No significant differences were seen in any parameter when comparing gating in the presence

of 300 nM PKA + 2 mM ATP with that following PKA washout, in the presence of 2 mM ATP only ($p > 0.23$ for $T_b$, $T_{ib}$ and $P_o$ for both WT-CFTR and YFP-WT-CFTR). Data, therefore, was pooled from the two groups.

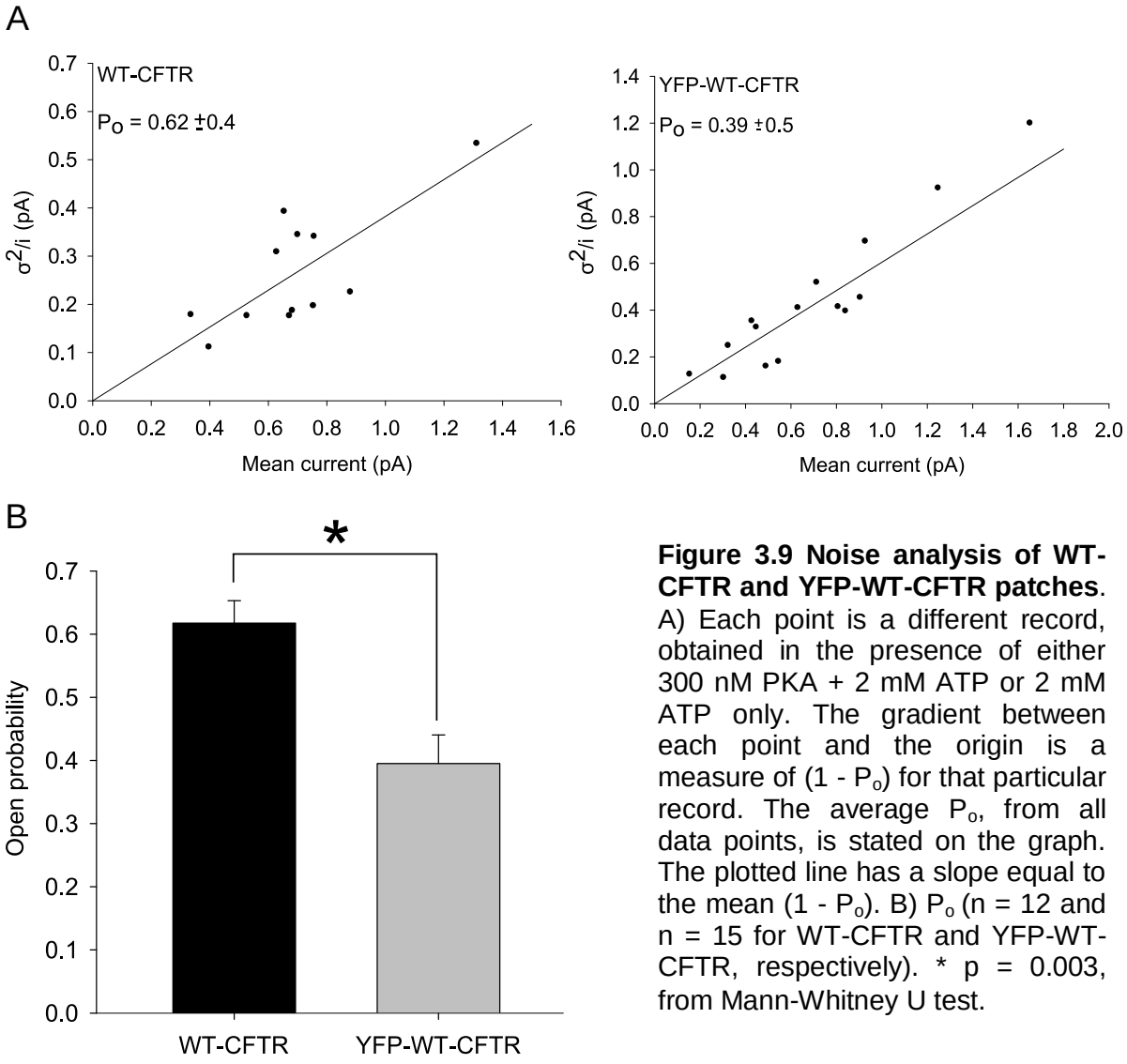


**Figure 3.9 Noise analysis of WT-CFTR and YFP-WT-CFTR patches**. A) Each point is a different record, obtained in the presence of either 300 nM PKA + 2 mM ATP or 2 mM ATP only. The gradient between each point and the origin is a measure of $(1 - P_o)$ for that particular record. The average $P_o$, from all data points, is stated on the graph. The plotted line has a slope equal to the mean $(1 - P_o)$. B) $P_o$ (n = 12 and n = 15 for WT-CFTR and YFP-WT-CFTR, respectively). * p = 0.003, from Mann-Whitney U test.

YFP-WT-CFTR had a significantly lower $P_o$ compared with untagged WT-CFTR (0.39 and 0.62 respectively, Figure 3.9). This indicated that the YFP tag did interfere with normal gating to some degree. However, this analysis did not allow us to determine which gating steps were affected.

Opening and closing rates ($r_{CO}$ and $r_{OC}$) were estimated using programs developed and provided by László Csanády (Semmelweis University, Hungary; Csanády 2000). Using these programs, the distributions of dwell times at multiple conductance levels were jointly fit to a three state gating model ($C_1 \leftrightarrow O \leftrightarrow C_2$).

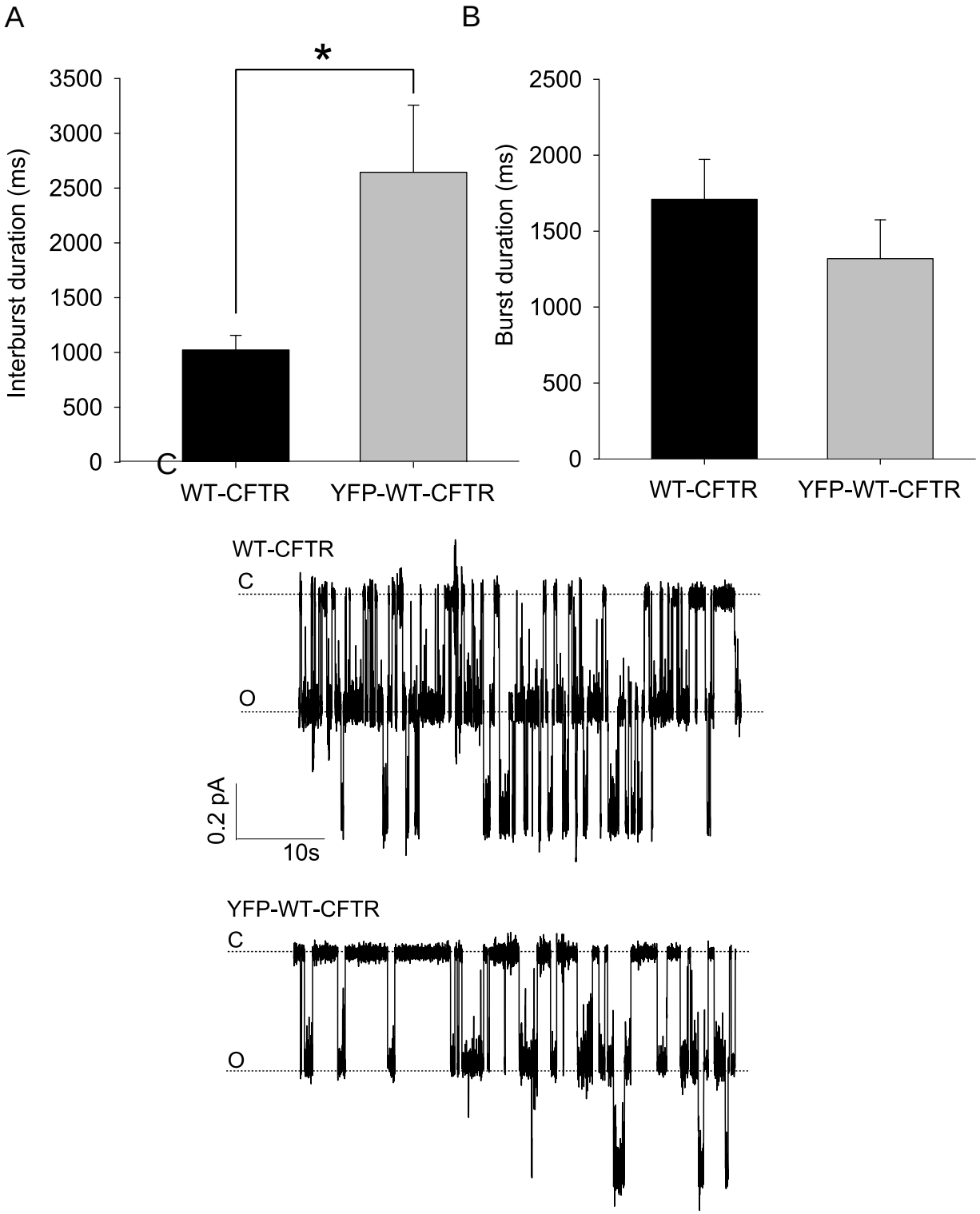


**Figure 3.10 Dwell time distribution analysis of WT-CFTR and YFP-WT-CFTR**. A) Average interburst duration derived from dwell time distribution if channel number is known, or calculated using Equation 3.1, with $P_o$ from noise analysis and burst duration from dwell time distribution analysis (p = 0.043, from Mann-Whitney U test). B) Average burst duration derived from dwell time distribution analysis (p = 0.177, from Mann-Whitney U test). For A and B, n = 11 and 15 for tagged and untagged, respectively. C) Example traces of WT-CFTR and YFP-WT-CFTR containing two gating channels in the presence of 2 mM ATP, following exposure to 300 nM PKA. C = closed state, O = open state conductance of one channel.

CFTR gating can be seen as occurring in "bursts": sojourns in a relatively long-lived closed state (interburst closure, $C_1$) are terminated by periods in which the channel toggles between short-lived closed states (flickery closures, $C_2$) and the full conductance open state (O). Evidence suggests that $C_1 \leftrightarrow O$ reflects channel opening and closing involving ATP-binding and ATP-hydrolysis respectively (Vergani et al., 2005; Csanády et al., 2010), and $O \leftrightarrow C_2$ represents short-lived closures, possibly caused by pore block (Zhou et al., 2001).

Maximum likelihood fitting allows estimation of the four rates in the three state gating model, and thus the most likely interburst and burst duration.

The decrease in $P_o$ seen for YFP-WT-CFTR compared to WT-CFTR was mainly due to an increase in interburst duration (Figure 3.10A). The YFP tag thus appears to slow opening in a manner similar to that seen with an N-terminal FLAG tag (Chan et al., 2000). Although average burst duration appeared to be slightly longer for untagged WT-CFTR, the difference was not significant (Figure 3.10B). Example traces of WT-CFTR and YFP-WT-CFTR in the presence of 2 mM ATP are shown in Figure 3.10C.

In summary, our characterisation of the effects of the N-terminal YFP tag on CFTR gating suggested that the functional disruption was relatively small. Forskolin concentration dependence (Figures 3.7D) and burst duration (Figure 3.10B) were unchanged, and there was a relatively minor reduction in $P_o$ (Figure 3.9B) reflecting slowed opening (Figure 3.10A). We thus concluded that the YFP-CFTR ion channel function was sufficiently similar to that of WT-CFTR for the continuation of this work.

## 3.7 YFP-CFTR basal phosphorylation levels

As seen in Figure 3.3, HEK293 cells do display some anion permeability, not dependent on CFTR expression or forskolin stimulation. Our study of untagged WT-CFTR concluded that this was not due to activation of CFTR by low, basal PKA activity (Figure 3.3), but rather due to alternative, endogenous, anion pathways present in HEK293 cells. YFP-CFTR activity preceding forskolin stimulation was studied to confirm the same was true when expressing the tagged channel.

As seen in Figure 3.5, upon addition of 100 mM $I^-$, some YFP-CFTR quenching occurs. This quenching represents either basal anion permeability of HEK293 cells, or activation of YFP-CFTR by resting levels of cAMP. To quantify the contribution of CFTR activation to basal anion permeability, YFP-WT-CFTR and YFP-G551D-CFTR quenching in the absence of forskolin was compared. G551D is a gating mutation which reduces CFTR $P_o$ to close to zero (Bompadre et al., 2007) without affecting cellular localisation (Gregory et al., 1991).

Therefore, it was hypothesised that if CFTR was phosphorylated by resting levels of PKA activity, the basal quenching rate would be higher for YFP-WT-CFTR than for YFP-G551D-CFTR.

Maximal rate of $I^-$ entry in the presence of 100 mM $I^-$ only (i.e. basal anion permeability) in HEK293 cells transfected with YFP-WT-CFTR or YFP-G551D-CFTR was similar (p = 0.7) (Figure 3.11).

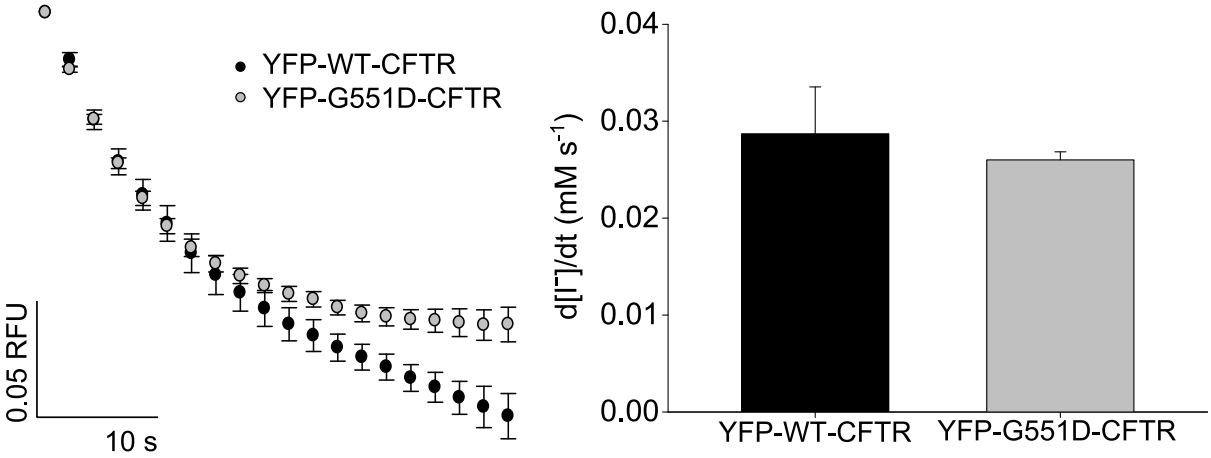


**Figure 3.11 Anion permeability in the absence of PKA stimulation**. Left: Fluorescence quenching traces shown from addition of extracellular $I^-$. Right: Quantified anion permeability (p = 0.7, from Mann-Whitney U test, WT n = 6, G551D n = 7).

However, the traces in Figure 3.11 show a slight difference in late stage quenching kinetics, suggesting that YFP-G551D-CFTR reaches a steady state faster than YFP-WT-CFTR. This is consistent with there being a small amount of YFP-WT-CFTR activity in the absence of exogenous phosphorylation. This activity is not great enough to increase the maximal rate at which $I^-$ enters the cells, but seems to result in a decrease in the $[I^-]_i$ reached at equilibrium in the case of YFP-G551D-CFTR. This possibly reflects a different steady state $V_M$. Note that the basal overall quenching rates are roughly one tenth of those seen after CFTR activation (e.g. Figure 3.7D for YFP-WT-CFTR).

The similarity between YFP-WT-CFTR and YFP-G551D-CFTR basal maximal quenching rates indicated that, although HEK293 cells transfected with YFP-CFTR display anion permeability, it occurs mainly via channels and pathways other than CFTR, with only a minimal contribution from basal CFTR activation. Figure 3.3, Chapter 6 (Figure 6.10), and Domingue *et al.* (2014) support lack of a large contribution from basal CFTR activation in HEK293 cells.

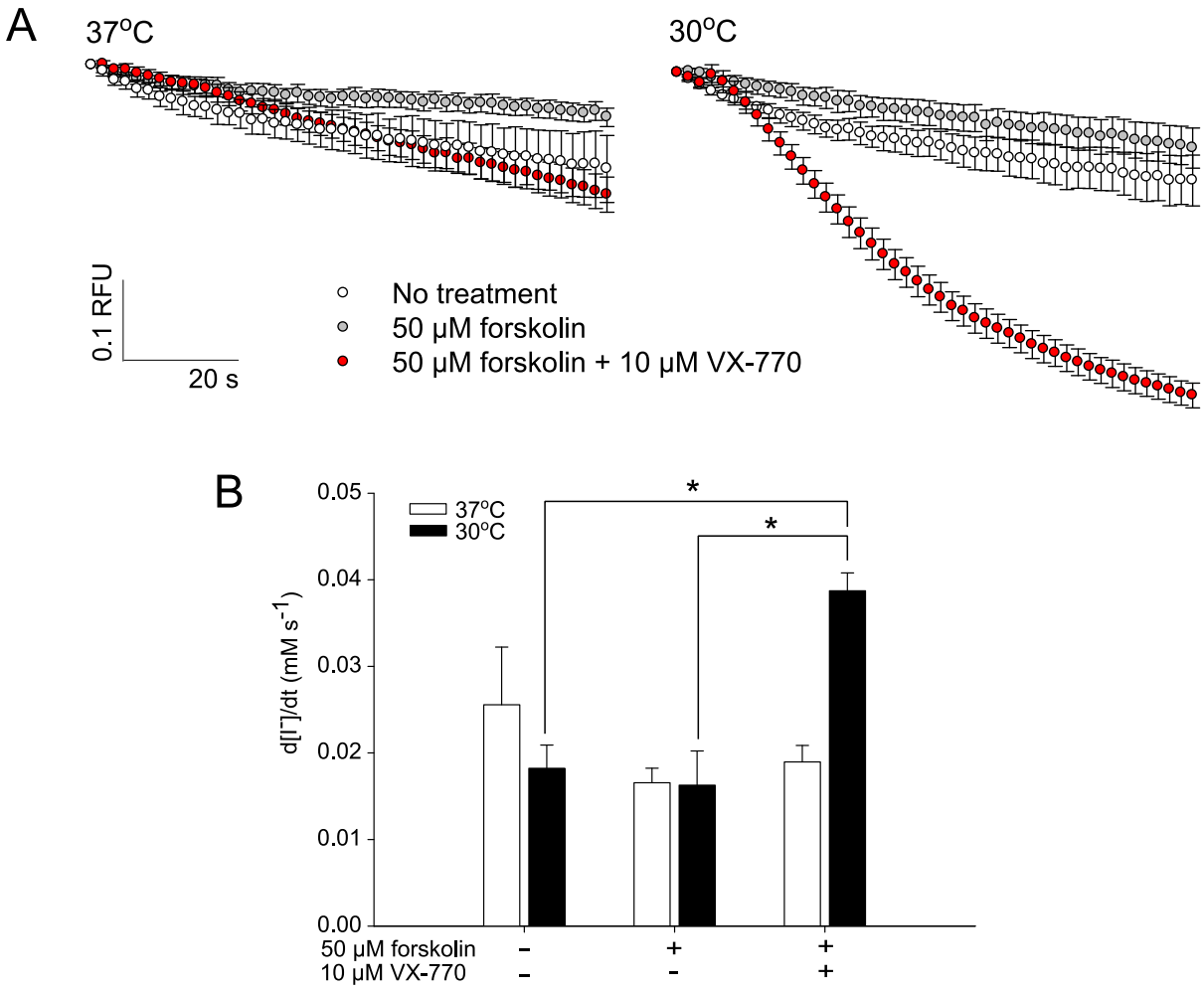


**Figure 3.12 Temperature correction of ΔF508-CFTR.** A) HEK293 cells expressing YFP-ΔF508-CFTR, incubated at 37°C or 30°C. Traces shown from treatment addition. B) Summary of YFP-ΔF508-CFTR activity. * = $p < 0.05$ Kruskal-Wallis one-way ANOVA on ranks and post-hoc Dunn's test. Treatments compared within temperature groups. Untreated n = 5, forskolin treated n = 6, forskolin + VX-770 treated n = 8.

## 3.8 Temperature correction of YFP-ΔF508-CFTR

In order to screen compounds for ΔF508-CFTR potentiator activity, low temperature incubation must be used to promote plasma membrane-localisation. ΔF508-CFTR rescue by low temperature incubation has been shown in HEK293 cells (Wang et al., 2008), and was confirmed using YFP-ΔF508-CFTR.

Fluorescence of YFP-ΔF508-CFTR incubated at 37°C was not quenched, not even in the presence of 50 μM forskolin + 10 μM VX-770 (Figure 3.12, no significant difference between any treatment at 37°C, $p = 0.434$). However, low temperature rescued ΔF508-CFTR was successfully activated by 50 μM forskolin + 10 μM VX-770 (Figure 3.12). Notice that, even after temperature correction, forskolin alone was still insufficient to activate ΔF508-CFTR, due to the severe gating defect caused by this mutation.

## 3.9 Assay validation using known potentiators

In order to validate the assay, concentration-response curves to known potentiators were constructed using YFP-ΔF508-CFTR (Figure 3.13). P2 and P5 show similar potency to that which is published (Yang et al., 2003; Pedemonte et al., 2005b). However, the VX-770 $EC_{50}$ is higher than published data (441 nM vs. 25 nM; Van Goor et al., 2009, and 12.8 nM; Veit et al., 2014). This could be caused by cell-specific differences in expression of CFTR-interacting proteins, as the publications mentioned employ epithelial cell lines (fisher rat thyroid and a CF bronchial epithelial cell line; CFBE41o$^-$). Alternatively, the YFP tag could alter the conformation to which VX-770 binds, reducing the apparent affinity.

Despite the increase in VX-770 $EC_{50}$ with respect to native, Figure 3.13 confirms that the YFP-ΔF508-CFTR assay is suitable for detecting potentiation in the presence of forskolin.

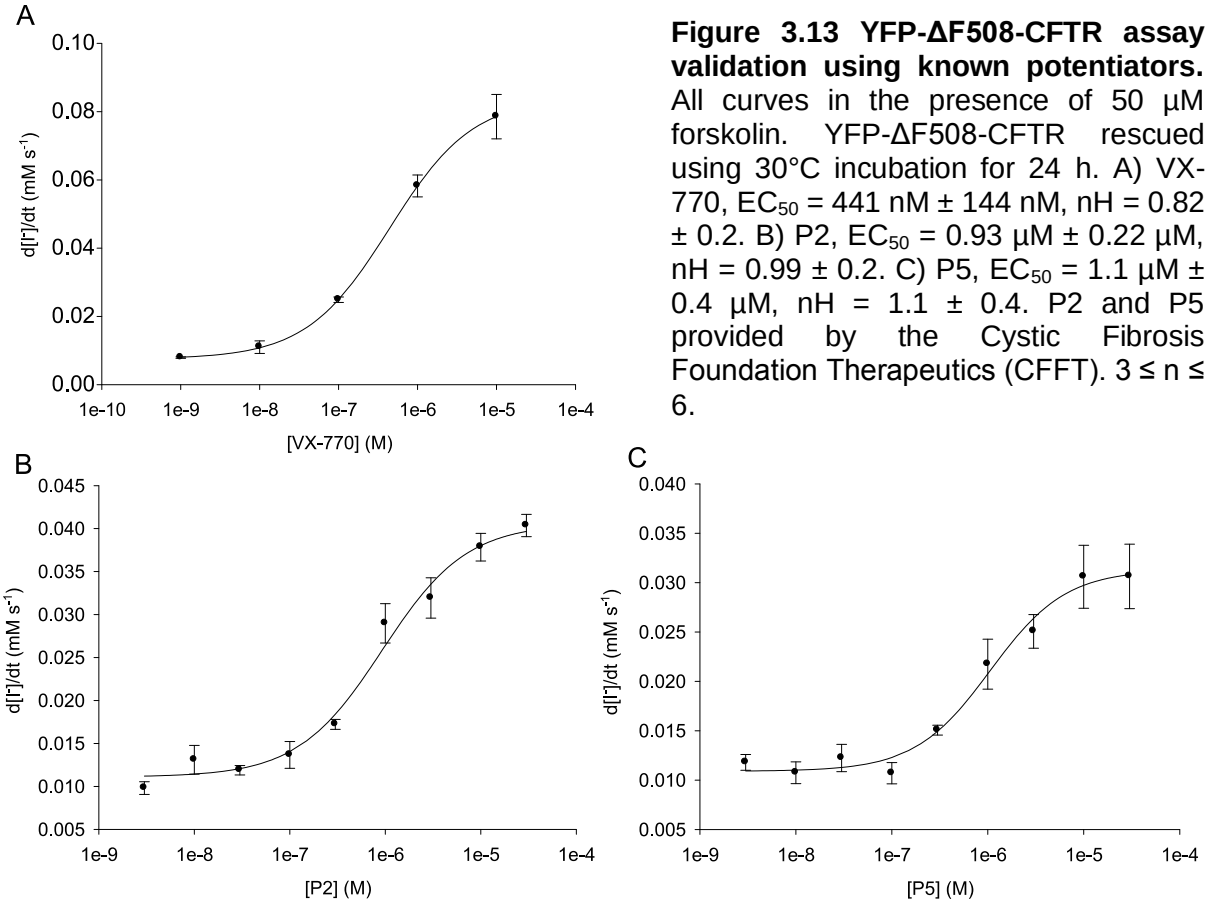


**Figure 3.13 YFP-ΔF508-CFTR assay validation using known potentiators.** All curves in the presence of 50 µM forskolin. YFP-ΔF508-CFTR rescued using 30°C incubation for 24 h. A) VX-770, $EC_{50}$ = 441 nM ± 144 nM, nH = 0.82 ± 0.2. B) P2, $EC_{50}$ = 0.93 µM ± 0.22 µM, nH = 0.99 ± 0.2. C) P5, $EC_{50}$ = 1.1 µM ± 0.4 µM, nH = 1.1 ± 0.4. P2 and P5 provided by the Cystic Fibrosis Foundation Therapeutics (CFFT). $3 \leq n \leq 6$.

## 3.10 Using YFP-CFTR to measure membrane localisation

As discussed in the Introduction, as well as a severe gating defect, ΔF508-CFTR is largely degraded following translation at the ER, causing a reduction in trafficking to the plasma

membrane. Therefore, a single tool capable of measuring both membrane density and gating would be highly valuable in the search for pharmacological agents to treat ΔF508-CF.

Methods currently employed to measure maturation and membrane density of ΔF508-CFTR are time consuming, often depend on antibody incubations, and can be difficult to quantify. Cellular expression patterns of proteins are often studied using fluorescent tags, leading us to investigate whether YFP-CFTR could also be used for this purpose.

The aim was to design an assay in which HEK293 cells expressing YFP-CFTR could be imaged at high magnification, in a high-throughput system, to screen compounds for their effect on CFTR membrane density. This would require reliable quantification of the cellular localisation of CFTR, using confocal fluorescence images. These same cells would then be used in parallel to quantify CFTR activity using the YFP-CFTR functional assay. To achieve this, we employed a high-throughput confocal microscope (Opera, PerkinElmer).

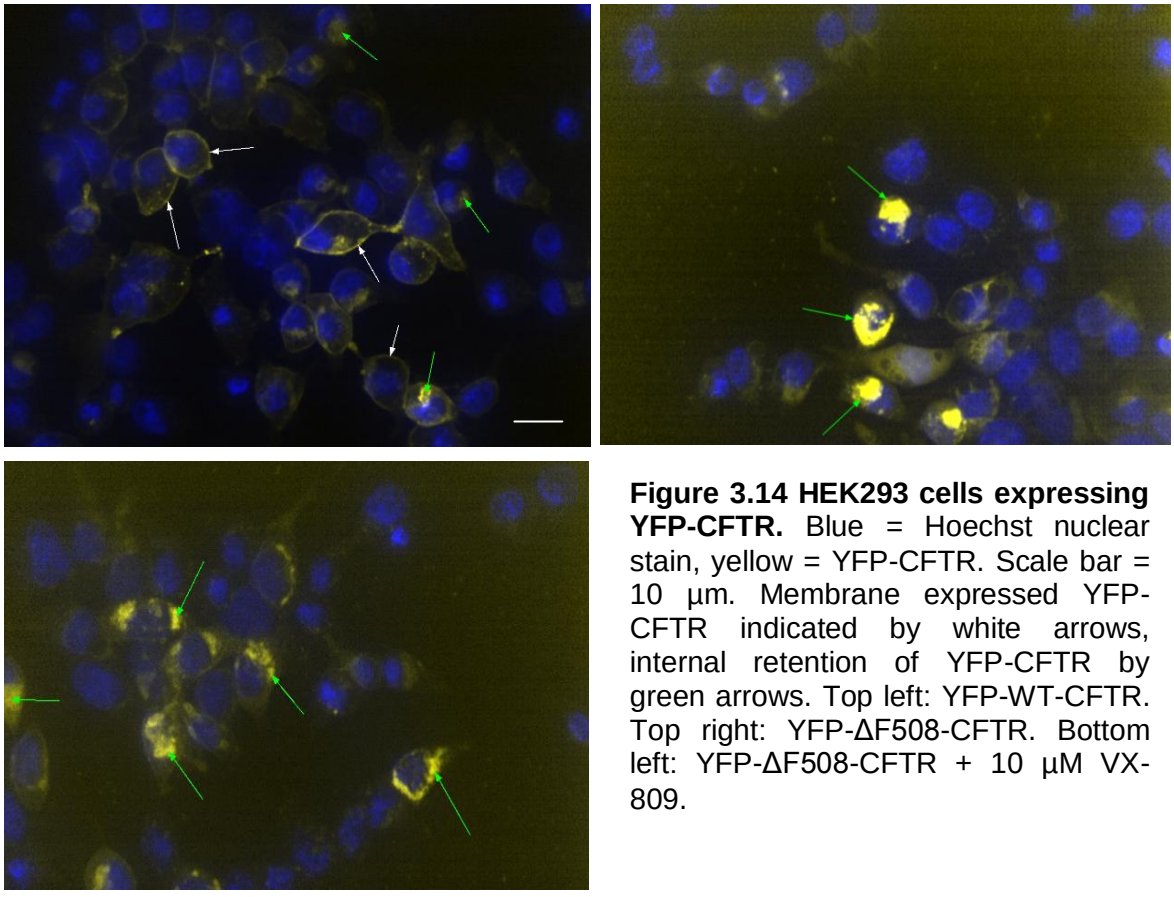

**Figure 3.14 HEK293 cells expressing YFP-CFTR.** Blue = Hoechst nuclear stain, yellow = YFP-CFTR. Scale bar = 10 µm. Membrane expressed YFP-CFTR indicated by white arrows, internal retention of YFP-CFTR by green arrows. Top left: YFP-WT-CFTR. Top right: YFP-ΔF508-CFTR. Bottom left: YFP-ΔF508-CFTR + 10 µM VX-809.

Figure 3.14 shows example images of YFP-WT-CFTR, YFP-ΔF508-CFTR and YFP-ΔF508-CFTR corrected using corrector compound VX-809 (10 µM for 24 h). The YFP-WT-CFTR image clearly shows membrane expression (white arrows), as well as some YFP-CFTR present in perinuclear locations, likely corresponding to ER vesicles, inside the cells (green arrows). YFP-ΔF508-CFTR images show probable ER retention as bright regions adjacent

to the Hoechst-stained nucleus. Due to increased degradation rate of ΔF508-CFTR, the overall fluorescence signal was significantly lower, so image brightness was increased. This resulted in the visibly higher background fluorescence seen in ΔF508-CFTR images (Figure 3.14).

Line analysis is a technique used to quantify membrane expression of fluorescent proteins. It involves drawing a line across the cell, and plotting the fluorescence intensity as a function of distance along the line. Membrane expression is characterised by the presence of two 'membrane expression' peaks, surrounding a low 'internal expression' fluorescence trough, which represents background fluorescence inside the cell. Examples of this can be seen in Figure 3.15A (Lines 1 and 2). However, the heterogeneity of the population is demonstrated by Line 3. A YFP peak next to a Hoechst peak suggests some degree of internal retention even of YFP-WT-CFTR.

Figure 3.15B demonstrates some cells with internal retention of YFP-ΔF508-CFTR (Lines 1 and 3). Line 2 shows how in cells expressing YFP-ΔF508-CFTR the low YFP signal can largely disappear in the background noise, giving no information on cellular localisation. The exposure used in these images was already extremely high, so any increase would have the potential to damage cells and cause photobleaching.

Using this method, membrane expression could theoretically be quantified using the ratio of 'membrane expression' peaks to 'internal expression' troughs. However, as Figure 3.15 shows, positioning of lines is highly subjective, and the low signal-to-noise ratio made this analysis insufficiently discriminating.

The expected ΔF508-CFTR correction caused by incubation with 10 μM VX-809 illustrates this point. The correction is only ~2-fold (He et al., 2013; Okiyoneda et al., 2013) and was not obviously visible in Figure 3.14. It was clearly not possible to quantify membrane density using line analysis of these images with enough robustness to reliably detect such small increases caused by ΔF508-CFTR correctors.

## 3.11 Discussion

This chapter described the characterisation of the YFP-CFTR fusion protein, and optimisation of an assay for the study of CFTR function. We carried out experiments to determine influence of expression cell line, to compare different imaging techniques, and to confirm relatively unchanged gating kinetics and ion channel function for the fusion protein.

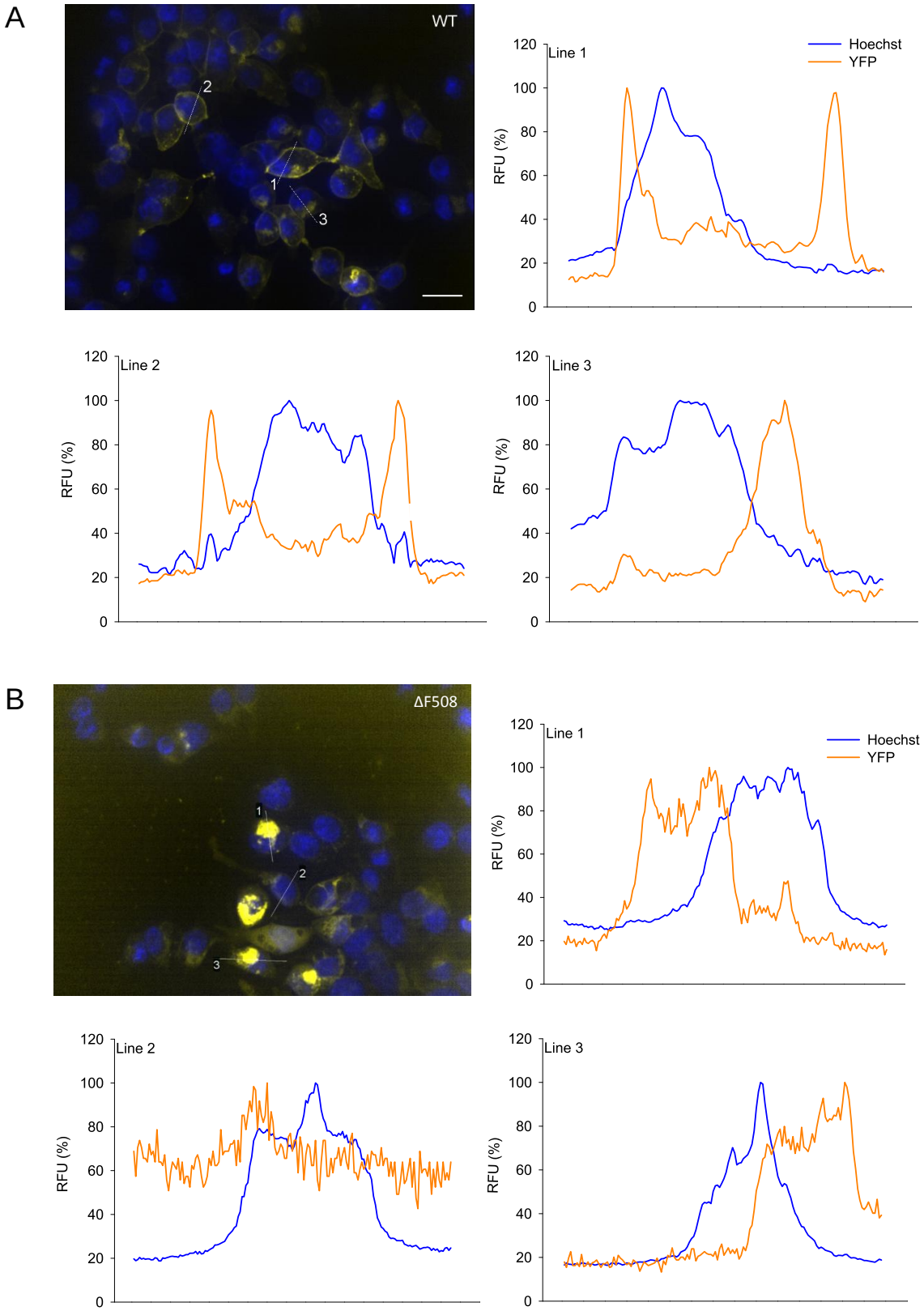


**Figure 3.15 YFP-CFTR confocal images and corresponding line analyses**. A) YFP-WT-CFTR and B) YFP-ΔF508-CFTR. Traces show fluorescence intensity along the line for Hoechst nuclear staining (blue) and YFP-CFTR (yellow). Scale bar = 10 µm.

### 3.11.1 Optimising the imaging technique

Initial fluorescence quenching traces obtained using FLIPR show a noisy signal with a high intensity fluorescence background and large addition artefacts (Figure 3.4). Clear improvement was obtained by changing the acquisition system from a fluorescence plate reader to an automated wide-field fluorescence microscope (Figure 3.5). Improvement was in part due to the analysis technique, in which image regions (containing cells) are selected and followed over time, with a concurrent background measurement, which is subtracted. This allows monitoring and removal of a well-specific background signal, which is not available when using a plate reader such as FLIPR. Image analysis thus allowed us to focus on image regions corresponding to cells expressing YFP, resulting in sensitive monitoring of small, localised fluorescence changes.

Another advantage of the fluorescence microscope is the ability to obtain information on the health of cells. Occasionally, during fluid addition, cells detach from the plate. This can be a sign of ill health, or poor PDL-coating of the plate. Detachment of cells is easily seen in the images when using ImageXpress, and wells with a high percentage of detached cells, or image regions containing several detached cells, can be discarded. This would not be seen using FLIPR, so recordings could be unknowingly taken from unhealthy or badly adhered cells.

In ImageXpress readings, due to smaller addition artefacts, the low rate of basal quenching seen upon addition of 100 mM $I^-$ became measurable (Figure 3.5). This forskolin-independent anion permeability readout can provide additional information on the cells' anion permeabilities. This was particularly valuable in later experiments, where a change in the basal permeability of the cells highlighted an interesting aspect of the mechanism of potentiator VX-770 (Chapter 6). Large addition artefacts obscured this quenching in FLIPR (Figure 3.4). Basal quenching was also not visible when using separately expressed YFP and CFTR in FLIPR (Figure 3.3A).

ImageXpress acquisition provides higher information content than FLIPR acquisition. However, this comes at the cost of a considerably longer length of time taken to read each plate. ImageXpress acquires images from individual wells, one well is read before moving to the next. Each well is monitored for 150 s, which, once fluid addition time is added, means ~3 min of imaging per well (compared to FLIPR, in which fluorescence measurements are done simultaneously in all wells such that the whole protocol is run on a full plate in around 5 min). ImageXpress is entirely automated, so the time taken for imaging a plate is not labour intensive.

The absolute value of the fluorescence signal obtained with the YFP-CFTR probe is much smaller than that obtained with co-expression of cytosolic YFP and CFTR. Indeed YFP-CFTR could not have been used for screening ΔF508-CFTR potentiators had the only available fluorescence acquisition system been FLIPR. The quenching signal of YFP-ΔF508-CFTR is even lower than that that of YFP-WT-CFTR (Figure 3.4), and small potentiation by compounds in the screen would not have been detected. Pairing YFP-CFTR and ImageXpress fluorescence acquisition, however, we have developed a tool that can be valuable to tackle projects in which a relatively small number of conditions needs to be tested but high sensitivity is required, such that small differences in the CFTR-dependent response can be detected.

### 3.11.2 YFP-CFTR normalises for different CFTR expression levels

We believe YFP-CFTR has further advantages over cytosolic YFP. In the fusion protein, the YFP signal is proportional to the amount of CFTR expressed in the cell. Therefore, in normalising to the initial YFP signal, before exposure to $I^-$, variability in CFTR expression between plates or wells is accounted for. The probe is therefore very flexible, easily adjusted for use in a number of different cells and screening conditions. This is not possible using cytosolic YFP, as fluorescence is unrelated to CFTR expression. CFTR expression levels would have to be tightly controlled, i.e. carefully selected cell lines need to be engineered, when using cytosolic YFP.

In this assay, the rate of $I^-$ entry into the cell is a function of $P_o$, the proportion of membrane-localised CFTR, and the driving force for $I^-$ entry. This assay uses acute addition of compounds to measure the immediate effect on CFTR function. Acute treatment, which remains on the cells for only a few minutes, will is not likely to have an effect on the proportion of CFTR at the membrane. However, it is possible that changes affecting the membrane potential would cause a change in the electrochemical potential gradient for $I^-$ entry and therefore appear to affect quenching rate (e.g. Figure 3.11). Therefore, changes in quenching rate can be interpreted mainly by changes in $P_o$, with possible impact from changes in driving force.

### 3.11.3 YFP-CFTR has function comparable to untagged CFTR

Published studies suggested that a GFP tag on the N-terminal of CFTR was not detrimental to either trafficking or function of the channel (Moyer et al., 1998; Vais et al., 2004; Ban et al., 2007).

Four critical acidic residues have been identified in the N-tail of CFTR. Mutation of each of these residues individually reduced CFTR currents, and combining the mutations further hindered CFTR gating (Naren et al., 1999). All four residues are expected to lie on the same surface of an α-helix, and play a positive regulatory role in CFTR gating, possibly by interacting with the R-domain. Mutating three or four of these residues decreased the $P_o$ to approximately 0.15 (from 0.5 for WT-CFTR), by reducing the burst duration (Naren et al., 1999; Fu et al., 2001).

To confirm that the N-terminal YFP tag did not have a similar effect, single channel patch-clamp analysis was used to compare gating kinetics of YFP-tagged and untagged WT-CFTR. $P_o$ is reduced by the tag to 64% that of WT-CFTR (Figure 3.9). The effect is not as large as that which is caused by the N-tail mutations, and the main cause is an increase in interburst duration (Figure 3.10). This suggests that whilst gating is slightly altered by the N-terminal tag, some, if not all, of the four critical residues are accessible. Similarly small basal phosphorylation (Figures 3.11 vs. 3.3), as well as similar forskolin concentration-dependence (Figures 3.7D and 3.8), suggests that control of gating of YFP-WT-CFTR is sufficiently similar to that of WT-CFTR to allow study of CFTR function using this fusion protein.

Accurate quantification of YFP-WT-CFTR localisation could not be achieved using the YFP signal. Work done by others suggested that trafficking of GFP-CFTR was normal (Moyer et al., 1998; Ban et al., 2007). Confocal images show mainly membrane expression of YFP-WT-CFTR and internal, ER-like retention of YFP-ΔF508-CFTR (Figures 3.14 and 3.15). YFP-CFTR fluorescence quenching experiments, (e.g. robust quenching in YFP-WT-CFTR-expressing cells; quenching dependence on incubation temperature for YFP-ΔF508-CFTR expressing cells etc.) also qualitatively confirm that the YFP tag has no dramatic effect on trafficking.

### 3.11.4 pH sensitivity of YFP-CFTR

As well as depending on halide concentration, YFP fluorescence is also sensitive to changes in pH, due to the interaction between protonation and anion binding. Using published information, and that shown in this chapter, the impact of pH sensitivity on YFP quenching in this assay has been estimated.

Figure 3.6C shows a $K_{0.5}$ of 39.3 mM, suggesting that when $[I^-]_e$ is 39.3 mM, $[I^-]_i$ is 1.9 mM (published $K_I$; Galietta et al., 2001b). This allows us to estimate $V_M$ at equilibrium, using the Nernst equation:

$$V_m = \frac{RT}{zF} ln \frac{[I^-]_i}{[I^-]_e} \qquad \text{[Equation 3.4]}$$

Where R is the gas constant (8.214 J $mol^{-1}$ $K^{-1}$), T is the temperature (310.15 K), F is Faraday's constant (96485 C $mol^{-1}$), and z is -1, the valency of $I^-$. At 37°C, when $[I^-]_e$ = 39.3 mM and $[I^-]_i$ = 1.9 mM, $V_M$ = -81 mV.

The good fit in Figure 3.6C to a simple hyperbolic binding equation suggests that the change in $V_M$ is not dramatic as $[I^-]_e$ is changed. This allows us to estimate $[I^-]_i$ in the presence of 100 mM $[I^-]_e$, by rearranging the Nernst equation:

$$[I^-]_i = [I^-]_e e^{\frac{V_m zF}{RT}} \qquad \text{[Equation 3.5]}$$

Using Equation 3.5, in the presence of 100 mM $[I^-]_e$, at equilibrium, we expect the $[I^-]_i$ in our assay to be ~5 mM. Using Equation 3.6 we estimate occupancy of the anion binding site in 5 mM $I^-$ to be 71%.

$$Receptor\ occupancy = \frac{[I^-]_i}{[I^-]_i + K_I} \qquad \text{[Equation 3.6]}$$

In the presence of 150 mM $Cl^-$, YFP has a $pK_a$ of 7.89 and receptor occupancy of 64% (Galietta et al., 2001b). Therefore, anion site occupancy is similar in 5 mM $I^-$ and in 150 mM $Cl^-$, and we can assume a similar $pK_a$. Galietta *et al.* (2001a) measured the intracellular pH change that occurred upon full activation of CFTR as a decrease from 7.35 to 7.2. Using the Hill equation, we can estimate the fluorescence at pH 7.35 and pH 7.2 (Equation 3.7).

$$F = \frac{1}{1+\left(\frac{pKa}{pH}\right)^{nH}} \qquad \text{[Equation 3.7]}$$

Where F = fluorescence, $pK_a$ = 7.89 and nH = 1. At pH 7.35, F = 0.482 and at pH 7.2, F = 0.477. Therefore, pH change accounts for only ~0.5% of the quenching seen upon maximal CFTR activation. A dramatic change in pH, such as a decrease to pH 6, still only induces ~5% quenching. Quenching seen upon activation of CFTR in this assay is, therefore, not strongly affected by changes in intracellular pH.

### 3.11.5 YFP-CFTR cannot be used for membrane density assay

Often in screening for ΔF508-CFTR corrector compounds, function of CFTR is used as an indicator of correction (for example see Pedemonte et al. 2005). Chronic treatment with potential corrector compounds is followed by a functional measure, an increase in which is assumed to indicate an increase in membrane density.

Due to the severe gating defect caused by ΔF508, this method also requires acute addition of a potentiator in order to see measurable channel activity. This further complicates the

assay and introduces possible drug:drug interactions, among other problems. For example, true correctors which stabilise a conformation to promote trafficking, but which cannot be potentiated by the compound in use, would not be detected.

A screen for CFTR correctors that does not rely on ion channel function quantification would be highly valuable in the field of CF pharmacology. To this end, we attempted to quantify membrane density using the YFP-CFTR signal. Section 3.10 demonstrates the problems encountered in using YFP-CFTR to measure membrane density. Although qualitative differences between WT-CFTR and ΔF508-CFTR distribution can be seen in the images, automating line analysis for the reliable, high-throughput quantitative analysis required for this screen proved problematic.

The cells represent a highly heterogenous population, and localisation of the signal is not only at the plasma membrane but also, to some extent, in biosynthetic vesicles in variable locations within the cells. Carrying out line analysis of enough cells to achieve a robust measure of membrane expression, avoiding any user-bias when selecting cells, would be extremely time consuming and thus could not achieve any degree of “high-throughput”. Additionally, due to the low signal associated with YFP-ΔF508-CFTR, caused by increased rate of degradation of the channel, the signal-to-noise ratio is so poor as to make much of the analysis unusable (Figure 3.15B).

A different type of image analysis was also attempted, by a collaborator at UCL (Janos Kriston-Vizi, MRC Laboratory for Molecular Cell Biology). He used a fluorescence threshold to select YFP-CFTR expressing cells, and then segmented each cell into an outer ring (representing membrane localisation) and an inner ring (representing fluorescence in the cytosol, just inside the membrane). The ratio of mean outer ring fluorescence/mean inner ring fluorescence was used to quantify membrane localisation. However, the low signal-to-noise ratio and lack of any fluorescence at the membrane with which to identify the correct location for the ‘outer ring’, made this analysis ineffective. For example, controls used for a pilot screen gave an average ratio of 0.86 for YFP-WT-CFTR, and a greater ratio of 1.1 for YFP-ΔF508-CFTR.

This hurdle in measuring membrane density led us to design the CFTR-pHTomato assay, discussed in the next chapter.

# Chapter 4

# CFTR-pHTomato: A novel CFTR localisation assay

## 4.1 Introduction

In recent years, a number of CFTR localisation assays have been developed, utilising fluorescence to improve the ease with which CFTR trafficking can be quantified (see Introduction). These assays have been used to identify ΔF508-CFTR correctors from compound libraries (Phuan et al., 2014; Robert et al., 2008). Fluorescence assays are an improvement on the slow, laborious immunoblot technique. However, these assays do suffer from a number of drawbacks. Some are only capable of measuring membrane-localised CFTR, such as HA-tagged and HRP-tagged CFTR. Others depend on antibody staining, which involves multiple washes and incubations. To enable rapid quantification of membrane density and total CFTR expression, we developed a fluorescence assay capable of reporting on both in live cells.

### 4.1.1 pHTomato

Our CFTR localisation assay utilises fluorescence of pHTomato; a pH sensitive, red derivative of GFP. The excitation/emission spectrum of pHTomato is strongly pH-dependent with a $pK_a$ of ~7.8 (Figure 4.1).

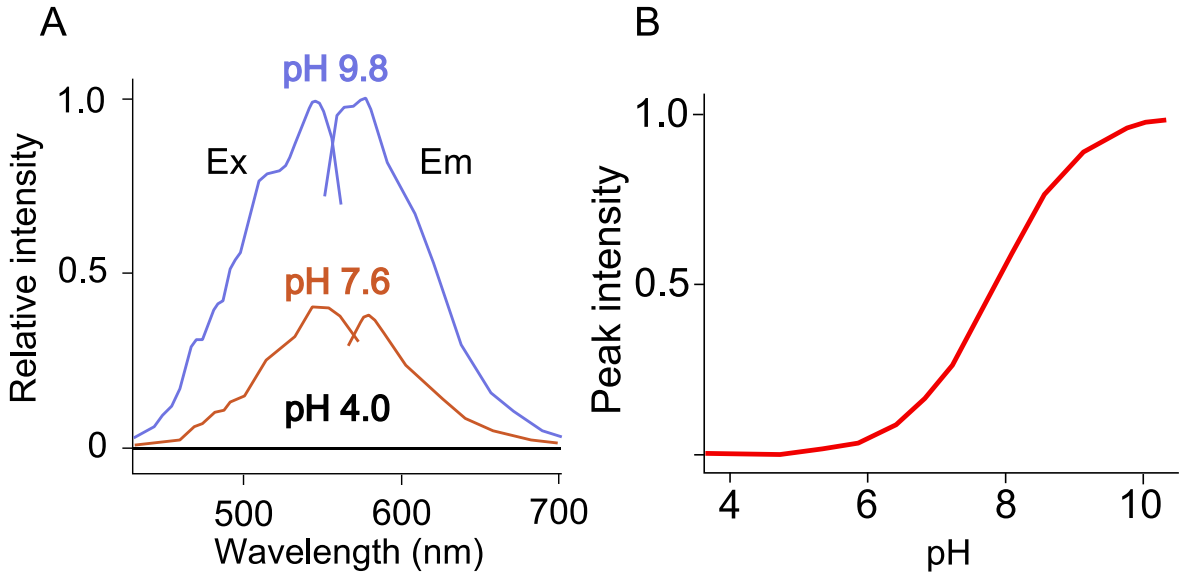


**Figure 4.1 pHTomato pH-sensing properties** (Modified from Li & Tsien, 2012). A) Upon protonation (in acidic pH), the intensity of the excitation/emission spectrum decreases. Maximal fluorescence occurs at ~pH 10. Excitation/emission peaks are at 550 nm and 580 nm, respectively. B) pH dependence of emission intensity. $pK_a$ is approximately 7.8.

The fluorescence intensity of protonated pHTomato is low. As pH increases, less pHTomato exists in the protonated form, and fluorescence increases (Figure 4.1). pH-sensing by pHTomato is not dependent on a shift in the excitation/emission spectrum, but rather a decrease in fluorescence intensity, accompanying protonation (Li and Tsien, 2012).

### 4.1.2 The fourth extracellular loop

The CFTR-pHTomato assay required CFTR to be inserted into an extracellular domain, for which we chose a site following position 901 in ECL4. This is known to be a permissive site for tag insertion to CFTR.

ECL4 is the largest extracellularly exposed loop in CFTR. Position 901 was originally chosen by other groups as a potentially permissive site because dogfish and *Xenopus* CFTR contain additional amino acids at this point. An M2 tag (eight amino acids) or 3HA tag (27 amino acids), introduced after position 901, allowed expression of functional CFTR, which could be labelled at the membrane using an antibody stain (Howard et al., 1995; Sharma et al., 2001).

Although not critical for the CFTR-pHTomato assay, it has been shown that CFTR tagged at this position is regulated by phosphorylation, undergoes ATP-induced gating, and has similar conductance to WT-CFTR (Schultz et al., 1997). Due to the close proximity to the glycosylated residue 900, tags on ECL4 interfered with glycosylation. However, the amount of immature and mature tagged-CFTR was similar to untagged, suggesting this interruption made little difference to CFTR expression patterns (Howard et al., 1995; Hildebrandt et al., 2015). Finally, insertion of a large tag, HRP (308 amino acids), at this position in ΔF508-CFTR did not alter drug response or revertant sensitivity of cellular localisation patterns (Phuan et al., 2014; Veit et al., 2014).

Therefore, CFTR with a tag at position 901 is expressed at the membrane, and is functional. This has also been confirmed in HEK293 cells (Hildebrandt et al., 2015). Results discussed in this chapter suggest that WT-CFTR-pHTomato is expressed at the membrane, ΔF508-CFTR-pHTomato is retained inside the cell, and the latter can be corrected using known corrector compounds, suggesting that a pHTomato insertion (273 amino acids), like the HRP tag, does not alter CFTR biogenesis.

Successful ΔF508-CF treatment will require identification of corrector compounds, capable of increasing ΔF508-CFTR membrane density. Drug discovery projects will likely now also be required to test the effect of chronic potentiator treatment on membrane density of ΔF508-CFTR (Cholon et al., 2014; Veit et al., 2014). This chapter describes the optimisation

and validation of the CFTR-pHTomato assay, capable of achieving these drug discovery aims.

## 4.2 The CFTR-pHTomato assay

pHTomato was inserted into ECL4 of CFTR by subcloning (molecular biology carried out with the help of undergraduate students Stefan Constantinou and Mahesh Pillai, supported by UCL Dean's Summer Student Scholarship and CF Trust Studentship, respectively, see Methods). The fusion protein was expressed in HEK293 cells for fluorescence imaging (assay described in Figure 4.2).

The fluorescence imaging begins in pH 7.4 buffer (*i*). Fluorescence from internal CFTR-pHTomato is very low, as the pH of internal vesicles is low (varies from neutral to pH 5; Wu et al., 2001). The fluorescence of membrane-localised CFTR-pHTomato, exposed to pH 7.4, is ~40%.

The extracellular buffer is then changed to pH 6. Only CFTR-pHTomato located at the plasma membrane is exposed to the acidic environment (*ii*). Therefore, the fluorescence of any pHTomato exposed to the extracellular buffer (i.e. membrane-localised CFTR) will decrease, but the fluorescence of internal CFTR-pHTomato will be unchanged.

The second fluid addition raises extracellular pH to pH 9, which increases the fluorescence of any membrane exposed pHTomato, whilst internal pHTomato fluorescence is, again, unchanged (*iii*).

The final step introduces 40 mM $NH_4Cl$ (*iv*). $NH_3$ permeates membranes and alkalises internal vesicles, increasing fluorescence of internal CFTR (Li and Tsien, 2012; Xu et al., 2014). The extracellular pH is maintained at pH 9, so the fluorescence of membrane-exposed pHTomato will not change.

The change in fluorescence seen upon extracellular pH change from pH 6 - pH 9 represents membrane-localised CFTR ($\Delta_F$ membrane). The fluorescence change induced by 40 mM $NH_4Cl$ reflects internal CFTR ($\Delta_F$ internal).

Example fluorescence traces of WT-CFTR-pHTomato and ΔF508-CFTR-pHTomato are shown in Figure 4.3A. $\Delta_F$ values were used to quantify the membrane density and internal expression of WT-CFTR and ΔF508-CFTR (Figure 4.3B).

Note that in order to compare raw CFTR quantification values ($\Delta_F$ membrane and $\Delta_F$ internal), data must come from within one plate. Exposure time and laser intensity are optimised for reading of each plate, so raw fluorescence values between plates cannot be

compared. Most comparisons in this chapter show raw fluorescence $\Delta_F$ values of two conditions within one plate, compared using paired t-tests. Each plot in these figures is the mean ± SEM of within-plate replicates (n = 3 or 4). In some cases, to allow pooling of data obtained from different plates, membrane density and internal CFTR values are expressed as -fold changes compared to within-plate negative controls.

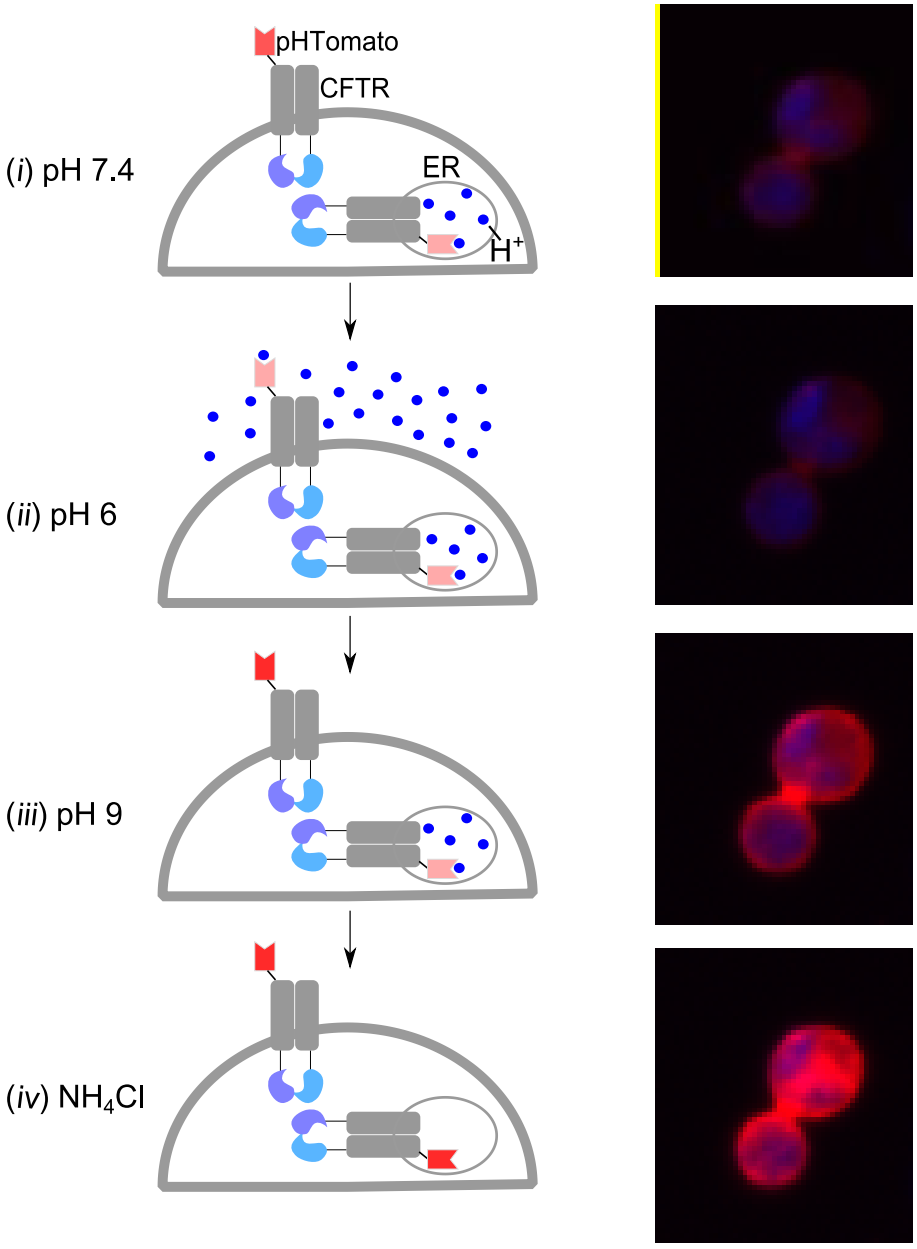


**Figure 4.2 The CFTR-pHTomato assay.** Left: Imaging begins in standard buffer, pH 7.4 (*i*). Extracellular buffer is changed to pH 6, which reduces fluorescence of membrane-exposed pHTomato (*ii*). Extracellular buffer is then changed to pH 9, which increases fluorescence of membrane-exposed pHTomato (*iii*). Addition of 40 mM $NH_4Cl$ (at pH 9) increases fluorescence of internal CFTR (*iv*). Right: Images of HEK293 cells expressing WT-CFTR-pHTomato, obtained at the four stages described on the left. Blue fluorescence = Hoechst nuclear stain, red fluorescence = WT-CFTR-pHTomato.

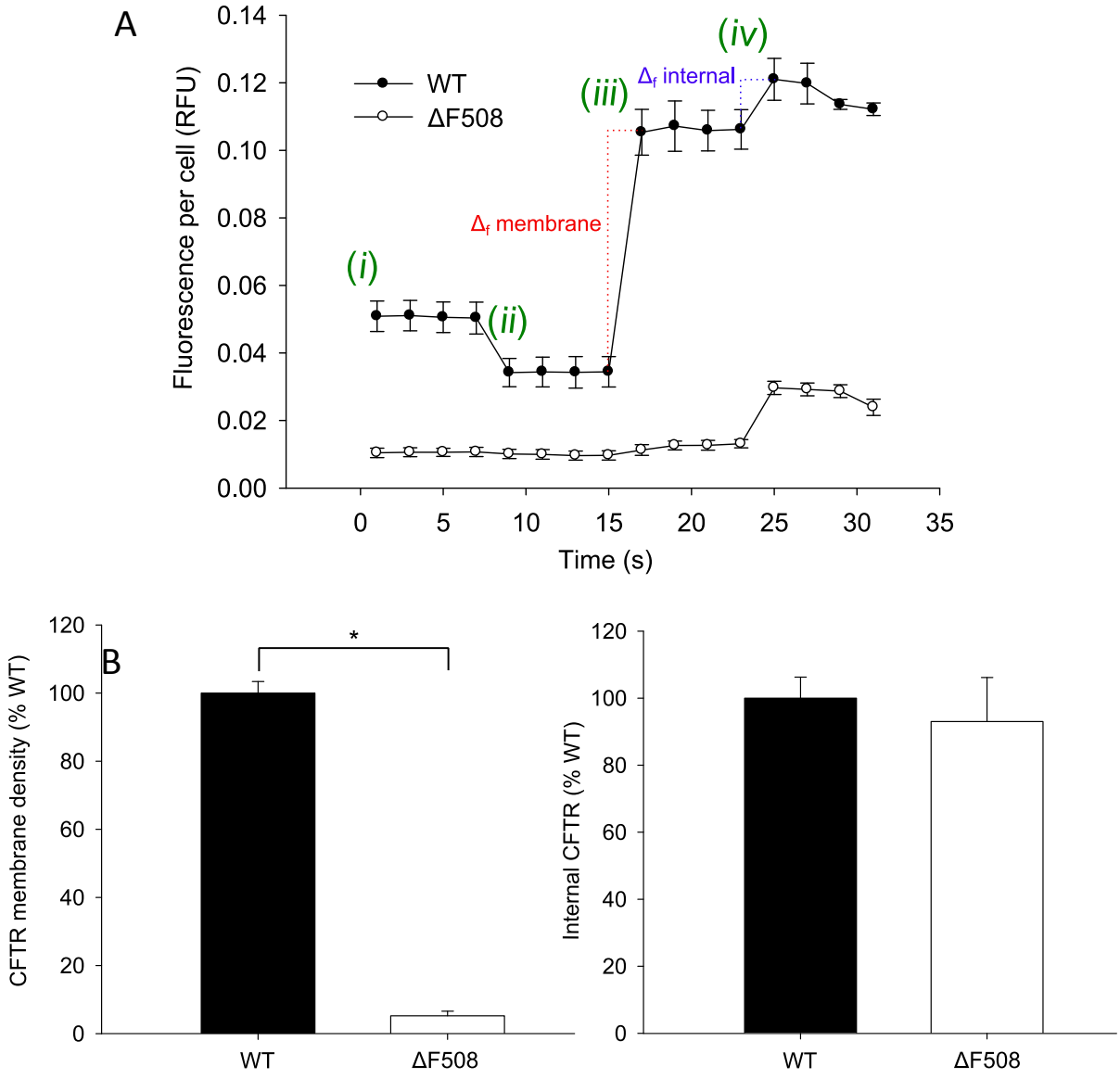


**Figure 4.3 WT-CFTR-pHTomato and ΔF508-CFTR-pHTomato cellular localisation quantification.** A) Fluorescence traces of WT-CFTR-pHTomato and ΔF508-CFTR-pHTomato. Fluorescence change when extracellular pH is increased from pH 6 to pH 9 represents membrane CFTR ($\Delta_F$ membrane). Fluorescence change upon addition of 40 mM $NH_4Cl$ represents internal CFTR ($\Delta_F$ internal). n = 3. Four images were taken in each condition. Following optimisation, this was reduced to two images per condition. (*i*) to (*iv*) indicate the stages in Figure 4.2. B) Membrane and internal CFTR quantified using $\Delta_F$ membrane and $\Delta_F$ internal. No significant difference in internal CFTR (p = 0.66). WT-CFTR n = 6, ΔF508-CFTR n = 5. * p = 0.004, from Mann-Whitney U test.

## 4.3 pIRES2-eGFP-CFTR-pHTomato

During the design of this assay, we aimed to avoid quantifying membrane CFTR as a percent of total CFTR, or as a ratio with internal CFTR. These are often used as measures of CFTR membrane expression (for examples see Van Goor et al., 2011 and Cholon et al., 2014). However, these ratios are not the most informative quantification. Should a ΔF508-

CFTR corrector compound increase total CFTR at the same rate as membrane CFTR, the ratio of the two would remain unchanged.

Independent quantification of membrane and internal CFTR could be achieved using raw $\Delta_F$ values. However, raw fluorescence values depend on the amount of protein present in the cells, which in turn depends on the transfection efficiency. A low CFTR-pHTomato signal could be caused by increased CFTR degradation, but it could also be caused by low transfection efficiency. Therefore, we required expression of an independent protein, the amount of which could be used to normalise CFTR expression. For this, we used the eGFP signal, resulting from translation of eGFP in the pIRES2-eGFP-CFTR-pHTomato plasmid.

The CFTR-pHTomato coding sequence was subcloned into an internal ribosome entry site (IRES) plasmid (pIRES2-eGFP). pIRES2-eGFP contains an IRES between the eGFP coding sequence, and the coding sequence for the protein of interest (CFTR-pHTomato). One strand of mRNA is transcribed from the plasmid, but two separate proteins are translated, as the ribosome initiates translation at the start of the bicistronic mRNA, as well as at the IRES. Therefore, CFTR-pHTomato expression is directly proportional to eGFP expression ($\rho$ = 0.71, in our system, Figure 4.4A). This can also be seen in the fluorescence values of individual cells (Figure 4.4B). Although the mean eGFP and pHTomato fluorescence changes, the ratio of the two remains unchanged. Critically, the excitation and emission peaks of pHTomato (550 nm and 580 nm) are distinct from those of eGFP (488 nm and 509 nm), so the two proteins can be imaged simultaneously (Li and Tsien, 2012). Normalising the CFTR-pHTomato signal to the eGFP signal normalised for differences in total protein. Any decrease or increase in the ratio between CFTR-pHTomato and eGFP signals was, therefore, due to changes in biosynthetic and/or degradation rates of the CFTR-pHTomato protein.

An eGFP image was taken at time point 1, and pHTomato images were taken at each successive time point. A Hoechst nuclear stain was used to enable cell counting. Analysis involved selecting regions of the image containing transfected cells, by applying a fluorescence threshold on the eGFP image. Mean fluorescence of each region was measured in the GFP channel ($F_{GFP}$) and pHTomato channel ($F_{PHTOMATO}$). $F_{PHTOMATO}$ was normalised to the $F_{GFP}$ signal, and each region was weighted for cell count. The sum of all regions was then divided by the sum of the cell count (Equation 4.1, excluding any regions that reached fluorescence saturation).

$$F = \frac{\sum\left(\frac{F_{PHTOMATO}}{F_{GFP}} X\ cell\ count\right)}{\sum(cell\ count)} \qquad \text{[Equation 4.1]}$$

This resulted in a weighted average fluorescence ratio, which was used to quantify $\Delta_F$ membrane and $\Delta_F$ internal (see Methods).

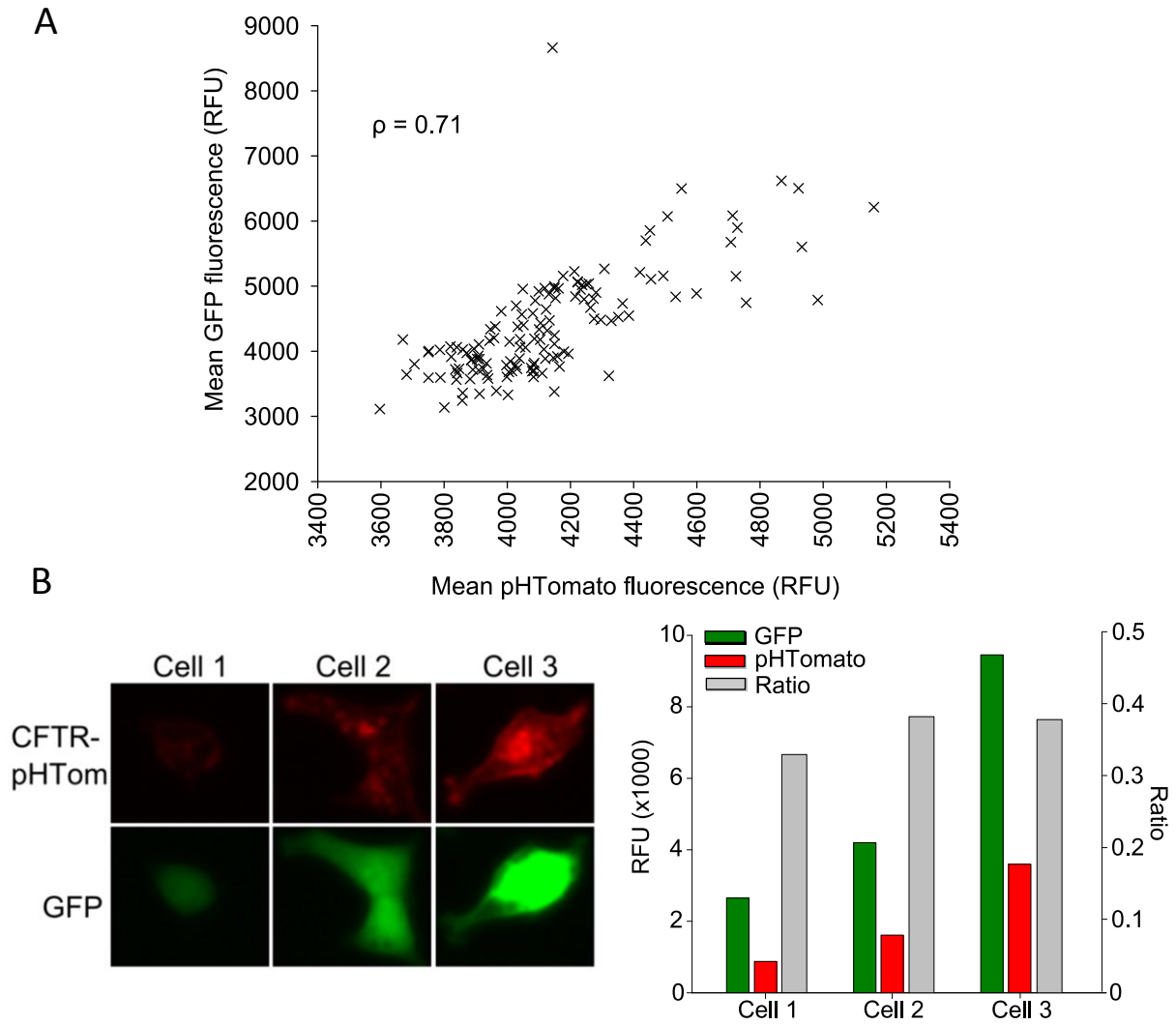


**Figure 4.4 Correlation of eGFP and WT-CFTR-pHTomato, coded in a pIRES2-eGFP plasmid.** A) Cell regions were identified using a fluorescence threshold on the eGFP image. The same regions were used to measure $F_{GFP}$ and $F_{PHTOMATO}$. Due to high cell density, only a small proportion of regions showing fluorescence above threshold included only a single nucleus. Therefore, each point represents a region including more than one cell (n = 4 images). Pearson product-moment correlation coefficient ($\rho$) = 0.71 ($p = 1.2^{-21}$). B) HEK293 cells expressing WT-CFTR-pHTomato in pIRES2-eGFP, and corresponding mean fluorescence values.

## 4.4 Validation of CFTR-pHTomato

### 4.4.1 Correction of ΔF508-CFTR-pHTomato by VX-809

One of the potential applications of this assay is to screen corrector compounds to identify those which increase membrane density of ΔF508-CFTR. Known corrector, VX-809, was used to confirm that ΔF508-CFTR-pHTomato was capable of measuring such correction. VX-809 is the corrector component of Orkambi, the corrector/potentiator combination

recently approved for the treatment of ΔF508-CF. This corrector stabilises the NBD1:ICL4 interaction to promote native folding and thus improve trafficking of ΔF508-CFTR to the membrane (Van Goor et al., 2011; Farinha et al., 2013a; Okiyoneda et al., 2013).

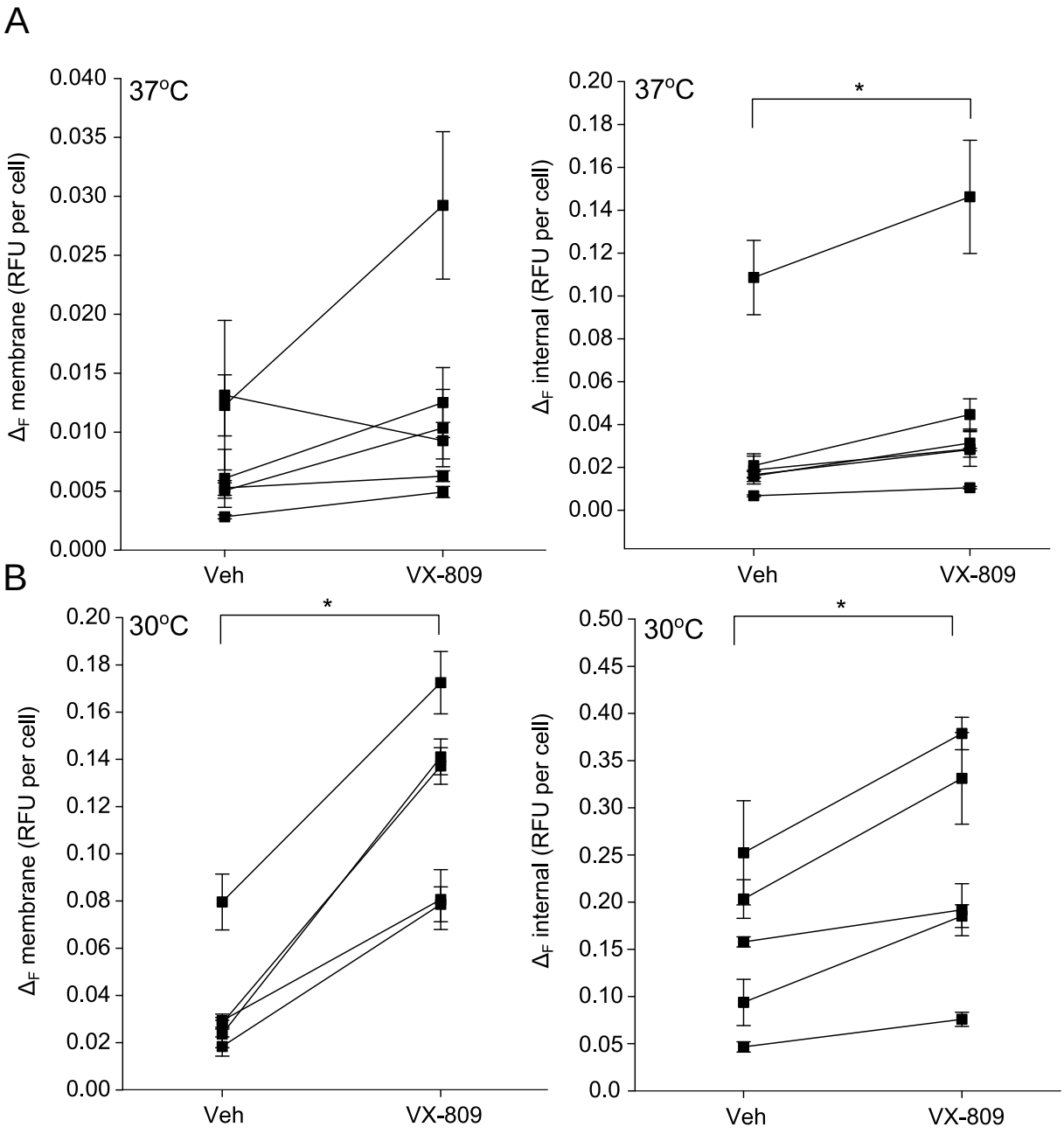


**Figure 4.5 Correction of ΔF508-CFTR-pHTomato by VX-809.** A) 24 h incubation with 10 μM VX-809 at physiological temperature (membrane ΔF508-CFTR p = 0.17, internal ΔF508-CFTR p = 0.018). B) As A, but alongside low temperature incubation (p = 0.003 and 0.019 for membrane and internal CFTR, respectively).

At physiological temperature, 24 h incubation with 10 μM VX-809 improved internal ΔF508-CFTR ~1.5-fold, compared to vehicle treated controls. A similar, but not significant, effect was seen on membrane-localised ΔF508-CFTR (Figure 4.5A). At 30°C, treatment with the

corrector compound induced a ~4-fold increase in membrane density, and a ~1.5-fold increase in internal ΔF508-CFTR (Figure 4.5B). This is similar to the level of correction observed in other experimental systems (He et al., 2013; Phuan et al., 2014). Temperature correction is known to increase the efficacy of VX-809, as thermal stability is conveyed to NBD1 (Farinha et al., 2013a; He et al., 2013; Okiyoneda et al., 2013).

These results confirm that ΔF508-CFTR-pHTomato can be used to detect correction by VX-809. However, the low levels of ΔF508-CFTR-pHTomato present at 37°C (especially membrane levels) make it difficult to obtain meaningful quantification. Therefore, all remaining ΔF508-CFTR work was carried out at 30°C, to enhance the ΔF508-CFTR-pHTomato signal.

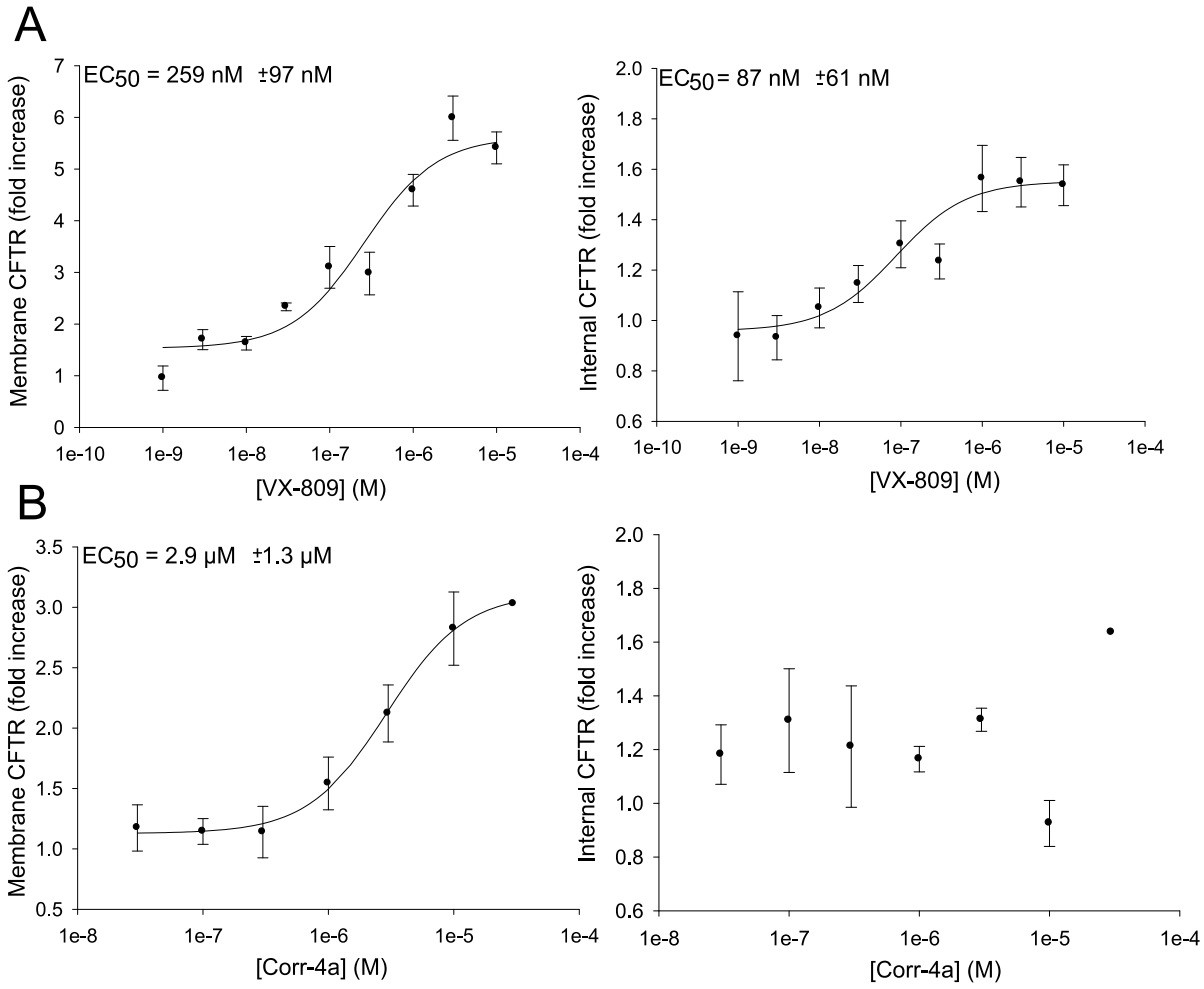


**Figure 4.6 ΔF508-CFTR-pHTomato concentration-response curves to known correctors.** A) 24 h incubation with VX-809 at 30°C increased both membrane and internal ΔF508-CFTR in a concentration-dependent manner ($3 \leq n \leq 6$). B) 24 h incubation with Corr-4a increased membrane CFTR but changes in internal CFTR were not dose-dependent ($1 \leq n \leq 3$). Values expressed as fold increase compared to vehicle controls. $EC_{50}$ values, where obtained, are stated on the graphs.

### 4.4.2 Concentration-response curves using known correctors

By way of further validation, concentration-response curves were constructed to two known correctors: VX-809 and Corr-4a.

Both correctors increased membrane CFTR in a concentration-dependent manner (Figure 4.6). The $EC_{50}$ values for both compounds were similar to those that have been published previously (259 nM ± 97 nM and 2.9 µM ± 1.3 µM for VX-809 and Corr-4a, respectively) (Pedemonte et al., 2005a; Van Goor et al., 2011). Correction by VX-809 was ~2-fold greater than that which was achieved by Corr-4a, which also confirms published results (Farinha et al., 2013a; He et al., 2013; Okiyoneda et al., 2013).

The similarity of these concentration-response curves to published data further confirmed that ΔF508-CFTR-pHTomato was capable of measuring correction by known corrector compounds, and that the pHTomato tag did not alter cellular trafficking in the presence of correctors to a great extent. Corr-4a did not induce a dose-dependent correction of internal CFTR, unlike VX-809 (Figure 4.6B).

## 4.5 ΔF508-CFTR destabilisation by chronic VX-770 treatment

Recently published studies have shown that chronic potentiator treatment reduces biosynthesis and decreases membrane stability of rescued ΔF508-CFTR (Cholon et al., 2014; Veit et al., 2014). Irrespective of the mechanism of rescue, chronic treatment with the majority of potentiators caused a concentration-dependent decrease in membrane-localised and internal ΔF508-CFTR. This recently discovered phenomenon is the most likely cause of relatively disappointing clinical effects of combination treatments (Wainwright et al., 2015).

CFTR-pHTomato was used to measure membrane density of ΔF508-CFTR following chronic treatment with VX-770. As shown in Figure 4.5, correction induced by VX-809 at 37°C is low. Therefore, the signal change caused by VX-770-induced destabilisation would be small, and difficult to detect. For this reason, chronic potentiator treatment was carried out at 30°C, and in the presence of 10 µM VX-809. Membrane ΔF508-CFTR decreased by approximately 20% following 24 h incubation with 10 µM VX-770 (Figure 4.7). This decrease is slightly smaller than that seen by others (~40%; Veit et al., 2014; Bali et al., 2016, or greater; Cholon et al., 2014), which could be caused by over-expression in the HEK293 cell system, or inclusion of low temperature incubation. There was no significant change in internal ΔF508-CFTR.

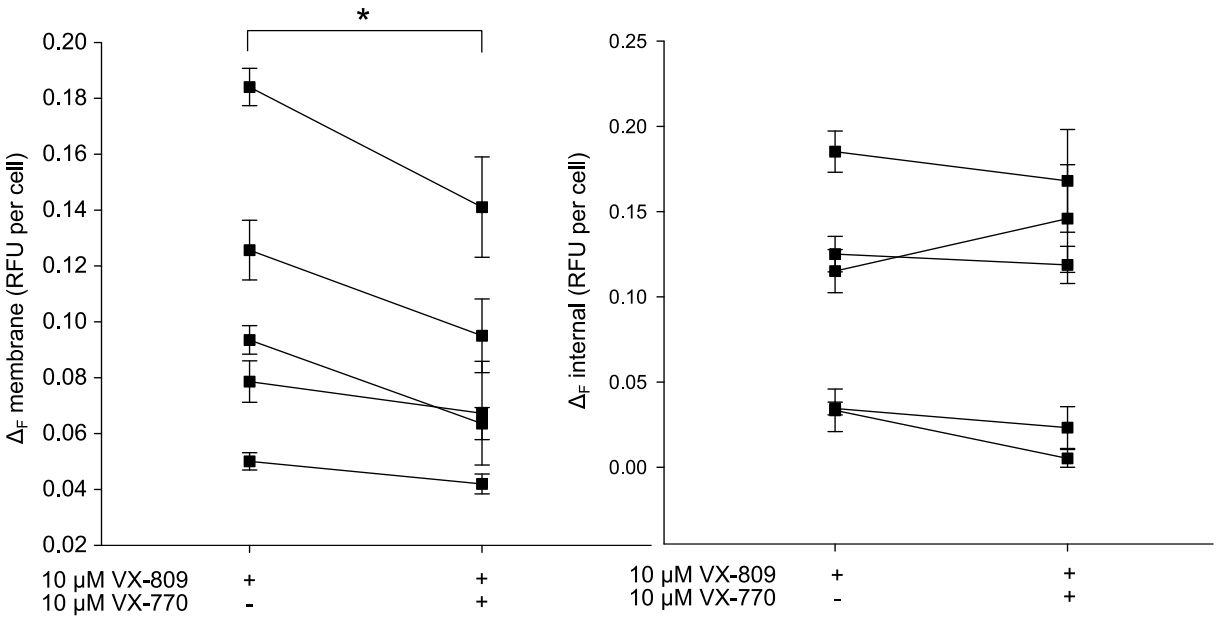


**Figure 4.7 VX-770 chronic treatment on ΔF508-CFTR.** Membrane and internal ΔF508-CFTR following low temperature and VX-809 rescue, ± 10 μM VX-770 ($p = 0.02$ and $p = 0.56$, respectively).

## 4.6 Destabilisation of WT-CFTR by chronic VX-770 treatment

There is some evidence that smoke exposure decreases WT-CFTR mediated anion transport in epithelial cells, leading to symptoms of COPD (Sloane et al., 2012). Therefore, CFTR potentiator treatment has been suggested as a treatment for COPD (Cantin et al., 2006; Sloane et al., 2012).

Work published to date is inconsistent on whether chronic VX-770 destabilises WT-CFTR. Veit *et al.* (2014) see no effect on WT-CFTR, whilst Cholon *et al.* (2014) see ~50% reduction in mature WT-CFTR expression and function. If VX-770 does destabilise WT-CFTR, this would reduce the suitability for treatment of COPD patients.

In our assay, WT-CFTR expression is not decreased by 24 h incubation with 1 μM VX-770 (Figure 4.8). This supports data published by Veit *et al.* (2014), and studies carried out by Sloane *et al.* (2012), which demonstrate effective potentiation of the anion current in non-CF epithelial cells, treated with chronic VX-770.

## 4.7 Discussion

This chapter detailed the generation and validation of a novel optical assay, capable of reporting on membrane and internal CFTR in live cells. A rapid and cost-effective measure of CFTR localisation could be instrumental for efficient identification of ΔF508-CFTR corrector compounds. Additionally, it is now apparent that testing for negative biosynthetic

effects of chronic potentiator treatment will be important for avoiding clinical trials with high risk of failure.

Recently published fluorescence assays have overcome the immediate need for techniques to quantify ΔF508-CFTR localisation without relying on channel function (Carlile et al., 2007; Phuan et al., 2014; Larsen et al., 2015). This chapter details efforts towards optimising a particularly simple and inexpensive localisation assay, to be used for medium/high throughput screens. As will become evident in Chapter 5, we were only partially successful in this aim.

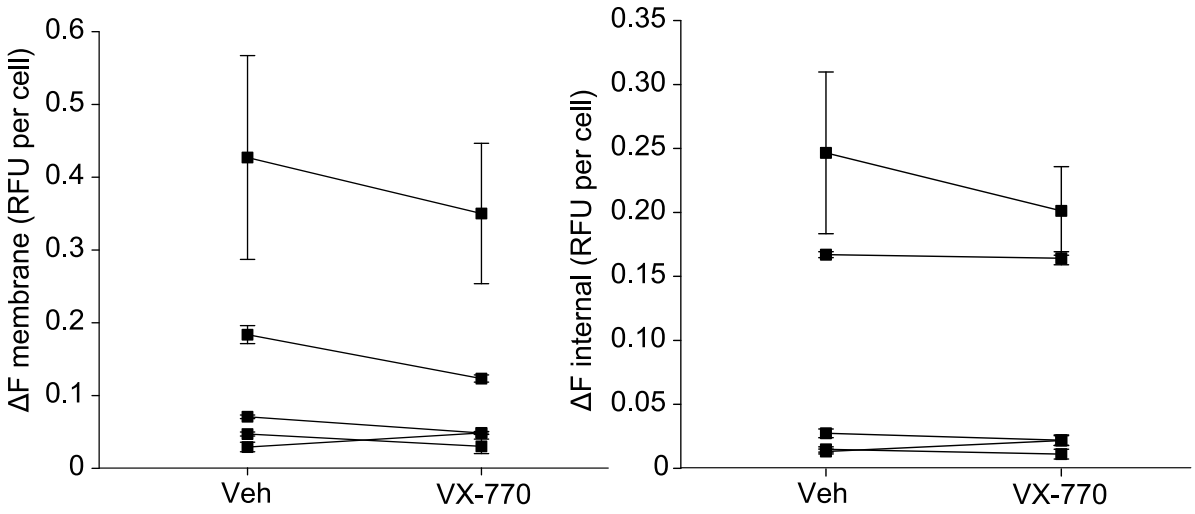


**Figure 4.8 VX-770 chronic treatment on WT-CFTR.** Membrane and internal WT-CFTR following chronic treatment with 1 µM VX-770 ($p = 0.14$ and $p = 0.35$, respectively).

### 4.7.1 Normalising for differences in transfection efficiency

One of the strengths of the CFTR-pHTomato assay is that it does not require membrane CFTR to be expressed as a percent of total CFTR, which inevitably results in a loss of information regarding overall expression levels. To avoid normalising the membrane density signal to total CFTR, raw fluorescence values were used. Transient transfection of cells has variable efficiency, with protein expression of individual cells dependent on the number of plasmids taken up during transfection. Should a cell take up many plasmids, the raw fluorescence change representing membrane CFTR would be larger than the corresponding change in a cell that took up very few plasmids.

To normalise for this, we expressed CFTR-pHTomato in a pIRES2-eGFP plasmid. The fluorescence intensity obtained on the GFP channel quantifies the amount of total protein transcribed from the plasmids present in each cell. It is this reading that is used to normalise

the pHTomato fluorescence, so CFTR levels are given as pHTomato/GFP fluorescence ratios. Figure 4.4 shows correlation of the eGFP and pHTomato signal, which confirms that eGFP can be used to normalise for transfection efficiency. As far as we are aware, no other CFTR localisation assay controls for transfection efficiency.

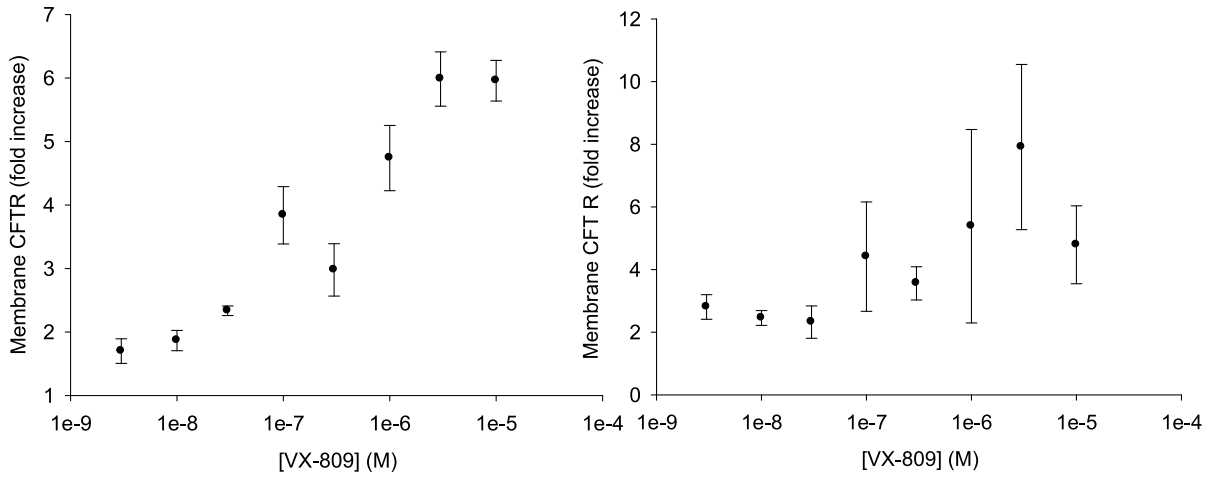


**Figure 4.9 Reduced variability following normalisation to eGFP signal.** ΔF508-CFTR correction by VX-809 and low temperature incubation. Data points collected from one experiment, and displayed using two analysis techniques. Left: pHTomato signal of each region in the image was normalised to the eGFP signal, to account for differences in transfection efficiency. Right: eGFP signal was not used.

Using the eGFP signal to normalise for transfection efficiency of individual regions also dramatically reduced the standard error (average error 9% vs. 27%, Figure 4.9). This shows that variability in transfection efficiency was one large source of error in this assay, which we were able to reduce.

### 4.7.2 Independent quantification of membrane and internal CFTR

Maturation is often expressed using mature CFTR (band C) as a percent of total CFTR, or the ratio of mature CFTR to immature. Both of these are a complex function of many rates, such as the rate of synthesis at the ER, of ER-associated CFTR degradation, of mature CFTR degradation, of ER to Golgi and Golgi to membrane trafficking etc. These ratios are, therefore, not always an effective quantification of CFTR maturation.

Figure 4.10 illustrates that these ratios do not always accurately represent correction of CFTR. Using membrane and total ΔF508-CFTR following treatment with VX-809 or Corr-4a, the trafficking efficiency (membrane CFTR as a percent of total) was calculated. According to the trafficking efficiency, Corr-4a is as efficacious as VX-809 (Figure 4.10, 10 µM VX-809 vs. 10 µM Corr-4a). However, Figure 4.6 shows that less ΔF508-CFTR reaches the membrane following correction with Corr-4a, than following correction with VX-809. Figures

4.6 and 4.10 demonstrate that the absolute level of membrane CFTR is not necessarily proportional to trafficking efficiency, and highlights the importance of independent quantification of membrane-localised CFTR.

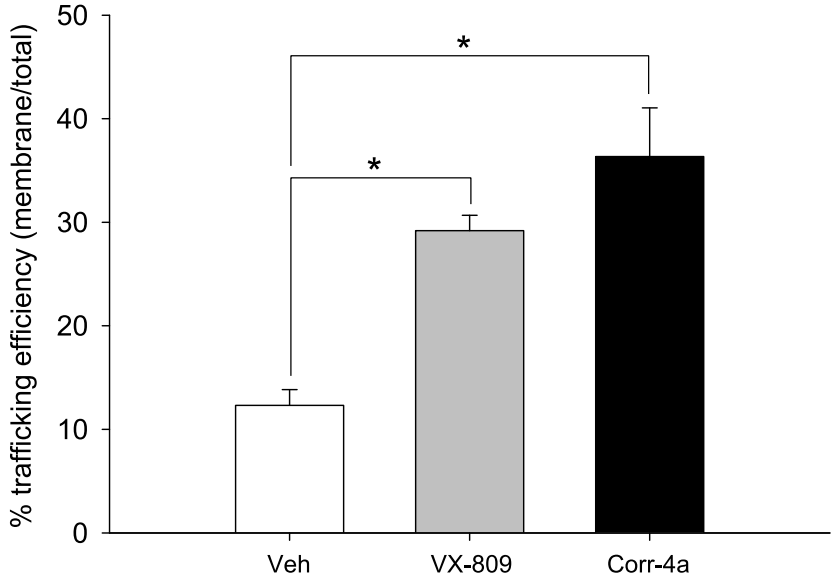


**Figure 4.10 ΔF508-CFTR trafficking efficiency in the presence of known correctors.** ΔF508-CFTR expressing cells incubated at 30°C + 10 μM of the indicated corrector (or vehicle control). * = $p < 0.05$, from Kruskal-Wallis one way ANOVA on ranks and post-hoc Dunn's test. Vehicle control n = 19, VX-809 n = 12, Corr-4a n = 3.

Whilst it is possible to measure changes to internal CFTR (Figures 4.5 and 4.6), high error makes the sensitivity of this assay insufficient to measure small changes in internal CFTR expression.

It is likely that this method of internal CFTR quantification does not only measure CFTR retained at the ER. $NH_3$ permeates all internal vesicles, such that CFTR in the recycling pathway, undergoing degradation, and held at the ER will be included. The only requirement being that the pHTomato tag is intact and inside a vesicle. Thus, an increase in $\Delta_F$ internal does not necessarily indicate an increase in immature, ER-associated CFTR.

### 4.7.3 Compound mechanism of action studies

#### 4.7.3.1 Corrector compounds

The mechanisms by which corrector compounds work to increase membrane density of ΔF508-CFTR are beginning to be understood. It is thought that VX-809 stabilises the NBD1:ICL1 or NBD1:ICL4 interface, whilst Corr-4a stabilises NBD2 or NBD2 interfaces (Okiyoneda et al., 2013).

A recent publication suggests that Corr-4a and VX-809 act at different stages of maturation to increase ΔF508-CFTR membrane density. VX-809 induces an accumulation of immature CFTR. The turnover of immature ΔF508-CFTR is decreased, and the processing efficiency to mature ΔF508-CFTR is increased, which together results in increased ΔF508-CFTR membrane density (Farinha et al., 2015). An increase in immature CFTR can be indicative of a compound which acts early in biosynthesis, before the protein achieves membrane-localisation. Corr-4a appears to stabilise only ΔF508-CFTR which reaches maturity (Farinha et al., 2015, but see Bali et al., 2016).

These different mechanisms are consistent with results in Figure 4.6. Whilst both membrane and internal CFTR increase in a dose-dependent manner when treated with VX-809, only membrane CFTR is increased by Corr-4a.

This highlights a potential use of the CFTR-pHTomato assay: to rapidly indicate levels of biogenesis intermediates, as well as mature CFTR. This is a first step in understanding the potential mechanisms by which corrector compounds promote membrane ΔF508-CFTR. However, the relatively high variability, especially of the internal readout, means that only very strong effects will be reliably detected.

#### 4.7.3.2 Quantification of membrane half-life

Quantification of membrane half-life can give important information on compound mechanism. Pulse-chase experiments are usually used to estimate CFTR protein half-life. This involves preventing the synthesis of new protein, using cycloheximide, and quantifying the remaining CFTR at multiple time points thereafter. Using a similar experimental procedure, it should be possible to measure membrane half-life using CFTR-pHTomato. Preliminary results are shown in Figure 4.11. Cells were transfected with ΔF508-CFTR, left to express the protein for 24 h, then treated with 100 µg/ml of cycloheximide, to prevent synthesis of new protein. CFTR-pHTomato assays were taken at multiple time points following initiation of cycloheximide treatment.

Figure 4.11 shows how membrane ΔF508-CFTR varied over time in the presence of cycloheximide. The data is noisy and cannot be fit for a time constant. Repeat experiments showed no significant decrease in ΔF508-CFTR membrane density, suggesting that cycloheximide treatment did not successfully prevent synthesis of new protein. A possible cause of this is over-expression of CFTR in the HEK293 cell system. Should ΔF508-CFTR be over-expressed, the protein could be overwhelming even this high concentration of cycloheximide. In future efforts, less plasmid could be used for transfection, or ΔF508-CFTR could be expressed in a different cell system, i.e. one less prone to over-expression.

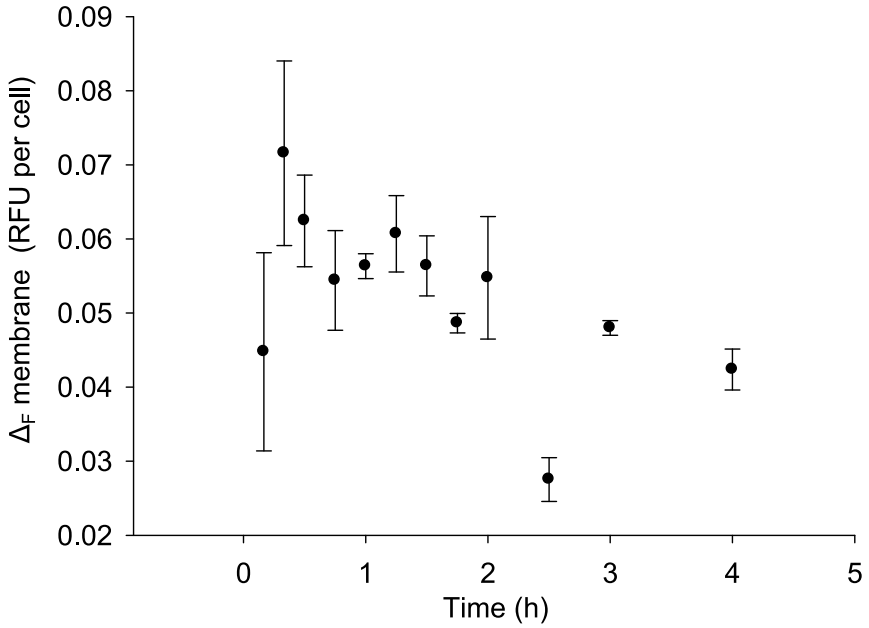


**Figure 4.11 ΔF508-CFTR-pHTomato membrane density following treatment with cycloheximide.** The time axis indicates the length of time in 100 µg/ml cycloheximide treatment. ΔF508-CFTR was rescued using 3 µM VX-809 and 30°C incubation. n = 3.

If membrane half-life measurements could be achieved using CFTR-pHTomato, compound mechanism studies would be easier and faster to acquire than techniques currently in use.

### 4.7.4 Expression in CF bronchial epithelial cells (CFBEs)

One of the weaknesses of the CFTR-pHTomato assay is the cell line in which the protein is expressed. CFTR folding and trafficking are complex processes, dependent on many accessory proteins, some of which are likely to be cell-specific. Indeed, corrector mechanisms have shown cell specificity. For example, whilst functional in recombinant cells, Corr-4a has only modest activity in primary cultures of bronchial cells derived from ΔF508-CF patients (Farinha et al., 2015). Should this assay be used for screening potential ΔF508-CFTR correctors, the number of false positives and negatives, and eventually the high attrition rate in drug development, will be reduced by a screen that more accurately represents the environment in which the drug will be used.

Some effort was directed at expressing CFTR-pHTomato in a more relevant cell line. Collaborators at the Institute of Child Health (Prof. Steve Hart and Dr. Mustafa Munye) have developed a semi-immortalised cell line using bronchial epithelial cells from healthy and CF donors (purchased from Lonza, Belgium). By knocking out a senescence gene, this group have made it possible to passage these cells up to 20 times. In submerged cultures (rather than air-liquid interface), these cells do not differentiate into epithelial cells, but are representative of an earlier basal airway cell. Using a lipid-peptide transfection technique

optimised by the Hart lab (Munye et al., 2015), we attempted transient transfection of CFBEs with CFTR-pHTomato. Unfortunately, transfection efficiency was too low to achieve a measurable signal (work carried out with the help of MSci Pharmacology student Pengxiang Zhao, supported by a British Pharmacological Society Summer Studentship).

In the future, it might be desirable to make a stable CFBE cell line expressing ΔF508-CFTR-pHTomato. However, the level of expression would need to be sufficiently high for reliable fluorescence imaging, a result that might not be easy to achieve.

### 4.7.5 Assay variability

The main advantage of the CFTR-pHTomato assay is the ability to measure membrane-localised CFTR, independent of both total CFTR expression, and function. The data presented in this chapter demonstrates this can, to some extent, be achieved. During the optimisation of this assay, effort was made to reduce the variability of measurements. As mentioned above, normalising the pHTomato signal to the eGFP signal (Figure 4.9) resulted in reduced variability. Additionally, acquisition settings were optimised on each plate to increase the pHTomato signal, to avoid very low fluorescence signals, too close to the plate noise.

Despite these efforts, as error bars in many figures show, variability remains high, particularly for internal CFTR measurements. This variability suggests that an uncontrolled factor within the assay is affecting fluorescence change. For example, fluid addition artefacts, similar to those discussed in Chapter 3, could impact $\Delta_F$ readings. Variation in the behaviour of individual HEK293 cells, within the culture, could also contribute to inconsistency of readings. To improve this, a new clonal cell line could be started for future experiments.

If variability could be reduced, the pHTomato assay could be exploited for other protein trafficking diseases, the only requirement being a suitable extracellular domain to which the pHTomato can be tagged. One obvious protein, related to CFTR, whose cellular localisation is an important determinant of disease severity is ABCA4, an ABC transporter mutated in Stargardt disease (Sabirzhanova et al., 2015).

In this thesis, CFTR-pHTomato is used to support the YFP-CFTR assay in the screening for potentiators. It is used as a secondary screen of the hit compounds, by measuring membrane density following chronic treatment with potential novel potentiator compounds. Recent results (Cholon et al., 2014; Veit et al., 2014) suggest that a sensitive quantification of membrane CFTR will be a requirement of any screen targeting CFTR, increasing the

chance of early detection of any negative effect a drug candidate might have on biogenesis. However, further reductions in variability will be required in order to make the CFTR-pHTomato really suited for this purpose (see Chapter 5).

# Chapter 5

# ΔF508-CFTR functional potentiator screen

## 5.1 Introduction

This chapter describes two pilot studies, in which compound libraries were screened using the YFP-ΔF508-CFTR assay. The first library included 138 compounds. Following the successful identification of hit compounds, another library was constructed based on the most promising hit compound. A further library included compounds selected directly by similarity to VX-770.

Identification of ΔF508-CFTR potentiator compounds is required for the successful treatment of ΔF508-CF patients. The majority of ΔF508-CFTR potentiators identified to date have a negative effect on the stability and biosynthesis of ΔF508-CFTR (Cholon et al., 2014; Veit et al., 2014). Potentiator/corrector combination treatment of ΔF508-CF resulted in marginal improvements in clinical trials (Wainwright et al., 2015), the modest results most likely reflecting destabilisation of ΔF508-CFTR by the VX-770 component (Cholon et al., 2014; Veit et al., 2014). These studies highlight the requirement for more ΔF508-CFTR potentiators, devoid of negative effects on stability and biosynthesis of the rescued protein.

Effective screening assays, capable of measuring both ΔF508-CFTR function and membrane density, are required to meet this need in CFTR pharmacology.

### 5.1.1 The ChemiBank Library

The pilot library of 138 compounds was donated by David Selwood from UCL ChemiBank (The Wolfson Institute for Biomedical Research). ChemiBank is a resource of 30,000 diverse compounds, available at UCL for identification of small molecule ligands for proteins. The pilot library was constructed for a different project (targeting Natriuretic Peptide Receptor C; CNP), but compounds bore structural resemblance to VX-770.

### 5.1.2 Ligand-based virtual screening

Novel compound libraries were constructed for this project using ligand-based virtual screening (LBVS), in collaboration with researchers at the University of Bern (Professor JL Reymond's group). LBVS is a compound selection method by which ligands from a large virtual compound database are identified based on their similarity to a starting ligand.

Chemical space is a vast and largely untapped resource, which, thanks to large database screening, is becoming accessible to drug discovery researchers. The Reymond lab have developed a virtual screening method in which atom pair fingerprints are used to characterise the 3D structure of a compound, in a time efficient manner to allow searches through millions of compounds to identify structural analogues. They have verified that the atom pair fingerprint is capable of matching compounds based on 3D structure (Awale and Reymond, 2014). The 3D-fingerprint method distinguishes between different stereoisomers of a compound, not possible with 2D-fingerprints (Awale et al., 2015).

By changing the way compound libraries are selected, they hope to reduce the exceedingly high attrition rate suffered by drug discovery efforts.

For this project, Professor Reymond's group used the lead hit compound from the pilot screen, and VX-770, as query ligands to construct two separate libraries. They searched the ZINC database (a virtual screening platform which contains > 10 million commercially available compounds; Irwin et al., 2012) to identify compounds similar in 3D structure to these starting ligands.

### 5.1.3 The YFP-CFTR potentiator screen

Following temperature rescue, compounds were screened for potentiator activity using the YFP-ΔF508-CFTR assay, in the presence of 50 μM forskolin (Figure 5.1).

Controls were run on every plate to allow within-plate normalisation of the function of test compounds. Negative controls contained 50 μM forskolin + DMSO (vehicle), whilst wells containing 50 μM forskolin + 10 μM VX-770 were used as positive controls.

Hit compounds identified in the YFP-CFTR screen were then tested chronically for effects on ΔF508-CFTR membrane stability, using the ΔF508-CFTR-pHTomato assay.

## 5.2 Screening conditions and positive and negative controls

The pilot screen consisted of 138 compounds organised over two 96-well plates, with column 12 reserved for control wells. Compounds were stored at 10 mM in DMSO, at -20°C.

Forskolin and the test compounds were both dissolved in DMSO, so cells were exposed to 0.35% vehicle during the assay. DMSO is a solvent, which can alter responses in cellular assays. To measure the effect of the vehicle, quenching caused by 0% and 0.35% DMSO was compared (Figure 5.2).

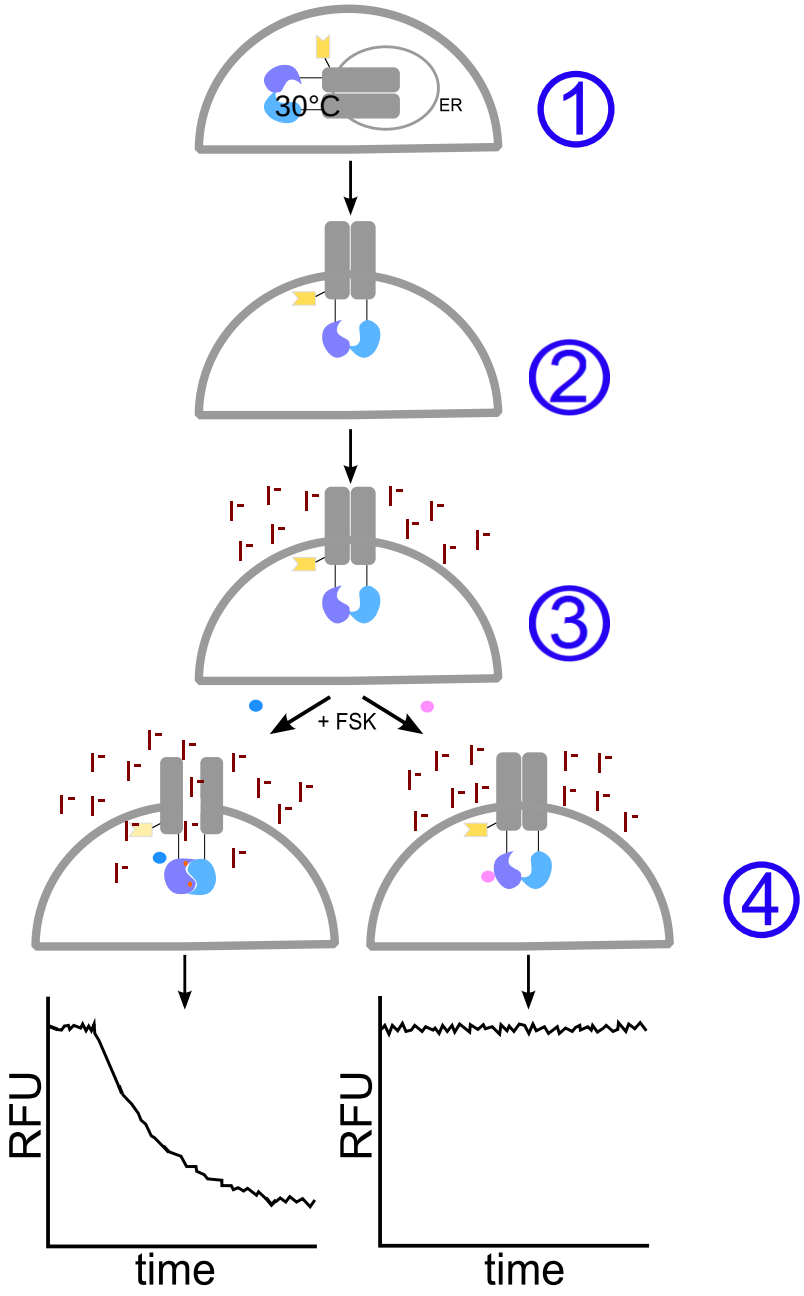


**Figure 5.1 YFP-ΔF508-CFTR potentiator screen protocol.** HEK293 cells in 96-well plates are transiently transfected with YFP-ΔF508-CFTR. 1) 24 h after transfection, cells are transferred to 30°C for 24 h to promote ΔF508-CFTR trafficking to the membrane. 2) During the assay, extracellular $I^-$ buffer is added to create a large $I^-$ gradient. 3) Each test compound is added in the presence of 50 μM forskolin. 4) Readout from wells receiving active compounds show quenching (left) in response to forskolin addition, whilst inactive compounds do not (right). FSK = forskolin.

The quenching in Figure 5.2A suggests that there is some vehicle effect caused by 0.35% DMSO. Upon addition of solution (0% or 0.35% DMSO), there was an initial apparent increase in YFP fluorescence (suggesting an efflux of $I^-$), which was larger in the presence of DMSO. This initial change is followed by fluorescence quenching, with DMSO causing a decrease in maximal $I^-$ entry rate by only ~0.7 μM $s^{-1}$ (Figure 5.2B). Although this effect

seems large in Figure 5.2A, the maximal $I^-$ entry rate achieved in the presence of 50 μM forskolin + 10 μM VX-770 is ~80 μM $s^{-1}$. Therefore, the reduction in $I^-$ entry rate caused by this DMSO effect was < 1% of the maximal quenching rate achieved by potentiators.

The delayed, relatively low YFP quenching seen in Figure 5.2 confirms that any increase in the rate of $I^-$ entry during the YFP-ΔF508-CFTR screen is an effect of the test compound, and not the vehicle.

As the potentiator with the highest efficacy, and the only potentiator compound approved for treatment, VX-770 was chosen as the positive control.

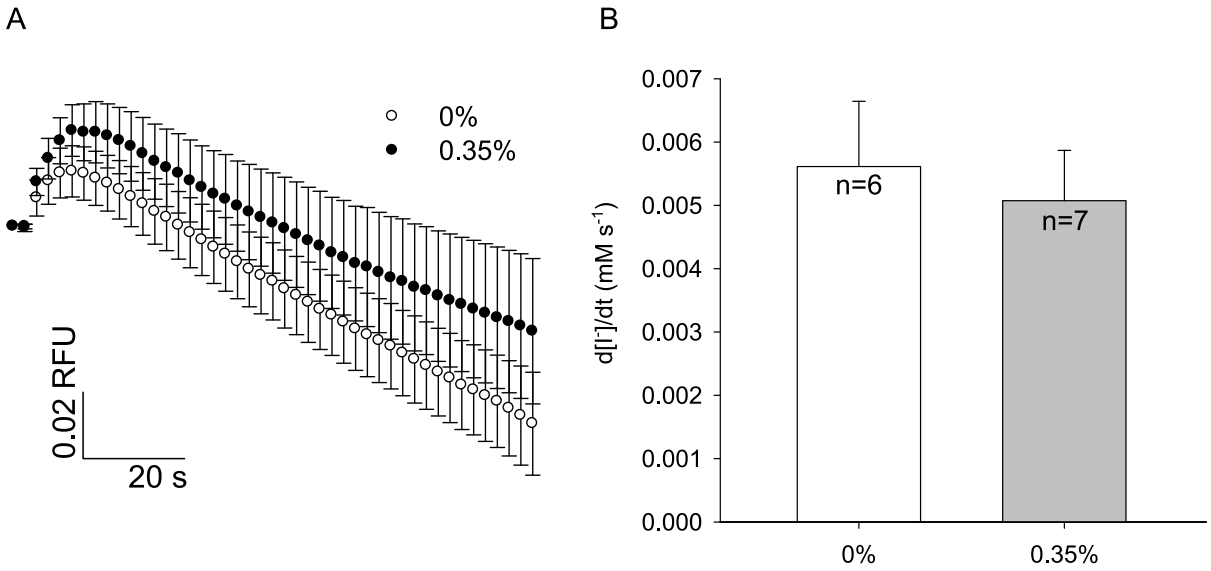


**Figure 5.2 DMSO tolerability of YFP-ΔF508-CFTR potentiator assay.** A) 0% and 0.35% DMSO in YFP-ΔF508-CFTR quenching assay. B) Quenching rates quantified using rate of $I^-$ entry of traces shown in A. No significant difference between treatments (p = 0.68).

## 5.3 Quality control

An indicator of the quality of a high-throughput screening assay is the ability to distinguish between positive and negative controls. Strictly standardised mean difference (SSMD) is a quantitative parameter measuring assay quality. Originally developed for use in RNA interference (RNAi) screens, SSMD is also suitable for assessing quality of small molecule screens (Zhang et al., 2007; Zhang, 2008, 2011). SSMD is defined as a measure of the difference between two groups (negative and positive references), penalised by the variability of the difference (Equation 5.1).

$$SSMD = \frac{\mu_P - \mu_N}{\sqrt{(\sigma_P)^2 + (\sigma_N)^2}} \qquad \text{[Equation 5.1]}$$

Where $\mu_P$ and $\mu_N$ are means of the positive and negative references, and $\sigma_P$ and $\sigma_N$ are the standard deviations of the positive and negative references (Zhang, 2007).

To reduce the impact of outliers, mean and standard deviation are replaced with median and median absolute deviation (MAD), in the calculation of robust SSMD ($SSMD_R$) (Equation 5.2).

$$SSMD_R = \frac{\tilde{X}_P - \tilde{X}_N}{\sqrt{(\tilde{s}_P)^2 + (\tilde{s}_N)^2}} \qquad \text{[Equation 5.2]}$$

Where $\tilde{X}_P$ and $\tilde{X}_N$ are medians of the positive and negative references, and $\tilde{s}_P$ and $\tilde{s}_N$ are the MADs of the positive and negative references (Zhang, 2007; Goktug et al., 2013).

The output of the SSMD calculation is an interpretable number, it is easy to calculate, and is not dependent on sample size (Bray and Carpenter, 2013). Zhang *et al.* (2007) interpret an SSMD value > 3 as a 95% chance that a value from the positive control group is greater than a value from the negative control group. Using Equation 5.2, $SSMD_R$ was calculated for each plate used in the pilot screen. The library covered two plates, which were each screened three times. Each plate contained three or four negative control wells (50 µM forskolin + vehicle) and three or four positive control wells (50 µM forskolin + 10 µM VX-770).

According to Bray and Carpenter (2013), small molecule screens with only one type of positive control should use the criteria in Table 5.1 to interpret SSMD quality control values. The $SSMD_R$ values in the pilot screen varied from 3.5 to 11.3. Three plates fell into the 'good' category, and three were 'excellent'. Data from all plates was used, since none fell into the 'poor' category.

| **Quality** | |
|---|---|
| Excellent | SSMD ≥ 5 |
| Good | 5 > SSMD ≥ 3 |
| Inferior | 3 > SSMD ≥ 2 |
| Poor | 2 > SSMD |

**Table 5.1 SSMD quality control criteria for small molecule screens with only 1 type of positive control** (Modified from Bray & Carpenter, 2013)**.**

## 5.4 Hit selection

High-throughput screening requires prior identification of criteria to be met in order for a compound to be considered a hit. SSMD was chosen as the method of hit selection, since it

is capable of incorporating the variability of test compounds in replicate screens (Zhang et al., 2007; Zhang, 2011).

To calculate SSMD, the measured value of each repeat is compared to the median of a negative reference within the plate. The mean and standard deviation of the difference between the test and the negative reference is used to calculate one SSMD value, which incorporates all replicates (Equation 5.3, $SSMD_i$, where i is n between 1 and 138 in the pilot screen).

When the standard deviation calculation is based on a very small n number (i.e. three replicates, as in this screen), variation estimates can become highly variable. Considering that most compounds will have the same variation, the standard deviation of all tests can be incorporated in order to stabilise the estimate (Zhang, 2011). In Equation 5.3, a combination of a common factor ($0.5s_o^2$), and the individual sample variance ($0.5s_i^2$) was used to penalise the difference between test and negative control (Zhang, 2011).

$$SSMD_i = \frac{\bar{d}_i}{\sqrt{0.5s_i^2 + 0.5s_o^2}} \qquad \text{[Equation 5.3]}$$

Where $\bar{d}_i$ is the mean of the differences between the test compound and negative reference, $s_i$ is the standard deviation of the same and $s_o^2$ is the median of all $s_i^2$ (Zhang, 2011).

A positive $SSMD_i$ value indicates that the effect of the test compound is consistently greater than the negative control. A negative $SSMD_i$ value indicates the effect of the test compound is consistently smaller than the negative control. In our screen, we are interested in identifying compounds with a positive effect. An $SSMD_i$ value > 2 indicates a strong positive effect (Zhang, 2011).

Equation 5.3 was used to calculate an $SSMD_i$ value for each compound in the pilot screen. Compounds with weak but very consistent effects will also have high $SSMD_i$ values. To avoid selecting these compounds as hits, data was plotted on a dual-flashlight plot, in which $SSMD_i$ is plotted against average percentage activation (Figure 5.3). Percentage activation is calculated using the within-plate positive controls (i.e. percentage activation compared to 10 µM VX-770), and averaged over three replicates. This allows compounds with a very high $SSMD_i$ value, but not a high percentage activation, to be discounted. Selected hits are therefore both statistically and biologically favourable (Zhang, 2011).

The points in Figure 5.3 appear as if they belong to two different populations. The distinct groups on the plot do represent the two separate compound plates (i.e. 88 compounds were

stored and screened on Plate 1, represented in black, and 50 compounds were stored and screened on Plate 2, represented in red). A negative $SSMD_i$ value, such as that of most compounds on Plate 2, suggests the quenching result is significantly smaller than the negative control. There are two explanations for a negative $SSMD_i$ value. Either the negative control wells do not accurately represent the population, or these compounds are acting as inhibitors of ΔF508-CFTR.

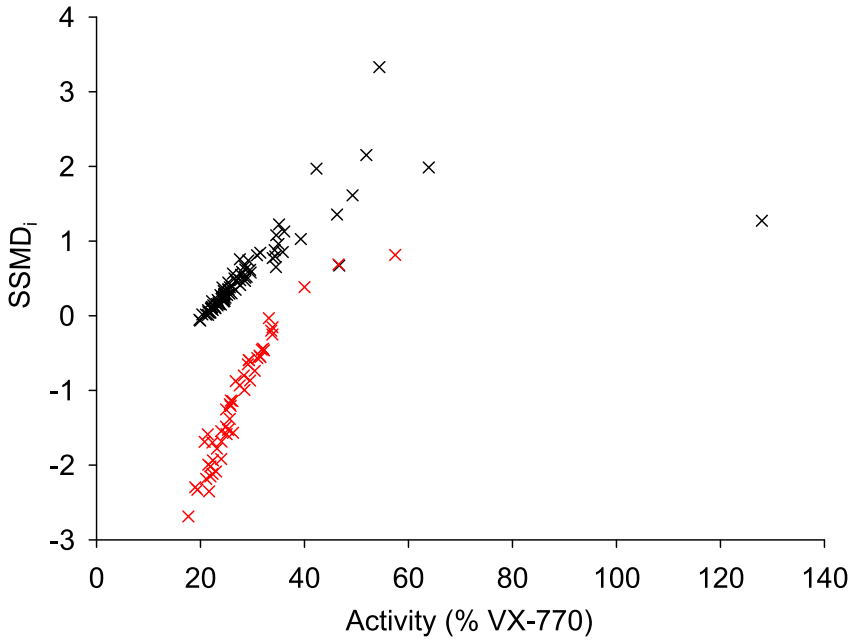


**Figure 5.3 Dual-flashlight plot of pilot screen results.** $SSMD_i$ calculated using Equation 5.3. Percentage activation calculated using within-plate positive controls (50 µM forskolin + 10 µM VX-770). The black and red plots represent two separate plates used in the screen (Plate 1 and Plate 2, respectively).

Temperature rescued ΔF508-CFTR is not activated by 50 µM forskolin (Chapter 3, Figure 3.12). Therefore, it seems unlikely that the compounds on Plate 2 are acting as inhibitors, as there is no "control activation" to inhibit. Additionally, the percentage activation of the two populations is not different (Figure 5.3: 25.6% (± 5%) and 25.4% (± 4%) median for the two populations).

It seems more likely that the negative control wells in this plate do not accurately represent the population. The negative control wells in Plate 1 (population with $SSMD_i$ ~ 0.2) have 18.6% (± 5%) activation compared to within plate positive controls. Plate 2 negative control wells have 34.9% (± 3%) activation. This is also reflected in the raw quenching rate data (5.7 ± 0.9 µM $s^{-1}$ vs. 10.3 ± 0.7 µM $s^{-1}$ for Plate 1 and Plate 2, respectively). Therefore, it seems the negative control wells on Plate 2 are unusually high. This gives a population with negative SSMD values, as test compounds have slower quenching rates than the abnormally high negative controls, to which they are compared.

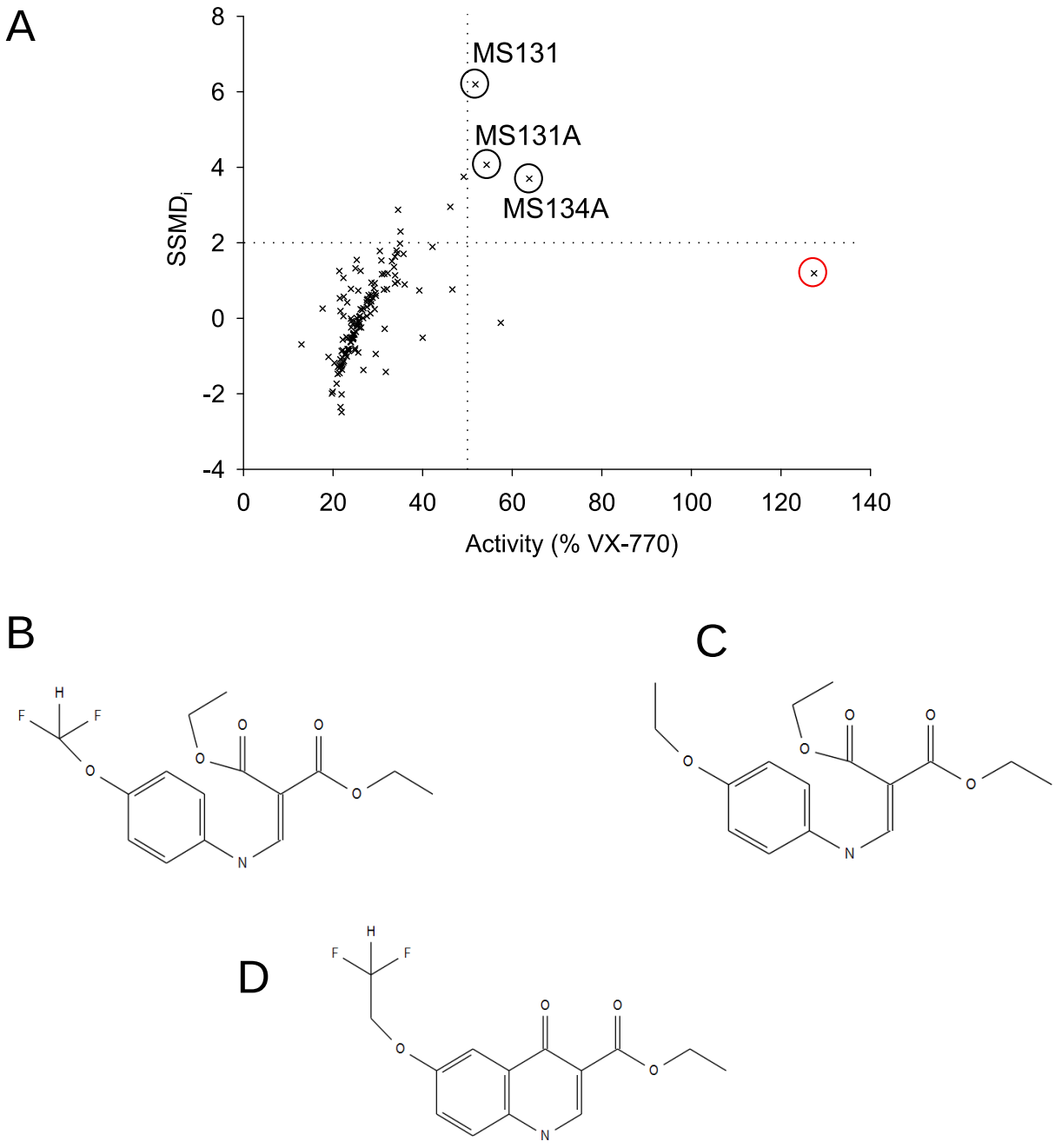


**Figure 5.4 Pilot screen results.** A) Dual-flashlight plot. $SSMD_i$ calculated using the median of test compounds as the negative control. Each cross represents one test compound, tested three times. Potentiators with an $SSMD_i$ value > 2 and activity > 50% compared to 10 μM VX-770 were selected as hits, structures shown in B-D. B) MS131A. C) MS134A. D) MS131.

Differences in controls can occur because control wells are usually located at the edge of the plate, which suffers more evaporation during culture, and they are run together, usually at the end of the experiment.

When only a few hits are expected per plate, the median of the test compounds can be used as a negative reference, and often better represents the sample (Goktug et al., 2013). Although this plate of compounds had some structural similarity to VX-770, an initial assessment of the data showed that not many compounds were active as ΔF508-CFTR potentiators (Figure 5.3). Therefore, the median of the test samples was used as the negative reference.

Figure 5.4 shows the dual-flashlight plot constructed when the median of the test compounds was used as the negative reference. This plot shows one population of compounds, with an average $SSMD_i$ of ~0, and ~25% activation compared to within plate positive controls. The three compounds with $SSMD_i > 2$ and activation > 50% were chosen for further study. One compound (circled in red, Figure 5.4A) showed high activation (mean 127% of VX-770 control). However, inspection of the images and quenching traces indicated this was an artefact, supported by the low $SSMD_i$ value.

Structures of hits from the ChemiBank library are shown in Figures 5.4B to 5.4D. Compounds had the expected molecular weights and high purity, confirmed using liquid chromatography mass spectrometry (LCMS, carried out by David Selwood, UCL Wolfson Institute for Biomedical Research).

## 5.5 Confirmation of hit activity

In order to confirm activity of hit compounds, concentration-response curves were constructed using both YFP-ΔF508-CFTR and YFP-G551D-CFTR (Figure 5.5). All solutions were prepared freshly from solid stock at 10 mM in DMSO. This was done to confirm that the potentiator activity was not caused by a contaminant of the sample.

MS131A and MS134A activity was confirmed on both mutations (Figures 5.5A and 5.5B). MS131 had little efficacy, with what appears to be very low affinity (Figure 5.5C). No further work was done with MS131, the least active compound in the screen, as precipitates were noted and insolubility became a major obstacle preventing further work.

Differences in potency and efficacy between ΔF508-CFTR and G551D-CFTR confirm that the activation detected in the screen is mediated by potentiation of CFTR, and not an alternative anion channel.

In summary, of the three compounds identified in the pilot screen, two were confirmed as ΔF508-CFTR potentiators using fresh compound stocks. This encouraged further characterisation of these novel potentiator compounds.

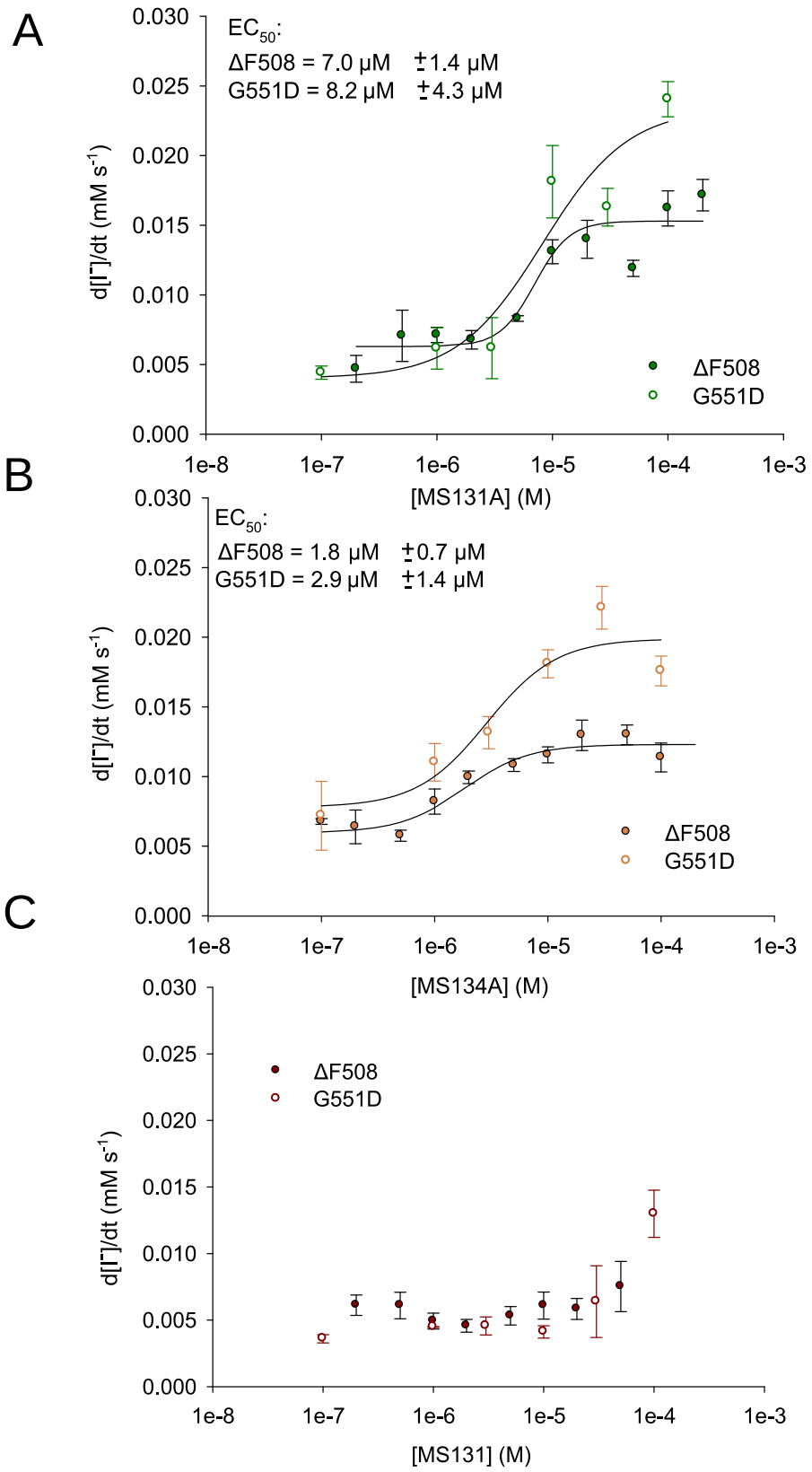


**Figure 5.5 Activity confirmation of hit compounds on ΔF508-CFTR and G551D-CFTR.** A) MS131A. B) MS134A. C) MS131. Best fit $EC_{50}$ values, where obtained, are shown on the graphs. $3 \leq n \leq 6$.

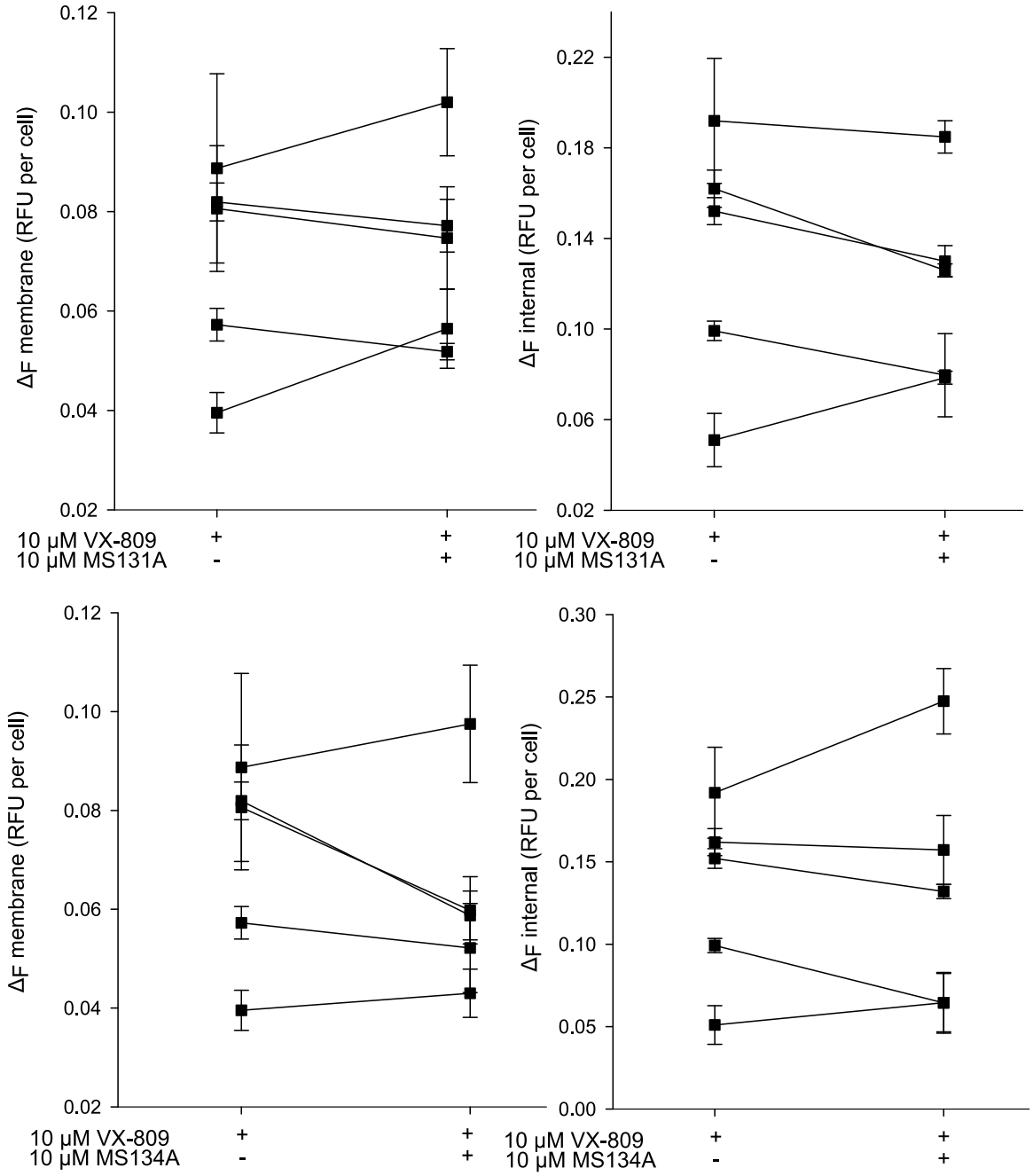


**Figure 5.6 Cellular levels of ΔF508-CFTR following 24 h incubation with novel potentiators.** Cells expressing ΔF508-CFTR-pHTomato were treated with 10 μM VX-809 at 30°C for 24 h, alongside novel potentiators MS131A and MS134A. Pairs (10 μM VX-809 ± compound) were compared using Wilcoxon signed rank test, and showed no significant differences.

## 5.6 Novel compound effects on ΔF508-CFTR following chronic treatment

The ΔF508-CFTR-pHTomato assay was used to assess whether the novel potentiators identified in the pilot screen had a negative effect on ΔF508-CFTR stability and biosynthesis when used chronically.

ΔF508-CFTR was corrected by 10 µM VX-809, alongside low temperature incubation. 24 h incubation with 10 µM MS131A or 10 µM MS134A had no significant effect on membrane density of ΔF508-CFTR (Figure 5.6). MS131A was chosen as the lead compound for the next step of this drug discovery project, due to a slightly higher efficacy on ΔF508-CFTR, compared to MS134A (Figure 5.5A vs. Figure 5.5B).

To confirm that the lack of destabilisation was not due to a degradation of MS131A occurring during chronic incubation, potentiator activity was confirmed following 24 h incubation. ΔF508-CFTR has an increased rate of $I^-$ entry after activation with forskolin alone, following 24 h incubation with MS131A, compared to vehicle-treated controls (Figure 5.7). Quenching rates are increased vs. Figure 5.5 because a different protocol was in use ($I^-$ second addition – see Chapter 6).

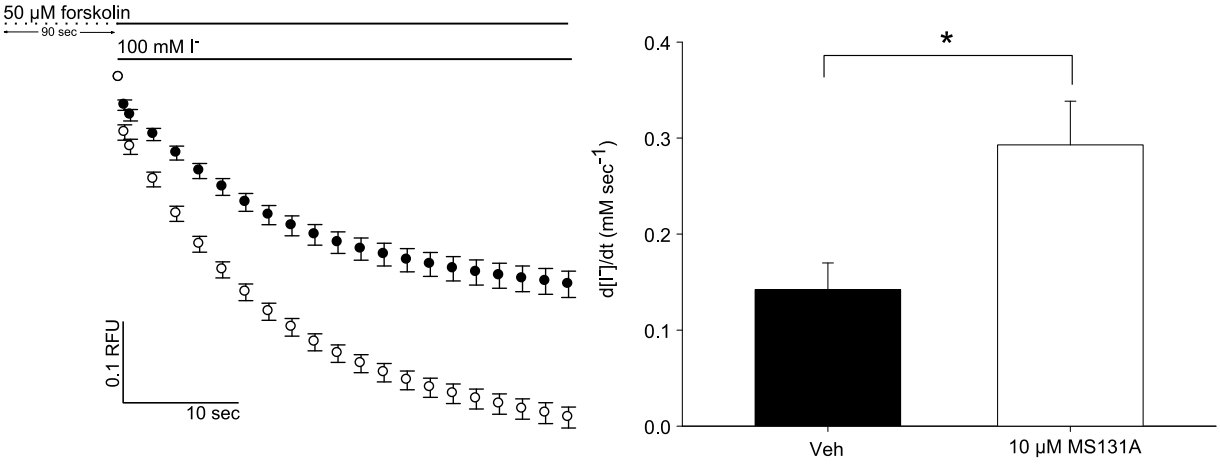


**Figure 5.7 MS131A potentiator activity following chronic treatment.** HEK293 cells expressing ΔF508-CFTR-YFP were treated chronically with 10 µM MS131A or vehicle. Cells were washed before imaging, and activated with 50 µM forskolin. Left: YFP quenching trace shown from addition of extracellular $I^-$. 50 µM forskolin added 90 s before $I^-$ (for protocol details see Chapter 6). Right: Quantified maximal quenching rates. * p = 0.01, from Mann-Whitney U test, n = 9.

## 5.7 Ligand-based virtual screening

Collaborators at the University of Bern selected new compound libraries, using LBVS (based on atom pair 3D-fingerprints), to identify compounds close in chemical space to the pilot screen hit MS131A, or VX-770 (see section 5.7.2), from the ZINC database of commercially available compounds (Irwin et al., 2012).

Two potentiator libraries were screened using YFP-ΔF508-CFTR: a 61 compound MS131A-like (MS13AL) library, and an 82 compound VX-770-like (VX-770L) library. Note that due to the high number of active compounds in these libraries, median of test compounds was not

an acceptable negative reference. The median of within-plate negative control wells (50 µM forskolin + vehicle), was used to calculate test compound $SSMD_i$ values. Examination of the data indicated that the negative control wells better represented the population than in the pilot study. Improvements were made before running the LBVS YFP-CFTR assay to increase the chance that control wells on the plate would represent the data.

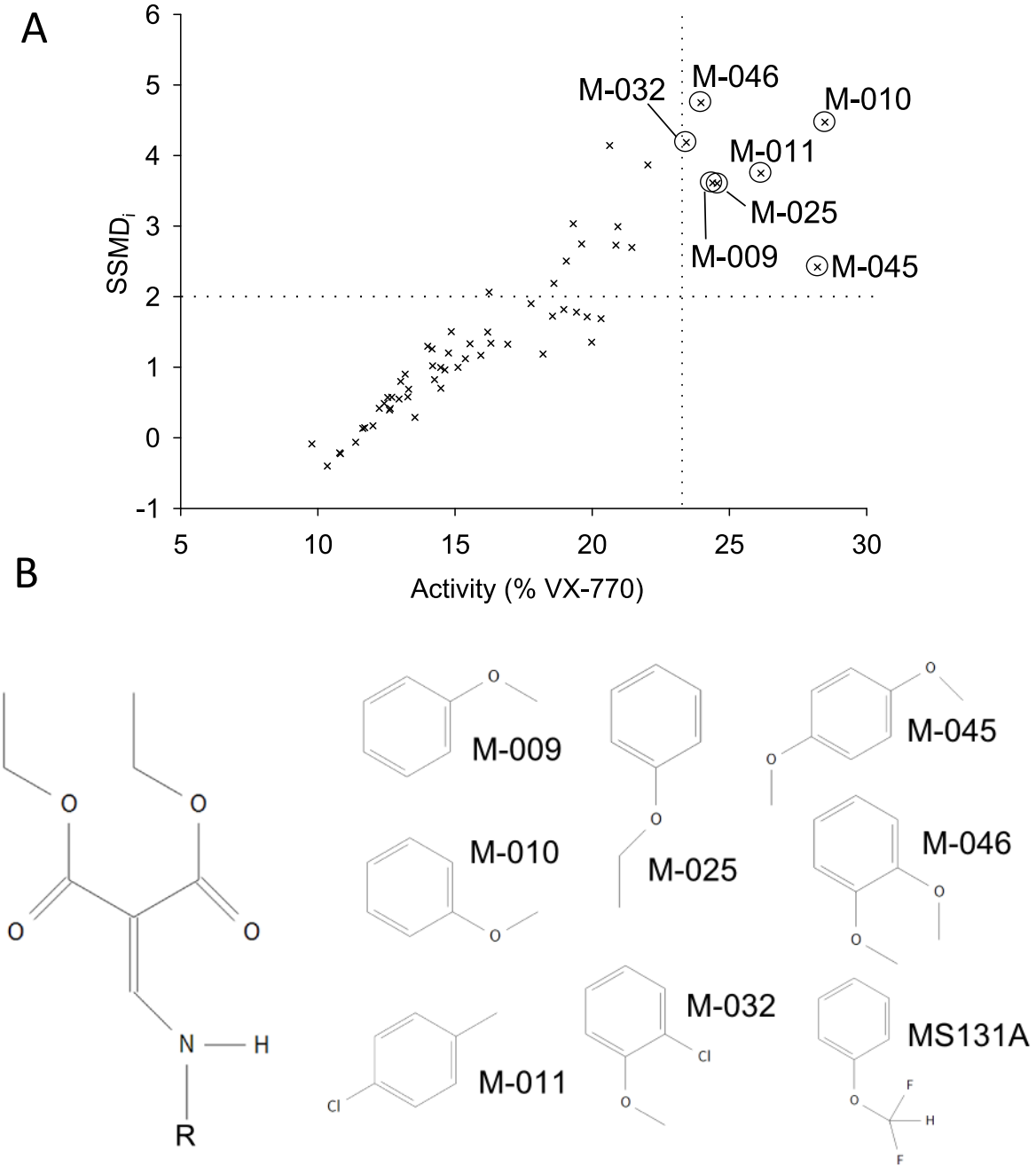


**Figure 5.8 MS131AL library screen for potentiator activity on YFP-ΔF508-CFTR.** A) Dual-flashlight plot. Hits selected using criteria of activity > 23% VX-770 and $SSMD_i$ > 2. B) Structures of hit compounds. Left: Structure common to all hits and MS131A. Right: R groups of hit compounds and MS131A for comparison.

## 5.7.1 MS131AL library

The MS131AL library was tested for ΔF508-CFTR potentiator activity using the YFP-ΔF508-CFTR assay, in triplicate. Quality control $SSMD_R$ values of these plates were 7.2, 16.8 and 116.8.

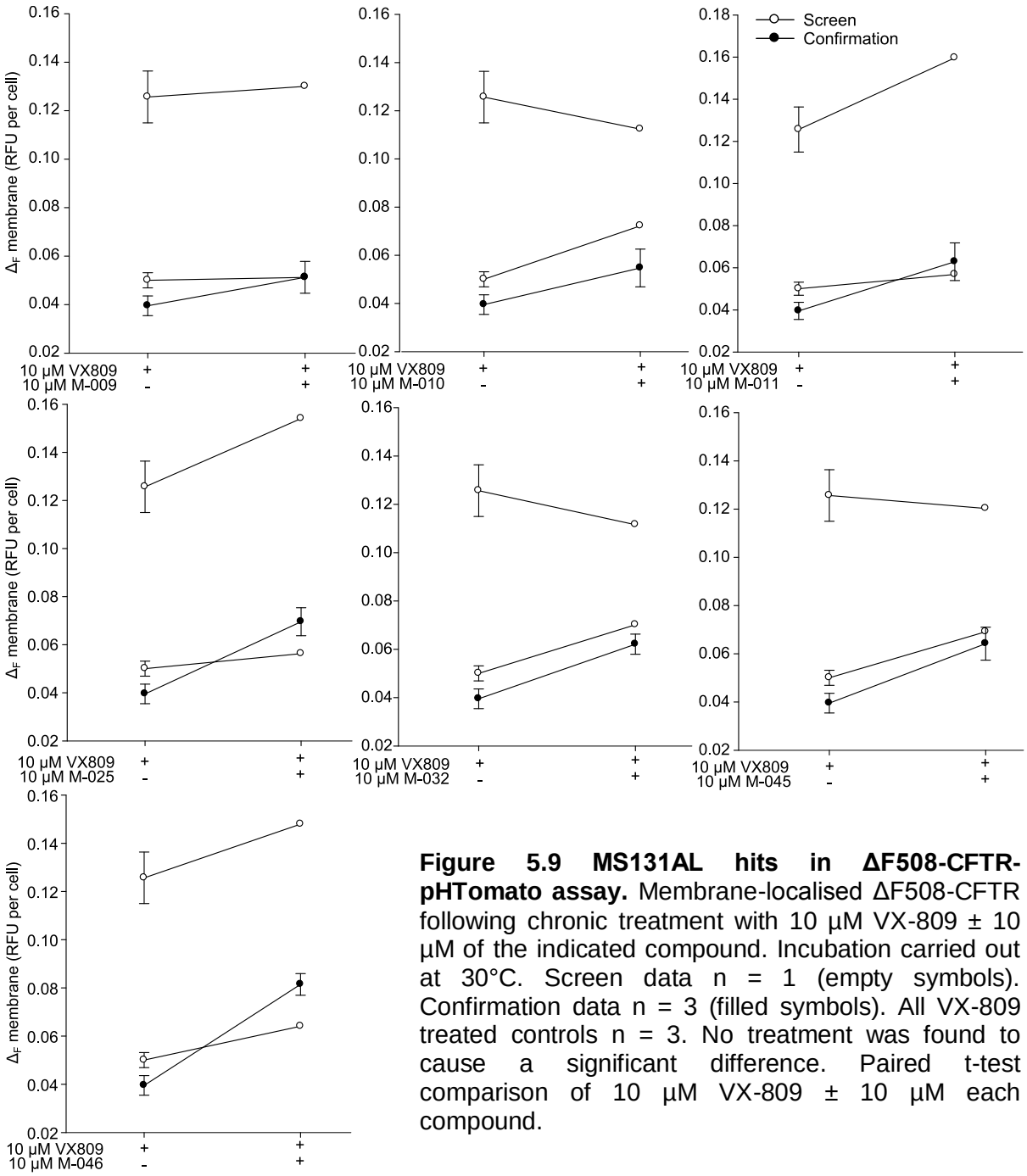


**Figure 5.9 MS131AL hits in ΔF508-CFTR-pHTomato assay.** Membrane-localised ΔF508-CFTR following chronic treatment with 10 μM VX-809 ± 10 μM of the indicated compound. Incubation carried out at 30°C. Screen data n = 1 (empty symbols). Confirmation data n = 3 (filled symbols). All VX-809 treated controls n = 3. No treatment was found to cause a significant difference. Paired t-test comparison of 10 μM VX-809 ± 10 μM each compound.

Although in the pilot screen MS131A had activity > 50% of VX-770, only lower levels of activity could be confirmed later. This was caused by an increase in the positive control reading for VX-770, following the purchase of new VX-770 stock (30 ± 2 µM $s^{-1}$ for old stock vs. 77 ± 4 µM $s^{-1}$ for new stock). Using a comparison of freshly prepared 10 µM MS131A and newly purchased 10 µM VX-770, i.e. those used at the time of screening LBVS plates, MS131A activity was measured as 23.3% ± 1.7% of VX-770 (n = 8). 23.3% of 10 µM VX-770 activity was therefore used as the cut-off to identify hit compounds in the MS131AL library screen.

The MS131AL library screen identified seven hit compounds with activity > 23.3% of 10 µM VX-770 and an $SSMD_i$ value > 2 (Figure 5.8A). All identified compounds had very similar structure to MS131A (Figure 5.8B).

Hit compounds were tested for effects on ΔF508-CFTR membrane density. ΔF508-CFTR-pHTomato was rescued by 10 µM VX-809 and low temperature incubation, and treated chronically with each test compound. Test compound treated cells (run in high-throughput screen format so n = 1), were compared to VX-809 treated controls (Figure 5.9, empty circles). No hit compounds from the MS131AL library appeared to cause a decrease of membrane ΔF508-CFTR. Compounds were then tested in triplicate for confirmation (Figure 5.9, filled circles).

### 5.7.2 VX-770L library

Our collaborators at University of Bern prepared a library of compounds similar in structure to VX-770. The VX-770L library was prepared as for the pilot screen, at 10 mM in DMSO. All compounds were stored on one plate, which was tested in triplicate. Quality control $SSMD_R$ values were 2.2, 9 and 105.6. Again, no plates fell into the “poor” category (Table 5.1), so data from all plates was analysed to measure the effect of the VX-770L library.

Five new hits were identified in the VX-770L library (Figure 5.10A). Hit compounds had potentiator activity > 50% of VX-770, and $SSMD_i$ > 2. Structures of the hit compounds are shown in Figure 5.10B, alongside VX-770. V-033, V-034, V-041 and V-042 have a very similar chemical scaffold to that of VX-770. Compound V-046 has quite a different structure. This confirms that the LBVS method of compound selection can identify structural analogues of the query ligand VX-770, sharing some aspects of its biological activity but not necessarily possessing the same chemical scaffold.

To determine the effect of hit compounds on membrane stability, the ΔF508-CFTR-pHTomato assay was used to measure membrane-localised ΔF508-CFTR following chronic

treatment with hit compounds. Overall, VX-770L hit compounds did not appear to destabilise membrane ΔF508-CFTR (Figure 5.11).

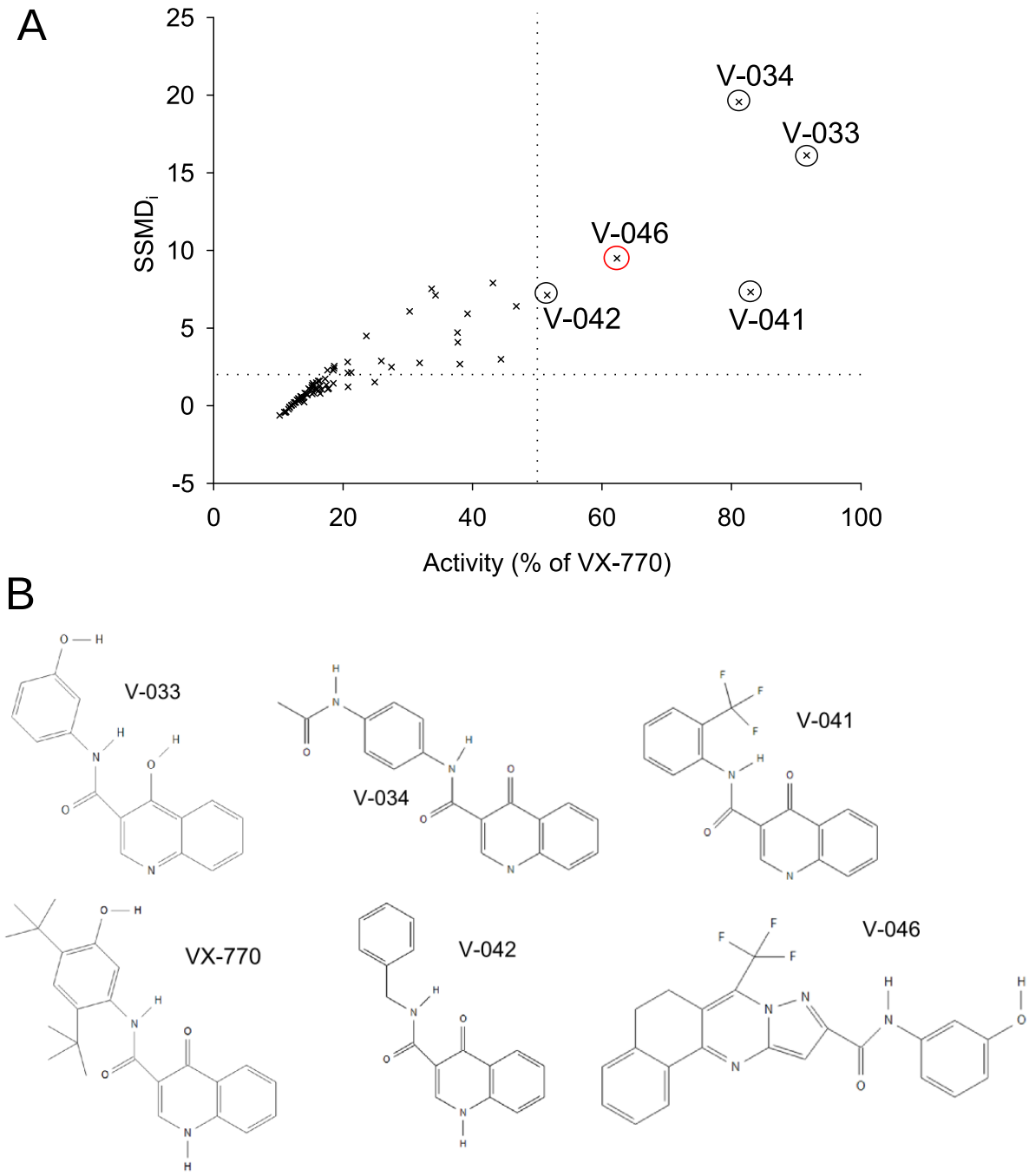


**Figure 5.10 VX-770L library screen for potentiator activity on YFP-ΔF508-CFTR.** A) Dual-flashlight plot. Hits selected using criteria of activity > 50% VX-770 and $SSMD_i$ > 2. V-046 is highlighted in red because of an interesting structure (discussed in text). B) Structures of hit compounds alongside VX-770 for comparison.

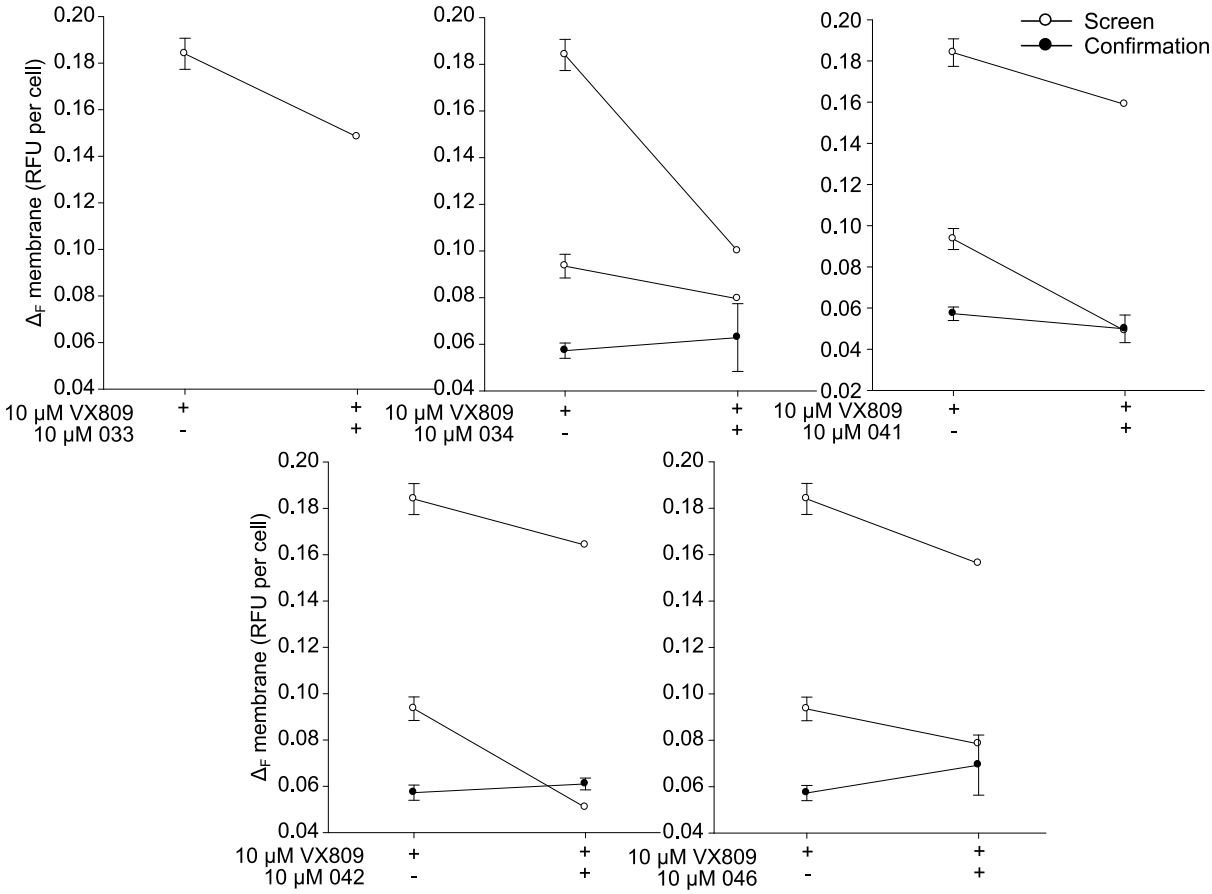


**Figure 5.11 VX-770L hits in ΔF508-CFTR-pHTomato destabilisation assay.** Membrane-localised ΔF508-CFTR following chronic treatment with 10 μM VX-809 ±10 μM of the indicated compound. Incubation carried out at 30°C. Screen data n = 1 (empty symbols). Confirmation data n = 3 (filled symbols). All VX-809 treated controls n = 3. No treatment was found to cause a significant difference. Paired t-test comparison of 10 μM VX-809 ± 10 μM each compound. Compound V-033 ran out so could not be retested.

## 5.8 Discussion

This chapter described pilot screens of compounds with some structural similarity to VX-770, to identify those with potentiator activity on ΔF508-CFTR. This study was prompted by the recent discovery of the negative effects most potentiators, including VX-770, have on ΔF508-CFTR biogenesis. The aim was to identify novel potentiators that do not possess such negative effects.

### 5.8.1 Pilot screen results

The initial pilot screen identified three hit compounds, two of which were confirmed using new compound stock. MS131A and MS134A showed different efficacy on ΔF508-CFTR compared to G551D-CFTR, which confirmed the activity was via potentiation of CFTR, rather than another anion pathway.

Although lower in efficacy and affinity than VX-770, chronic treatment with MS131A did not reduce membrane density of ΔF508-CFTR (Figure 5.6). Unfortunately, this compound does not represent a good drug candidate. The two ester groups are likely to be readily hydrolysed by esterases present in the plasma, in the intestine and in the liver (Oda et al., 2015). The lack of effect of MS131A on membrane-localisation, however, is not caused by hydrolysis of the compound during chronic treatment. This is shown by Figure 5.7, in which MS131A is still functional as a potentiator following 24 h chronic incubation on cells.

To identify improved starting ligands for future screens, LBVS was used to construct libraries based on the structures of VX-770 and MS131A. Both LBVS plates identified a number of hit compounds. During the screening of LBVS compounds for membrane destabilisation effects, some problems with the CFTR-pHTomato assay were identified.

### 5.8.2 ΔF508-CFTR-pHTomato in membrane density screen

ΔF508-CFTR-pHTomato was used in this chapter to measure destabilisation of ΔF508-CFTR following chronic treatment with novel potentiators.

There appears to be some inconsistency in membrane ΔF508-CFTR measurements, demonstrated by chronic treatment with VX-770L potentiators (Figure 5.11). Screen test data points (empty circles) showed a decrease in membrane ΔF508-CFTR. This suggested that potentiator compounds identified in this screen caused similar membrane destabilisation to VX-770. However, the confirmation data points (filled circles) show that upon re-testing, in triplicate, the destabilisation effect was lost.

In Chapter 4 we showed that the ΔF508-CFTR-pHTomato assay can be used to construct concentration-response curves to known corrector compounds (Figure 4.6). The increase in membrane density caused by corrector treatment is sufficiently large to be reliably detected. ΔF508-CFTR-pHTomato also successfully identified ~20% destabilisation by VX-770 (Figure 4.7). In Figure 5.11, membrane density in the presence of novel compounds is compared to VX-809 treated controls. Therefore, quantification of the membrane density of VX-809 treated controls must be extremely reliable, reproducible, and representative of the plate. Additionally, depending on only one reading for each test compound means that this measurement must also be highly reliable. This is especially important when identifying small effects, such as those caused by chronic potentiator treatment. For this small effect to be identified during a screen, such as the one described here, readings must be extremely sensitive and reproducible. It appears, from Figure 5.11, that this is not the case in the ΔF508-CFTR-pHTomato destabilisation screen.

This is reflected by the poor quality control $SSMD_R$ values of some plates, e.g. 1.6 and 1.7. These $SSMD_R$ values were calculated using membrane density of 10 μM VX-809-treated wells (positive controls) and 10 μM VX-809 + 10 μM VX-770-treated wells (negative controls). Low $SSMD_R$ values show that the difference between the positive and negative controls is not great enough to withstand the variability in the measurements. If we expect a similar change in membrane ΔF508-CFTR in the presence of test compounds, then the ΔF508-CFTR-pHTomato assay as a screen is not sensitive or reliable enough to make these measurements in a high-throughput screen format.

Therefore, membrane density measurements in this chapter must be interpreted with caution. Whilst it would appear that MS131A and MS131AL compounds do not destabilise membrane ΔF508-CFTR (Figures 5.6 and 5.9), this should be confirmed by further testing, or using an alternative assay.

### 5.8.3 LBVS results

#### 5.8.3.1 MS131AL library

LBVS was used to construct a new library, with MS131A as a starting ligand. Unfortunately, all hit compounds identified by the MS131AL screen had the same ester structure as MS131A (Figure 5.8). These are not promising drug leads, as it is likely that all these hit compounds will be degraded by esterases before reaching the target CFTR (i.e. in airways).

Had this library produced a ΔF508-CFTR potentiator with a drug-like structure, alongside no negative effects on membrane density, this ligand would have been used for another round of virtual screening, to create a new library. However, given the results shown in this chapter, none of the identified compounds are suitable for continuation of this aspect of the project.

#### 5.8.3.2 VX-770L library

Functional screening of the VX-770L library identified an active compound with a different structural backbone to VX-770 (V-046, Figure 5.10). As discussed above, is not yet clear whether this compound also causes destabilisation of ΔF508-CFTR. Further testing must be carried out with ΔF508-CFTR-pHTomato, or another membrane density assay.

### 5.8.4 Screening summary

The YFP-CFTR screen was successfully used in this chapter to achieve one aim of this thesis: to identify novel ΔF508-CFTR potentiators. It appears that the hits identified in the inital pilot screen, MS131A and MS134A, do not destabilise ΔF508-CFTR (Figure 5.6).

However, testing more compounds in a high-throughput screen protocol for effects on stability of ΔF508-CFTR was not as successful.

Chapter 4 described an assay in which membrane-localised ΔF508-CFTR could be quantified to measure the effect of corrector compounds and chronic potentiator treatment. However, the data discussed in this chapter suggests that this assay is not reliable or reproducible enough to detect small changes in a screen dependent upon a single measurement for each condition, and is also heavily dependent upon controls which represent the sample.

# Chapter 6

# VX-770 mechanism of action

## 6.1 Introduction

Following the publication of the structure of potentiator compound VX-770 in 2009, a handful of studies were published on its mechanism of action. Nevertheless, the mechanism is not yet fully understood. This chapter describes VX-770 mechanism studies, using the YFP-CFTR gating probe.

Two aspects of VX-770 mechanism are investigated: Is phosphorylation of CFTR necessary for VX-770 to potentiate gating? Does VX-770 stabilise the post-hydrolytic $O_2$ state in our system, as has been proposed?

### 6.1.1 Gating of CFTR mutants

A number of CFTR gating mutants which have been extensively studied in the past were used to investigate the mechanism by which VX-770 potentiates gating.

G551D, the CF-associated mutation for which treatment with VX-770 was approved, is located in the signature sequence of NBD1, which contributes to forming one face of the catalytic ATP-binding site 2. Due to this mutation, electrostatic repulsion likely destabilises the NBD dimer with an ATP molecule bound at site 2 (Lin et al., 2014; Corradi et al., 2015). Therefore, ATP-dependent opening is virtually abolished (Drumm et al., 1991; Bompadre et al., 2007). Only ATP-independent gating is retained in these channels (also present in WT-CFTR; Mihalyi et al., 2016), with a $P_o$ ~120-fold lower for G551D-CFTR than for WT-CFTR (Bompadre et al., 2007).

As discussed earlier, the vast majority of WT-CFTR opening events are initiated after ATP binding at site 2, and terminated by hydrolysis of that ATP, whilst a very small proportion of events close via non-hydrolytic closing (Figure 6.1). K464A and D1370N are gating mutations that alter the proportion of events closing via the non-hydrolytic pathway (Csanády et al., 2010).

K464 is located in the Walker A motif of NBD1. The alanine replacement reduces the turnover rate of ATP hydrolysis ~10-fold, and destabilises the pre-hydrolytic dimer (Ramjeesingh et al., 1999; Csanády et al., 2010). Dwell-time distribution analysis suggests

that approximately 80% of K464A-CFTR opening events close via non-hydrolytic closing, thus reducing the proportion of openings entering the post-hydrolytic $O_2$ state (Figure 6.1). A longer interburst duration reduces the $P_o$ to ~25% that of WT-CFTR (in *Xenopus* oocytes) (Vergani et al., 2003; Csanády et al., 2010).

D1370N is located in the Walker B motif of NBD2, at the interface of the catalytic ATP-binding site 2. The corresponding mutation abolishes ATP-hydrolysis in other ABC transporters (Urbatsch et al., 1995; Rai et al., 2006). In CFTR, a prolonged burst duration is observed, presumably reflecting impaired hydrolysis. In oocytes, both the interburst duration and the burst duration are increased, giving a $P_o$ similar to WT-CFTR (Vergani et al., 2003; Csanády et al., 2010). Open dwell-time distribution data are consistent with 100% of opening events terminating via the non-hydrolytic closing pathway, so D1370N-CFTR would not enter the post-hydrolytic $O_2$ state during ATP-dependent gating (Figure 6.1). However, D1370N-CFTR has a higher rate of spontaneous ATP-independent gating than WT-CFTR (Csanády et al., 2010).

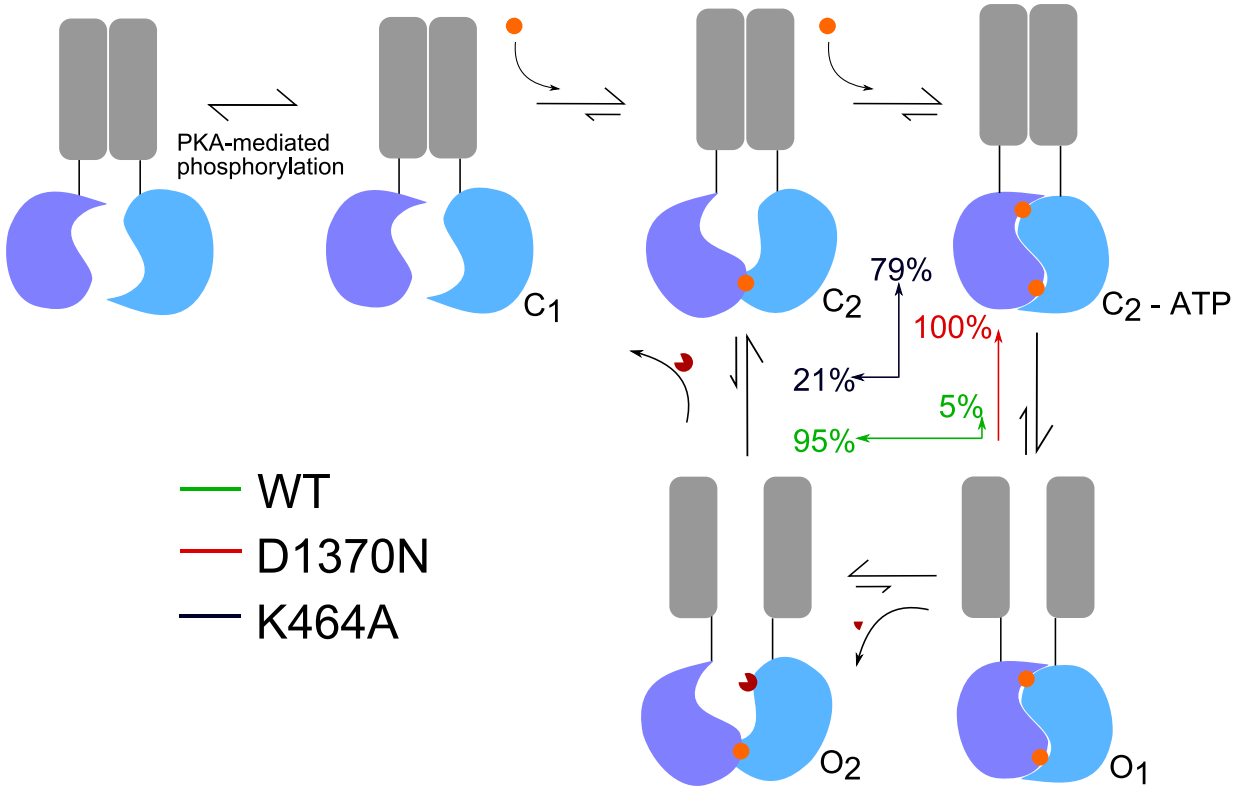


**Figure 6.1 Gating mechanisms of WT-CFTR, K464A-CFTR and D1370N-CFTR.** Modified from Csanády et al., 2010. The majority of WT-CFTR opening events terminate via hydrolysis of ATP (95%). All D1370N-CFTR and 79% of K464A-CFTR opening events terminate via non-hydrolytic closing.

Very little is known about the structure of the post-hydrolytic $O_2$ state, or the state occupied during ATP-independent gating. The fact that ATP inhibits G551D-CFTR gating (Lin et al., 2014; Corradi et al., 2015), suggests that, during G551D-CFTR opening events, the NBDs are tightly dimerised, forming composite ATP binding sites similar to those formed during ATP-dependent opening. In G551D-CFTR, electrostatic repulsion occurs between the gamma phosphates and the negatively charged aspartic acid in the signature sequence. Additionally, a recent study used mutant cycles to show that other mutants undergoing ATP-independent gating also likely adopt an open channel conformation in which the NBDs are tightly dimerised (Mihalyi et al., 2016).

R352C-CFTR is a mutation in which two distinct open states with different conductance levels can be observed. During ATP-dependent gating, the channels follow a preferential C $\rightarrow O_1 \rightarrow O_2 \rightarrow$ C sequence of transitions, suggesting that the $O_2$ state indeed reflects a post-hydrolytic conformation. When tested in the absence of ATP, most R352C-CFTR opening events followed a C $\rightarrow O_2 \rightarrow$ C transition, leading to the suggestion that ATP-independent events, at least in this mutant, utilise an $O_2$-like state (Jih et al., 2012a). However, the difference in conductance results in a minute difference in current between these two states (~0.1 pA on a channel with maximal single-channel current of ~0.3 pA; Jih et al., 2012a), which makes reliable quantification of these events challenging and prone to error.

Whilst it is not clear which state is populated during spontaneous ATP-independent gating, potentiation of G551D-CFTR does suggest that this state of CFTR is stabilised by VX-770.

### 6.1.2 VX-770 mechanism of action

VX-770 increases the $P_o$ of CFTR, via a prolonged mean open time, and an increased opening rate, as seen in single channel patching experiments (Van Goor et al., 2009; Yu et al., 2012; Jih and Hwang, 2013; Kopeikin et al., 2014). VX-770 is able to potentiate purified CFTR in reconstituted liposomes (Eckford et al., 2012), suggesting that the drug binds directly to the CFTR protein. The compound itself is incapable of phosphorylating CFTR (Pyle et al., 2011) and does not induce an increase in intracellular cAMP (Van Goor et al., 2009). In the absence of PKA in the reconstituted liposome system, no VX-770 potentiation of WT-CFTR was detected (Eckford et al., 2012). This led to the hypothesis that VX-770 can act only on phosphorylated CFTR.

VX-770 is capable of potentiating G551D-CFTR, ΔF508-CFTR and WT-CFTR *in vitro* (Van Goor et al., 2009). Therefore, this compound increases the open time of both WT-CFTR, terminated by ATP-hydrolysis (Vergani et al., 2005), and G551D-CFTR, which likely opens via a mechanism independent of ATP binding and hydrolysis (Bompadre et al., 2007).

It has been hypothesised that VX-770 achieves potentiation via stabilisation of the $O_2$ state (Eckford et al., 2012; Jih and Hwang, 2013). However, the evidence supporting this conclusion (mostly involving the conductance mutant R352C-CFTR), is not entirely convincing (Jih and Hwang, 2013). Furthermore, Kopeikin *et al.* (2015), demonstrate that non-hydrolytic closing is slowed by VX-770. Closure of E1371S-CFTR channels used in these experiments does not involve hydrolysis, and so these channels do not enter the post-hydrolytic $O_2$ state. Therefore, slowing the closure of these events suggests stabilisation of $O_1$, rather than $O_2$.

We used the YFP-CFTR probe to attempt to clarify some aspects of the VX-770 mechanism.

## 6.2 VX-770 dependence on phosphorylation

First, the phosphorylation status of CFTR potentiated by VX-770 was investigated.

We were initially alerted to this aspect of the VX-770 mechanism whilst studying the effect of VX-770 pre-treatment on WT-CFTR. Following 1 h pre-incubation with 5 µM VX-770, WT-CFTR showed a high degree of forskolin-independent anion permeability. Upon addition of extracellular $I^-$, rapid quenching occurred immediately (i.e. before addition of forskolin, Figure 6.2A). A simple interpretation consistent with this observation was that potentiation of CFTR by VX-770 was independent of exogenous phosphorylation.

Even without VX-770 pre-incubation, quenching upon acute addition of forskolin + VX-770 did not follow the same kinetics as activation by forskolin alone (Figure 6.2B). The time delay seen upon forskolin addition, before quenching begins, is attributed to the time required for accumulation of cAMP, necessary to activate PKA, which phosphorylates CFTR. This interpretation is supported by the forskolin concentration-dependence of the time delay (Figure 6.3). No time delay was present when WT-CFTR was activated in the presence of VX-770 (Figure 6.2B).

Others have observed a small degree of VX-770 activity in the absence of exogenous phosphorylation, but this has been attributed to basal phosphorylation of CFTR in the specific material investigated (G551D/ΔF508-CFTR human bronchial epithelial cells, HBE cells; Van Goor et al., 2009). That is not likely to be the case in our experiments, as figures in Chapter 3 demonstrate that very little basal phosphorylation of CFTR is detected in our system.

The maximal $I^-$ entry rate following 1 h pre-incubation with 5 µM VX-770 was 263 µM $s^{-1}$ ± 25 µM. It is clear from Figure 6.2A that this rate of $I^-$ entry was achieved by VX-770 alone, before the addition of 1 µM forskolin. In the absence of VX-770, the maximal quenching rate

induced by 1 µM forskolin was 59 µM $s^{-1}$ ± 4 µM (Figure 6.2A). This indicates that, in these conditions, addition of VX-770 in the absence of phosphorylation, resulted in faster anion entry than addition of 1 µM forskolin. This could reflect either a higher $P_o$, or a stronger driving force for $I^-$ entry.

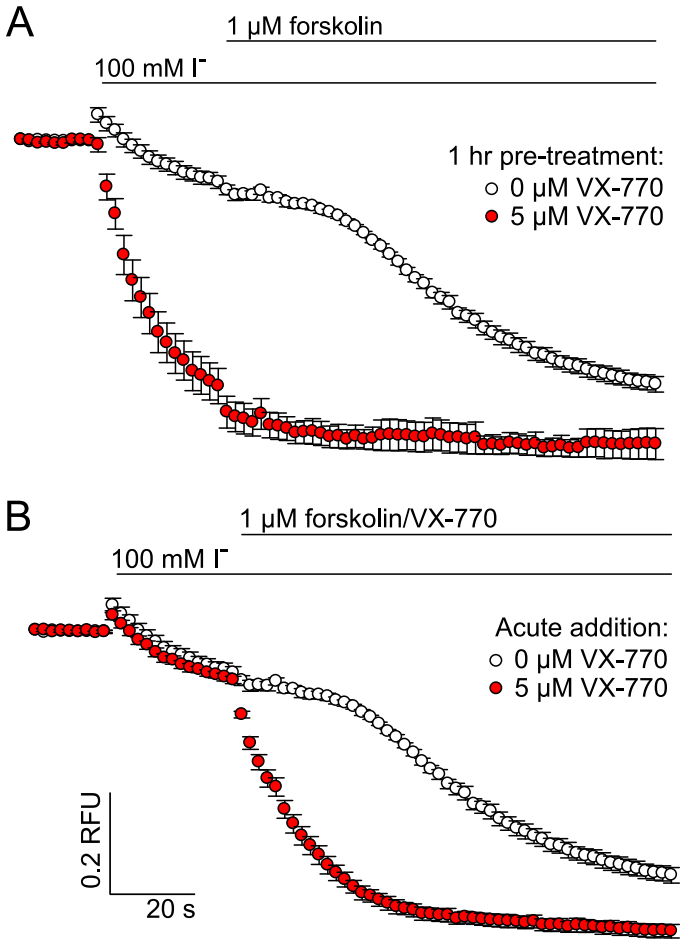


**Figure 6.2 Activation of WT-CFTR by VX-770 occurs independently of exogenous phosphorylation.** A) HEK293 cells expressing YFP-WT-CFTR were pre-incubated with DMSO or 5 µM VX-770 for 1 h, then treated acutely with 1 µM forskolin. B) Cells were not pre-treated. CFTR activation was obtained acutely, via addition of 1 µM forskolin with or without 5 µM VX-770. n = 6.

The quenching kinetics of the two curves in Figure 6.2B are visibly different. Quenching triggered by VX-770 was immediate, whereas that which was brought about by 1 µM forskolin followed a delay, during which time slow quenching occurred. In the absence of VX-770, when forskolin-induced quenching reaches the maximal rate, the driving force for $I^-$ entry will have fallen, because of previous $I^-$ influx into the cytosol. Therefore, no quantitative comparison of CFTR $P_o$ (induced by VX-770, vs. that induced by forskolin), is possible.

In order to minimise the effect of different activation kinetics in the study of VX-770 mechanism, the $I^-$ second addition protocol was used.

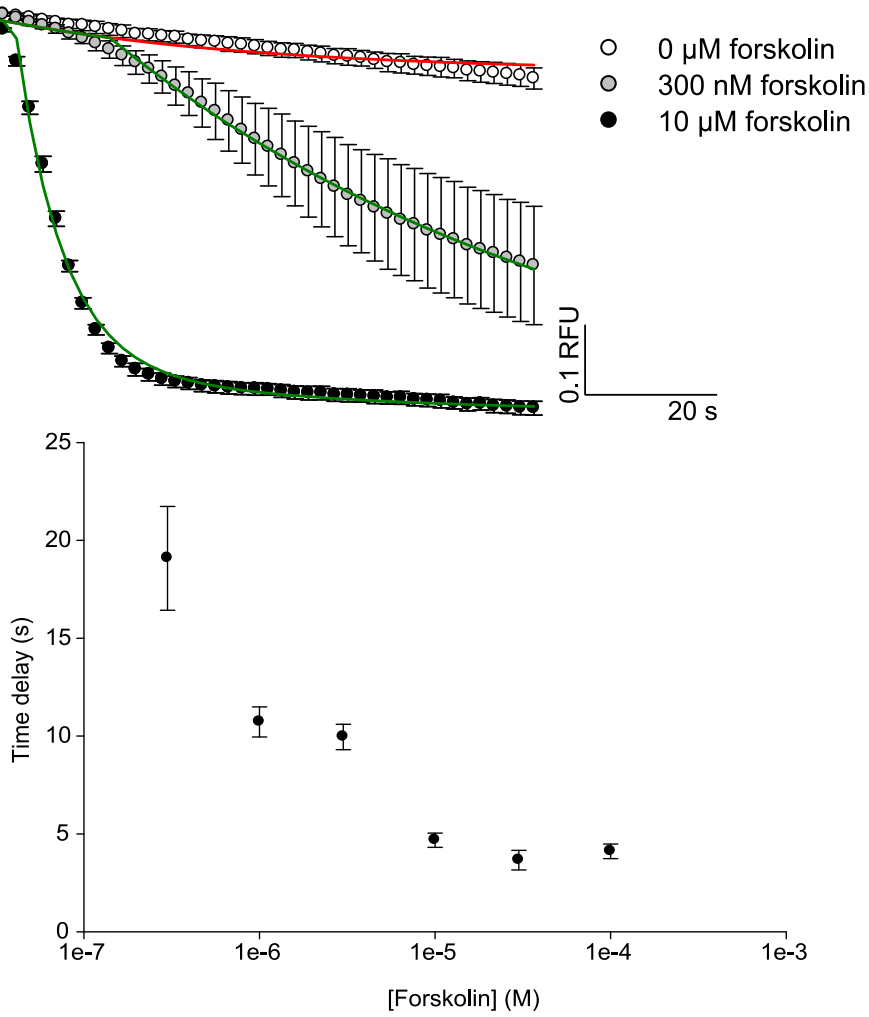


**Figure 6.3 Forskolin concentration-dependence of quenching time delay.** Top: Time delay was estimated by fitting quenching curves to an exponential decay with two components: one slow exponential, common to all curves (red solid line), and one faster exponential starting after a time delay, specific to the forskolin concentration. Green solid lines show representative fits. Bottom: The estimated time delay decreased in the presence of increasing forskolin. Only higher forskolin concentration points can be fit using this method, as two distinct components cannot be identified in low concentration traces. n = 3.

## 6.3 $I^-$ second addition protocol and quantification

In the $I^-$ second addition protocol, CFTR is activated for 90 s in standard buffer (Figure 6.4). During this period, no quenching takes place due to the absence of extracellular $I^-$. After 90 s, CFTR is assumed to have reached steady state activation and 100 mM extracellular $I^-$ is

added. At this time point, the rate at which $I^-$ can enter the cell is dependent only on the level of this activation, and not on the kinetics of activation. Whilst this minimises the effect of different activation kinetics, direct conclusions relating to $P_o$ must remain cautious, as the driving force for $I^-$ entry (also a function of $V_M$ and the $I^-$ concentration gradient), and the proportion of YFP-CFTR located at the membrane, might not be identical in all conditions.

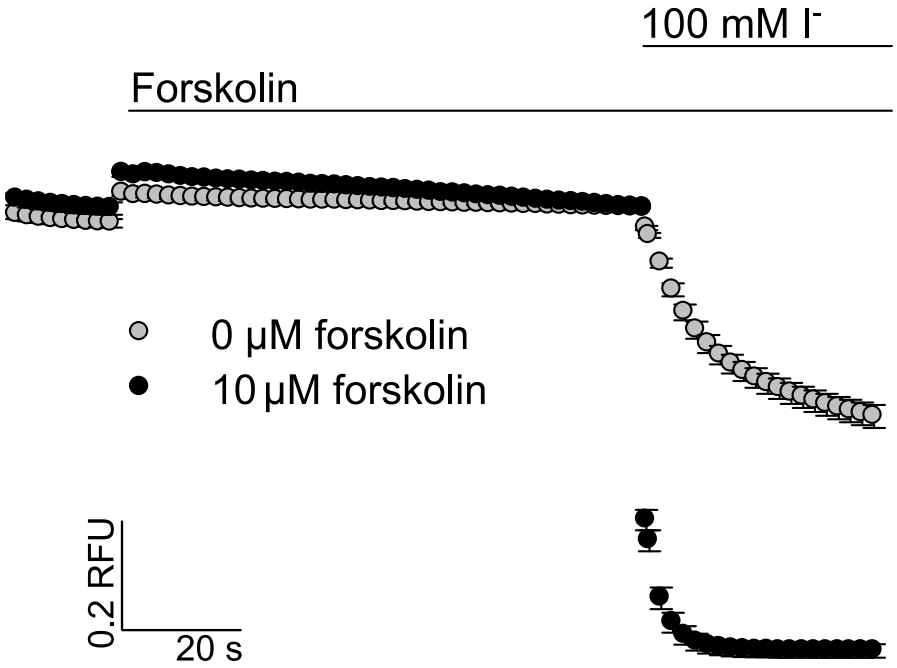


**Figure 6.4 $I^-$ second addition protocol.** Fluorescence traces of YFP-WT-CFTR obtained during the $I^-$ second addition protocol, in response to 0 µM (n = 20) or 10 µM forskolin (n = 9).

This protocol is more susceptible to noise caused by fluid addition artefacts. Any artefact caused by addition of extracellular $I^-$ will occur at the exact time point used to quantify CFTR activity, i.e. the time point following $I^-$ addition, at which the $I^-$ concentration gradient is steepest. A cause of artefact at this time point is the movement of cells upon fluid addition. Steps were taken to minimise the effect of this artefact during image analysis (for more information see Methods, page 42). The relatively small errors on traces in Figure 6.4 suggest that fluid addition artefacts did not greatly affect the readout.

The analysis which was described in Chapter 3 was also applied to this protocol, to construct a forskolin concentration-response curve on WT-CFTR (Figure 6.5A), with the response quantified in terms of rate of change in $[I^-]_i$. The fastest rate of $I^-$ entry observed was again used to quantify CFTR activation, but in this case the maximal rate was observed immediately upon $I^-$ addition to the bath. The $EC_{50}$ for forskolin was similar to that which was

obtained using the $I^-$ first addition protocol (2.1 µM ± 0.4 µM vs. 2.2 µM ± 0.3 µM, Figure 3.7D).

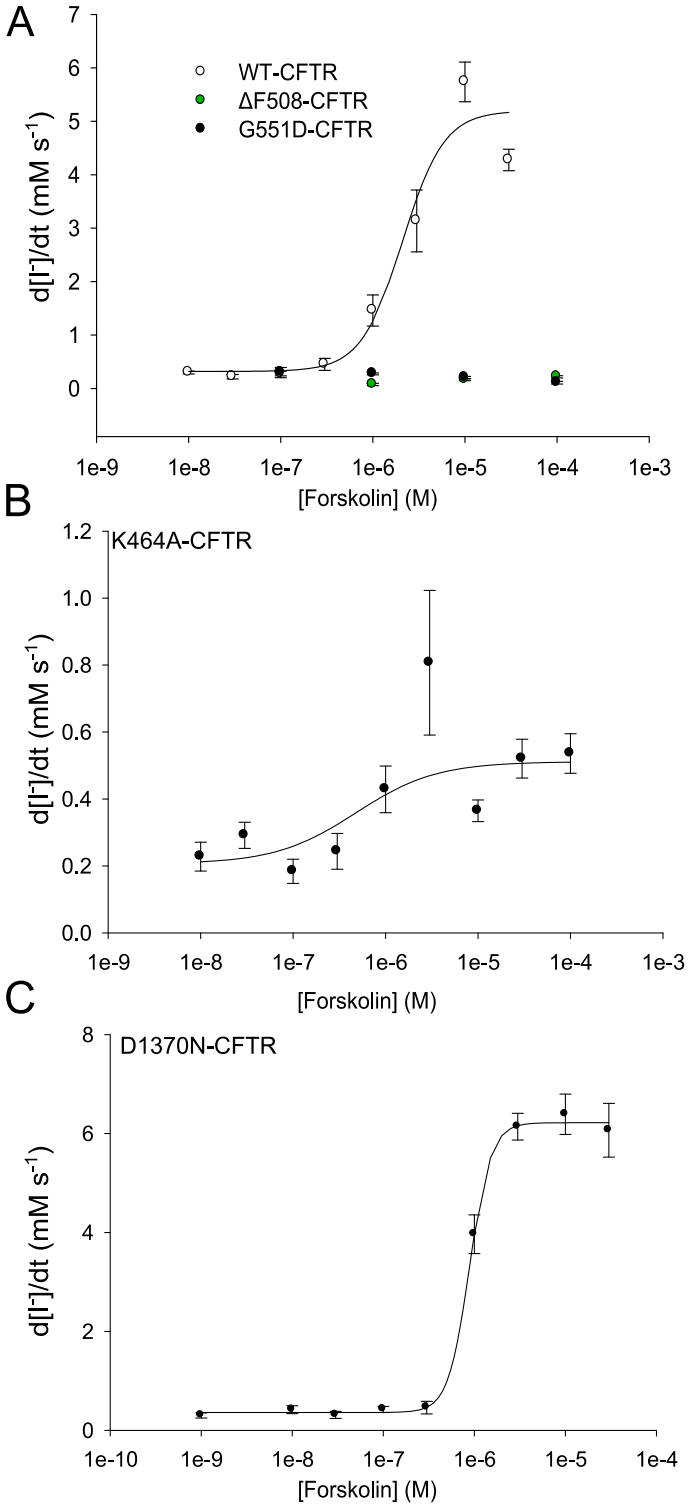


**Figure 6.5 CFTR mutation characterisation.** A) YFP-WT-CFTR forskolin concentration-response curve, quantified using fastest rate of $I^-$ entry ($EC_{50}$ = 2.1 µM ± 0.4, nH = 1.9 ± 0.5). Temperature rescued ΔF508-CFTR and G551D-CFTR did not respond to forskolin. B) K464A $EC_{50}$ = 0.48 µM ± 0.56 µM. nH constrained to 1 for fitting. D) D1370N-CFTR $EC_{50}$ = 0.88 µM ± 0.06 µM, nH = 3.7 ± 1.5. $3 \leq n \leq 12$.

Forskolin-dependence of gating mutants was also characterised using the $I^-$ second addition protocol. Neither ΔF508-CFTR nor G551D-CFTR responded to forskolin alone, due to severe gating defects caused by these mutations (Figure 6.5A).

Maximal forskolin induced ~10-fold smaller anion permeability in K464A-CFTR, compared to WT-CFTR (Figure 6.5B). The published $P_o$ of K464A-CFTR, measured using single channel patching, is ~4-fold smaller than WT-CFTR (Vergani et al., 2003; Csanády et al., 2010). Anion influx in the YFP-CFTR assay is also dependent on the proportion of CFTR that reaches the membrane. A low proportion of channels at the membrane is predicted to result in a slower maximal rate of $I^-$ entry. K464A is also known to cause a trafficking defect (Thibodeau et al., 2010), which could explain the greater reduction in K464A-CFTR activity vs. WT-CFTR in our system, compared to published gating data.

D1370N-CFTR had a slightly higher maximal $I^-$ entry rate than WT-CFTR (6.2 mM $s^{-1}$ ± 0.2 vs. 5.2 mM $s^{-1}$ ± 0.3; Figure 6.5C). $EC_{50}$ values, where obtained, were comparable (0.48 µM, 0.88 µM and 2.1 µM for K464A-CFTR, D3170N-CFTR and WT-CFTR, respectively; Figure 6.4).

All remaining work described in this chapter was carried out using the $I^-$ second addition protocol.

## 6.4 Phosphorylation-independent activation of WT-CFTR by VX-770

Figure 6.2 shows that VX-770 activates WT-CFTR in the absence of exogenous phosphorylation. However, due to the differences in quenching kinetics, the extent of WT-CFTR gating in the presence and absence of phosphorylation could not be quantitatively compared. This comparison was achieved using the $I^-$ second addition protocol.

Figure 6.6 compares concentration-response curves to VX-770, in the absence (left) and presence (right) of phosphorylation by 1 µM forskolin. The maximal steady state activation induced by VX-770 alone was ~15% that which was achieved by VX-770 in the presence of 1 µM forskolin (Figure 6.6; 0.77 mM $s^{-1}$ vs. 5.2 mM $s^{-1}$). In other words, the effect of VX-770 was enhanced ~7-fold by phosphorylation with 1 µM forskolin. A simple interpretation of these results is that VX-770-bound CFTR can gate, albeit at a low $P_o$, in the absence of phosphorylation.

In summary, VX-770 is capable of activating WT-CFTR in the absence of forskolin, in a system in which basal phosphorylation of WT-CFTR is minimal (see Chapter 3, Figures 3.3, 3.11 and Domingue et al., 2014). This has not been seen previously. The anion current

carried by VX-770-activated CFTR in the absence of phosphorylation is low, which could explain how this effect has so far been missed.

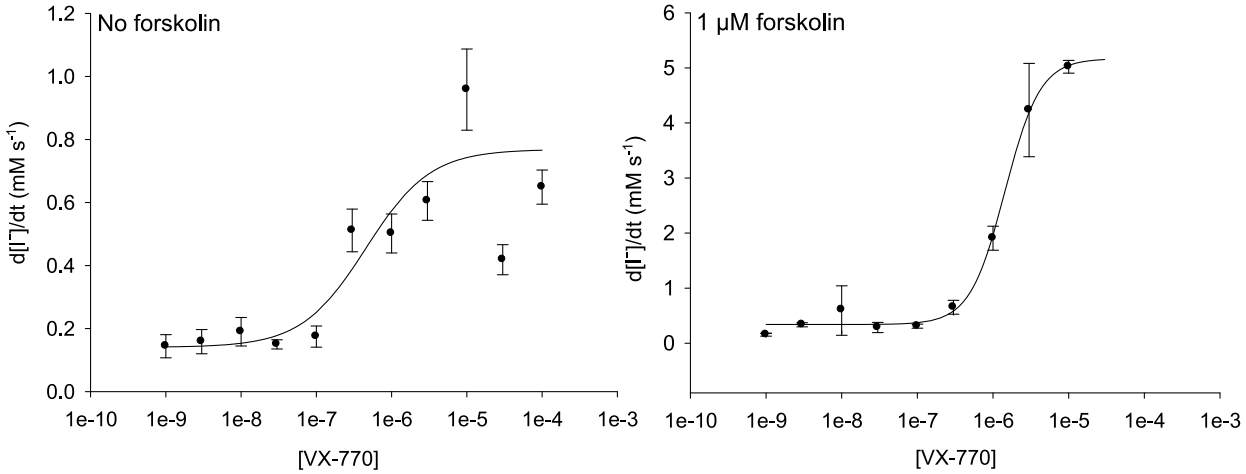


**Figure 6.6 VX-770 concentration response curve, in the absence and presence of exogenous phosphorylation.** Top: YFP-WT-CFTR treated with VX-770 in the absence of forskolin. $EC_{50}$ = 456 nM ± 215 nM, nH = 1.0 ± 0.4, 3 ≤ n ≤ 11. Bottom: In the presence of 1 µM forskolin. $EC_{50}$ = 1.4 µM ± 243 nM, nH = 1.9 ± 0.5, 2 ≤ n ≤ 6. Note the different y-axis scale.

## 6.5 Activation of CFTR gating mutants by VX-770

The second aim of this chapter was to investigate whether the $O_2$ state is potentiated by VX-770, as has been proposed. To achieve this, gating mutants which alter the gating cycle were utilised.

Due to severe gating defects, G551D-CFTR and low temperature rescued ΔF508-CFTR did not respond to forskolin alone (Figure 6. 5A). However, we know from published work and data presented in Chapter 5 that both mutations are potentiated by VX-770 (Van Goor et al., 2009).

We measured the response of G551D-CFTR, ΔF508-CFTR and K464A-CFTR to VX-770, in the presence and absence of 10 µM forskolin (Figure 6.7). In the case of all three mutants, VX-770 increased the response to forskolin ~4-fold. Whilst the potentiation on WT-CFTR appears to be lower, the very high quenching rate observed with 10 µM forskolin + 10 µM VX-770 on WT-CFTR could be saturating the assay. Therefore, VX-770 potentiation of WT-CFTR was measured in the presence of a lower concentration of forskolin, to enable accurate estimation of the fold increase caused by VX-770. In these conditions, VX-770 again increased the response to forskolin ~4-fold. In the same conditions, potentiation of K464A-CFTR by VX-770 is undetectable (Figure 6.8).

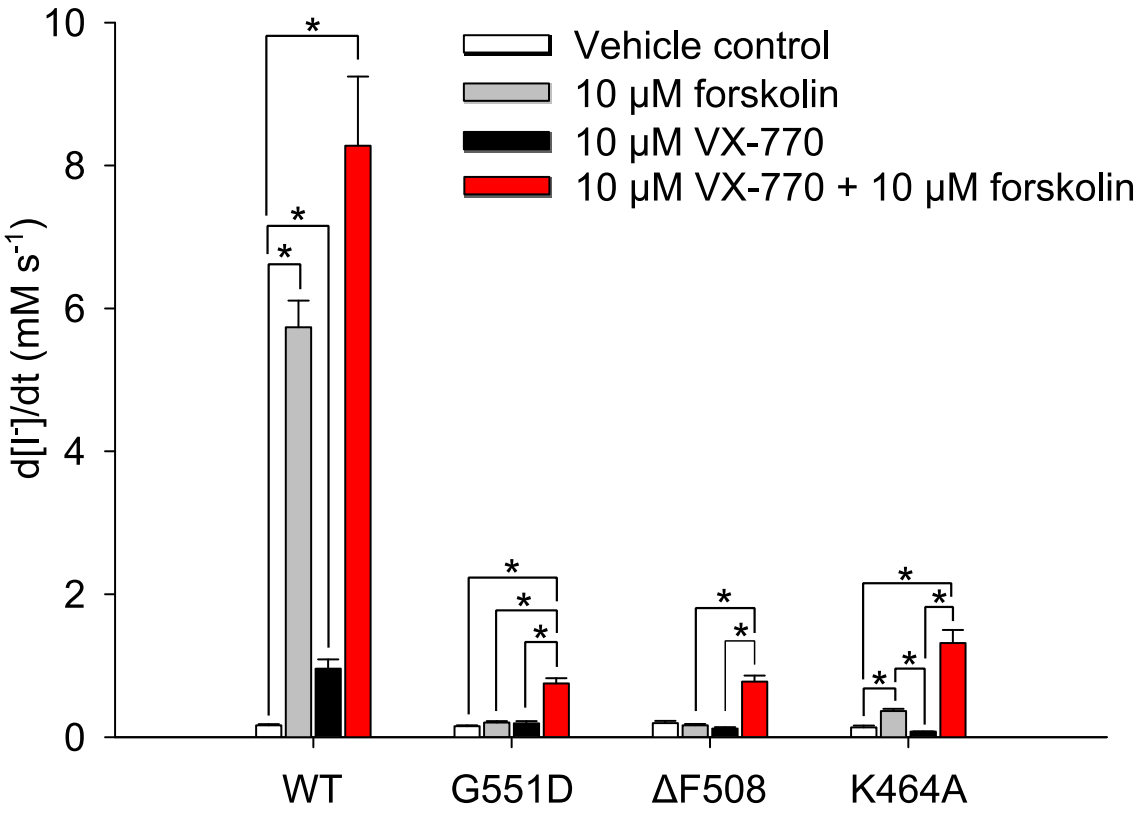


**Figure 6.7 Phosphorylation-dependence activity of VX-770 on WT-CFTR and mutants.** Cells were treated with 10 μM forskolin, 10 μM VX-770 or 10 μM VX-770 + 10 μM forskolin. * = $p < 0.05$. Conditions compared within a mutation using Kruskal-Wallis one way ANOVA and post-hoc Dunn's test. $3 \leq n \leq 29$.

To avoid saturation of the assay whilst measuring D1370N-CFTR quenching (higher anion permeability that WT-CFTR; Figure 6.5), an even lower concentration of forskolin was used to measure VX-770 activation of D1370N-CFTR (Figure 6.9). 1 μM VX-770 increased the response to 300 nM forskolin ~2.5-fold. Upon lowering the phosphorylation status of WT-CFTR, the effect of VX-770 was reduced to an undetectable level (Figure 6.9).

In summary, regardless of the gating mutant in question, 10 μM VX-770 increased the response to forskolin ~4-fold, and 1 μM forskolin, induced a 2.5-fold increase in D1370N-CFTR. Therefore, VX-770 potentiates to a similar degree, whether the channel displays no ATP-dependent gating (G551D-CFTR), or reduced time spent in the $O_2$ state (K464A-CFTR and D1370N-CFTR).

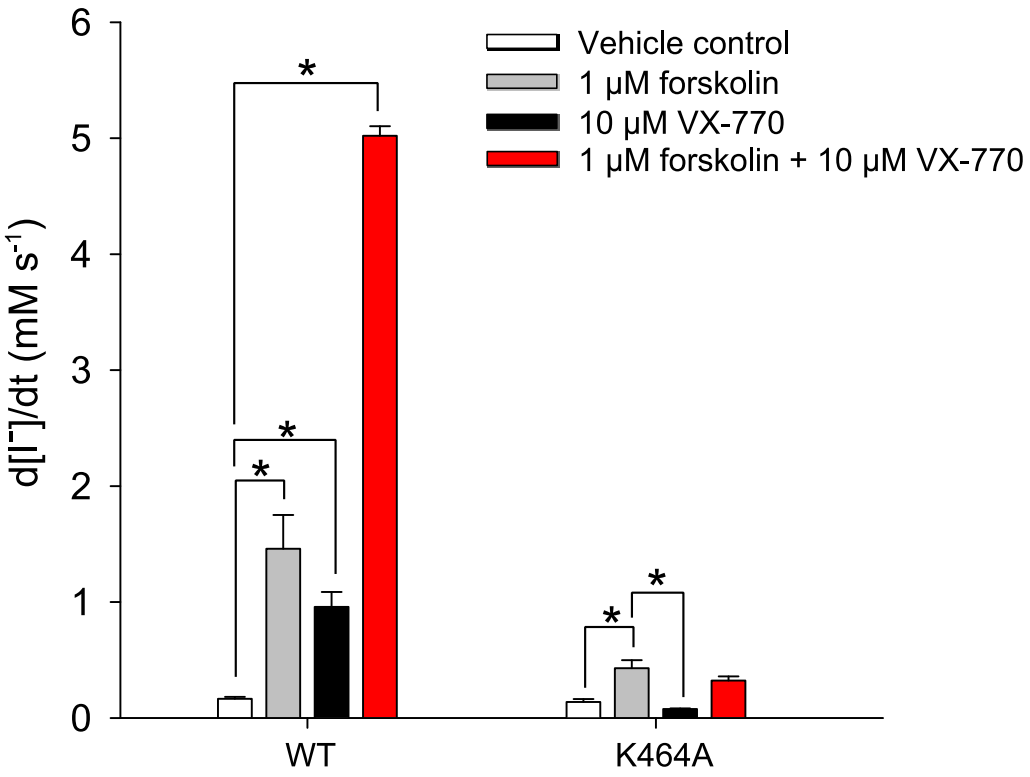


**Figure 6.8 Potentiation of K464A-CFTR by VX-770.** WT-CFTR is potentiated by 10 μM VX-770 in the presence of 1 μM forskolin, whilst potentiation of K464A-CFTR is undetectable. * p < 0.001. WT-CFTR forskolin n = 10, + VX-770 n = 6, K464A-CFTR n = 3.

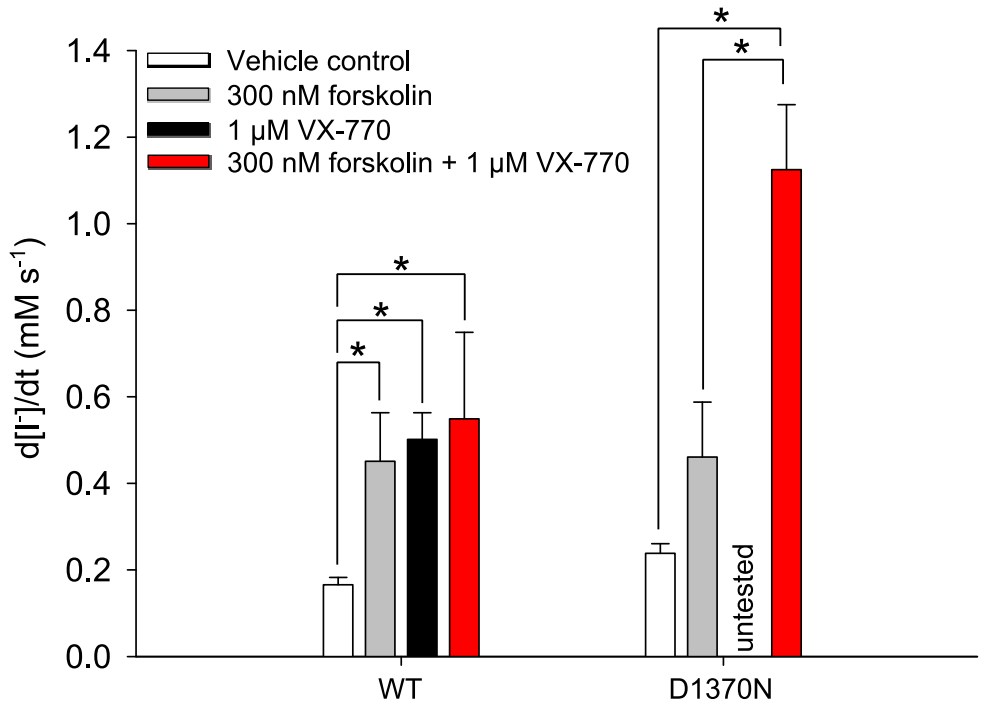


**Figure 6.9 Potentiation of D1370N-CFTR by VX-770.** D1370N-CFTR is potentiated by 1 μM VX-770 in the presence of 300 nM forskolin. The effect on WT-CFTR is lost at low phosphorylation level. WT-CFTR 300 nM forskolin n = 15, + 1 μM VX-770 n = 3. D1370N-CFTR n = 6. * p < 0.05, from Kruskal-Wallis ANOVA on ranks and post-hoc Dunn's test.

## 6.6 Discussion

### 6.6.1 Phosphorylation is not a pre-requisite for activation by VX-770

A study published in 2012 showed that VX-770 did not potentiate WT-CFTR which had not been pre-phosphorylated prior to reconstitution in liposomes (Eckford et al., 2012). It has since been assumed that phosphorylation is a pre-requisite for VX-770 activity. Experiments of pre-treatment of WT-CFTR with VX-770 led us to believe that this was not the case (Figure 6.2).

It seems unlikely that the increased quenching seen in the absence of forskolin, following 1 h VX-770 pre-incubation, could be entirely via potentiation of basally phosphorylated CFTR, since basal phosphorylation of WT-CFTR in HEK293 cells is minimal (WT-CFTR vs. G551D-CFTR in Chapter 3 and Figure 6.10). In addition it has been shown that VX-770 incubation does not increase accumulation of cAMP, or directly induce phosphorylation of CFTR in other systems (Van Goor et al., 2009; Pyle et al., 2011).

Activation in the absence of phosphorylation suggests that phosphorylation is not necessarily a pre-requisite for WT-CFTR gating. Phosphorylation of the R-domain is thought to relieve an inhibition in the protein, allowing gating when the NBDs dimerise (Csanády et al., 2000). However, it has been shown that in some conditions CFTR can be activated without pre-phosphorylation. With all phosphorylation sites mutated to alanine, a mutant CFTR can be activated to near WT-CFTR levels by using deoxy-ATP as a ligand (Aleksandrov et al., 2002). Another small molecule CFTR activator, $C_{act}$-A1, activates CFTR without the need for exogenous phosphorylation (Namkung et al., 2013). Interestingly, VX-770 has been shown to potentiate ΔF508-CFTR in the presence of $C_{act}$-A1 in fisher rat thyroid cells (Namkung et al., 2013). Therefore, it is possible to circumvent the need for CFTR phosphorylation, and VX-770 is functional in these circumstances.

To investigate the phosphorylation dependence of VX-770 activity on gating mutants, mutants were treated with the potentiator in the absence of forskolin. G551D-CFTR, ΔF508-CFTR and K464A-CFTR were not potentiated by VX-770 in the absence of exogenous phosphorylation (Figure 6.7, compare white and black bars). It is possible that the low anion permeability state achieved by VX-770 in the absence of phosphorylation is not detectable in mutants which already have a low $P_o$.

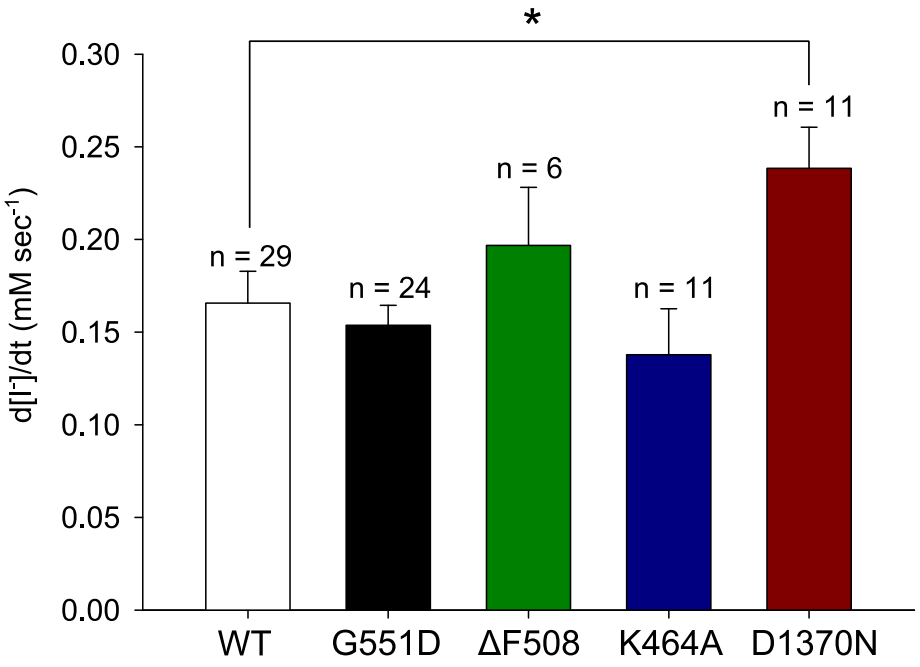


**Figure 6.10 $I^-$ entry rates of CFTR mutations, in the absence of exogenous phosphorylation.** * p = 0.02, mutations tested for significance vs. WT-CFTR control using Kruskal-Wallis one way ANOVA and post-hoc Dunn's test.

We have shown that phosphorylation enhances the effect of VX-770 on WT-CFTR (Figure 6.6). Figures 6.7 and 6.8 clearly show a synergistic effect of forskolin and VX-770, compared to the effects when used separately. This suggests that phosphorylation and VX-770 increase CFTR $P_o$ via different pathways. At low phosphorylation levels (for example K464A-CFTR in Figure 6.8 and WT-CFTR in Figure 6.9), this synergistic activity is lost. This suggests that a certain level of phosphorylation, different depending upon the $P_o$, must be achieved in order for synergistic activity of the two to be seen.

To confirm effectiveness of VX-770 on unphosphorylated WT-CFTR, it would be interesting to patch WT-CFTR channels in the absence of PKA phosphorylation, verifying activity by applying ATP, without and with VX-770.

### 6.6.2 Stabilisation of the $O_2$ state?

It has been proposed that VX-770 potentiates CFTR via stabilisation of the $O_2$ state (Jih and Hwang, 2013). This is understood to potentiate WT-CFTR during ATP-dependent gating by stabilisation of the post-hydrolytic state, and G551D-CFTR during ATP-independent gating. However, as discussed above, it is not known which state is occupied during ATP-independent gating. Additionally, it has been shown that VX-770 slows closure of E1371S-CFTR channels, presumably by stabilisation of the $O_1$ state during ATP-dependent gating

(Kopeikin et al., 2014). In order to study this mechanism using YFP-CFTR, CFTR mutations which alter the gating cycle were utilised.

K464A is a mutation which destabilises the pre-hydrolytic NBD dimer to increase the rate of non-hydrolytic closing. The proportion of opening events which close via the $O_2$ state is approximately 20%. D1370N likely prevents ATP-hydrolysis at the catalytic site, consistent with all ATP-dependent opening events closing via non-hydrolytic closing (Figure 6.1) (Csanády et al., 2010). Additionally, studies in particular conditions in which differential buffer susceptibility resulted in different conductance levels being detected in pre- and post-hydrolytic open channels, showed that D1370N-CFTR only resides in the $O_1$ state (Gunderson and Kopito, 1995).

It was hypothesised that, should VX-770 stabilise the $O_2$ state, K464A-CFTR would be potentiated to a lesser extent than WT-CFTR, simply because fewer opening events would reach $O_2$. Similarly, it was expected that the extent of potentiation of D1370N-CFTR would be far less than of WT-CFTR, as this channel has been shown to only reside in $O_1$ (Gunderson and Kopito, 1995; Csanády et al., 2010). Unexpectedly, the fold increase in K464A-CFTR gating caused by 10 µM VX-770 was similar to WT-CFTR (~4-fold, Figures 6.7 and 6.8), and D1370N-CFTR gating was increased ~2.5-fold by the lower concentration of 1 µM VX-770 (Figure 6.9).

This data suggests that stabilisation of the $O_2$ state is not the main mechanism by which VX-770 potentiates gating, as it is difficult to explain this level of potentiation in mutants that rarely enter the $O_2$ state. Even if D1370N-CFTR enters the $O_2$ state during ATP-independent gating (which occurs more than for WT-CFTR; Csanády et al., 2010), the extent of potentiation is too great to be entirely via stabilisation of these events (Figure 6.9). Equally in the case of K464A-CFTR – only one fifth of opening events enter $O_2$, yet potentiation is similar to that of WT-CFTR, in which 95% of opening events enter $O_2$ (Csanády et al., 2010).

The simplest explanation of this data is that VX-770 stabilises the $O_1$ state during both ATP-dependent and ATP-independent gating. This would explain the similar level of potentiation of WT-CFTR, G551D-CFTR, which only gates via ATP-independent opening events, and D1370N-CFTR and K464A-CFTR, which rarely enter the $O_2$ state.

### 6.6.3 Mechanism summary

In summary, combining the YFP-CFTR assay with known gating mutations provides a way of testing hypotheses and obtaining an initial assessment of compound mechanism of action.

Further mechanistic insights can be gained only by patch clamp. To test our first hypothesis, that WT-CFTR does not require phosphorylation for VX-770 to increase anion permeability, we would need to patch WT-CFTR in the absence of PKA. Our second hypothesis, that VX-770 stabilises the $O_1$ state during ATP-dependent and ATP-independent gating, has, to an extent, already been tested using E1371S-CFTR patching by Kopeikin *et al.* (2014), although different interpretations of those data were given. Similar experiments, in which the closing rate of D1370N-CFTR opened in the presence of ATP, was measured, could provide further evidence for stabilisation of the $O_1$ state.

This chapter describes the investigation of the mechanism by which VX-770 potentiates CFTR gating. Using a cell free assay it has been shown that phosphorylation is a pre-requisite for activation by VX-770 (Eckford et al., 2012). Data presented in this chapter shows that this is not necessarily the case, and that phosphorylation and VX-770 potentiate gating of CFTR via distinct mechanisms. Other data presented in this chapter suggests that the proposed mechanism of action for VX-770, i.e. stabilisation of the $O_2$ state, is unlikely.

# Chapter 7

# Conclusions

The aims of this research, to optimise two fluorescence assays for use in compound screening and mechanism studies, were set out at the start of this thesis. Below, I discuss how these aims were met, and summarise future research directions.

## 7.1 The search for novel ΔF508-CFTR potentiators

We have demonstrated the use of the YFP-CFTR functional assay to screen compounds for ΔF508-CFTR potentiator activity. The pilot screen identified two novel compounds, with activity ~50% of VX-770 positive controls.

It is likely that destabilisation of membrane ΔF508-CFTR by chronic VX-770 treatment contributed to the relatively small improvement in $FEV_1$ seen in clinical trials of Orkambi (Cholon et al., 2014; Veit et al., 2014; Wainwright et al., 2015). The pilot screen hit compounds, MS131A and MS134A, had no negative effect on ΔF508-CFTR membrane-localisation or internal expression, measured using ΔF508-CFTR-pHTomato (Figure 5.6).

Based on these results, we carried out further compound screening, using LBVS for library selection. Two libraries were assembled; using either VX-770 or MS131A as starting ligands. Both screens identified a number of further potentiators, the majority of which were very similar to the starting ligand. However, one compound with a very different structure was identified in the VX-770L library: compound V-046.

The identification of a structurally different compound supports the use of LBVS to identify novel potentiators with different scaffolds. The next step in this iterative process will be to create a library using V-046 as a starting ligand. It is possible that compounds based on this structure could maintain potentiator activity, but lose the negative effects on stability. Once more compounds have been tested for both effects it will be possible to draw some conclusions on structure-activity relationship.

## 7.2 VX-770 potentiator mechanism

As well as compound screening, YFP-CFTR was used to study the mechanism of action by which VX-770 potentiates CFTR.

We showed, for the first time, that WT-CFTR does not require phosphorylation in order for VX-770 to exert potentiator effects. The anion flux is small in the absence of phosphorylation, and was not detectable if basal $P_o$ was reduced, as in many gating mutants.

Gating mutants were employed to study whether stabilisation of the post-hydrolytic $O_2$ state is a likely mechanism of potentiation by VX-770. Well-studied mutations and dose-response curves linking forskolin concentration to $I^-$ permeation were used as tools to investigate which gating steps might be affected by VX-770 binding. The K464A and D1370N mutations reduce the proportion of gating events which terminate via hydrolysis, thus reducing the amount of time spent in the $O_2$ state. Unexpectedly, potentiation of K464A-CFTR and D1370N-CFTR was not reduced compared to WT-CFTR (Figures 6.7 to 6.9). This work suggests that stabilisation of the $O_2$ state is an unlikely mechanism for VX-770. Whilst YFP-CFTR studies can be used to test an initial hypothesis, patch clamping is required to obtain further insight into mechanism.

## 7.3 Two CFTR-YFP protocols

This thesis described the use of two CFTR-YFP protocols: $I^-$ first addition (Chapter 3) and $I^-$ second addition (Chapter 6). The advantages and drawbacks of both protocols are summarised here.

The fastest rate of $I^-$ entry into the cells depends on CFTR $P_o$, the proportion of CFTR-YFP at the membrane, and the driving force for $I^-$ entry. How the driving force affects the readout is the main difference between the two assays. In the $I^-$ first addition protocol, the driving force for $I^-$ entry changes during activation of CFTR. A treatment that is slow to reach steady state activation will reach such activation only once $I^-$ influx into the cytosol has reduced the driving force. This can be seen in Figure 6.2. Forskolin-only treated cells activate slower than VX-770 treated cells, resulting in a slower maximal $I^-$ entry rate.

This change in driving force over time is overcome using the $I^-$ second addition protocol. The maximal rate of $I^-$ entry occurs upon addition of $I^-$ (Figure 6.4A). At this point, the driving force for $I^-$ entry will be the same, irrespective of the rate of CFTR activation. Two assumptions are made in using $I^-$ second addition protocol assay readouts to compare CFTR activity in two separate wells: the presence of a similar transmembrane electrochemical gradient for $I^-$, and that a maximal $P_o$ has been reached. In most conditions these assumptions are likely to be true.

In summary, the assay to use depends on the experiment. The $I^-$ first addition protocol is less susceptible to noise caused by fluid addition, and gives qualitative information about the rate of CFTR activation. However, quantitative comparisons between conditions/mutants can be complicated by differences in activation rate. The $I^-$ second addition protocol is less influenced by CFTR activation rate, so can be used to quantitatively compare situations in which the rate of CFTR activation is different.

## 7.4 Future work

### 7.4.1 CFTR-pHTomato assay for ΔF508-CFTR corrector screens

This thesis focused on identification of novel ΔF508-CFTR potentiators. However, successful treatment of ΔF508-CF will likely also require corrector compounds, like VX-809. Most corrector screens in other labs have been carried out using functional assays. Due to the severe gating defect associated with ΔF508-CFTR, it would not be possible to detect correction in a functional screen without the use of a potentiator. This means compounds that stabilise a form of ΔF508-CFTR which cannot be activated by the potentiator in use, will not be detected as correctors. In using a functional assay as a corrector screen, it is also impossible to distinguish between effects on trafficking and function, resulting in some compounds with potential beneficial effects being missed.

Both the trafficking and gating defects are caused by aberrant folding, so it is possible that a corrector compound which promotes native folding would also restore some level of function to ΔF508-CFTR. Searching for compounds with this characteristic would provide information on how channel folding is related to function, as well as moving towards monotherapy for ΔF508-CF patients.

Investigating these compound effects using the two assays described will allow us to discriminate between effects on ion channel gating and on membrane-localisation, allowing us a better understanding of both.

Figure 7.1A shows how this discrimination is possible. Untreated ΔF508-CFTR has low membrane density and low function compared to WT-CFTR. 30°C incubation restores some membrane density, but does not increase ΔF508-CFTR function. VX-809 incubation has an even greater effect on membrane density, and also restores a small amount of function to ΔF508-CFTR. This suggests that VX-809 stabilises a form of ΔF508-CFTR that has some rescued function, without the need for potentiators. This effect of VX-809 has also been shown by other groups (Eckford et al., 2014).

To test this method of discrimination using novel compounds, LBVS was used to construct a pilot library of compounds based on VX-809. The functional and membrane density assays were both carried out following chronic treatment (24 h), alongside low temperature correction (Figure 7.1B).

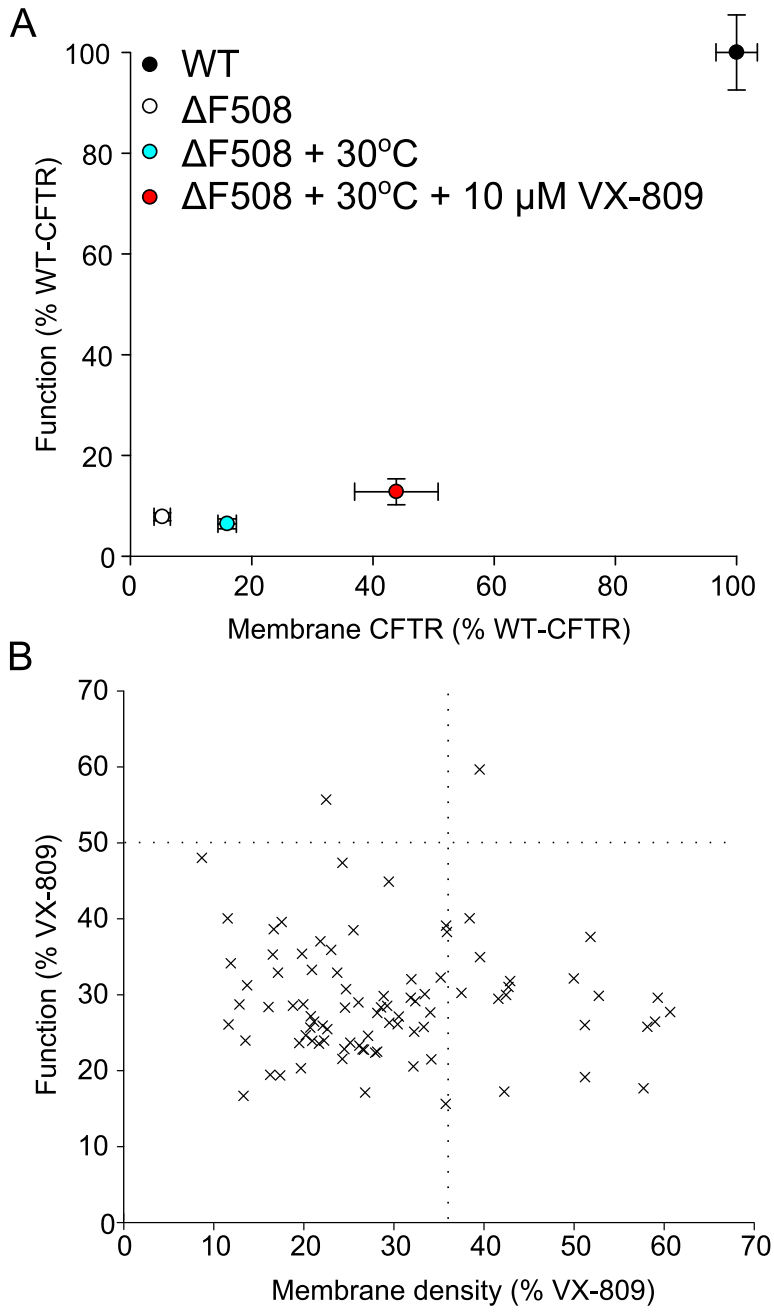


**Figure 7.1 Function vs. membrane CFTR in ΔF508-CFTR corrector screens.** A) Function and membrane CFTR of controls, expressed as a percentage of WT-CFTR. Plots are mean ± SEM, 3 ≤ n ≤ 6. B) Screening of compound library constructed using LBVS with VX-809 as a query ligand. Each point is the mean of an individual compound, tested twice in each assay. Dotted lines indicate control values obtained for untreated, temperature rescued ΔF508-CFTR. Data points expressed as percentage of ΔF508-CFTR treated with 10 μM VX-809. Both screens carried out following 24 h low temperature incubation.

Unfortunately, all of the VX-809 like (VX-809L) library compounds showed similar, or even lower, activity and membrane expression than temperature rescued ΔF508-CFTR (Figure 7.1B, ΔF508-CFTR indicated by the dotted lines).

A potential problem with using the CFTR-pHTomato assay to screen compound libraries is the strength of the assay for high-throughput screening. As discussed in Chapter 5, $SSMD_R$ is a measure of the suitability of an assay for high-throughput screening. The $SSMD_R$ scores for the two VX-809L screen repeats were 1.5 and 6.5. An $SSMD_R$ score of 1.5 indicates a plate of poor quality (Table 5.1). It is likely that data from this plate would not be used in a high-throughput screen. Again, although the effect of corrector compounds on membrane density is greater than the effect of potentiator compounds, it seems that the reliability of the CFTR-pHTomato assay is insufficient to be used in high-throughput screening.

$SSMD_R$ is calculated using the difference between positive and negative controls, penalised by the variability in the difference. Therefore, causes of a low $SSMD_R$ are a poor response to the positive control, or large variability in the assay. As has already been mentioned, the CFTR-pHTomato assay does suffer from high variability, which contributed to the low $SSMD_R$ score. At this time, there is no better positive control available for corrector screens.

Ultimately, for the CFTR-pHTomato assay to be used in high-content screening to identify small effects of destabilisation or correctors with limited efficacy, reliability of the assay must be improved.

### 7.4.2 YFP-CFTR for CFTR membrane localisation studies

Initially, it was thought that YFP-CFTR could be used for localisation studies as well as functional tests. However, heterogeneity in the cells, and a low fluorescence signal made automated quantification of CFTR localisation impossible (see Section 3.10). For these reasons, the CFTR-pHTomato assay was developed.

The CFTR-pHTomato assay is capable of measuring membrane-localised and internal CFTR. For the reasons described above, it is useful to quantify localisation independent of function. However, measuring localisation and function in different assays means both YFP-CFTR and CFTR-pHTomato assays must be run if both parameters are to be quantified (for example in Figure 7.1). Measuring both parameters, independently, but on the same cells, would save time and resources, as well as give more accurate, informative, readings.

A future project will be focussed on using YFP-CFTR for a CFTR localisation assay. To achieve this, YFP-CFTR will be expressed in a pIRES2-mCherry plasmid. The mCherry signal will act as a control for total amount of protein, similar to the function of eGFP in the

CFTR-pHTomato assay. mCherry expression in the cytosol will also allow for automated algorithms capable of accurately recognising cells, and localising the cell membrane. High resolution, high magnification images will allow quantification of membrane and internal YFP-CFTR. Presence of the mCherry signal will aid in identifying the cell membrane, which was a problem suffered in using the YFP-CFTR signal only (Figure 3.14). The same cell samples will also be used in the YFP-CFTR functional screen. By using estimates of the number of channels present at the membrane, it will be possible to better infer $P_o$ of these channels from measurements of YFP quenching rate.

When optimised, this high-content assay will provide similar information to whole cell recordings, but with the added benefit of informing on channel cellular distribution. For example, in Chapter 6, the function of K464A-CFTR was deemed to be ~10-fold lower than WT-CFTR (Figure 6.5). However, K464A is also known to cause a trafficking defect (Thibodeau et al., 2010). A lower proportion of CFTR at the membrane is predicted to decrease the maximal quenching rate. Using the proposed YFP-CFTR/mCherry assay, the effect of the change in channel distribution could be measured, and accounted for, resulting in a more accurate quantification of CFTR activity.

# Appendix

## A.1 LBVS plate data in CFTR-pHTomato screen

As described in Chapters 4 and 5, the CFTR-pHTomato assay is susceptible to variation. Data in Chapter 5 showed that the assay was not reliable enough to measure small changes in membrane density, in a high-throughput screen protocol. Here, we show CFTR-pHTomato data from the entire LBVS libraries, unlike Chapter 5 in which only hit compounds were presented. In examining the full plates, including controls, we have identified a source of irregularities in the CFTR-pHTomato screen.

MS131AL compounds had little effect on membrane-localised or internal ΔF508-CFTR (Figure A1.A, all compounds ~100% compared to VX-809 treated controls). However, surprisingly, the majority of compounds in the VX-770L library appeared to increase internal ΔF508-CFTR (Figure A1.B).

Other have shown that chronic incubation with VX-770 causes a decrease in immature ΔF508-CFTR, by increasing cotranslational degradation or decreasing translation (Cholon et al., 2014; Veit et al., 2014). In our assay, we see no significant change in internal ΔF508-CFTR expression following chronic VX-770 treatment (Chapter 4, Figure 4.7).

An increase in internal ΔF508-CFTR in our VX-770L screen could suggest an effect on biosynthesis, different to that of VX-770. For example, stabilisation of a conformation that is unable to be exported from the ER, but which does not undergo faster degradation, causing an accumulation of internal ΔF508-CFTR.

Alternatively, these compounds could be having off-target effects on a chaperone protein, preventing export from the ER. Although there is strong evidence that VX-770 binds directly to CFTR (Eckford et al., 2012; Jih and Hwang, 2013) and these compounds are based on the VX-770 structure, we have no evidence of direct binding of these compounds.

There is a third, more likely, explanation. All compounds in Figure A1 are normalised to within-plate controls (treated with 10 µM VX-809 only), to allow comparison of fluorescence values between different plates. Upon inspection of the within-plate controls, both membrane-localised and internal measurements appear normal (Figure A2.A and A2.B, left), i.e. 10 µM VX-770 decreased membrane-localised ΔF508-CFTR, and had no significant effect on internal ΔF508-CFTR.

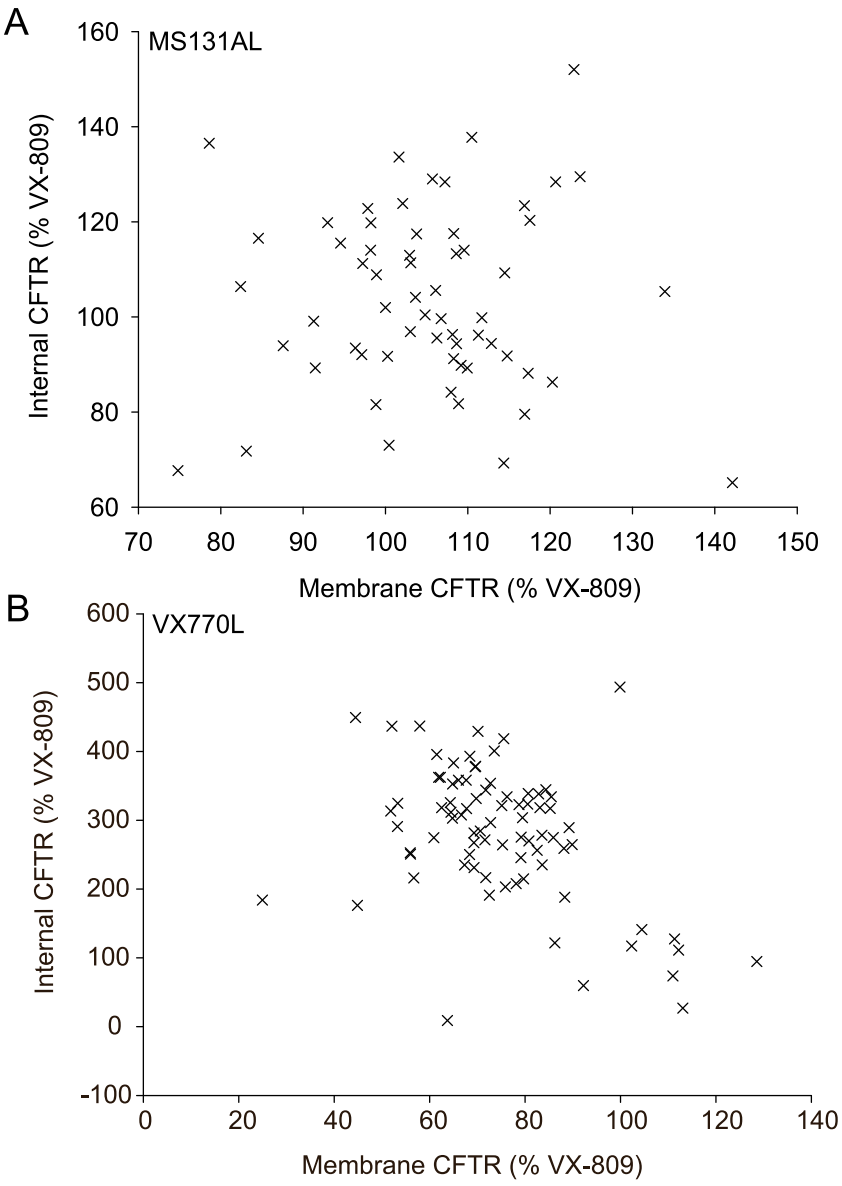


**Figure A1 Internal and membrane ΔF508-CFTR from LBVS plates.** A) MS131AL and B) VX-770L libraries screened for destabilisation effects using ΔF508-CFTR-pHTomato. Membrane-localisation corrected using 24 h 10 µM VX-809 and low temperature incubation. Membrane and internal ΔF508-CFTR normalised to VX-809 treated wells (i.e. 100% = no change caused by 24 h compound treatment).

Comparison of membrane-localised ΔF508-CFTR controls with data from the entire plate shows the expected pattern, i.e. values of within-plate controls correlate to values in the rest of the plate, and are within the same range (Figure A2.A, compare left and right).

However, comparison of the within-plate internal controls with the full plate data reveals an inconsistency. Internal ΔF508-CFTR within-plate controls on VX-770L plates show much lower values than the respective plate data (Figure A2.B, compare triangles on left to triangles on right). When compound results are normalised to (abnormally low) VX-809-

treated wells, this gives the illusion that all VX-770L compounds have caused an increase in internal ΔF508-CFTR. It seems more likely that abnormally low internal ΔF508-CFTR readings from VX-809 treated controls is the cause of the results seen in Figure A1.B, rather than a genuine ~3-fold increase in internal ΔF508-CFTR.

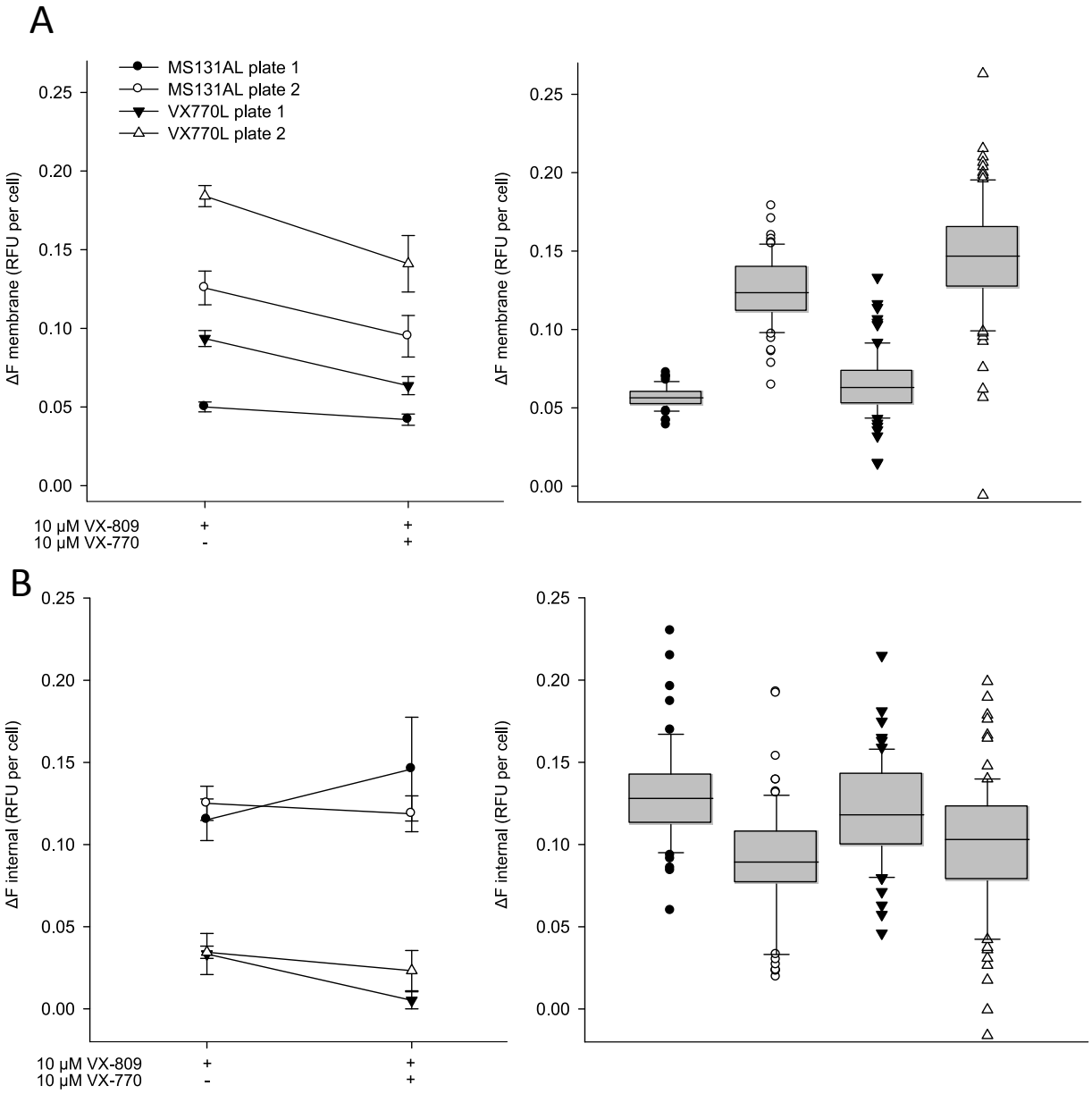


**Figure A2 ΔF508-CFTR-pHTomato within-plate controls.** A) Membrane-localised ΔF508-CFTR and B) Internal ΔF508-CFTR, from MS131A and VX-770L libraries, each run twice. Left: 10 μM VX-809 treated controls, ± 10 μM VX-770. Right: All compound data from corresponding plates.

Again, it seems that depending too heavily on controls, which do not necessarily represent the sample, leads to irregularities in the destabilisation screen.

Following the YFP-CFTR pilot ChemiBank screen, steps were taken to improve within-plate controls. For example, control wells were run at regular intervals throughout the plate, rather than only at the end, and were not placed in wells on the edges of the plate. Whilst these steps have improved controls in the YFP-CFTR screen (see section 5.7), the same does not appear to be true of CFTR-pHTomato.

In the YFP-CFTR pilot screen, to circumvent the problem caused by negative controls which did not accurately represent the plate data, the median quenching rate of the test compounds was instead used as the negative control (see section 5.4). This was possible because inspection of quenching traces showed that not many compounds had potentiator activity. This cannot be used for CFTR-pHTomato plate data. $\Delta_F$ values, used to quantify CFTR, are not comparable between plates. Therefore, there is no 'normal' negative control range to which plate data can be compared. If we cannot be confident that only a few compounds in the library are having an effect on membrane density, then obviously we cannot use the test compounds as the negative control.

**A.2 Imaging movies**

Examples of the images obtained during YFP-CFTR and CFTR-pHTomato imaging are stored on a DVD attached to the back cover.

M1.A and M1.B show YFP-WT-CFTR quenching in the presence and absence, respectively, of 10 μM forskolin, using the $I^-$ first addition protocol described on page 41 of the thesis. M2.A and M2.B show the same, using the $I^-$ second addition protocol described on page 41. The speed of these movies is increased 20X.

M3.A shows WT-CFTR-pHTomato imaging described on page 44 of the thesis. The speed of this movie is increased 2X. M3.B and M3.C show GFP and Hoechst, respectively, obtained during WT-CFTR-pHTomato imaging.

All images are 717.12 μm x 717.12 μm.

# References

Aleksandrov, A. a, Aleksandrov, L., and Riordan, J.R. (2002). Nucleoside triphosphate pentose ring impact on CFTR gating and hydrolysis. FEBS Lett. *518*: 183–8.

Ameen, N., Silvis, M., and Bradbury, N.A. (2007). Endocytic trafficking of CFTR in health and disease. J. Cyst. Fibros. *6*: 1–14.

Anderson, M.P., Gregory, R.J., Thompson, S., Souza, D.W., Paul, S., Mulligan, R.C., et al. (1991). Demonstration that CFTR is a chloride channel by alteration of its anion selectivity. Science *253*: 202–5.

Awale, M., Jin, X., and Reymond, J.-L. (2015). Stereoselective virtual screening of the ZINC database using atom pair 3D-fingerprints. J. Cheminform. *7*: 3.

Awale, M., and Reymond, J.L. (2014). Atom pair 2D-fingerprints perceive 3D-molecular shape and pharmacophores for very fast virtual screening of ZINC and GDB-17. J. Chem. Inf. Model. *54*: 1892–1907.

Bachhuber, T., König, J., Voelcker, T., Mûrie, B., Schreiber, R., and Kunzelmann, K. (2005). Cl- interference with the epithelial Na+ channel ENaC. J. Biol. Chem. *280*: 31587–31594.

Bali, V., Lazrak, A., Guroji, P., Matalon, S., and Bebok, Z. (2016). Mechanistic Approaches to Improve Correction of the Most Common Disease-Causing Mutation in Cystic Fibrosis. PLoS One *11*: e0155882.

Ban, H., Inoue, M., Griesenbach, U., Munkonge, F., Chan, M., Iida, A., et al. (2007). Expression and maturation of Sendai virus vector-derived CFTR protein : functional and biochemical evidence using a GFP-CFTR fusion protein. Gene Ther. *14*: 1688–1694.

Bompadre, S.G., Sohma, Y., Li, M., and Hwang, T.-C. (2007). G551D and G1349D, two CF-associated mutations in the signature sequences of CFTR, exhibit distinct gating defects. J. Gen. Physiol. *129*: 285–98.

Botelho, H.M., Uliyakina, I., Awatade, N.T., Proença, M.C., Tischer, C., Sirianant, L., et al. (2015). Protein Traffic Disorders: an Effective High-Throughput Fluorescence Microscopy Pipeline for Drug Discovery. Sci. Rep. *5*: 9038.

Boucher, R.C. (2007). Airway surface dehydration in cystic fibrosis: pathogenesis and

therapy. Annu. Rev. Med. *58*: 157–70.

Boyle, M.P., and Boeck, K. De (2013). A new era in the treatment of cystic fibrosis: correction of the underlying CFTR defect. Lancet Respir. Med. *1*: 158–163.

Bozoky, Z., Krzeminski, M., Muhandiram, R., Birtley, J.R., Al-Zahrani, A., Thomas, P.J., et al. (2013). Regulatory R region of the CFTR chloride channel is a dynamic integrator of phospho-dependent intra- and intermolecular interactions. Proc. Natl. Acad. Sci. U. S. A. *110*: E4427–36.

Bray, M., and Carpenter, A.E. (2013). Advanced Assay Development Guidelines for Image-Based High Content Screening and Analysis Assay Guidance Manual. Assay Guid. Man.

Bregestovski, P., Waseem, T., and Mukhtarov, M. (2009). Genetically encoded optical sensors for monitoring of intracellular chloride and chloride-selective channel activity. Front. Mol. Neurosci. *2*: 15.

Cantin, A.M., Hanrahan, J.W., Bilodeau, G., Ellis, L., Dupuis, A., Liao, J., et al. (2006). Cystic fibrosis transmembrane conductance regulator function is suppressed in cigarette smokers. Am. J. Respir. Crit. Care Med. *173*: 1139–1144.

Carlile, G.W., Robert, R., Zhang, D., Teske, K. a, Luo, Y., Hanrahan, J.W., et al. (2007). Correctors of protein trafficking defects identified by a novel high-throughput screening assay. Chembiochem *8*: 1012–20.

Chalfie, M., Tu, Y., Euskirchen, G., Ward, W.W., and Prasher, D.C. (1994). Green fluorescent protein as a marker for gene expression. Science *263*: 802–805.

Chan, K.W., Csanády, L., Seto-young, D., Nairn, A.C., and Gadsby, D.C. (2000). Severed Molecules Functionally Define the Boundaries of the Cystic Fibrosis Transmembrane Conductance Regulator's NH2 -terminal Nucleotide Binding Domain. J. Gen. Physiol. *116*: 163–180.

Chang, X.B., Cui, L., Hou, Y.X., Jensen, T.J., Aleksandrov, a a, Mengos, a, et al. (1999). Removal of multiple arginine-framed trafficking signals overcomes misprocessing of delta F508 CFTR present in most patients with cystic fibrosis. Mol. Cell *4*: 137–42.

Chang, X.B., Tabcharani, J. a, Hou, Y.X., Jensen, T.J., Kartner, N., Alon, N., et al. (1993). Protein kinase A (PKA) still activates CFTR chloride channel after mutagenesis of all 10 PKA consensus phosphorylation sites. J. Biol. Chem. *268*: 11304–11.

Cheng, S.H., Gregory, R.J., Marshall, J., Paul, S., Souza, D.W., White, G. a, et al. (1990).

Defective intracellular transport and processing of CFTR is the molecular basis of most cystic fibrosis. Cell *63*: 827–34.

Cholon, D.M., Quinney, N.L., Fulcher, M.L., Jr, C.R.E., Das, J., Dokholyan, N. V, et al. (2014). Potentiator ivacaftor abrogates pharmacological correction of D F508 CFTR in cystic fibrosis. Sci. Transl. Med. *6*: 1–11.

Coakley, R.D., Grubb, B.R., Paradiso, A.M., Gatzy, J.T., Johnson, L.G., Kreda, S.M., et al. (2003). Abnormal surface liquid pH regulation by cultured cystic fibrosis bronchial epithelium. Proc. Natl. Acad. Sci. U. S. A. *100*: 16083–16088.

Coppinger, J. a, Hutt, D.M., Razvi, A., Koulov, A. V, Pankow, S., Yates, J.R., et al. (2012). A chaperone trap contributes to the onset of cystic fibrosis. PLoS One *7*: e37682.

Cormack, B.P., Valdivia, R.H., and Falkow, S. (1996). FACS-optimized mutants of the green fluorescent protein (GFP). Gene *173*: 33–8.

Corradi, V., Vergani, P., and Tieleman, D.P. (2015). Cystic fibrosis transmembrane conductance regulator (CFTR): closed and open state channel models. J. Biol. Chem. jbc.M115.665125.

Csanády, L. (2000). Rapid kinetic analysis of multichannel records by a simultaneous fit to all dwell-time histograms. Biophys. J. *78*: 785–99.

Csanády, L., Chan, K.W., Seto-Young, D., Kopsco, D.C., Nairn, a C., and Gadsby, D.C. (2000). Severed channels probe regulation of gating of cystic fibrosis transmembrane conductance regulator by its cytoplasmic domains. J. Gen. Physiol. *116*: 477–500.

Csanády, L., Vergani, P., and Gadsby, D.C. (2010). Strict coupling between CFTR's catalytic cycle and gating of its Cl- ion pore revealed by distributions of open channel burst durations. Proc. Natl. Acad. Sci. U. S. A. *107*: 1241–6.

Cui, L., Aleksandrov, L., Chang, X.-B., Hou, Y.-X., He, L., Hegedus, T., et al. (2007). Domain interdependence in the biosynthetic assembly of CFTR. J. Mol. Biol. *365*: 981–94.

Cui, L., Aleksandrov, L., Hou, Y.-X., Gentzsch, M., Chen, J.-H., Riordan, J.R., et al. (2006). The role of cystic fibrosis transmembrane conductance regulator phenylalanine 508 side chain in ion channel gating. J. Physiol. *572*: 347–58.

Dalemans, W., Barbry, P., Champigny, G., Jallat, S., Dott, K., Dreyer, D., et al. (1991). Altered chloride ion channel kinetics associated with the deltaF508 cystic fibrosis mutation. Nature *354*: 526–528.

Dautzenberg, F.M., Higelin, J., and Teichert, U. (2000). Functional characterization of corticotropin-releasing factor type 1 receptor endogenously expressed in human embryonic kidney 293 cells. Eur. J. Pharmacol. *390*: 51–9.

Davies, J.C., Wainwright, C.E., Canny, G.J., Chilvers, M.A., Howenstine, M.S., Munck, A., et al. (2013). Efficacy and safety of Ivacaftor in patients aged 6 to 11 years with cystic fibrosis with a G155D mutation. Am. J. Respir. Crit. Care Med. *In press.*:

Denning, G.M., Anderson, M.P., Amara, J.F., Marshall, J., Smith, A.E., and Welsh, M.J. (1992). Processing of mutant cystic fibrosis transmembrane conductance regulator is temperature-sensitive. Nature *358*: 761–764.

Dodge, J. a, Lewis, P. a, Stanton, M., and Wilsher, J. (2007). Cystic fibrosis mortality and survival in the UK: 1947-2003. Eur. Respir. J. *29*: 522–6.

Domingue, J.C., Ao, M., Sarathy, J., George, A., Alrefai, W. a, Nelson, D.J., et al. (2014). HEK-293 cells expressing the cystic fibrosis transmembrane conductance regulator (CFTR): a model for studying regulation of Cl- transport. Physiol. Rep. *2*: 1–16.

Drumm, M.L., Wilkinson, D.J., Smit, L.S., Worrell, R.T., Strong, T. V, Frizzell, R.A., et al. (1991). Chloride Conductance Expressed by delF508 and Other Mutant CFTRs in Xenopus Oocytes. Science (80-. ). *254*: 1797–1799.

Du, K., and Lukacs, G.L. (2009). Cooperative Assembly and Misfolding of CFTR Domains In Vivo. Mol. Biol. Cell *20*: 1903–1915.

Du, K., Sharma, M., and Lukacs, G.L. (2005). The DeltaF508 cystic fibrosis mutation impairs domain-domain interactions and arrests post-translational folding of CFTR. Nat. Struct. Mol. Biol. *12*: 17–25.

Eckford, P.D.W., Li, C., Ramjeesingh, M., and Bear, C.E. (2012). Cystic fibrosis transmembrane conductance regulator (CFTR) potentiator VX-770 (ivacaftor) opens the defective channel gate of mutant CFTR in a phosphorylation-dependent but ATP-independent manner. J. Biol. Chem. *287*: 36639–49.

Eckford, P.D.W., Ramjeesingh, M., Molinski, S., Pasyk, S., Dekkers, J.F., Li, C., et al. (2014). VX-809 and Related Corrector Compounds Exhibit Secondary Activity Stabilizing Active F508del-CFTR after Its Partial Rescue to the Cell Surface. Chem. Biol. *18*: 1–13.

Farinha, C.M., and Amaral, M.D. (2005). Most F508del-CFTR is targeted to degradation at an early folding checkpoint and independently of calnexin. Mol. Cell. Biol. *25*: 5242–5252.

Farinha, C.M., King-Underwood, J., Sousa, M., Correia, A.R., Henriques, B.J., Roxo-Rosa, M., et al. (2013a). Revertants, low temperature, and correctors reveal the mechanism of F508del-CFTR rescue by VX-809 and suggest multiple agents for full correction. Chem. Biol. *20*: 943–955.

Farinha, C.M., King-Underwood, J., Sousa, M., Correia, A.R., Henriques, B.J., Roxo-Rosa, M., et al. (2013b). Revertants, Low Temperature, and Correctors Reveal the Mechanism of F508del-CFTR Rescue by VX-809 and Suggest Multiple Agents for Full Correction. Chem. Biol. *20*: 943–55.

Farinha, C.M., Sousa, M., Canato, S., Schmidt, A., Uliyakina, I., and Amaral, M.D. (2015). Increased efficacy of VX-809 in different cellular systems results from an early stabilization effect of F508del-CFTR. Pharmacol. Res. Perspect. *3*: e00152.

Flume, P. a, Liou, T.G., Borowitz, D.S., Li, H., Yen, K., Ordoñez, C.L., et al. (2012). Ivacaftor in subjects with cystic fibrosis who are homozygous for the F508del-CFTR mutation. Chest *142*: 718–24.

Fu, J., Ji, H.L., Naren, A.P., and Kirk, K.L. (2001). A cluster of negative charges at the amino terminal tail of CFTR regulates ATP-dependent channel gating. J. Physiol. *536*: 459–70.

Galietta, L. V, Jayaraman, S., and Verkman, a S. (2001a). Cell-based assay for high-throughput quantitative screening of CFTR chloride transport agonists. Am. J. Physiol. Cell Physiol. *281*: C1734–42.

Galietta, L.J., Haggie, P.M., and Verkman, a S. (2001b). Green fluorescent protein-based halide indicators with improved chloride and iodide affinities. FEBS Lett. *499*: 220–4.

Galietta, L.J., Springsteel, M.F., Eda, M., Niedzinski, E.J., By, K., Haddadin, M.J., et al. (2001c). Novel CFTR chloride channel activators identified by screening of combinatorial libraries based on flavone and benzoquinolizinium lead compounds. J. Biol. Chem. *276*: 19723–8.

Garland, A.L., Walton, W.G., Coakley, R.D., Tan, C.D., Gilmore, R.C., Hobbs, C. a, et al. (2013). Molecular basis for pH-dependent mucosal dehydration in cystic fibrosis airways. Proc. Natl. Acad. Sci. U. S. A. *110*: 15973–8.

Goktug, A.N., Chai, S.C., and Chen, T. (2013). Data analysis approaches in high throughput screening. In Drug Discovery, P.H. El-Shemy, ed.

González, J.E., Oades, K., Leychkis, Y., Harootunian, A., and Negulescu, P.A. (1999). Cell-

based assays and instrumentation for screening ion-channel targets. Drug Discov. Today *4*: 431–439.

Gregory, R.J., Rich, D.P., Cheng, S.H., Souza, D.W., Paul, S., Manavalan, P., et al. (1991). Maturation and function of cystic fibrosis transmembrane conductance regulator variants bearing mutations in putative nucleotide-binding domains 1 and 2. Mol. Cell. Biol. *11*: 3886–93.

Groot-Kormelink, P.J., Beato, M., Finotti, C., Harvey, R.J., and Sivilotti, L.G. (2002). Achieving optimal expression for single channel recording: A plasmid ratio approach to the expression of ??1 glycine receptors in HEK293 cells. J. Neurosci. Methods *113*: 207–214.

Gunderson, K.L., and Kopito, R.R. (1995). Conformational states of CFTR associated with channel gating: the role ATP binding and hydrolysis. Cell *82*: 231–9.

Haws, C.M., Nepomuceno, I.B., Krouse, M.E., Wakelee, H., Law, T., Xia, Y., et al. (1996). Delta F508-CFTR channels : kinetics , activation by forskolin , and potentiation by xanthines. Am. J. Physiol. Cell Physiol. *270*: C1544–1555.

He, L., Kota, P., Aleksandrov, A. a, Cui, L., Jensen, T., Dokholyan, N. V, et al. (2013). Correctors of ΔF508 CFTR restore global conformational maturation without thermally stabilizing the mutant protein. FASEB J. *27*: 536–45.

Heda, G.D., Tanwani, M., and Marino, C.R. (2001). The Delta F508 mutation shortens the biochemical half-life of plasma membrane CFTR in polarized epithelial cells. Am. J. Physiol. Cell Physiol. *280*: C166–74.

Heim, R., Cubitt, A.B., and Tsien, R.Y. (1995). Improved green fluorescence. Nature *373*: 663–664.

Heim, R., Prasher, D.C., and Tsien, R.Y. (1994). Wavelength mutations and posttranslational autoxidation of green fluorescent protein. Proc. Natl. Acad. Sci. U. S. A. *91*: 12501–4.

Hildebrandt, E., Ding, H., Mulky, A., Dai, Q., Aleksandrov, A.A., Bajrami, B., et al. (2015). A Stable Human-Cell System Overexpressing Cystic Fibrosis Transmembrane Conductance Regulator Recombinant Protein at the Cell Surface. Mol. Biotechnol.

Hoelen, H., Kleizen, B., Schmidt, A., Richardson, J., Charitou, P., Thomas, P.J., et al. (2010). The primary folding defect and rescue of ΔF508 CFTR emerge during translation of the mutant domain. PLoS One *5*: e15458.

Holleran, J.P., Glover, M.L., Peters, K.W., Bertrand, C. a, Watkins, S.C., Jarvik, J.W., et al. (2012). Pharmacological rescue of the mutant cystic fibrosis transmembrane conductance regulator (CFTR) detected by use of a novel fluorescence platform. Mol. Med. *18*: 685–96.

Howard, M., DuVall, M.D., Devor, D.C., Dong, J.Y., Henze, K., and Frizzell, R. a (1995). Epitope tagging permits cell surface detection of functional CFTR. Am. J. Physiol. *269*: C1565–76.

Irwin, J.J., Sterling, T., Mysinger, M.M., Bolstad, E.S., and Coleman, R.G. (2012). ZINC: A Free Tool to Discover Chemistry for Biology. J. Chem. Inf. Model. *52*: 1757–1768.

Jayaraman, S., Haggie, P., Wachter, R.M., Remington, S.J., and Verkman, a S. (2000). Mechanism and cellular applications of a green fluorescent protein-based halide sensor. J. Biol. Chem. *275*: 6047–50.

Jih, K.-Y., and Hwang, T.-C. (2013). Vx-770 potentiates CFTR function by promoting decoupling between the gating cycle and ATP hydrolysis cycle. Proc. Natl. Acad. Sci. U. S. A. 1–6.

Jih, K.-Y., Sohma, Y., and Hwang, T.-C. (2012a). Nonintegral stoichiometry in CFTR gating revealed by a pore-lining mutation. J. Gen. Physiol. *140*: 347–59.

Jih, K.-Y., Sohma, Y., Li, M., and Hwang, T.-C. (2012b). Identification of a novel post-hydrolytic state in CFTR gating. J. Gen. Physiol. *139*: 359–70.

Kanelis, V., Hudson, R.P., Thibodeau, P.H., Thomas, P.J., and Forman-Kay, J.D. (2010). NMR evidence for differential phosphorylation-dependent interactions in WT and DeltaF508 CFTR. EMBO J. *29*: 263–77.

Kopeikin, Z., Yuksek, Z., Yang, H.-Y., and Bompadre, S.G. (2014). Combined effects of VX-770 and VX-809 on several functional abnormalities of F508del-CFTR channels. J. Cyst. Fibros.

Larsen, M.B., Hu, J., Frizzell, R.A., and Watkins, S.C. (2015). Simple image-based no-wash method for quantitative detection of surface expressed CFTR. METHODS.

Lazrak, A., Fu, L., Bali, V., Bartoszewski, R., Rab, A., Havasi, V., et al. (2013). The silent codon change I507-ATC->ATT contributes to the severity of the ΔF508 CFTR channel dysfunction. FASEB J. *27*: 4630–45.

Lewis, H. a, Zhao, X., Wang, C., Sauder, J.M., Rooney, I., Noland, B.W., et al. (2005). Impact of the deltaF508 mutation in first nucleotide-binding domain of human cystic fibrosis

transmembrane conductance regulator on domain folding and structure. J. Biol. Chem. *280*: 1346–53.

Li, C., Ramjeesingh, M., Wang, W., Garami, E., Hewryk, M., Lee, D., et al. (1996). ATPase activity of the cystic fibrosis transmembrane conductance regulator. J. Biol. Chem. *271*: 28463–8.

Li, Y., and Tsien, R.W. (2012). pHTomato, a red, genetically encoded indicator that enables multiplex interrogation of synaptic activity. Nat. Neurosci. *15*: 1047–53.

Lin, W.-Y., Jih, K.-Y., and Hwang, T.-C. (2014). A single amino acid substitution in CFTR converts ATP to an inhibitory ligand. J. Gen. Physiol. *144*: 311–320.

Linsdell, P., Tabcharani, J. a, Rommens, J.M., Hou, Y.X., Chang, X.B., Tsui, L.C., et al. (1997). Permeability of wild-type and mutant cystic fibrosis transmembrane conductance regulator chloride channels to polyatomic anions. J.Gen.Physiol. *110*: 355–364.

Loo, M. a, Jensen, T.J., Cui, L., Hou, Y., Chang, X.B., and Riordan, J.R. (1998). Perturbation of Hsp90 interaction with nascent CFTR prevents its maturation and accelerates its degradation by the proteasome. EMBO J. *17*: 6879–87.

Lozano, R., Mohsen Naghavi, Kyle Foreman, Stephen Lim, Kenji Shibuya, Victor Aboyans*, Jerry Abraham*, Timothy Adair*, Rakesh Aggarwal*, S.Y.A., Mohammad A AlMazroa*, Miriam Alvarado*, H Ross Anderson*, Laurie M Anderson*, Kathryn G Andrews*, Charles Atkinson*, Larry M Baddour*, S.B.-C., David H Bartels*, Michelle L Bell*, Emelia J Benjamin*, Derrick Bennett*, Kavi Bhalla*, Boris Bikbov*, Aref Bin Abdulhak*, Gretchen Birbeck*, Fiona Blyth*, I.B., Soufi ane Boufous*, Chiara Bucello*, Michael Burch*, Peter Burney*, Jonathan Carapetis*, Honglei Chen*, David Chou*, Sumeet S Chugh*, Luc E Coff eng*, S.D.C., Samantha Colquhoun*, K Ellicott Colson*, John Condon*, Myles D Connor*, Leslie T Cooper*, Matthew Corriere*, Monica Cortinovis*, Karen Courville de Vaccaro*, W.C., et al. (2012). Global and regional mortality from 235 causes of death for 20 age groups in 1990 and 2010: a systematic analysis for the Global Burden of Disease Study 2010. Lancet *380*: 2095–128.

Lu, Y., Xiong, X., Helm, A., Kimani, K., Bragin, A., and Skach, W.R. (1998). Co- and Posttranslational Translocation Mechanisms Direct Cystic Fibrosis Transmembrane Conductance Regulator N Terminus Transmembrane Assembly. J. Biol. Chem. *273*: 568–576.

Lubamba, B., Dhooghe, B., Noel, S., and Leal, T. (2012). Cystic fibrosis: insight into CFTR

pathophysiology and pharmacotherapy. Clin. Biochem. *45*: 1132–44.

Lukacs, G.L., Chang, X.B., Bear, C.E., Kartner, N., Mohamed, a, Riordan, J.R., et al. (1993). The DF508 mutation decreases the stability of cystic fibrosis transmembrane conductance regulator in the plasma membrane. J Biol Chem *268*: 21592–21598.

Ma, T., Thiagarajah, J.R., Yang, H., Sonawane, N.D., Folli, C., Galietta, L.J. V, et al. (2002). Thiazolidinone CFTR inhibitor identified by high-throughput screening blocks cholera toxin – induced intestinal fluid secretion. J. Clin. Invest. *110*: 1651–1658.

Matthes, E., Goepp, J., Carlile, G.W., Luo, Y., Dejgaard, K., Billet, A., et al. (2015). Low free drug concentration prevents inhibition of F508del CFTR functional expression by the potentiator VX-770 (ivacaftor). Br. J. Pharmacol. *770*: n/a–n/a.

Meacham, G.C., Patterson, C., Zhang, W., Younger, J.M., and Cyr, D.M. (2001). The Hsc70 co-chaperone CHIP targets immature CFTR for proteasomal degradation. Nat. Cell Biol. *3*: 100–5.

Middleton, P.G., and House, H.H. (2010). Measurement of airway ion transport assists the diagnosis of cystic fibrosis. Pediatr. Pulmonol. *45*: 789–795.

Mihalyi, C., Torocsik, B., and Csanady, L. (2016). Obligate coupling of CFTR pore opening to tight nucleotide-binding domain dimerization. Elife *1.*:

Miki, H., Zhou, Z., Li, M., Hwang, T.-C., and Bompadre, S.G. (2010). Potentiation of disease-associated cystic fibrosis transmembrane conductance regulator mutants by hydrolyzable ATP analogs. J. Biol. Chem. *285*: 19967–75.

Moyer, B.D., Loffing, J., Schwiebert, E.M., Loffing-cueni, D., Halpin, P.A., Karlson, K.H., et al. (1998). Membrane Trafficking of the Cystic Fibrosis Gene Product , Cystic Fibrosis Transmembrane Conductance Regulator , Tagged with Green Fluorescent Protein in Madin-Darby Canine Kidney Cells *. J. Biol. Chem. *273*: 21759–21768.

Muanprasat, C., Sonawane, N.D., Salinas, D., Taddei, A., Galietta, L.J. V, and Verkman, a S. (2004). Discovery of glycine hydrazide pore-occluding CFTR inhibitors: mechanism, structure-activity analysis, and in vivo efficacy. J. Gen. Physiol. *124*: 125–37.

Mueller, C., Braag, S.A., Keeler, A., Hodges, C., Drumm, M., and Flotte, T.R. (2011). Lack of cystic fibrosis transmembrane conductance regulator in CD3+ lymphocytes leads to aberrant cytokine secretion and hyperinflammatory adaptive immune responses. Am. J. Respir. Cell Mol. Biol. *44*: 922–929.

Munye, M.M., Ravi, J., Tagalakis, A.D., McCarthy, D., Ryadnov, M.G., and Hart, S.L. (2015). Role of liposome and peptide in the synergistic enhancement of transfection with a lipopolyplex vector. Sci. Rep. *5*: 9292.

Namkung, W., Park, J., Seo, Y., and Verkman, A.S. (2013). Novel Amino-Carbonitrile-Pyrazole Identified in a Small Molecule Screen Activates Wild-Type and Δ F508 Cystic Fibrosis Transmembrane Conductance Regulator in the Absence of a cAMP Agonist. Mol. Pharmacol. *84*: 384–392.

Naren, A.P., Cormet-Boyaka, E., Fu, J., Villain, M., Blalock, J.E., Quick, M.W., et al. (1999). CFTR Chloride Channel Regulation by an Interdomain Interaction. Science (80-. ). *286*: 544–548.

Oda, S., Fukami, T., Yokoi, T., and Nakajima, M. (2015). A comprehensive review of UDP-glucuronosyltransferase and esterases for drug development. Drug Metab. Pharmacokinet. *30*: 30–51.

Okiyoneda, T., Barrière, H., Bagdány, M., Rabeh, W.M., Du, K., Höhfeld, J., et al. (2010). Peripheral protein quality control removes unfolded CFTR from the plasma membrane. Science *329*: 805–10.

Okiyoneda, T., Veit, G., Dekkers, J.F., Bagdany, M., Soya, N., Xu, H., et al. (2013). Mechanism-based corrector combination restores deltaF508-CFTR folding and function. Nat. Chem. Biol.

Ormo, M., Cubitt, A.B., Kallio, K., Gross, L.A., Tsien, R.Y., and Remington, S.J. (1996). Crystal structure of the Aequorea victoria green fluorescent protein. Science (80-. ). *273*: 1392–1395.

Pasyk, S., Molinksi, S., Ahmadi, S., Ramjeesingh, M., Huan, L.-J., Chin, S., et al. (2015). The Major Cystic Fibrosis Causing Mutation Exhibits Defective Propensity for Phosphorylation. Proteomics *15*: 447–461.

Pedemonte, N., Lukacs, G.L., Du, K., Caci, E., Zegarra-moran, O., Galietta, L.J. V, et al. (2005a). Small-molecule correctors of defective ΔF508-CFTR cellular processing identified by high-throughput screening. J. Clin. Invest. *115*: 2564–2571.

Pedemonte, N., Sonawane, N.D., Taddei, A., Hu, J., Zegarra-moran, O., Suen, Y.F., et al. (2005b). Phenylglycine and Sulfonamide Correctors of Defective delF508 and G551D Cystic Fibrosis Transmembrane Conductance Regulator Chloride-Channel Gating. Mol. Pharmacol. *67*: 1797–1807.

Pezzulo, A.A., Tang, X.X., Hoegger, M.J., Alaiwa, M.H.A., Ramachandran, S., Moninger, T.O., et al. (2012). Reduced airway surface pH impairs bacterial killing in the porcine cystic fibrosis lung. Nature *487*: 109–13.

Phuan, P.-W., Veit, G., Tan, J., Finkbeiner, W.E., Lukacs, G.L., and Verkman, A.S. (2015). Potentiators of Defective ΔF508-CFTR Channel Gating that do not Interfere with Corrector Action. Mol. Pharmacol. *88*: mol.115.099689–.

Phuan, P.-W., Veit, G., Tan, J., Roldan, A., Finkbeiner, W.E., Lukacs, G., et al. (2014). Synergy-based Small-Molecule Screen Using a Human Lung Epithelial Cell Line Yields F508-CFTR Correctors that Augment VX-809 Maximal Efficacy. Mol. Pharmacol. *86*: 42–51.

Prince, L.S. (1999). Efficient Endocytosis of the Cystic Fibrosis Transmembrane Conductance Regulator Requires a Tyrosine-based Signal. J. Biol. Chem. *274*: 3602–3609.

Pyle, L.C., Ehrhardt, A., Mitchell, L.H., Fan, L., Ren, A., Naren, A.P., et al. (2011). Regulatory domain phosphorylation to distinguish the mechanistic basis underlying acute CFTR modulators. Am. J. Physiol. Lung Cell. Mol. Physiol. *301*: L587–97.

Rabeh, W.M., Bossard, F., Xu, H., Okiyoneda, T., Bagdany, M., Mulvihill, C.M., et al. (2012). Correction of both NBD1 energetics and domain interface is required to restore ΔF508 CFTR folding and function. Cell *148*: 150–63.

Rai, V., Gaur, M., Shukla, S., Shukla, S., Ambudkar, S. V., Komath, S.S., et al. (2006). Conserved Asp327 of Walker B motif in the N-terminal nucleotide binding domain (NBD-1) of Cdr1p of Candida albicans has acquired a new role in ATP hydrolysis. Biochemistry *45*: 14726–14739.

Ramjeesingh, M., Li, C., Garami, E., Huan, L.J., Galley, K., Wang, Y., et al. (1999). Walker mutations reveal loose relationship between catalytic and channel-gating activities of purified CFTR (cystic fibrosis transmembrane conductance regulator). Biochemistry *38*: 1463–1468.

Ramsey, B.W., Jane, D., McElvaney, N.G., Tullis, E., Bell, S.C., Dřevínek, P., et al. (2011). A CFTR Potentiator in Patients with Cystic Fibrosis and the G155D mutation. N. Engl. J. Med. *365*: 1663–1672.

Ratner, D., and Mueller, C. (2012). Immune responses in cystic fibrosis: Are they intrinsically defective? Am. J. Respir. Cell Mol. Biol. *46*: 715–722.

Robert, R., Carlile, G.W., Pavel, C., Liu, N., Anjos, S.M., Liao, J., et al. (2008). Structural Analog of Sildenafil Identified as a Novel Corrector of the F508del-CFTR Trafficking Defect.

Mol. Pharmacol. *73*: 478–489.

Roxo-Rosa, M., Xu, Z., Schmidt, A., Neto, M., Cai, Z., Soares, C.M., et al. (2006). Revertant mutants G550E and 4RK rescue cystic fibrosis mutants in the first nucleotide-binding domain of CFTR by different mechanisms. Proc. Natl. Acad. Sci. U. S. A. *103*: 17891–6.

Sabirzhanova, I., Lopes Pacheco, M., Rapino, D., Grover, R., Handa, J.T., Guggino, W.B., et al. (2015). Rescuing trafficking mutants of the ATP-binding cassette protein, ABCA4, with small molecule correctors as a treatment for Stargardt eye disease. J. Biol. Chem. *290*: 19743–19755.

Schultz, B.D., Takahashi, a, Liu, C., Frizzell, R. a, and Howard, M. (1997). FLAG epitope positioned in an external loop preserves normal biophysical properties of CFTR. Am. J. Physiol. *273*: C2080–9.

Serohijos, A.W.R., Aleksandrov, A.A., He, L., Cui, L., Dokholyan, N. V, and Riordan, J.R. (2008). Phenylalanine-508 mediates a cytoplasmic – membrane domain contact in the CFTR 3D structure crucial to assembly and channel function. Proc. Natl. Acad. Sci. U. S. A. *105*: 3256–3261.

Shah, K., Cheng, Y., Hahn, B., Bridges, R., Bradbury, N. a., and Mueller, D.M. (2015). Synonymous Codon Usage Affects the Expression of Wild Type and F508del CFTR. J. Mol. Biol. *427*: 1464–1479.

Sharma, M., Benharouga, M., Hu, W., and Lukacs, G.L. (2001). Conformational and temperature-sensitive stability defects of the delta F508 cystic fibrosis transmembrane conductance regulator in post-endoplasmic reticulum compartments. J. Biol. Chem. *276*: 8942–50.

Sharma, M., Pampinella, F., Nemes, C., Benharouga, M., So, J., Du, K., et al. (2004). Misfolding diverts CFTR from recycling to degradation: quality control at early endosomes. J. Cell Biol. *164*: 923–33.

Shaw, G., Morse, S., Ararat, M., and Graham, F.L. (2002). Preferential transformation of human neuronal cells by human adenoviruses and the origin of HEK 293 cells. FASEB J. *16*: 869–71.

Sloane, P. a, Shastry, S., Wilhelm, A., Courville, C., Tang, L.P., Backer, K., et al. (2012). A pharmacologic approach to acquired cystic fibrosis transmembrane conductance regulator dysfunction in smoking related lung disease. PLoS One *7*: e39809.

Sorum, B., Czégé, D., and Csanády, L. (2015). Timing of CFTR Pore Opening and Structure of Its Transition State. Cell *163*: 724–733.

Stoltz, D.A., Meyerholz, D.K., Pezzulo, A.A., Ramachandran, S., Rogan, M.P., Davis, G.J., et al. (2010). Cystic Fibrosis Pigs Develop Lung Disease and Exhibit Defective Bacterial Eradication at Birth. Sci. Transl. Med. *2*: 29ra31–29ra31.

Stutts, M.J., Canessa, C.M., Olsen, J.C., Hamrick, M., Cohn, J.A., Rossier, B.C., et al. (1995). CFTR as a cAMP-Dependent Regulator of Sodium Channels. Science (80-. ). *269*: 847–850.

Thibodeau, P.H., Richardson, J.M., Wang, W., Millen, L., Watson, J., Mendoza, J.L., et al. (2010). The cystic fibrosis-causing mutation deltaF508 affects multiple steps in cystic fibrosis transmembrane conductance regulator biogenesis. J. Biol. Chem. *285*: 35825–35.

Tirouvanziam, R., Bentzmann, S. De, Hubeau, C., Hinnrasky, J., Jacquot, J., Péault, B., et al. (2000). Inflammation and infection in naive human cystic fibrosis airway grafts. Am. J. Respir. Cell Mol. Biol. *23*: 121–127.

Tsai, M.-F., Li, M., and Hwang, T.-C. (2010). Stable ATP binding mediated by a partial NBD dimer of the CFTR chloride channel. J. Gen. Physiol. *135*: 399–414.

Urbatsch, I.L., Sankaran, B., Weber, J., and Senior, A.E. (1995). P-glycoprotein is stably inhibited by vandate-induced trapping of nucleotide at a single catalytic site. J. Biol. Chem. *270*: 19383–19390.

Vais, H., Gao, G.-P., Yang, M., Tran, P., Louboutin, J.-P., Somanathan, S., et al. (2004). Novel adenoviral vectors coding for GFP-tagged wtCFTR and deltaF508-CFTR: characterization of expression and electrophysiological properties in A549 cells. Pflugers Arch. *449*: 278–87.

Van Goor, F., Hadida, S., Grootenhuis, P.D.J., Burton, B., Cao, D., Neuberger, T., et al. (2009). Rescue of CF airway epithelial cell function in vitro by a CFTR potentiator, VX-770. Proc. Natl. Acad. Sci. U. S. A. *106*: 18825–30.

Van Goor, F., Hadida, S., Grootenhuis, P.D.J., Burton, B., Stack, J.H., Straley, K.S., et al. (2011). Correction of the F508del-CFTR protein processing defect in vitro by the investigational drug VX-809. Proc. Natl. Acad. Sci. U. S. A. *108*: 18843–8.

Van Goor, F., Straley, K.S., Cao, D., González, J., Hadida, S., Hazlewood, A., et al. (2006). Rescue of DeltaF508-CFTR trafficking and gating in human cystic fibrosis airway primary

cultures by small molecules. Am. J. Physiol. Lung Cell. Mol. Physiol. *290*: L1117–30.

Van Goor, F., Yu, H., Burton, B., and Hoffman, B.J. (2013). Effect of ivacaftor on CFTR forms with missense mutations associated with defects in protein processing or function. J. Cyst. Fibros.

Veit, G., Avramescu, R.G., Perdomo, D., Phuan, P.-W., Bagdany, M., Apaja, P.M., et al. (2014). Some gating potentiators, including VX-770, diminish F508-CFTR functional expression. Sci. Transl. Med. *6*: 246ra97–246ra97.

Vergani, P., Lockless, S.W., Nairn, A.C., and Gadsby, D.C. (2005). CFTR channel opening by ATP-driven tight dimerization of its nucleotide-binding domains. Nature *433*: 876–80.

Vergani, P., Nairn, A.C., and Gadsby, D.C. (2003). On the Mechanism of MgATP-dependent Gating of CFTR Cl- Channels. J. Gen. Physiol. *120*: 17–36.

Wachter, R.M., Yarbrough, D., Kallio, K., and Remington, S.J. (2000). Crystallographic and energetic analysis of binding of selected anions to the yellow variants of green fluorescent protein. J. Mol. Biol. *301*: 157–71.

Wainwright, C.E., Elborn, J.S., Ramsey, B.W., Marigowda, G., Huang, X., Cipolli, M., et al. (2015). Lumacaftor–Ivacaftor in Patients with Cystic Fibrosis Homozygous for Phe508del *CFTR*. N. Engl. J. Med. 150517100015004.

Wang, F., Zeltwanger, S., Hu, S., and Hwang, T.C. (2000). Deletion of phenylalanine 508 causes attenuated phosphorylation-dependent activation of CFTR chloride channels. J. Physiol. *524 Pt 3*: 637–48.

Wang, X., Koulov, A. V, Kellner, W. a, Riordan, J.R., and Balch, W.E. (2008). Chemical and biological folding contribute to temperature-sensitive DeltaF508 CFTR trafficking. Traffic *9*: 1878–93.

Wang, X., Matteson, J., An, Y., Moyer, B., Yoo, J.-S., Bannykh, S., et al. (2004). COPII-dependent export of cystic fibrosis transmembrane conductance regulator from the ER uses a di-acidic exit code. J. Cell Biol. *167*: 65–74.

Wellhauser, L., Chiaw, P.K., Pasyk, S., Li, C., Ramjeesingh, M., and Bear, C.E. (2009). A Small-Molecule Modulator Interacts Directly with Phe508- CFTR to Modify Its ATPase Activity and Conformational Stability. Mol. Pharmacol. *75*: 1430–1438.

Wu, M.M., Grabe, M., Adams, S., Tsien, R.Y., Moore, H.P.H., and Machen, T.E. (2001). Mechanisms of pH Regulation in the Regulated Secretory Pathway. J. Biol. Chem. *276*:

33027–33035.

Xu, J., Chai, H., Ehinger, K., Egan, T.M., Srinivasan, R., Frick, M., et al. (2014). Imaging P2X4 receptor subcellular distribution, trafficking, and regulation using P2X4-pHluorin. J. Gen. Physiol. *144*: 81–104.

Yang, H., Shelat, A. a, Guy, R.K., Gopinath, V.S., Ma, T., Du, K., et al. (2003). Nanomolar affinity small molecule correctors of defective Delta F508-CFTR chloride channel gating. J. Biol. Chem. *278*: 35079–85.

Yang, Y., Janich, S., Cohn, J.A., and Wilson, J.M. (1993). The Common Variant of Cystic Fibrosis Transmembrane Conductance Regulator is Recognized by hsp7O and Degraded in a Pre-Golgi Nonlysosomal Compartment. Proc. Natl. Acad. Sci. U. S. A. *90*: 9480–9484.

Yu, H., Burton, B., Huang, C.-J., Worley, J., Cao, D., Johnson, J.P., et al. (2012). Ivacaftor potentiation of multiple CFTR channels with gating mutations. J. Cyst. Fibros. *11*: 237–45.

Zhang, L., Aleksandrov, L.A., Riordan, J.R., and Ford, R.C. (2011). Do main location within the cystic fibrosis transmembrane conductance regulator protein investigated by electron microscopy and gold labelling. Biochim. Biophys. Acta - Biomembr. *1808*: 399–404.

Zhang, X.D. (2007). A pair of new statistical parameters for quality control in RNA interference high-throughput screening assays. Genomics *89*: 552–561.

Zhang, X.D. (2008). Novel analytic criteria and effective plate designs for quality control in genome-scale RNAi screens. J. Biomol. Screen. Off. J. Soc. Biomol. Screen. *13*: 363–377.

Zhang, X.D. (2011). Illustration of SSMD, z score, SSMD*, z* score, and t statistic for hit selection in RNAi high-throughput screens. J. Biomol. Screen. Off. J. Soc. Biomol. Screen. *16*: 775–785.

Zhang, X.D., Ferrer, M., Espeseth, A.S., Marine, S.D., Stec, E.M., Crackower, M. a, et al. (2007). The use of strictly standardized mean difference for hit selection in primary RNA interference high-throughput screening experiments. J. Biomol. Screen. Off. J. Soc. Biomol. Screen. *12*: 497–509.

Zhou, Z., Hu, S., and Hwang, T.C. (2001). Voltage-dependent flickery block of an open cystic fibrosis transmembrane conductance regulator (CFTR) channel pore. J. Physiol. *532*: 435–448.